Politecnico di Torino

ScuDo
Scuola di Dottorato ~ Doctoral School
WHAT YOU ARE, TAKES YOU FAR

Doctoral Dissertation
Doctoral Program in Civil and Environmental Engineering (36th Cycle)

Seismic reliability of 3D isolated bridges accounting for spatial variability of earthquake ground motion

Guglielmo Amendola

* * * * * *

Supervisors
Prof. Paolo Castaldo, Supervisor
Prof. Luca Giordano, Co-Supervisor

Politecnico di Torino

2024-06-26

I hereby declare that the contents and organization of this dissertation constitute my own original work and does not compromise in any way the rights of third parties, including those relating to the security of personal data.

…….....

Guglielmo Amendola

Turin, June 26, 2024

Summary

In the last decades, the detrimental effects of the asynchronous excitation on long-extended structures such as bridges and viaducts have drawn the attention of the scientific community. The observed damages from past earthquakes together with the data collected by dense seismic arrays installed all over the world and the increasing computational power have given rise to a comprehensive study of the main causes of the spatial variability of earthquake ground motion (SVEGM).

Bridges have long been studied due to their crucial role in the socioeconomic life of modern communities. Their closure, whether permanent or temporary, can trigger significant ripple effects, including business losses and delays in emergency operations.

It is nowadays well recognized that the causes of SVEGM are primarily the following: a) wave passage effect; b) loss of seismic waves coherency as the distance between further away support points increases, resulting from multiple reflections, refractions, and superimposition of seismic waves when traveling through the soil layers; c) local site effects corresponding to the different local soil conditions under the structure supports. This latter point is particularly relevant for structures that extend over significant distances.

The above sources of SVEGM are mathematically expressed in terms of the degree of correlation between seismic time histories, which is a decreasing function of both distance and time.

Among the different simulation techniques discussed in the literature, this work of thesis adopts the spectral-representation method. In this method, the ground motion at different support points is modeled as a one-dimensional, multi-variate (1D-*m*V), quasi-stationary stochastic Gaussian vector process, where only the amplitude of the process is considered to vary with time. Within this framework, a specific correlation function is introduced alongside a spectrum-compatible power spectral density function.

The overarching goal of this PhD thesis is to enhance the understanding of SVEGM effects on isolated bridges, with a particular focus on those equipped with friction pendulum isolators. This task is accomplished through a full-probabilistic seismic structural analysis approach, comparing the bridge seismic response under uniform and spatially variable input conditions. Additionally, the seismic reliability concerning the main isolated bridge components-piers and isolation devices (friction pendulum isolators)-is assessed.

The testbed bridge adopted for the aforementioned seismic analysis is an existing reinforced concrete bridge with an overall length of 163.0 m, simply supported on four piers and two seat-type abutments at the ends. The bridge is located in central Italy, near the well-known city of L'Aquila, which serves as a reference site for seismic hazard derivation. The testbed bridge is considered to have been retrofitted through a friction-type seismic isolation system due to the lack of design seismic details in the reinforced concrete piers. In addition, a 7-span bridge configuration derived from the original design is studied to explore the effects of the SVEGM on increasing bridge lengths (*i.e.*, number of spans). To perform a parametric analysis concerning the friction pendulum isolator, three different radii of curvature and consequently three different isolation periods are selected. In this study, the friction pendulum behaviour is described assuming the friction coefficient as a function of the sliding velocity. Due to the significant variability of friction caused by environmental effects, this coefficient is treated as a random variable with ten samples extracted from a standard normal probability density function.

The entire set of structural bridge models is implemented in *Opensees*, an open-source finite element software, adopting a three-dimensional spine line model approach. The bridge's response is assessed through nonlinear time history analysis with seismic input generated as previously described and scaled to increasing intensity levels such as to perform incremental dynamic analysis (IDA). Two different incidence angle conditions of 30° and 60° relative to the longitudinal bridge axis are additionally included in the analysis.

The results obtained are expressed at first in terms of IDA curves pertaining to isolator displacements and piers' drift and curvature ductility, assumed as engineering demand parameters (EDPs).

Following the definition of specific damage limit states for the selected EDPs, the seismic fragility curves for both the piers and the isolators are derived.

Finally, considering the seismic hazard curves related to the reference site of L'Aquila (Italy), the seismic reliability related to both the piers and FP isolators is assessed through the convolution integral between seismic hazard and seismic

fragility. The seismic reliability denotes the probability of exceeding a specific damage limit state in the time frame of interest (*e.g.* 50 years). In this study, a seismic reliability-based approach is particularly valuable since it permits the computation of seismic reliability-based design (SRBD) abacuses for the design of the friction pendulum isolator's radius in plan.

The results indicate that SVEGM is always detrimental when compared to the uniform input conditions, especially as the overall bridge length and isolation period increase. It has been also derived that SVEGM can require friction pendulum isolator radii in plan up to nearly 20cm greater than those required under uniform excitation conditions.

Additionally, using the reliability-based design (SRBD) abacuses, design safety factors have been computed based on the seismic isolation period and the number of spans of the bridge, implicitly considering spatial variability of earthquake ground motion (SVEGM). While these results are not exhaustive, as a broader range of bridge lengths should be analyzed, they provide insights into the seismic design of friction pendulum system (FPS) under SVEGM input condition. The design safety factors tend to increase with the number of spans, isolation period, and quasi-orthogonal incidence angles. For this combination of seismic input and structural properties, the analyses suggest a design safety factor ranging from SF=1.10 to SF=1.40.

This thesis is dedicated to all the suffering animals around the world. May our advances in research and knowledge lead to a brighter, more compassionate future for all sentient beings.

Contents

List of Tables

List of Figures

Preface

This dissertation aims to evaluate the seismic reliability of multi-span reinforced concrete (RC) bridges seismically isolated with friction pendulum system (FPS) devices, considering spatial variability of earthquake ground motion (SVEGM). The goal is to understand how it affects the response of these structures and to provide design abacuses for the friction pendulum bearings following the performance-based-earthquake engineering (PBEE) methodology.

Chapter 1 intends to provide an overlook of the most important aspects regarding seismic risk evaluation with specific attention on the concept of structural reliability, within the context of Performance-Based Earthquake Engineering (PBEE). At first, the methodology approach, following the PBEE, as framed by the Pacific Earthquake Engineering Research (PEER) Center, is examined. Next, the concept of seismic risk is explained both in qualitative and quantitative terms, emphasizing the key components involved: seismic hazard, seismic vulnerability, and exposure. A specific focus is given to the assessment of seismic vulnerability for a specific asset at risk, such as bridge structures. In this context, the derivation of analytical fragility functions, which are used to describe seismic vulnerability, is presented next.

Finally, the chapter delves into the concept of structural reliability, exposing the main source of uncertainties involved in the reliability assessment. It also discusses different approaches (reliability methods), that may be employed for evaluating seismic and structural reliability. Additionally, these approaches may require the use of simulation techniques such as the Monte Carlo technique or the more efficient Latin Hypercube sampling method. Both techniques are discussed in this chapter within the framework of reliability assessment.

Chapter 2 begins with an overview of the typical damage patterns caused to bridges from past earthquakes, with a particular emphasis on those damages observed to bridge configurations more susceptible to the spatial variability of ground motion. Following this, it provides a brief description of the primary bridge structural components. Finally, the chapter illustrates the basic principles of seismic isolation as applied to bridge structures, highlighting the effectiveness of this technique in mitigating or preventing structural damage caused by earthquakes.

Chapter 3 presents an overview of the elastic seismic isolation theory. It begins with an introduction of the basic principles of seismically isolated systems, originally developed by Prof. J. Kelly in 1996 for building structures. It follows a detailed description of friction pendulum bearings, specifically emphasizing their dynamic behavior and the friction-related properties that characterize these devices. Furthermore, the chapter explores the key factors influencing the friction coefficient, including apparent pressure, sliding velocity, temperature variations, and the loading history.

Finally, a proposed numerical model is presented for multi-span continuous deck bridges that are seismically isolated using friction pendulum devices.

Chapter 4 explores the fundamental concepts of spatial variability of earthquake ground motion (SVEGM). It starts with a historical overview of the key studies and findings in the scientific literature regarding the topic. It is nowadays well established that SVEGM primarily arises from factors such as the loss of coherence, the so-called wave-passage effect, and the site-response effect. Given the complexity of the phenomenon, a deterministic analysis approach is impractical, requiring the use of probabilistic methods instead. Before delving into the adopted simulation techniques, a brief description of the equation of motions valid for a multi-degree-of-freedom (MDOF) system, subjected to different input ground motions, is provided. Following this, it discusses the main aspects of the spectral representation method used to simulate spatially variable earthquake ground motions. Within this method, particular attention is given to the specifically selected power spectral density (PSD), coherency function, and modulating function. Additionally, this study adopts a generation procedure that accounts for spectrum compatibility with the specific site of interest. Thus, this procedure is described along with its implementation to the case study, which refers to a friction pendulum seismically isolated multi-span reinforced concrete bridge located near the site of L'Aquila, in Italy.

Finally, the chapter presents a validation of the adopted procedure, which particularly compares the simulated coherency functions with the target ones initially integrated into the adopted procedure.

Chapter 5 describes the testbed bridge adopted in the analysis: an existing simply supported reinforced concrete (RC) bridge located in central Italy, near the site of L'Aquila.

Due to the lack of design seismic details, primarily in the pier component, the bridge will be retrofitted with a seismic isolation system using friction-type devices (i.e., FP system).

The chapter includes an in-depth focus on the numerical model of each bridge component implemented in Opensees, the open-source software for structural and geotechnical problems. The model uses a three-dimensional spine line approach with elastic beam-column elements for the deck and fiber-section, force-based beam-column elements for the piers. Additionally, the FP devices are modeled through the built-in element of Opensees, while the soil-structure interaction at the abutments is implemented through a zero-length element with specific stiffnesses assigned along the longitudinal and transverse bridge directions.

Furthermore, details are provided regarding the parametric analysis carried out, which encompasses a wide range of bridge properties (i.e., the total number of spans and the isolation period), different seismic intensity levels along with two incidence angle conditions. Additionally, the friction coefficient at large velocities and the uncertainties related to the seismic input are treated as random variables relevant to the problem.

Finally, the chapter illustrates the procedure for implementing multiple-support excitation in Opensees.

Chapter 6 focuses on the seismic reliability assessment of two configurations of isolated bridges equipped with friction pendulum devices. It examines both 5-span and 7-span bridge configurations across three different isolation periods, analyzing their seismic response under both uniform input condition and spatially variable earthquake ground motion (SVEGM). The friction coefficient is treated as a random variable in the analysis. Additionally, to ensure convergence between the target response spectrum for the reference site of L'Aquila and the ensemble-averaged spectra derived from simulations, 30 ground motions are artificially generated for each bridge support station. Two different incidence angle conditions (30° and 60° relative to the bridge longitudinal axis) are also considered. The reliability assessment begins with Incremental Dynamic Analysis (IDA), involving a total of 3600 3D simulations for each of the 9 Intensity Measure Levels (IMLs) considered in the IDA. Engineering demand parameters (EDPs), chosen to evaluate the response statistics related to both bridge piers and

bridge isolation system, are presented next. Subsequent steps in the seismic reliability estimation include the derivation of fragility curves for the bridge piers and friction pendulum devices, assuming different damage levels and limit state thresholds.

Finally, considering the seismic hazard curves at different isolation periods related to the reference site of L'Aquila (Italy), the seismic reliability of both bridge piers and friction pendulum devices is evaluated in the time frame of interest through the convolution integral between seismic fragility and seismic hazard.

Additionally, SRBD (Seismic Reliability-Based Design) abacuses are derived and proposed with a twofold objective:

a) to define the radius in plan of the friction pendulum bearings, accounting for both uniform excitation and spatial variability of earthquake ground motion (SVEGM), as a function of the bridge configuration, isolation period and expected reliability level.
b) To establish specific design safety factors for the seismic design of friction pendulum isolators adopted to retrofit conventional highway bridges, implicitly considering the adverse effects of SVEGM.

1 Seismic risk assessment

This dissertation aims to evaluate the seismic reliability of multi-span reinforced concrete (RC) bridges seismically isolated with friction pendulum system (FPS) devices, considering spatial variability of earthquake ground motion (SVEGM). The goal is to understand how it affects the response of these structures and to provide design abacuses for the FP bearings following the performance-based-earthquake engineering (PBEE) methodology [1].

This chapter intends to provide an overlook of the most important aspects regarding seismic risk evaluation with specific attention on the concept of structural reliability, within the context of Performance-Based Earthquake Engineering (PBEE). At first, the methodology approach, following the PBEE, as framed by the Pacific Earthquake Engineering Research (PEER) Center, is examined. Next, the concept of seismic risk is explained both in qualitative and quantitative terms, emphasizing the key components involved: seismic hazard, seismic vulnerability, and exposure. A specific focus is given to the assessment of seismic vulnerability for a specific asset at risk, such as bridge structures. In this context, the derivation of analytical fragility functions, which are used to describe seismic vulnerability, is presented next.

Finally, the chapter delves into the concept of structural reliability, exposing the main source of uncertainties involved in the reliability assessment. It also discusses different approaches (reliability methods), that may be employed for evaluating structural reliability. Additionally, these approaches may require the use of simulation techniques such as the Monte Carlo technique or the more efficient Latin Hypercube sampling method. Both techniques are discussed in this chapter within the framework of reliability assessment.

1.1 Introduction

Bridges are among the most vulnerable components within a transportation network during natural disasters, playing a crucial role in the socioeconomic life of modern society.

Earthquakes are one of the most harmful natural environmental disasters that heavily impact human lives, social, and economic assets, as evidenced during the numerous strong earthquakes occurred worldwide, which made the seismic risk widely recognized. Notable events include 1971 San Fernando (USA), 1989 Loma Prieta (USA), 1994 Northridge (USA), 1995 Kobe (Japan), 2009 L'Aquila (Italy),

and 2012 Emilia Romagna (Italy). Such events have demonstrated that even in countries with seismic regulations most of the buildings and bridges, especially the older, non-retrofitted, and non-isolated ones, have experienced extensive damage or collapse. Bridge failure and the consequent bridge downtime can have significant adverse consequences for industry, commerce, and for emergency response operations in the case of a catastrophic event.

Two main examples can be quoted between others: during the 1989 Loma Prieta earthquake, the Oakland Bay Bridge was closed to traffic leading to the interruption in the transportation network between San Francisco and Oakland; likewise, the 1995 Kobe earthquake caused the closure of relevant bridges between Kobe and Port Island resulting in significant loss of business and delays in delivery of essential goods. It is therefore essential to redefine the assessment of existing bridge structures or adequately design new ones in the seismic-prone areas [2], recognizing that collapse prevention, especially for bridge structures, is one of the objectives but not the only one, in the efforts to build resilient cities and communities.

To address this need, seismic provisions have gradually moved from a traditional “adequate strength” approach to a “performance-based” one, conceptually formalized in the report “Vision 2000” [SEAOC 1995] under the concept of Performance-Based Earthquake Engineering. This approach was at first based on the definition of acceptable levels of failure probability (with some energy dissipation systems considered) of individual structural components. Today, it is more oriented towards system-level considerations, including risk of collapse, fatalities, repair costs, and post-earthquake loss of functionality which are more comprehensible to decision-makers. While the new paradigm of performance-based Earthquake Engineering (PBEE) is now aligned with public expectations of infrastructure performance, it needs to be accompanied by the same advances in reliability methods and risk assessment tools, to quantitatively link between engineer's practice and its social consequences [3].

1.2 Performance-based earthquake engineering (PBEE) methodology

Performance-based engineering stands for a novel philosophy approach in structural engineering that better aligns building performances with the expectations of building owners, occupants, and the public.

In the field of earthquake engineering, performance-based earthquake engineering (PBEE) has been framed by the Structural Engineers Association of California (SEAOC), which produced the Vision 2000 report in 1995. This framework has been further supported by documents such as FEMA 273 (ATC1997a), ATC-40 [ATC1996], FEMA 356 (ASCE 2000), and (ASCE 7-16) driven primarily by economic considerations.

The Vision 2000 report [1] aims to recognize that different design facilities must have a multiplicity of performance under a set of discrete hazard levels. The

general concept is displayed in a performance matrix (Figure 1.1) in which one axis includes different levels of seismic excitation or severity of hazard based on the return periods (frequent 43 years, occasional 72 years, rare 475 years, and very rare 975 years). The other axis represents seismic performance levels (fully operational, operational, life safety, and near collapse). Seismic performances and excitations are indeed coupled for three categories of structures based on their importance (basic, essential/hazardous, and safety-critical). Performance levels are typically defined by setting allowable limits for displacement demand metrics, such as inter-storey drift index.

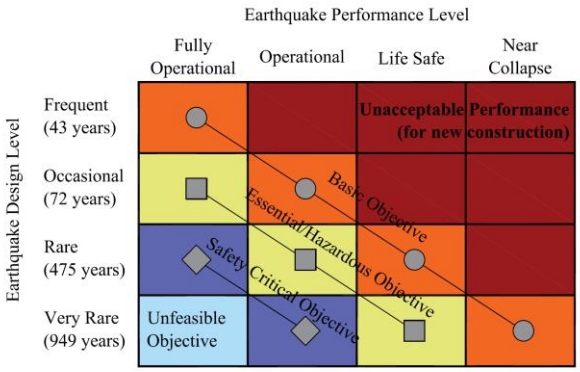

Figure 1.1. Performance matrix proposed by Vision 2000 [1].

1.2.1 PEER (Pacific Earthquake Engineering Research) center-PBEE approach

Whereas the first-generation PBEE approach expressed the seismic performance primarily in terms of structural response such as inter-storey drifts, the PEER approach focuses on global-level performance metrics in probabilistic terms. These metrics involve economic losses (costs), casualties (deaths and injuries), and loss-of-use duration (downtime) which are more useful to stakeholders and policymakers to decide for acceptable performance and risk [4].

The PEER methodology approach involves four main stages that are: hazard analysis, structural analysis, damage analysis, and loss analysis as reported in (Figure 1.2).

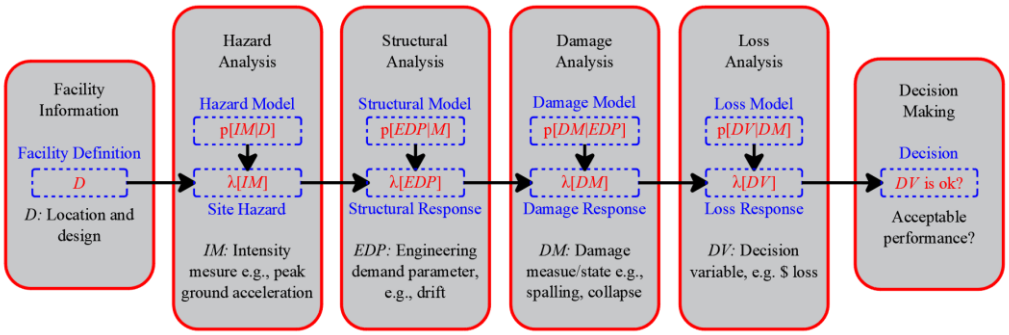

Figure 1.2. PEER-PBEE methodology [33].

Hazard analysis: at this first stage, given a certain seismic environment (nearby faults, magnitude-frequency recurrence rates, site distance, local soil conditions) the mean hazard curve, which describes the mean annual frequency λ_s (MAF) of exceeding various seismic excitation levels is constructed for the site of interest via probabilistic seismic hazard analysis (PSHA) [5]. Seismic excitation is represented through an intensity measure (*IM*), which can be expressed by the peak ground acceleration, PGA, peak ground velocity, PGV, spectral acceleration at a given period $S_a(T_1)$, and Arias intensity I_a, among others.

Structural analysis: at this stage, a representative numerical structural model of the facility is created by engineer analysts to perform nonlinear time-history analysis. These analyses are used to estimate the uncertainty in the structural response as measured by specifically selected engineering demand parameters (EDPs).

Damage analysis: The aforementioned EDPs are used at this stage as input to a set of fragility functions that model the probability of various levels of physical damage (*DLS*-i) to be exceeded.

Loss analysis: At this final stage the probabilistic estimation of performances that are of interest to the building's owners or stakeholders, known as decision variables (DVs) is conducted. These decision variables, which can include costs (dollars), casualties (deaths), or facility downtime, are evaluated based on the conditioned damage measures (DM).

All these four stages are summarized into the following triple integral as for Eq.(1.1):

$$\lambda(DV) = \iiint p[DV \mid DM]p[DM \mid EDP]p[EDP \mid IM]\lambda_s[IM]dIMdEDPdDM \quad (1.1)$$

Where $p[X \mid Y]$ is the probability density function of X conditioned on the level of Y, whereas λ_s represents the mean annual frequency of exceeding a given level of the intensity measure (*IM*), as derived from the hazard evaluation.

Accordingly, the analysis yields the mean annual frequency (MAF) at which various levels of decision variables (DV) are exceeded. For instance, it can

determine the MAF of economic losses exceeding a specified amount. This data is crucial for risk management strategies, helping to assess whether a bridge or building meets acceptable thresholds for economic losses.

1.3 Elements of seismic risk evaluation

After an earthquake occurs, buildings or bridges can experience physical damage and/or loss of functionality. Seismic risk is consequently defined as the probability that within an interval of time, specific asset types (residential buildings, infrastructures, critical facilities, etc.) will reach predetermined seismic performance levels in a region of interest. Quantitatively, risk can be expressed as a relation that involves seismic hazard, seismic vulnerability of the assets at risk, and their exposure.

Seismic Risk= Seismic Hazard x Vulnerability x Exposure

Where:

Seismic Hazard of an assigned region is defined as the probability of exceedance, in a given interval of time, a given level of a certain earthquake intensity measure (*IM*). Another perspective characterizes seismic hazard as the expected number of events that in a unit of time (generally years) exceeds a certain intensity measure (*IM*) threshold or level.

Seismic hazard is quantified through probabilistic seismic hazard assessment (PSHA) whose final outcome is the hazard curve (Figure 1.3), which links the generic intensity measure (*IM*) level *IM*=im, to the mean annual rate of exceedance such level $\lambda_{IM}(im)$ [5].

According to J. Baker [6], PSHA integrates models describing the potential location and size of future seismic events with estimates of the resulting shaking intensity.

At a larger territorial scale, the implementation of PSHA produces hazard maps, a spatial distribution representation of the intensity level of a certain *IM* having a given probability of exceedance in an assigned interval of time (Figure 1.5).

It is possible to demonstrate that, by applying the Total Probability Theorem, $\lambda_{IM}(im)$ is expressed as:

$$\lambda_{IM}(im) = \nu \cdot \int_{M\min}^{M\max} \int_{R\min}^{R\max} P[IM > im \mid M = m \cap R = r] \cdot f_R(r) \cdot f_M(m) \cdot dm \cdot dr \quad (1.2)$$

Where:

ν is the rate of occurrence of earthquakes at the source;

$P[IM > im \mid M = m \cap R = r]$ is the probability of exceeding the *IM*=im level and is given by the ground motion prediction model;

$f_R(r)$ and $f_M(m)$ are the distances and magnitudes' PDFs.

The integral in probabilistic seismic hazard assessment (PSHA) is computed across all considered magnitudes and distances. This involves summing the conditional probabilities of exceedance (given specific magnitudes and distances), weighted by the probability of occurrence associated with those magnitudes and distances. For more in-depth information on the implementation of PSHA, refer to [6].

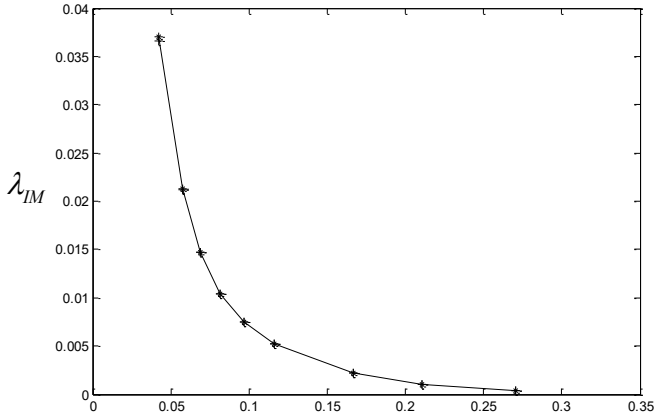

Figure 1.3. Hazard curve.

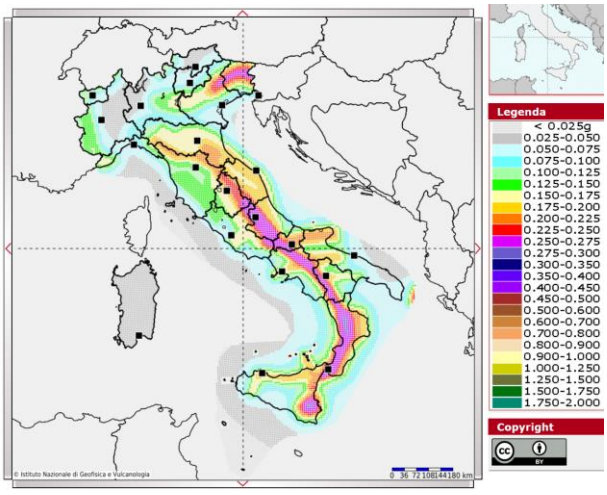

Figure 1.4. Seismic Hazard map in Italy in terms of PGA and exceeding probability of 10% in 50 years [7].

Vulnerability for the specific asset at risk, such as bridges, is defined as their susceptibility to suffer damages or losses caused by a given earthquake with a given intensity measure. Such damages can bring the facility to a temporary closure or temporary loss of its functions, even causing their complete collapse.

The vulnerability is typically described by means of fragility curves, which express the conditional probability of exceeding a given limit state damage limit state (*DLS-i*), or more generally a performance level, as a function of the seismic intensity measure *IM* (Figure 1.5).

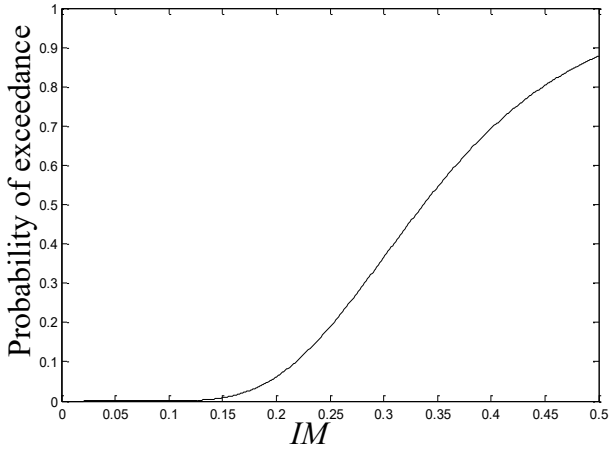

Figure 1.5. Fragility curve.

Exposure is meant to represent the quality and quantity of facilities exposed to the seismic hazard at the site of interest, the number of people involved, and their ability to respond. The exposure is generally viewed as responsibility of urban planning decision-makers and so assumed as negligible in the seismic risk calculation (equal to unity).

Given a generic intensity measure *IM* (e.g., spectral acceleration at the fundamental period of the structure $S_a(T_1)$) and for a generic asset, the mean annual rate $\lambda_{f,LS}$ of an earthquake that causes the attainment of a damage limit state DLS, can be expressed as for Eq. (1.3):

$$\lambda_{f,LS} = \int_{-\infty}^{+\infty} P_{f,LS}(DLS[im]) \cdot \left| d\lambda_{IM}(im) \right| \tag{1.3}$$

Where $P_{f,LS}(DLS[im])$ represents the *vulnerability* (*fragility*) of the asset (e.g., buildings or bridges) concerning the specific damage limit state under consideration, when subjected to an earthquake with ground motion intensity level *IM*=im.

$\lambda_{IM}(im)$ is the seismic hazard at the site of interest (reference site), defined as the mean annual rate of exceeding a given ground motion intensity level *IM*=im.

The term $\left| d\lambda_{IM}(im) \right| = \left| \frac{d\lambda_{im}}{d(im)} \right| \cdot d(im)$ denoted the absolute value of the derivative of the hazard curve, indicating the rate of change of the hazard with increasing ground motion intensity level, multiplied by $d(im)$.

The mean annual rate $\lambda_{f,LS}$ can be used to compute the probability $p_{f,LS}$ of exceeding the generic damage limit state DLS in a given interval of time Δt. This probability is given by Eq. (1.4):

$$p_{f,LS}[N(\Delta t) \geq 1] = 1 - e^{-\lambda_{f,LS}\Delta t} \tag{1.4}$$

Where N is the number of seismic events that cause the attainment of the damage limit state DLS.

A fundamental hypothesis in Eq. (1.4) is that the occurrence of earthquakes follows a stationary stochastic Poisson process with distribution given in Eq. (1.5):

$$p_{f,LS}[N(\Delta t) \geq 1] = \frac{(\lambda_{f,LS} \cdot \Delta t)^n}{n!} \cdot e^{-\lambda_{f,LS}\Delta t} \tag{1.5}$$

It follows that Eq. (1.4) represents the probability that at least one event causes the attaining of a damage limit state DLS in the interval of time Δt.

This interpretation arises because the probability of at least one damaging event happening is the complement of the probability of zero events causing damage, which sums up to 1.

It can be further demonstrated that for really small values of $\lambda_{f,LS}$ (rare events) then $p_{f,LS} \approx \lambda_{f,LS}$ when $\Delta t = 1$, so that the rate of occurrences $\lambda_{f,LS}$ and the probability of having at least one event causing damage in the unit of time, with rate $\lambda_{f,LS}$, are interchangeably used.

In simpler terms, seismic risk can be interpreted as the convolution integral between seismic fragility and seismic hazard. This relation can be read as follows: "The Seismic risk is the Vulnerability at each level of intensity weighted for the Seismic hazard".

1.3.1 Seismic vulnerability assessment

Fragility functions are typically computed using various methods, which can be categorized into the following groups: empirical, judgmental, analytical, and hybrid [8].

In this work of thesis the focus is specifically on those fragility functions derived from linear or nonlinear dynamic structural analysis to simulate damage statistics [9]. These fragility functions, also called analytical fragility functions, are nowadays increasingly adopted due to the advancements in computer capabilities, which enable analysts to have greater control over the derived data and incorporate if needed different sources of uncertainties. Other methods rely on a combination of damage data sources (e.g., post-seismic surveys or expert judgments and opinions). Each method has its advantages and disadvantages, such as the lack of data in the case of non-frequent large earthquakes.

1.3.1.1 Generation of analytical fragility functions

Analytical fragility functions rely on the implementation of a numerical model to be analyzed under seismic loads scaled at different levels of the selected intensity measure. Regarding the seismic assessment of bridge structures, the implementation involves generating a comprehensive model where different

bridge components are represented. For instance, beam-column elements may be used for the deck and piers, while spring elements are employed for abutments and bearings/isolators. Regarding analysis methods, elastic spectral analysis, non-linear static analysis, and nonlinear time history analysis are commonly utilized. Among these methods, nonlinear time history analysis is often preferred for its accuracy, despite being computationally demanding. Then, depending on the ground motion selection and scaling approach within the nonlinear time history analysis framework, different procedures can be implemented. Incremental Dynamic Analysis (IDA) [10] involves scaling the selected ground motions from a single suite of records to various *IM* levels (generally until the onset of the structure collapse). The major drawback of such a method is that it may need for excessive down-scaling and/or up-scaling possibly causing to deal with inconsistent ground motions. Rather than adopting incremental dynamic analysis the analyst can select different ground motions at each *IM* level. This is generally the approach followed by the multiple stripe analysis (MSA) method [11] that is commonly used when ground motions are selected such as to match a Target Conditional Spectrum [12], which is indeed representative of a specific site and *IM* level. Due to different ground motions selected for each *IM* level, it is possible to have that for higher ground motion intensities there will be a reduction of the fractions of collapses and vice-versa. The third method refers to cloud analysis (CA) [11]. This method deals with a set of unscaled ground motions selected at different *IM* values and yields a "cloud" of the response rather than stripes, but it requires for a much more careful choice of records [13].

The ground motion intensity measure *IM* plays the role of interface between hazard and variability in the resulting outcomes [14]. Selecting an appropriate *IM* is crucial, as it should possess properties such as sufficiency, efficiency, and scaling robustness [15]. However, no one single *IM* can fully capture all aspects of ground motion characteristics [16]. Accordingly, an intensity measure *IM* is assumed to be sufficient if the probability distribution of the structural response conditioned on that specific *IM*, remains independent of other ground motion features such as magnitude and distance. The *IM* must be sufficient with respect to all the variables that affect the seismic hazard. An intensity measure *IM* is instead defined as efficient if a small variability emerges from the structural response.

The choice of a more efficient *IM* allows for a reduction in the number of analyses without reducing the accuracy of the response.

Scaling robustness refers to the practice of scaling the accelerograms. The chosen *IM* should ensure that the structural response at a generic *IM* level is the same as would be if an unscaled ground motion with that *IM* level is applied to the structure [17]. Peak ground acceleration (PGA) has been largely used in the last decades mainly because hazard models and particularly the ground motion prediction equations (GMPE) were formulated in terms of PGA [18]-[19]. However, PGA is more suitable for short-period structures under low-intensity levels [20]. Nowadays the commonly used *IM*s are the spectral acceleration or spectral displacement at the fundamental period of the structure $S_a(T_1)$, $S_d(T_1)$

[21]-[22]. In this thesis, which focuses on isolated bridges, the spectral acceleration at the isolation period of the structure is used for the analysis.

More recently, [23] studied the efficiency of several *IM*s in predicting the response of non-isolated reinforced concrete bridges, and found out that the average spectral acceleration $(AvgSA)$ over a certain bridge period range is much more reliable than PGA, PGV, and $S_a(T_1)$ as it limits the dispersion in the fragility curves for all the analyzed bridges and intensity measure levels. However, because this work of thesis deals with isolated reinforced concrete bridges, whose dynamic behavior is mainly influenced by the isolation period, the choice of the spectral acceleration or spectral displacement at the fundamental period of the structure will provide sufficiently accurate results.

Once the structural response, obtained from the structural analysis, has been gathered in the form of the specifically selected engineering demand parameters (EDPs), seismic fragility functions are estimated by fitting the sample data with a lognormal cumulative distribution function according to Eq. (1.6) [24]-[25]:

$$P[f \mid im] = P[IM_f \le im] = \Phi\left(\frac{\ln(im/\hat{\eta})}{\hat{\beta}}\right) \tag{1.6}$$

In Eq. (1.6) a sample of n values, $\underline{im} = \{im_1, im_2, ..., im_n\}$ is considered extracted from the distribution of the ground motion intensity causing the failure of the structure, called IM_f.

The term $\Phi(\bullet)$ is representative of the standard normal cumulative distribution function of this random variable and it is indeed the seismic fragility. $\hat{\eta}$ is the median of the fragility function (*IM* level with 50% probability of failure) whereas $\hat{\beta}$ is the standard deviation of the $\ln(im)$. These two terms can be estimated through the following equations:

$$\hat{\eta} = \frac{1}{n} \cdot \sum_{i=1}^{n} \log(im_i) \tag{1.7}$$

$$\hat{\beta}^2 = \frac{1}{n-1} \cdot \sum_{i=1}^{n} [\log(im_i) - \hat{\eta}]^2 \tag{1.8}$$

Being n the number of the selected ground motions and im_i the value of IM_f associated with the onset of failure coming from the *i*-th ground motion.

The parameters $\hat{\eta}$ and $\hat{\beta}$, as reported in [24], are characterized by uncertainty because of the record-to-record variability (for an assigned structure different ground motions can cause different seismic responses even if the same *IM* level is considered) and as such they have to be estimated based on the observed data.

The two common statistical approaches generally followed for this estimation depend on the nonlinear dynamic analysis procedure adopted [24]. They are generally categorized as follows:

a. The method of moments finds can define a model distribution with the same sample moments of the observed data;
b. The maximum likelihood estimation finds the parameters such that the corresponding distribution has the highest likelihood of having produced the observed data.

For further details on the fragility parameters estimation refer to [24].

1.3.2 Seismic reliability

Society expects buildings and bridges to be designed such to withstand the demands imposed by their service requirements and natural hazards with a reasonable and acceptable level of safety. To meet these expectations, structural reliability methods have progressively imposed into code developments, and evolved to include several sources of uncertainty in the design criteria. In particular, a structure should be conceived, designed, and executed to sustain all the actions that may occur during its design working life while maintaining its performances. These requirements should be achieved with predefined and appropriate levels of reliability and economic sustainability. In this context, the acceptable safety levels that are currently prescribed in the building codes are strongly influenced by values that stakeholders, politicians, and decision-makers assign to human life, material loss, interruption of services, and so on.

The *reliability of structures* can be defined as their ability to fulfill given performance requirements under specific load conditions during their design working life. Quantitatively, the term *reliability* may be considered as the complement to one of the probability of structural failure, where the term failure does not necessarily mean catastrophic failure but can refer to a structure that does not achieve the desired performances. The *design working life* is intended as the period of time for which a structure or a structural component should be able to satisfy its requests without needing for major repairing actions. Structural reliability concepts can be applied to new building design and to the assessment of the existing ones providing the instruments to decide about repair, rehabilitation, or replacement strategies. Particularly, according to *fib Model Code 2010* and *fib Bulletin 80*, the *design* process can be recognized as a series of activities devoted to allowing the structural reliability in the design working life of a new structural realization, whereas, the *assessment* process represents the set of activities performed in order to verify the actual reliability of an existing structural system or component accounting for its residual service life. As mentioned earlier, the term failure is note associated to a unique definition: for a simply supported steel beam one analyst can say that the structure fails if the maximum deflection is attained whereas the other can claim that the structure will only fail when a plastic

hinge is developed. These comments make clear that before performing structure reliability analysis a failure criteria needs to be defined by introducing the concept of *Limit States* that, according to [26], is defined as: *"the condition beyond which the structure, or a part of it, does no longer satisfy one of its performance requirements"*. For a bridge structure, as an example, the failure can be assumed as its inability to carry traffic loads. Other undesired performances or *limit states* can be the following: concrete cracking, steel corrosion, excessive material deformations, exceeding shear or flexural capacity and so on. The main performance requirements for structural design are represented by *safety (i.e.*, *structural resistance and ductility)*, *serviceability*, *durability,* and *robustness.*

Related to the abovementioned performance requirements, in structural reliability three *limit states* are generally selected and considered:

- *ultimate limit states (ULSs),* that refer directly to the structural safety, the safety of people and/or protection of the content of a structure. Beyond *ultimate limit state* the bearings or members capacity of the structure is exceeded and the whole system can fail. Commonly, different *ULSs* can be defined in bridge structures such as: excessive bearing displacements, exceeding moment-carrying capacity in the piers, displacements that cause a 'walk-out' phenomenon in the superstructure and so on.
- *serviceability limit states (SLSs)*, which refer to the functionality, users' comfort, and visual aspect of the structures during their daily use. The serviceability of the structures is generally related to *deformations*, *vibrations,* and *damages* that may influence their integrity. Excessive deflection can interfere with surgery performed in a hospital structure and as so should be limited to prescribed values.
- *Fatigue limit states (FLSs)* refer to loss of strength under repeated (cyclic) loads and are mainly due to the accumulation of damage. The *FLSs* can occur in steel elements and reinforcement bars in concrete. In any fatigue analysis, the critical factor is both the magnitude and the load frequency.

1.3.2.1 Uncertainties and their classification

Many sources of uncertainty are present in structural design, loading parameters and capacity of structural members are not deterministic quantities but rather random variables, making a zero probability of failure not achievable.

Consequently, structures are always designed to perform their functions with a finite and acceptable probability of failure. These uncertainties may be of different nature and are primarily represented by:

- *randomness* (or *inherent variability*): it represents the natural variability that can be considered as intrinsic to physical process or properties (*e.g.*, material properties, natural variation of wind pressure, earthquakes, live loads etc). The randomness can not be affected or reduced by external (*i.e.,* human) intervention.
- *model uncertainty:* it is the uncertainty related to the idealization and simplification of mathematical models adopted to describe and make

predictions related to the physical process or property. It can be reduced by increasing the knowledge and improving the quality of the model.

- *statistical uncertainty*: this type of uncertainty arises from estimating parameters based on a limited size of sample of observations for statistical analysis and it can be reduced by increasing the data from experience (*e.g.*, experimental results).

Alternatively, uncertainties can be gategorized into two major groups based on their causes:

- *natural causes*: these arise from unpredictability of loads such as wind, earthquake, snow, etc.
- *human causes:* these result in approximations, calculation errors during the design phase and can be associated with the use of inadequate materials, construction methods and so on, during the construction phase.

All the different sources of uncertainty affect the *reliability analysis* of a structural system to varying degrees.

Furthermore, it can be observed that if the *randomness* (*i.e.*, *inherent variability*) of a physical process or property can be considered as inherent in nature and not reducible, other sources of uncertainty may be reduced by improving, for example, experiments, measurement procedures, and predictive models. Generally, in the scientific literature, two different macro-families of uncertainty are recognized namely *aleatory* and *epistemic*.

Specifically, concerning structural reliability analysis, the *aleatory* uncertainties concern the intrinsic randomness of the variables that govern a specific structural problem, whereas the *epistemic* uncertainties are mainly related to the inaccuracy in the prediction of reality. For example, in order to estimate the response of a structural system, different numerical models or material properties may be adopted. These choices can affect the global level of uncertainty within reliability analysis.

A typical example regarding the difference between aleatory and epistemic uncertainties is provided in [27] with regard to the concrete material: if the reference is on both new and existing structures, then the concrete compressive strength may be considered as aleatory in the former case and as epistemic in the latter case. Indeed, the concrete compressive strength is assumed to be affected by an aleatory uncertainty in the case of a new structure as there is no way of improving our knowledge by means of measurements and experiments on something that still does not exist at the design phase. Conversely, in an existing structure, concrete has been already casted, its compressive strength exists even if it is the actual realization of a random variable and as such unknown. Nevertheless, the problem can be accomplished by performing an adequate number of tests and inspections to increase the knowledge about the structural properties.

1.3.2.2 General formulation of the structural reliability problem

The procedure to estimate the reliability of a structural system requires for the definition of a unit of measure that can quantify the available level of reliability, and to provide the mathematical idealization of the *limit state* conditions. In this section these two aspects are clarified.

1.3.2.2.1 The measure of structural reliability

In reliability analysis, the state of a structure can be described by using a vector of random variables $\underline{X}$:

$$\underline{X} = \left(X_1, X_2, ..., X_i, ..., X_N\right) \qquad i = 1, 2, ..., N \tag{1.9}$$

where the *i*-th variable X_i may be representative of load and resistance variables such as dead load, live load, geometric data, compressive strength, and yield strength. These basic load and resistance variables are also called *state* or *basic variables*. Considering the probabilistic nature of the variables involved in the structural design, it is necessary to express the level of protection concerning a given limit state in a probabilistic sense. The most common measure of structural reliability is represented by the *probability of exceeding a limit state* $P_{f,LS}$ at least once during the design working life of the structure. This means to check that the following inequality is satisfied:

$$P_{f,LS} \le P_f^* \tag{1.10}$$

Where P_f^* is a target value for the probability of collapse, that is strictly related to the acceptable risk determined by the socioeconomic consequences that the attainment of the limit state under consideration may cause. Indeed, minimizing P_f^* means to reduce the probability of collapse by designing more expensive structures with costs that can be incompatible with the function of the structure itself or with the socioeconomic conditions of a country. As such, the definition of the acceptable value of the probability of collapse is something that involves not only the structural engineering field but also political and socioeconomic competencies.

An alternative measure of structural reliability is represented by the *reliability index β,* which formally can be defined as the negative value of the inverse of the standard normal variable corresponding to the probability of exceeding a limit state $P_{f,LS}$:

$$\beta = -\Phi(P_f)^{-1} \tag{1.11}$$

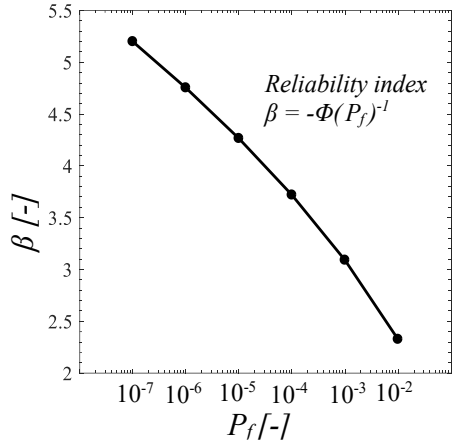

Figure 1.6. Relationship between the probability of failure and the reliability index.

where Φ represents the cumulative standard normal distribution. The bigger the *reliability index β,* the more reliable the structure (*i.e.* lower $P_{f,LS}$*).*

The numerical correspondence between the *reliability index* β and the *probability of failure* P_f is reported in Figure 1.6.

1.3.2.2.2 The limit state function

To numerically define the attainment of a limit state it is possible to introduce a *limit state function* $G = G(\underline{X})$ which, in general, is defined as a function of the basic variables vector $\underline{X} = (X_1, X_2, ..., X_i, ..., X_N)$ and is denoted as performance function. Conventionally, in the space of the $\underline{X}$ variables, the condition G>0 defines the sub-space of the structure's survival states whereas the condition G<0 is associated with the failure domain (Figure 1.7). For a vector $\underline{X}$ of N-state variables the condition G=0 defines a failure surface in a N-dimensional space.

$$G(X_1, X_2, ..., X_N): \begin{cases} G > 0 \rightarrow \textit{safe region} \\ G \leq 0 \rightarrow \textit{failure region} \end{cases} \tag{1.12}$$

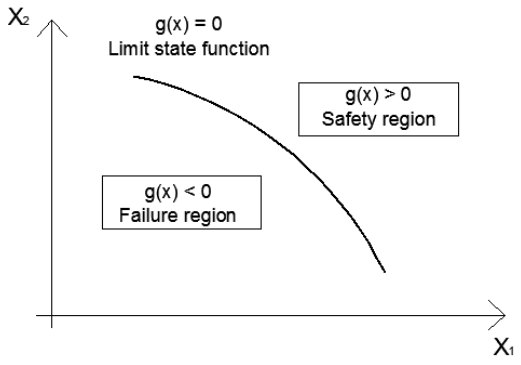

Figure 1.7. General representation of the limit state domain with 2 random variables X_1 and X_2.

Based on this definition the probability of failure P_f can be calculated as:

$$P_f = P[G(X) \le 0] \tag{1.13}$$

If the joint probability density function $f_{\underline{X}}(X_1, X_2, ..., X_N)$ is introduced to express the uncertainty in the $\underline{X}$ vector of the state variables then the probability of failure P_f can be expressed in the following integral form:

$$P_f = \int_{G<0} f_{\underline{X}}(X_i) d\underline{X} \qquad i = 1, 2, ..., N \tag{1.14}$$

The Probability of failure must always be calculated relative to a specific time frame of interest Δt, which commonly, though not necessarily, corresponds to the design or residual working life.

1.3.2.3 Reliability methods and theory background

The evaluation of the structural reliability and consequently the probability of survival, can be performed using various approaches. These methods generally offer an increasing level of approximation while demanding less computational efforts, thereby facilitating the introduction of reliability concepts into engineering practice. These different levels of approximation for the evaluation of structural reliability are listed below:

- *III level methods* (probabilistic);
- *II level methods* (probabilistic);
- *I level methods* (semi-probabilistic);
- *0 level methods* (deterministic).

Progressively, starting from the *III level methods* to the *0 level methods* the computational efforts for estimation of structural reliability decrease significantly, but this comes with a considerable increase in the level of approximation.

1.3.2.3.1 Level III methods

The so-called *III level methods* have as main objective the calculation of the integral expressed in Eq. (1.14) via analytical solutions, numerical integration, or Monte Carlo simulations.

Analytical solutions are feasible in a limited number of situations when the number of variables involved in the reliability calculations is limited. For more complex systems is otherwise possible to take advantage of various simulation techniques, such as the Monte Carlo method, which are very efficient tools to solve the integral expressed by Eq. (1.14).

In the following paragraph, a simple example is presented to show the application of the analytical solution in the context of *III level methods*. In this example, the basic variables vector $\underline{X} = (X_1, X_2, ..., X_i, ..., X_N)$ consists of just two random variables: R (structural resistance or capacity) and Q (structural loads or demand).

1.3.2.3.1.1 Reliability analysis with two independent random variables

In the simple case where two variables R and Q are considered the limit state function G can be defined as G(R,Q)=R-Q. The limit state, corresponding to the boundary between desired and undesired performance, would be: $G(R,Q)=0 \Leftrightarrow R=Q$ (Figure 1.8). Clearly, if Q is greater than R, meaning $G(R,Q)\le 0$ the structure is not safe, otherwise when G(R,Q)>0 the structure is safe. The probability of failure is equal to the probability that the undesired performance occurs, *i.e.*:

$$P_f = P(R-Q\le 0) = P[G(R,Q)\le 0] \tag{1.15}$$

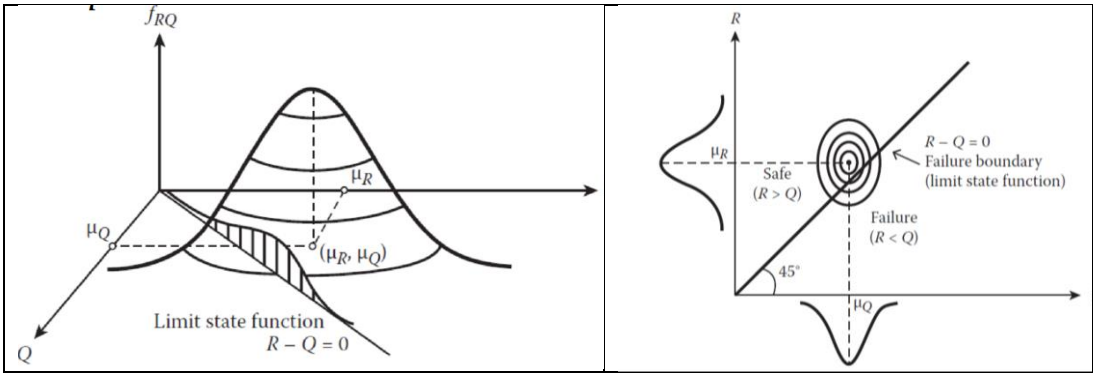

Figure 1.8. Limit state function for the case of a 2-dimensional space with variables R and S.

Assuming that the two random variables are statistically independent then the joint pdf f_{X_i} in Eq. (1.14) can be expressed as the product of the two marginal Pdfs of R and Q, $f_R(r)$ and $f_Q(q)$, so that the probability of failure expressed through Eq. (1.14) is defined as follows:

$$P_f = \int_{G<0} f_{\underline{X}}(X_i)d\underline{X} = \int_{G<0} f_R(r)\cdot f_Q(q)drdq \tag{1.16}$$

Exploiting Eq. (1.16) is it possible to derive the following:

$$P_f = \int_{G<0} f_R(r)\cdot f_Q(q)drdq = \int_{-\infty}^{\infty} f_Q(q)\left[\int_{-\infty}^{q} f_R(r)\right]dq = \int_{-\infty}^{\infty} f_Q(q)F_R(q)dq \tag{1.17}$$

Therefore P_f is given by the convolution integral of two functions of q, $f_Q(q)$ and $F_R(q)$.

In general, both R and Q can be functions of other random variables (*e.g.*, the flexural capacity of a beam section can be a function of the steel yield strength), and so are random variables themselves. It follows that resolving analytically the problem of reliability through Eq. (1.17) becomes difficult if not impossible in

some cases and therefore it requires the adoption of numerical solutions in the form of simulation techniques such as the Monte Carlo method [28].

1.3.2.3.1.2 The Monte Carlo method

The Monte Carlo method [28] is a simulation technique used to directly calculate the probability of failure P_f of a structural system solving the integral in Eq. (1.17). It starts with the introduction of an indicator function $I(\underline{X})$ that is equal to zero for those values of the vector $\underline{X}$ that makes the limit state function G positive, $G>0$, and equal to one in those cases where the vector $\underline{X}$ is such that $G<0$:

$$I(\underline{X}):\begin{cases}0 & if\ G(\underline{X})\geq 0\\ 1 & if\ G(\underline{X})<0\end{cases} \tag{1.18}$$

With the introduction of the indicator function $I(\underline{X})$ Eq. (1.17) can be rewritten in the following form:

$$P_f=\int_{G<0} f_{\underline{X}}(X_i)d\underline{X}=\int_{G<0} I(\underline{X})f_{\underline{X}}(X_i)d\underline{X}\approx\frac{n_k}{n} \tag{1.19}$$

In the last member of Eq. (1.19) it is easy to recognize as the probability of failure can be approximated with the ratio between the total number of simulations n and the number n_k of times of observed collapses, meaning that $G(\underline{X})<0$. The Monte Carlo simulation is therefore based on the generation of a large number of samples of the random variables X_i and on the subsequent evaluation of the limit state function $G=G(\underline{X})$ used to check if it is greater or less than zero.

Nevertheless, the so-obtained probability is inevitably affected by uncertainties depending on the number of simulation *n* that is adopted. Indeed, can be demonstrated that the variance of the ratio n_k/n and so of the probability of failure, tends to decrease as *n* grows. To check the accuracy of the probability of failure estimation through the Monte Carlo technique, the *coefficient of variation* of P_f may be estimated assuming that each simulation cycle constitutes a "Bernoulli trial", and the number of failures in *n* trials can be considered to follow a binomial distribution. Then the coefficient of variation of P_f at the $j-th$ sample, $COV(P_j^j)$, may be calculated as:

$$COV(P_f^j)=\frac{\sqrt{\dfrac{(1-P_f^j)P_f^j}{j}}}{P_f^j}\qquad j=1,2,...,n \tag{1.20}$$

It is possible to demonstrate that the number of simulations to be used is directly proportional to the inverse of the target probability of failure to be estimated. Consequently, the number of simulations required for the structural

reliability analysis, where the probabilities of collapse are very low (10^{-3}-10^{-4}) is then extremely high (commonly around 10^5 – 10^6 simulations).

To reduce the number of simulations and consequently the computational effort, several advanced sampling techniques have been developed and reported in scientific literature. These methods are more efficient than the so-called 'brute-force sampling methods', where elements of the statistical population are generated purely at random. More refined techniques can generate statistical samples that maintain good representativeness with fewer simulations by following appropriate criteria.

In the following section one of these methods, specifically the *Latin hypercube sampling method (LHS)* [29], is described.

1.3.2.3.1.3 Latin Hypercube sampling method

The *Latin hypercube sampling method* (*LHS)* [29], is a stratified sampling method that is proposed to subdivide ('stratify') the sampling space into *n* non-overlapped intervals and extract from each of them a random variable in a random way. This procedure is able to avoid the possibility of having unallocated sampling over the domain of the random variable and as such it represents a more efficient sampling technique with respect to the Monte Carlo simulation. The basic concept on which the *LHS* method is based on is the following: the input range is represented by the cumulative distribution function opportunely divided into *n* disjoint intervals with the same probability of occurrence equal to $1/n$. For each of these intervals, the sampling algorithm extracts randomly between 0 and 1 in such a way that, depending on the considered interval, permits the computation of the correct value of the cumulative function which can be inverted to compute the random variable (Figure 1.9).

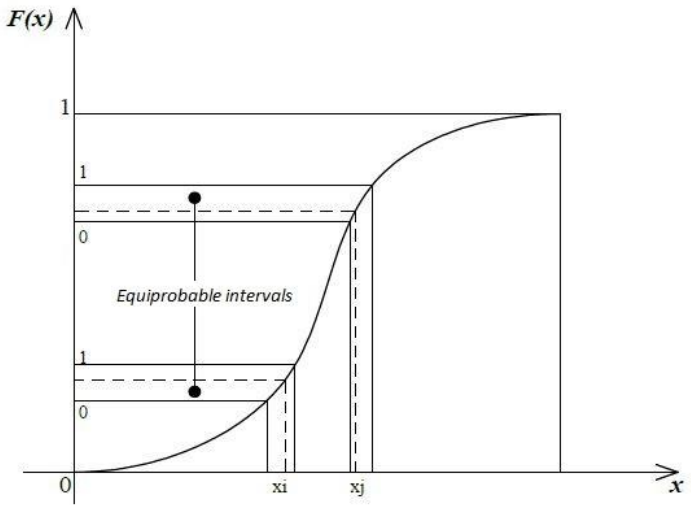

Figure 1.9. Latin hypercube sampling technique.

Specifically, the procedure consists of the following steps:

1) for each of the n intervals, the cumulative probability is evaluated throughout a linear transformation expressed by the following relationship:

$$P_m = \frac{1}{n} U_m \cdot \left(\frac{m-1}{n} \right) \tag{1.21}$$

Where *m* is an integer number included between 1 and n; U_m is the randomly generated number between 0 and 1, and P_m is the value of the cumulative distribution function to be calculated belonging to the *m*-th interval.

Eq. (1.21) ensures that one and only one of the so-obtained values of the probability P_m will belong to the interval $\frac{m-1}{n} < P_m < \frac{m}{n}$, where $\frac{m-1}{n}$ and $\frac{m}{n}$ are respectively the lower extreme and the upper extreme of the m-*th* interval.

2) Once the value P_m is obtained, the m-*th* value of the k-*th* random variable of interest , $X_{k,m}$, is generated through the following Eq. (1.22):

$$X_{k,m} = F_x^{-1}(P_m) \tag{1.22}$$

by inverting the cumulative distribution function.

3) A random permutation between the *m* values sampled for each variable $X_{k,m}$ is performed to randomly couple the outcomes. In this way, the vector of n basic random variables is finally defined to perform the simulations.

1.3.2.3.2 Level II methods

The II Level methods deal with statistical moments of the basic random variables to perform reliability analysis. Specifically, first and second-order moments, including the covariance matrix, are selected within this approach.

In this method, it is advantageous to work with the 'standard form' of the basic variables. For simplicity, if the problem is reduced to two variables R (structural resistance) and Q (structural loads), the standard form can be expressed as:

$$Z_R = \frac{R - \mu_R}{\sigma_R} \tag{1.23}$$

$$Z_Q = \frac{Q - \mu_Q}{\sigma_Q} \tag{1.24}$$

Where Z_R and Z_Q are sometimes called 'reduced variables'.

In this case the limit state function $G(Z_R, Z_Q)$ takes a linear form expressed by:

$$G(Z_R, Z_Q) = \mu_R + Z_R\sigma_R - (\mu_Q + Z_Q\sigma_Q) = (\mu_R - \mu_Q) + Z_R\sigma_R - Z_Q\sigma_Q \tag{1.25}$$

Eq. (1.25), as shown in Figure 1.10, defines a straight line in the space of the reduced variables Z_R and Z_Q, delineating the boundary between the safe and unsafe (failure) domains. The shortest distance from the origin of the reduced variables space, to the line $G(Z_R, Z_Q) = 0$ represents the so-called *reliability index* β as defined by Cornell in 1969 [30].

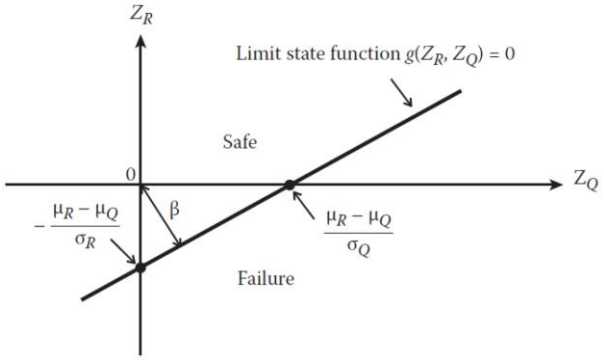

Figure 1.10. Reliability index β, defined as the shortest distance in the space of the reduced variables.

Using geometry, the reliability index β can be calculated as:

$$\beta = \frac{\mu_R - \mu_Q}{\sqrt{\sigma_R^2 + \sigma_Q^2}} = \frac{\mu_G}{\sigma_G} \tag{1.26}$$

This reliability index is called a *first-order, second-moment, mean value reliability index* (FOSM). It means that:
First-order: we use first-order terms in the Taylor series expansion;
Second moment: only statistical means and variances are needed;
Mean value: the Taylor series expansion is about the mean values;

Due to the invariance issue associated with the First-Order Second-Moment (FOSM) reliability index (where the index value depends on the specific form of the limit state function), Hasofer and Lindt proposed a modified reliability index in 1974 [31] to resolve this problem. Specifically, the correction consists of evaluating the limit state function at a point known as the *design point* or *most likely failure point* instead of the mean value. The design point z* is always a point on the failure surface $G(Z_R, Z_Q) = 0$ that is not known in advance and as such requires for an iteration technique. This leads to the so-called *First-order Reliability Methods* (FORM) developed almost 30 years ago.

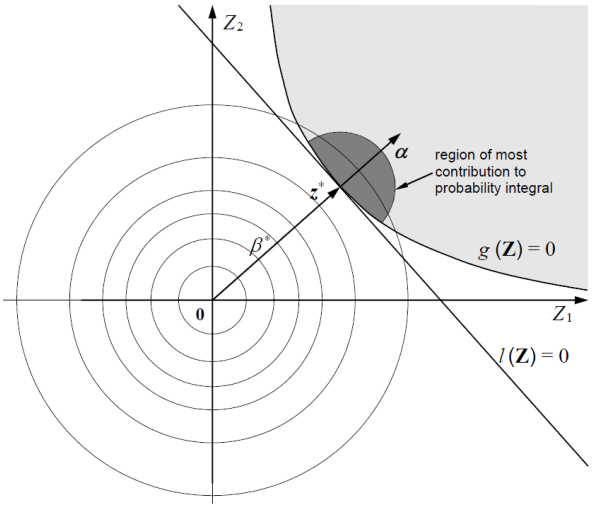

Figure 1.11. Definition of design point and reliability index [31].

The *design point z** represents the point associated with the limit state surface having the highest probability density. According to the FORM method, the procedure is based on the introduction of the vector α (Figure 1.11), which is defined as the outward-directed normal vector to the failure surface (*i.e.* a vector of unit length perpendicular to the limit state hyperplane) defined in the design point z*, which is the point on the linearized failure surface with the shortest distance β from the origin. The components of the vector α are known as *sensitivity factors* as they assign a weighted importance to the individual random variables for the evaluation of the reliability index. Furthermore, their signs indicate whether the corresponding variables are related to a resistance component or to a load component. In the case of two variables R and Q the design point coordinates can be expressed as:

$$R_d = \mu_R - \alpha_R \beta \sigma_R \tag{1.27}$$

$$Q_d = \mu_Q - \alpha_Q \beta \sigma_Q \tag{1.28}$$

And the FORM sensitivity factors α_R and α_Q of the random variables R and Q can be evaluated as the direction cosines of the *design point*:

$$\alpha_R = \frac{\sigma_R}{\sqrt{\sigma_Q^2 + \sigma_R^2}} \tag{1.29}$$

$$\alpha_Q = \frac{\sigma_Q}{\sqrt{\sigma_Q^2 + \sigma_R^2}} \tag{1.30}$$

with:

$$\alpha_Q^2 + \alpha_R^2 = 1 \tag{1.31}$$

In *EN 1990* an approximation of these values according to [32] is introduced. Specifically, the value of α_R is set equal to 0.8 and the value of α_Q is set equal to 0.7. Though, the validity of this approximation is limited by the following inequality: $0.16< \sigma_R/\sigma_Q <7.6$.

In the case that R and Q are normally distributed random variables, the design point coordinates can be evaluated according to the following probabilities:

$$P[Q > Q_d] = \Phi(\alpha_Q \beta) = \Phi(-0.7\beta) \tag{1.32}$$

$$Q_d = \mu_Q + 0.7\beta\sigma_Q$$

$$P[R \le R_d] = \Phi(\alpha_R \beta) = \Phi(0.8\beta) \tag{1.33}$$

$$R_d = \mu_R - 0.8\beta\sigma_R$$

1.3.2.3.3 Level I methods

The Level I method or *load-resistance-factor-design (LFRD)* method is centered on the probabilistic assessment of structural safety without directly computing it, which is indeed carried out in a simplified (*i.e.* scalar verification) way. In this approach the basic variables are assumed equal to their characteristic values, which correspond to a low quantile in case of resistance R or to a high quantile in case of action loads Q. Furthermore, partial safety factors are introduced with values that are based on Level II calculations.

The basic verification format consists as said of a scalar relationship that checks whether the design resistance $R_d = R_n / \gamma_m$ is at least equal to the design value of the load effects $Q_d = \sum \gamma_q Q_i$:

$$\sum \gamma_q Q_i \le \frac{R_n}{\gamma_m} \tag{1.34}$$

Being R_d and Q_d function of the following quantities:

$$Q_d = Q\left(F_{d,1}, F_{d,1}, ...; a_{d,1}, a_{d,2}, ...; \vartheta_{d,1}, \vartheta_{d,1}\right) \tag{1.35}$$

$$R_d = R\left(X_{d,1}, X_{d,1}, ...; a_{d,1}, a_{d,2}, ...; \vartheta_{d,1}, \vartheta_{d,1}\right) \tag{1.36}$$

Where $F_{d,i}$ represents an external action; $X_{d,i}$ represents a material property; $a_{d,i}$ is a geometrical property; $\vartheta_{d,i}$ is the model uncertainty.

The partial safety factors for material properties (*i.e.*, γ_m) and actions (*i.e.*, γ_q), in general, are derived from their characteristic values according to:

$$\gamma_m = \frac{R_k}{R_d} \quad \textit{for resistances} \tag{1.37}$$

$$\gamma_q = \frac{Q_d}{Q_k} \quad \textit{for load effects} \tag{1.38}$$

The design values R_d and E_d may be evaluated according to Eq.s (1.32)-(1.33) as derived from Level II methods. In general, the characteristic value is considered as the 5% quantile of the probabilistic distribution of the resistance, the 50% quantile of the probabilistic distribution of permanent actions, and the 95% quantile in the case of variable actions.

2 Seismic damage in bridges and seismic isolation

This chapter begins with an overview of the typical damage patterns caused to bridges from past earthquakes, with a particular emphasis on those damages observed to bridge configurations more susceptible to the spatial variability of ground motion. Additionally, the chapter illustrates the basic principles of seismic isolation as applied to bridge structures, highlighting the effectiveness of this technique in mitigating or preventing structural damage caused by earthquakes.

2.1 Bridge structures

A bridge can be intended as a structure that is needed when an obstacle such as a river or a sea is present and has to be traversed. It can be named differently depending on the obstacle: are indicated as viaducts those bridges that span over valleys or overpasses, and underpasses those bridges that pass over or under main roads. Other terminologies are in general adopted depending on the various bridge uses: highway bridges are facilities that support vehicular and pedestrian traffic, canal bridges are devoted to the transportation of water, and pipeline bridges are used for transferring liquids and gasses.

Bridge structures are made of two main parts: the superstructure, which is the ensemble of components that are needed to cross over the obstacle, and the substructure, whose scope is twofold: it carries the loads acting on the superstructure (vertical and horizontal) and transfers it to the ground.

The superstructure is generally made up of the deck slab and the girders, whereas the substructure includes beam caps (with or without shear keys), piers, abutments, and their respective foundation systems that, depending on the soil conditions, may be shallow foundations (footing) or deep foundations (piles).

Despite several configurations (*e.g.*, frame, arch, truss, and suspension bridges) and materials (*e.g.*, masonry, steel, and reinforced concrete/post-tensioned concrete/pre-tensioned concrete) could be adopted or have been adopted in the past for the bridge design, the most commonly encountered typology, especially in Italy, is the reinforced concrete beam bridge that for this reason will be the testbed bridge adopted in this work of thesis.

Beam bridges are relatively simple structures having spans supported by abutments at each end and piers. They are typically adopted for highway bridges

(Figure 2.1) where they span over relatively short distances. The connection between superstructure and substructure is generally non-monolithic as they are connected through simple bearings or seismic isolation bearings in the case of an isolated bridge. Seismic isolators as will be specified next, are generally classified into two categories: those that make use of elastomeric components (*e.g.*, lead-rubber-bearings (LRB)) and those that use sliding components (*e.g.*, friction pendulum system (FPS)).

When the superstructure comprises multiple spans it is generally discontinuous at each span end because of the presence of an expansion joint that needs to accommodate movements due to temperature variations or other horizontal actions (creep and shrinkage deformations).

As far as the pier is concerned, a wide variety of reinforced concrete (RC) and steel sections, as well as composite steel-concrete sections are in use [34]. The circular section is the most desirable for those cases where longitudinal and transverse demands are similar. Rectangular sections have the disadvantage of not providing adequate protection of longitudinal bars against buckling, unlike circular sections. Finally, the hollow sections are used in those cases where the height of the piers is excessive.

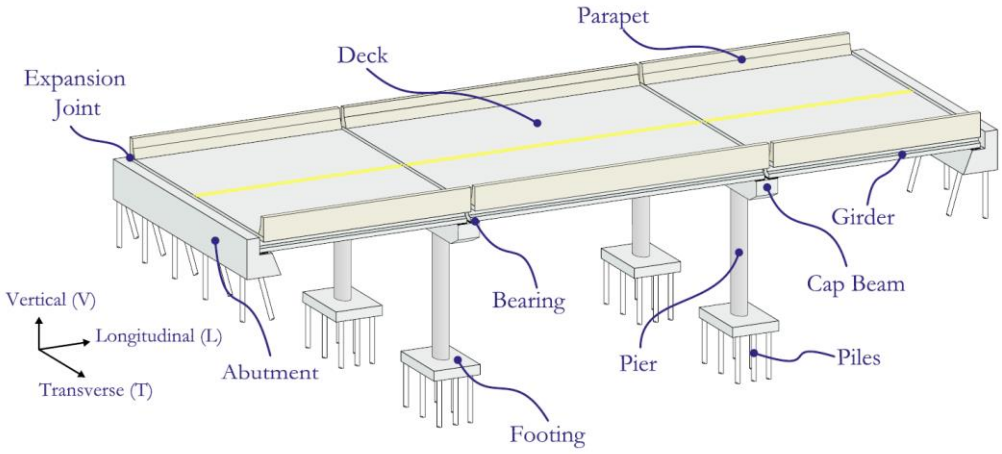

Figure 2.1. Components of a typical highway bridge [33].

2.2 Observed damage patterns to reinforced concrete bridges from past earthquakes

During the last four decades, earthquakes caused several damages, and in the most severe cases, complete collapse to bridge structures. These events have revealed the high vulnerability of specific components belonging to the bridge layout.

Bridges are generally designed to have piers that are more flexible than the deck to which they are connected. Consequently, seismic damage can likely be concentrated on the piers, which are demanded to possess high ductility to withstand the deformations imposed during an earthquake. Conversely, the

superstructure assembly (diaphragm slab and girder) is assumed to remain fundamentally elastic when an earthquake occurs and is mainly devoted to transferring the lateral forces to the substructure components.

Based on the previous comments, typical damages observed concern foundation failure, piers damage (flexural failure or shear failure), shear keys failure, and deck unseating or pounding of adjacent deck spans at expansion joints [35].

2.2.1 Deck damages

One of the most dangerous types of failure regarding superstructure is associated with unseating at abutments and expansion joints. This risk arises primarily from the spatial variability of earthquake ground motion at different bridge supports (piers and abutments), leading to dynamic relative displacements of the superstructure (adjacent bents may move out of phase). As adjacent bents move out of phase, significant openings can occur at expansion joints, potentially causing the deck to become unseated. This kind of event has been observed even in those bridges provided with restraining devices. Typical examples of bridges that collapsed through unseating are the Nishinomiyako simply supported bridge during the Kobe 1995 earthquake and the Oakland Bay steel truss bridge in San Fernando earthquake which lost a full span because of inadequate seat width (Figure 2.2). The cited examples show that the necessary seat width cannot be replaced by restrainers or fixed bearings as they can undergo unpredictable high horizontal forces even during low seismic events leading to their failure [36].

Local destructions in the superstructure can also occur due to pounding between adjacent spans or against abutments, resulting in very high forces that may exceed the material strength limit. This scenario often occurs when expansion joints, designed to accommodate unrestrained relative movements in long bridges, fail to sustain the large displacements imposed by seismic actions, leading to the gap closure followed by high pounding forces. While this type of damage may not critically endanger structural safety by causing bridge collapse or significantly altering seismic behavior, it can pose a greater concern for bridges that are essential to the lifeline transportation network. Pounding damage between spans or against abutments has the potential to impede the timely transportation of emergency supplies following an earthquake, thereby affecting the bridge's operational resilience in post-disaster scenarios.

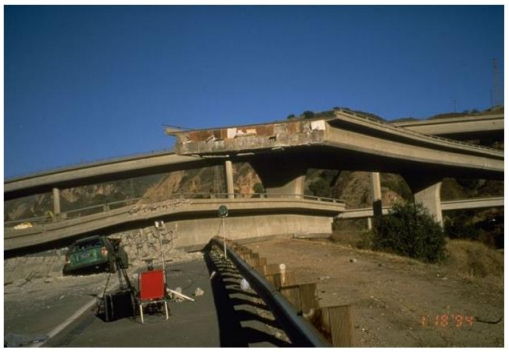

Figure 2.2. Typical superstructure unseating during the Northridge 1994 and Loma Prieta 1989 earthquakes [36].

Figure 2.3. Local damage at the expansion joint during the Northridge 1994 earthquake [36].

2.2.2 Pier damages

Bridge piers can experience various types of failure, primarily associated with the attainment of flexural and/or shear capacity, or due to the axial failure. Axial failure, in particular, can lead to a potential total collapse of the bridge, as the substructure cannot carry the loads coming from the above. It is worth mentioning that in a robust structure where multiple load paths exist, even if a pier undergoes heavy damage with flexural degradation, can happen that other less damaged piers or abutments still contribute to the bridge's horizontal capacity. The same is not true for the case of an axial failure because generally, the axial loads have just one possible path from the superstructure to the foundation that cannot be replaced by other members.

Typical observed damages of piers are a consequence of yielding or buckling of reinforcing longitudinal steel bars, spalling of concrete cover, or sudden fracture of transverse reinforcements. Buckling it’s likely to occur when longitudinal bars are not restrained by transverse reinforcements as could be the

case of rectangular cross-sections where only the hoop corners provide enough transverse restraint. Generally, the primarily flexural failure is related to the absence of seismic details that limit the possibility for the pier to deform inelastically. Another issue that can occur is associated with lap-splices that represent a typical weak point especially under cyclic loading and mainly in those pier regions that are prone to be subjected to significant cyclic-inelastic strains (pier bases).

Shear failure is generally suffered by short and massive cross-section piers that result in a very high stiffness capable of attracting high levels of inertia forces. Shear failure is particularly critical because is rather brittle and accompanied by small horizontal displacements, and may lead to subsequential loss of axial load capacity (Figure 2.4).

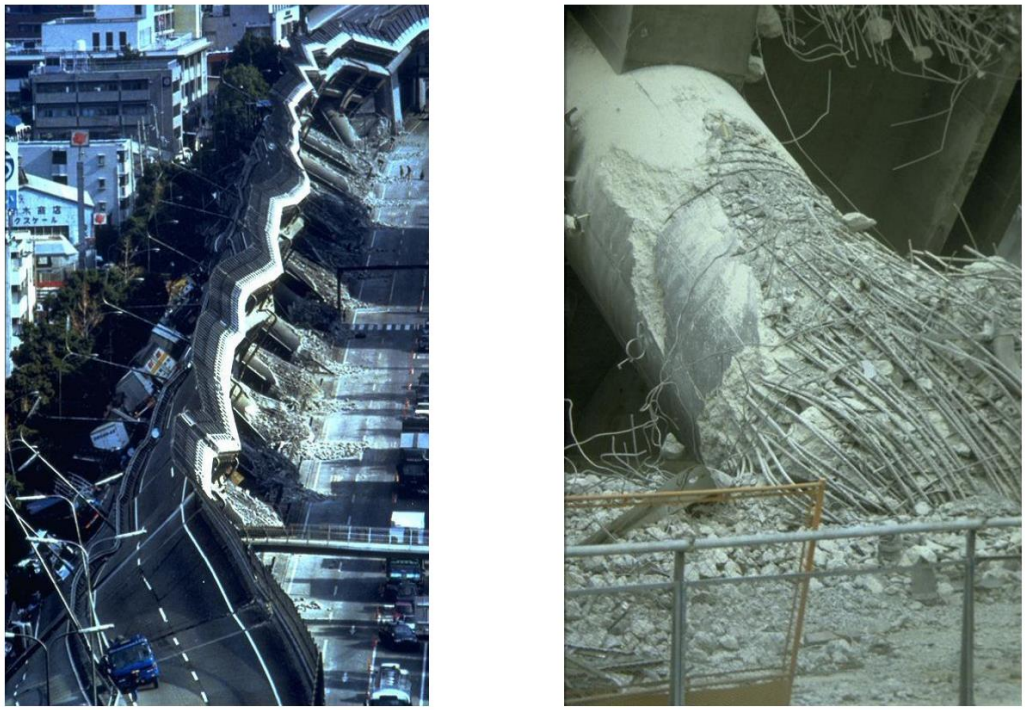

Figure 2.4. Typical piers failure during the Kobe 1995 earthquake [36].

2.2.3 Abutment damages

The seismic behavior of abutments is significantly influenced by both soil-structure interaction and interaction with the superstructure. As mentioned earlier, during a seismic event, the superstructure can transfer pounding forces to the abutments, further complicating their response. The latter phenomenon is likely to occur if the gap between superstructure and abutment is small or is reduced because of thermal deformations. The typical damage pattern for the abutments consists of movements (sliding) and rotations along the transverse axis, especially in those cases where the passive earth pressure coming from the backfill soil increases significantly due to dynamic effects. Even if bridge collapse due to

abutment failure is rather uncommon it can produce high economic costs for post-earthquake repair measures.

Figure 2.5. Typical abutment damages during the Northridge 1994 earthquake [36].

2.2.4 Foundation damages

As mentioned earlier, abutments and piers can be funded either on spread footings or deep foundations. In new bridge design, these foundations are typically required to remain elastic under seismic actions. This is not the case for the existing structures, where foundations were mainly designed for gravity loads without considering for seismic effects. During the Kobe 1995 earthquake, several damages were observed to footings which happened to fail mainly due to the development of shear cracking or rocking type of behavior. Particularly, this latter phenomenon is associated to a significant moment demand caused by seismic actions coupled with uplifting of the foundation.

2.3 Seismic isolation of highway bridges

Seismic isolation is an effective tool for improving the seismic performance of bridges and mitigating seismic damages. This technique permits to uncouple the bridge superstructure from the substructure by interposing mechanical devices with a reduced (very low) horizontal stiffness (Figure 2.6) [37]. This has the effect that when an earthquake occurs the deformations mainly focus on the seismic isolation devices rather than on the substructure elements. As shown in Figure 2.7, the isolators' flexibility shifts the response of an isolated bridge towards

higher fundamental periods with the advantage of reducing the seismic forces in the substructure while providing additional damping that can limit relative displacements between the superstructure and substructure. Simultaneously, the isolator devices possess an adequate rigidity under service loads such as wind, and vehicle braking and can accommodate with no restraints environmental effects such as thermal expansion, creep, and shrinkage.

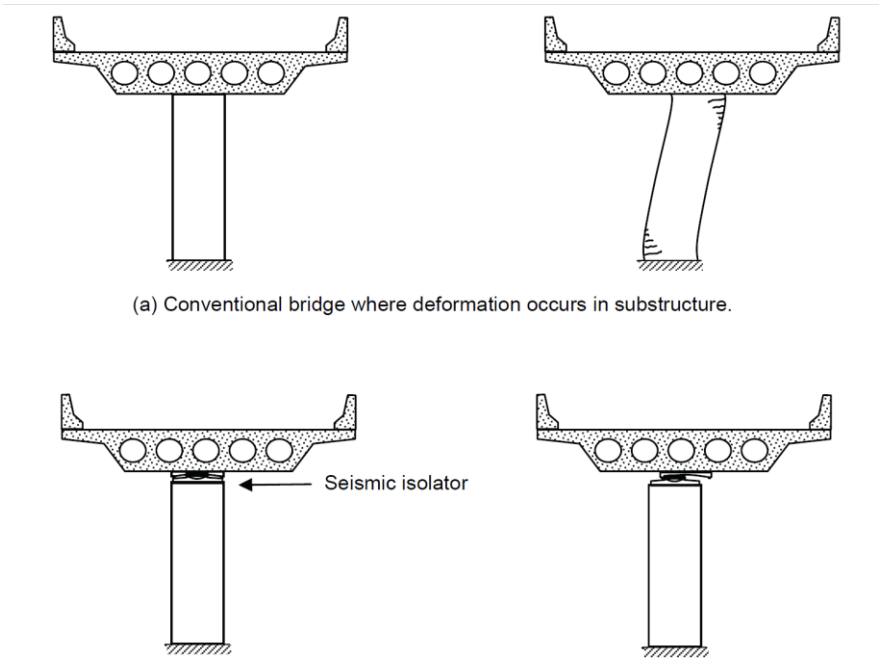

(a) Conventional bridge where deformation occurs in substructure.

(b) Seismically isolated bridge where deformation occurs in the isolator.

Figure 2.6. Seismically isolated bridge vs ordinary bridge: a comparison [37].

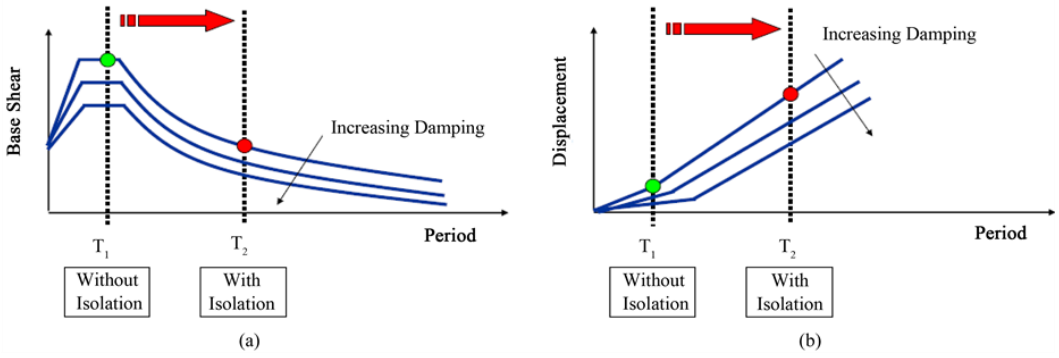

Figure 2.7. Effects of seismic isolation on the shear forces (a); and on the displacements (b), for various levels of damping.

Even though in the case of isolated bridges it is possible to work with reduced seismic forces, they are at the same time characterized by higher superstructure displacements that should be accommodated by increasing seat lengths and/or with wider expansion joints. This is the reason why isolator devices are generally provided with specific energy dissipation mechanisms aimed at introducing a significant level of additional damping into the bridge such as to limit these displacements. In Figure 2.8 a typical force-displacement relationship for a seismic isolator is presented: the energy dissipated over one cycle of motion E_d is

represented by the shaded area under the bilinear curve, which is not recovered during unloading because it is lost in the form of heat from the system.

In order to simplify the derivation of the energy dissipation it is common in literature to introduce an effective elastic stiffness, K_{eff} (Figure 2.8), and an equivalent viscous damping ratio β_e such that:

$$C_L = 2 \cdot \beta_e \cdot \omega \cdot m \tag{2.1}$$

Where C_L is the linear viscous damping constant.

It is indeed possible to demonstrate that the energy dissipated by a linear viscous damper in each cycle E_{vd} (that is the area under the force-displacement relationship presented in Figure 2.9) is the same as the energy dissipated by a generic hysteretic device E_D (Figure 2.8).

$$E_{vd} = C_L \pi \omega D_{\max}^2 \tag{2.2}$$

Where $D_{\max}$ is the maximum displacement exhibited from the isolator.

Based on this assumption the equivalent viscous damping ratio β_e is calculated by imposing the following equality:

$$E_{vd} = C_L \pi \omega D_{\max}^2 = E_D \tag{2.3}$$

$$C_L = 2 \cdot \beta_e \cdot \omega \cdot m = \frac{E_D}{\pi \omega D_{\max}^2} \tag{2.4}$$

And so:

$$\beta_e = \frac{E_D}{2\pi\omega^2 m D_{\max}^2} = \frac{E_D}{2\pi k_{eff} D_{\max}^2} \tag{2.5}$$

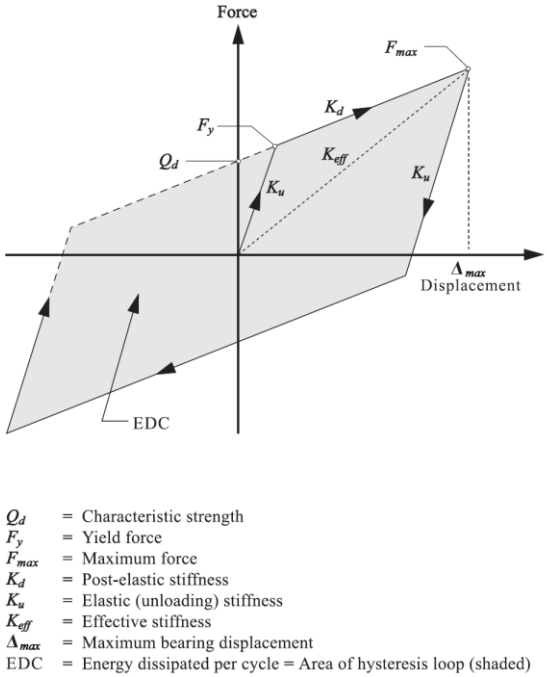

Q_d = Characteristic strength
F_y = Yield force
F_{max} = Maximum force
K_d = Post-elastic stiffness
K_u = Elastic (unloading) stiffness
K_{eff} = Effective stiffness
Δ_{max} = Maximum bearing displacement
EDC = Energy dissipated per cycle = Area of hysteresis loop (shaded)

Figure 2.8. Force-displacement relationship for an isolator [37].

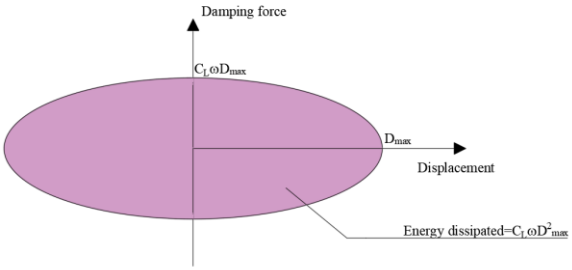

Figure 2.9. Force-displacement relationship for a linear viscous damper.

Seismic isolators generally adopted for bridge structures or ordinary structures can be grouped into two categories that are:

- Elastomeric bearings (with or without lead core for the energy dissipation);
- Sliding isolators that use friction as an energy dissipator mechanism.

2.3.1 Elastomeric isolators

Elastomeric bearings are the most adopted devices for bridge isolation and have been around for more than 50 years as they were initially implemented to accommodate thermal expansion in bridges.

They are characterized by the superimposition of elastomer layers (5-20mm) and steel sheets (2-3mm), that are solidarized by a vulcanization process. Elastomeric bearings were initially non-reinforced and this caused high axial deformability to the rubber with a potential rocking effect to the device (rotation of the isolator about a horizontal axis). The presence of the steel reinforcing plates is therefore fundamental to provide confinement, vertical stiffness, and vertical

load capacity to the rubber layers, which are specifically designed to be larger than the steel layers such as to protect them from corrosion (Figure 2.10).

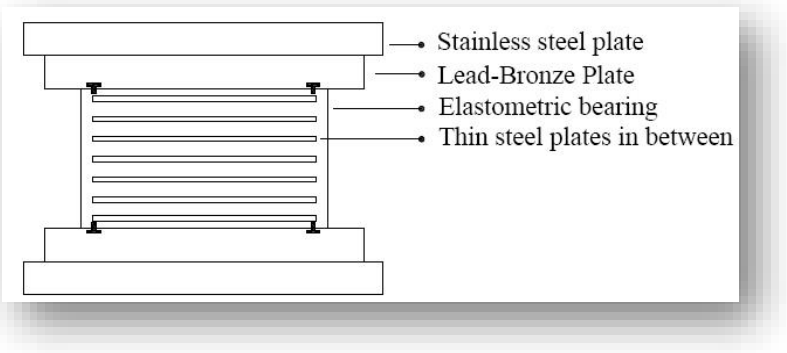

Figure 2.10. Schematic representation of laminated rubber bearing.

The performance of such devices also depends on the kind of rubber they are made with; based on this aspect the following typologies are distinguished:

- *Natural rubber* elastomeric bearings;
- *Synthetic rubber* elastomeric bearings.

Rubber is a hydrocarbon called isoprene and *natural rubber* consists of regular sequences of isoprene arranged in a chain fashion that provides elasticity to the material. The chains can be stretched out when an external force is applied until the point when the connections are broken. This behavior manifests itself at a macroscopic scale with large displacements that the rubber can accommodate.

On the other hand, *synthetic rubber* is made up of neoprene with some advantages when compared to isoprene: it has higher fire-resistant capacities, it is less prone to aging, and much more impermeable to gas. Nevertheless, neoprene has been extensively used in thermal expansion devices for bridges and rarely for the manufacturing of elastomeric bearings due to lower elongation at break, when compared to natural rubber.

Independently of the rubber type adopted, three types of elastomeric bearings have developed over the years to meet different requirements. These are:

- *Low-damping* rubber bearings: these are natural rubber bearings with standard low-damping rubber: to withstand the damping forces required in seismic isolation design they are generally coupled to viscous dampers for energy dissipation;
- *High-damping* rubber bearings: these are manufactured with high-damping rubber (natural rubber) for energy dissipation purposes;
- *Lead-rubber* bearings: manufactured with natural rubber equipped with an internal lead core for energy dissipation.

2.3.1.1 Low-damping rubber bearings (LDRB)

They can be made with either natural rubber or neoprene. The isolator response is essentially elastic with the increase of displacements (Figure 2.11). The main advantages of these devices are: very easy to assemble, low production costs, and mechanical properties independent of temperature and aging. Contrarily, they are characterized by low damping value (in the order of 2-4%) and do not provide enough rigidity under service loads (*e.g.*, wind). Because of this last feature, they are generally coupled with additional energy dissipator devices such as hysteretic or viscous dampers.

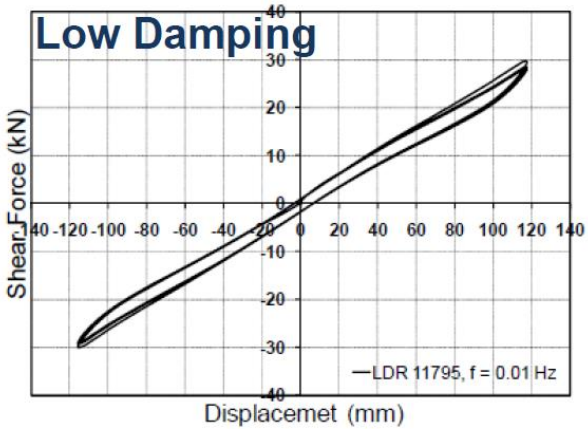

Figure 2.11. Force-displacement relationship for LDRB.

2.3.1.2 High-damping rubber bearings (HDRB)

These devices were first developed by Prof. Kelly in 1995 [40], at the University of California, Berkeley. They are generally made up of natural rubber 'charged' with special additives such as carbon black and silicon that give higher damping capacity to the rubber (between 10% and 20% at a 100% shear deformation). This kind of property makes the HDRB an efficient and complete device that does not need to be coupled with mechanical dissipation systems, as it provides by itself the required flexibility and dissipation properties.

By looking at the force-deformation relationship (Figure 2.12) it is possible to highlight the following features:

- High initial lateral stiffness that enhances to withstand the service loads (*e.g.* wind) with low displacements;
- The mechanical properties of the isolator change in dependence of the loading history (*e.g.* scragging effect);
- Non-linear strain rate dependence;
- The hysteretic behavior depends on temperature variations (low temperature generally causes an increase in stiffness and characteristic strength);
- Aging effects generally result in increasing both the stiffness and the characteristic strength, even if of a relatively small amount (10%-20% over 30 years).

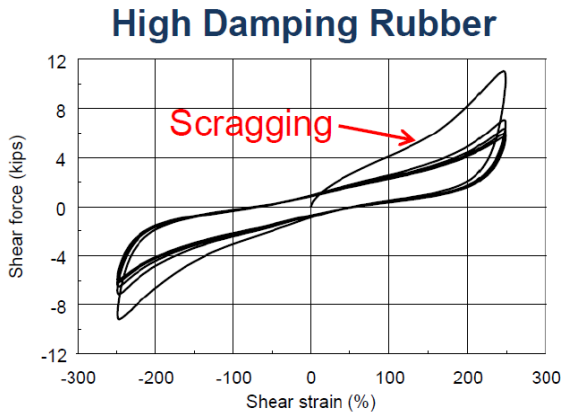

Figure 2.12. Force-displacement relationship for HDRB.

2.3.1.3 Lead-rubber bearings (LRB)

This type of device is the most common isolator in bridge applications. Similar to LDRB, it incorporates a cylindrical lead core fitting inside the center of the isolator (Figure 2.13-Figure 2.14). The lead core is meant to dissipate energy by yielding during lateral displacements. The constitutive force-deformation behavior is a bilinear type as it is the combination of the typical linear elastic model of LDRB and the elastoplastic behavior of the lead core. Overall the bearing is very stiff in the vertical direction and flexible in the horizontal direction, provided that the lead core yields. Under service loads the combined lateral stiffness of rubber layers and lead core offers a sufficient stiffness. However, during a seismic event, the lead core deforms in shear and yields at a low shear stress of about 9.0Mpa. This mechanism reduces the overall lateral stiffness of the bearing, leading to large deformations in the rubber layers that provide the required flexibility to elongate the bridge period.

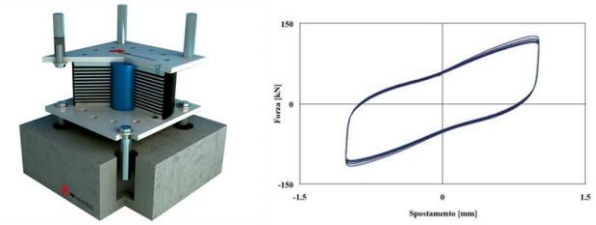

Figure 2.13. Lead rubber bearing isolator (a); Force-displacement relationship for LRB (b).

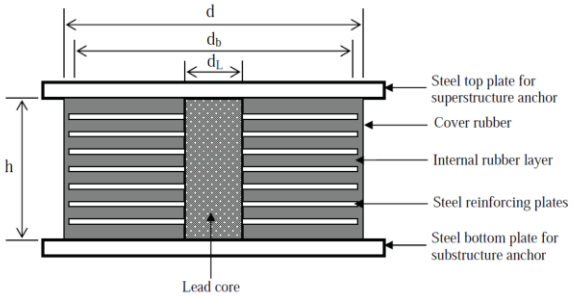

Figure 2.14. Section view of LRB [37].

In the force deformation behavior, because the elastomer is a low-damping natural rubber, the yield force F_y and the characteristic strength Q_d (Figure 2.8) come from the lead core alone as specified in the following Eq. (2.6)[37]:

$$F_y = \frac{1}{\psi} f_{yL} \frac{\pi d_L^2}{4} \tag{2.6}$$

Where:

f_{yL} = shear yield stress of the lead (9.0Mpa);

d_L = diameter of the lead plug;

ψ = load factor that takes into account the creep effect in lead (= 1.0 for seismic loads; = 2.0 for service loads);

The characteristic strength is then provided by:

$$Q_d = F_y \left(1 - \frac{k_d}{k_u}\right) \tag{2.7}$$

Where:

k_d = post-elastic stiffness;

$k_u = n \cdot k_d$ elastic loading and unloading stiffness, with n=10 for seismic loads, n=8 for service loads;

The post-elastic stiffness k_d is a function of the initial elastic stiffness coming from the contribution of the rubber, given by:

$$k_r = \frac{GA_b}{h_r} \tag{2.8}$$

Where:

G = shear modulus of the rubber;

h_r = total height of the rubber;

A_b = neat area of the rubber, that is the total area of the rubber minus the lead core area: $A_b = \frac{\pi(d_b^2 - d_L^2)}{4}$.

Indeed, the post-elastic stiffness is equal to:

$$k_d = fk_r \tag{2.9}$$

Being f a correction factor that accounts for the presence of the lead core, generally assumed equal to *f=1.1*.

From the hysteretic behavior of Figure 2.8 it derives that the horizontal force F at the generic displacement D is given by:

$$F = Q_d + k_d D \tag{2.10}$$

Then the effective stiffness k_{eff} is simply obtained by dividing Eq. (2.10) for the displacement D, as follows:

$$k_{eff} = \frac{Q_d}{D} + k_d \tag{2.11}$$

The equivalent viscous damping ratio is finally calculated according to Eq. (2.5):

$$\beta_e = \frac{4Q_d(D - D_y)}{2\pi k_{eff} D^2} = \frac{2Q_d(D - D_y)}{\pi D(Q_d + k_d D)} \tag{2.12}$$

The elastomeric bearings need to be checked for axial instability in the undeformed and deformed state. The relations that express the buckling loads are strongly dependent on the type of connection between the isolator and the structure, which can be of two types:

- A bolted connection, in which the rotation is constrained properly and only instability coming from axial loads is possible;
- A dowelled connection, in which also instability by overturning can occur.

Undeformed state

In the undeformed state, the buckling load for the two configuration types is theoretically the same and equal to:

$$P_{cr} = \sqrt{\frac{\pi^2 \cdot E_c \cdot I \cdot G \cdot A}{3h_r^2}} \tag{2.13}$$

Where:

$I =$ moment of inertia along the weak axis of the isolator;

$A =$ the area of the rubber attached to the plates (must be reduced to take into account the lateral displacement);

$G =$ shear modulus of the rubber;

$E_c = \dfrac{1}{\left(\dfrac{1}{6GS^2} + \dfrac{4}{3K}\right)}$ is the modulus of elasticity of rubber in compression; K= bulk modulus of rubber ($\approx$2000Mpa); S is the shape factor of rubber layer of thickness t.

The safety check against instability is carried out by dividing the critical load P_{cr} by the combination of dead loads and live loads.

Deformed state

In the deformed state, the critical load depends on which of the two configurations is adopted. For the bolted connection case the critical load is given by:

$$P'_{cr} = P_{cr} \frac{A_r}{A} \tag{2.14}$$

Where:

$P'_{cr} =$ buckling load in the deformed state;

$A =$ bonded elastomeric area;

$A_r =$ overlapped area during lateral displacements between the top bonded area and the bottom bonded area.

As shown in Figure 2.15, in the case of a circular hollow bearing $\dfrac{A_r}{A} \approx \dfrac{(\delta - \sin\delta)}{\pi}$, being $\delta = 2\cos^{-1}\left(\dfrac{d_t}{B}\right)$ such that:

$$P'_{cr} \approx P_{cr} \frac{(\delta - \sin\delta)}{\pi} \tag{2.15}$$

Eq. (2.15) is valid for the case of circular hollow bearings.

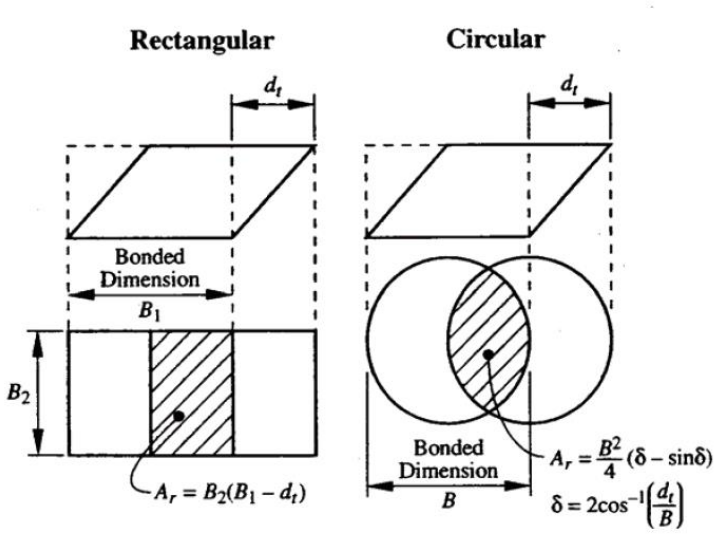

Figure 2.15. Overlapped area in an elastomeric bearing [37].

In the case of the second configuration, dowelled bearings may experience roll-over or overturn when subjected to large lateral displacements. Specifically, the critical value of the lateral displacement at which overturning occurs is given by:

$$D_{cr} = \frac{P \cdot B - Q_d \cdot h}{P + k_d \cdot h} \tag{2.16}$$

Where:

$P =$ axial load on the bearing;

$B =$ bearing diameter;

$Q_d =$ characteristic strength;

$h =$ total height of the bearing (sum of the rubber layers and steel layers).

2.3.2 Sliding isolators

Sliding isolators can be of two types:

- Unidirectional (generally adopted for bridges)
- Multi-directional (mostly adopted for buildings).

2.3.2.1 Flat surface sliding device (SD)

They are multi-directional devices with two sliding surfaces with a circular or squared shape that slide one on another with a low friction coefficient (Figure 2.16). They are manufactured with stainless steel and PTFE (Teflon), properly selected to develop a slow friction resistance. Accordingly, the dynamic friction coefficient is comprised between 5% and 20% and it can drastically reduce in the case of lubrication.

The friction coefficient is greatly influenced by factors such as the sliding velocity, temperature, and contact pressure. Due to the variability in friction and

uncertainties in environmental conditions, it is common practice to disregard friction forces and their associated energy dissipation. Instead, reliance is placed on the lateral deformability of the isolation devices for seismic mitigation purposes. However, such systems lack of restoring force capability, and can thus generally undergo significant permanent displacements.

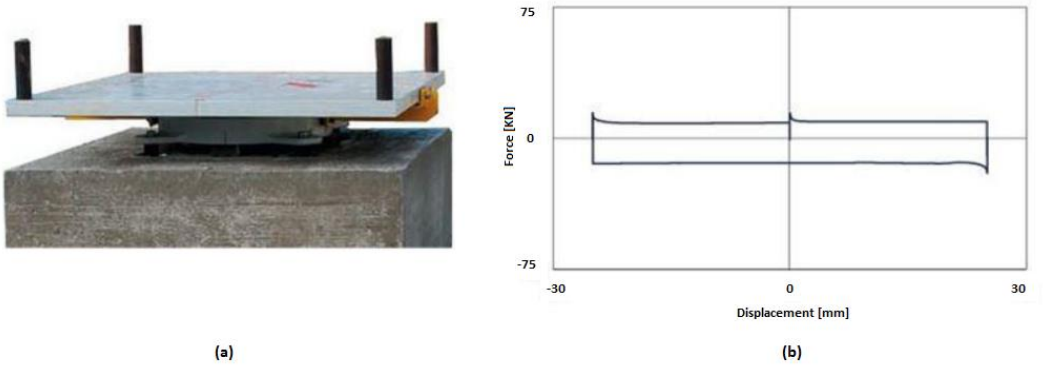

Figure 2.16. SD isolator (a); typical SD hysteretic loop (b) [Fip Industriale catalogue].

2.3.2.2 Friction Pendulum System (FPS)

Friction Pendulum System (FPS) stands for those sliding devices with a curved surface that allows the movement between superstructure and substructure. These devices are provided with an energy dissipation capacity based on friction, and with a recentering mechanism that uses gravity according to the pendulum law. The system consists of an articulated slider that moves on a spherical concave surface generally made of Polytetrafluoroethylene (PTFE) applied on a stainless steel surface (Figure 2.17).

The most valuable characteristics of these sliding isolators are summarized next:

- The radius of curvature of the spherical surface controls the concavity-related stiffness and the fundamental isolation period of vibration of the structure;
- The isolation period is independent of the structural mass;
- The friction coefficient is responsible for the energy dissipation.

In the upcoming chapter, these isolation devices will be examined in greater detail. They are the chosen isolation system intended for retrofitting an existing highway bridge, which serves in this thesis as the testbed bridge for analyzing seismic response under spatial variability of earthquake ground motion.

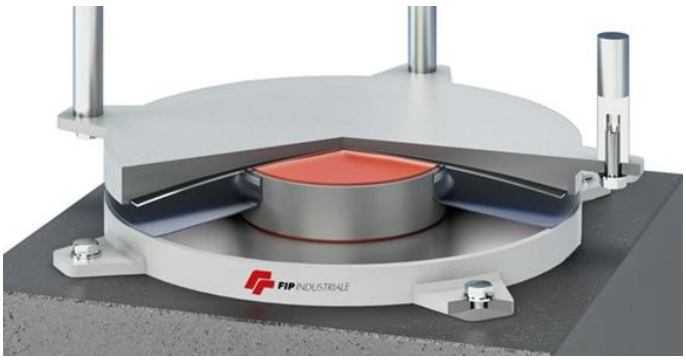

Figure 2.17. Typical single curvature FPS device [Fip Industriale catalog].

3 Elastic theory of isolated bridges with friction pendulum system (FPS)

In this chapter, an overview of the elastic seismic isolation theory is presented. It begins with an introduction of the basic principles of seismically isolated systems, originally developed by Prof. J. Kelly in 1996 for building structures. It follows a detailed description of friction pendulum bearings, specifically emphasizing their dynamic behavior and the friction-related properties that characterize these devices. Furthermore, the chapter explores the key factors influencing the friction coefficient, including apparent pressure, sliding velocity, temperature variations, and the loading history.

Finally, a proposed numerical model is presented for multi-span continuous deck bridges that are seismically isolated using friction pendulum devices.

3.1 Basis of the isolation theory

The present section is extensively based on the theoretical analysis of seismic isolation developed by Prof. J. Kelly at the University of California and detailed in [40-41-45].

Similar to the case of fixed-base structures where the theory starts with the analysis of a single-degree-of-freedom system, the study of base-isolated systems is applied to a two-degrees-of-freedom (2DOF) system, one accounting for the isolation level and the other for the superstructure level.

The theory developed by Prof. J. Kelly assumes that the 2DOF system behaves linearly and as such, being many of the isolation devices intrinsically nonlinear, it can be considered, as also Prof. J. Kelly pointed out, the theory is only an approximation of the real dynamic behavior of the isolated structures, necessitating for the application of various linearization techniques within its framework.

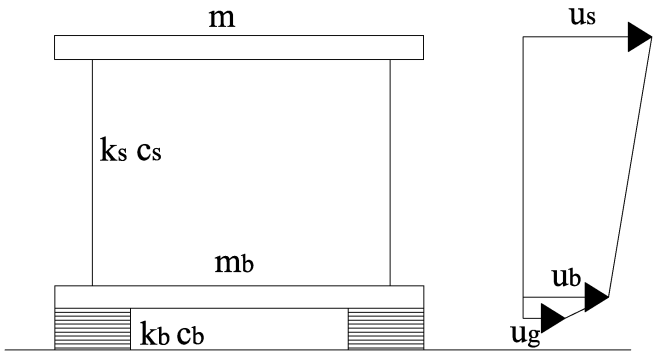

Figure 3.1. 2DOF model of a base-isolated system [40-41].

The mechanical and kinematic parameters governing the dynamic behavior of a single-story structure are introduced next:

- $m_s =$ mass of the superstructure;
- $k_s, c_s =$ stiffness and damping of the superstructure;
- $m_b =$ mass of the slab level over the isolation system;
- $k_b, c_b =$ stiffness and damping of the isolation system;
- $u_g =$ ground motion displacement;
- $u_s =$ absolute lateral displacement at the superstructure level;
- $u_b =$ absolute lateral displacement at the isolation level;

Applying the Newton's second law to both the slab mass and the superstructure mass determines the following equation of motions (expressed in terms of absolute displacements):

$$m_s \ddot{u}_s = -c_s(\dot{u}_s - \dot{u}_b) - k_s(u_s - u_b) \tag{3.1}$$

$$m_s \ddot{u}_s + m_b \ddot{u}_b = -c_b(\dot{u}_b - \dot{u}_g) - k_b(u_b - u_g) \tag{3.2}$$

It is convenient to work in terms of relative displacements v_s and v_b, respectively equal to the relative displacement of the superstructure with respect to the isolation level and the relative displacement of the isolation level to the ground:

$$v_s = (u_s - u_b) \tag{3.3}$$

$$v_b = (u_b - u_g) \tag{3.4}$$

Substituting Eq.s (3.3)-(3.4) into Eq.s (3.1)-(3.2) yields:

$$m_s(\ddot{v}_b + \ddot{v}_s + \ddot{u}_g) + c_s\dot{v}_s + k_s v_s = 0 \tag{3.5}$$

$$m_b(\ddot{v}_b + \ddot{u}_g) + m_s(\ddot{v}_b + \ddot{v}_s + \ddot{u}_g) + c_b\dot{v}_b + k_b v_b = 0 \tag{3.6}$$

And then highlighting the ground motion-related terms:

$$m_s\ddot{v}_b + m_s\ddot{v}_s + c_s\dot{v}_s + k_s v_s = -m_s\ddot{u}_g \tag{3.7}$$

$$(m_s + m_b)\ddot{v}_b + m_s\ddot{v}_s + c_b\dot{v}_b + k_b v_b = -(m_s + m_b)\ddot{u}_g \tag{3.8}$$

It is worth noting that if the relative motion between the superstructure and isolation level is suppressed ($v_s = 0$), then Eq. (3.8) becomes:

$$(m_s + m_b)\ddot{v}_b + c_b\dot{v}_b + k_b v_b = -(m_s + m_b)\ddot{u}_g \tag{3.9}$$

That is the equation of motion of a system with total mass $M = m_s + m_b$ supported on the isolation level.

Similarly, if the relative motion between the isolation level and the ground is restrained ($v_b = 0$), Eq. (3.7) becomes the equation of motion valid for the more general fixed-base SDOF system:

$$m_s\ddot{v}_s + c_s\dot{v}_s + k_s v_s = -m_s\ddot{u}_g \tag{3.10}$$

It is possible to rewrite the equations of motion of the 2DOF in a matrix notation:

$$\begin{bmatrix} M & m_s \\ m_s & m_s \end{bmatrix}\begin{Bmatrix} \ddot{v}_b \\ \ddot{v}_s \end{Bmatrix} + \begin{bmatrix} c_b & 0 \\ 0 & c_s \end{bmatrix}\begin{Bmatrix} \dot{v}_b \\ \dot{v}_s \end{Bmatrix} + \begin{bmatrix} k_b & 0 \\ 0 & k_s \end{bmatrix}\begin{Bmatrix} v_b \\ v_s \end{Bmatrix} = -\begin{bmatrix} M & m_s \\ m_s & m_s \end{bmatrix}\begin{Bmatrix} 1 \\ 0 \end{Bmatrix}\ddot{u}_g \tag{3.11}$$

Or even in a more compact form:

$$[M]\{\ddot{v}\} + [C]\{\dot{v}\} + [K]\{v\} = -[M]\{r\}\ddot{u}_g \tag{3.12}$$

It is at this stage convenient to introduce the following quantities:

- $\omega_s = \sqrt{\frac{k_s}{m_s}}$ the natural frequency of the fixed base structure;
- $\omega_b = \sqrt{\frac{k_b}{M}}$ the natural frequency of the isolation system with stiffness k_b ;
- $\xi_s = \frac{c_s}{2m\omega_s}$ the viscous damping ratio for the superstructure;

- $\xi_b = \dfrac{c_b}{2M\omega_b}$ the viscous damping ratio for the isolation level;

Being M equal to $M = m_s + m_b$.

Additionally, the following order of magnitudes hypothesis can be done considering the properties of the isolation system and superstructure:

- $\omega_s >> \omega_b$; this means that if the following quantity is defined $\varepsilon = \left(\dfrac{\omega_b}{\omega_s}\right)^2$, then it is assumed to be of the order 10^{-2};
- $m_b < m_s$ but of the same order of magnitude;
- ξ_b and ξ_s are of the same order of magnitude as ε.

Also, defining the mass ratio γ as:

$$\gamma = \frac{m_s}{m_s + m_b} = \frac{m_s}{M} < 1 \tag{3.13}$$

It is finally possible to express the system of the equation of motions governing the problem in a dimensionless form, dividing Eq. (3.7) for m_s and Eq. (3.8) for $M = m_s + m_b$:

$$\frac{m_s}{m_s}\ddot{v}_b + \frac{m_s}{m_s}\ddot{v}_s + \frac{c_s}{m_s}\dot{v}_s + \frac{k_s}{m_s}v_s = -\frac{m_s}{m_s}\ddot{u}_g \tag{3.14}$$

$$\frac{(m_s + m_b)}{M}\ddot{v}_b + \frac{m_s}{M}\ddot{v}_s + \frac{c_b}{M}\dot{v}_b + \frac{k_b}{M}v_b = -\frac{(m_s + m_b)}{M}\ddot{u}_g \tag{3.15}$$

Obtaining:

$$\ddot{v}_b + \ddot{v}_s + 2\xi_s\omega_s\dot{v}_s + \omega_s^2 v_s = -\ddot{u}_g \tag{3.16}$$

$$\ddot{v}_b + \gamma\ddot{v}_s + 2\xi_b\omega_b\dot{v}_s + \omega_b^2 v_s = -\ddot{u}_g \tag{3.17}$$

The natural frequencies of the system can be found by solving the eigenvalue problem:

$$\left|[K] - \omega^2[M]\right| = 0$$

That leads to the following characteristic equation for ω:

$$(1-\gamma)\omega^4 - (\omega_b^2 + \omega_s^2)\omega^2 + \omega_b^2\omega_s^2 = 0 \tag{3.18}$$

The solution of Eq. (3.18) consists of two roots (ω_1, ω_2) given by:

$$\omega_1^2, \omega_2^2 = \frac{1}{2(1-\gamma)}\left\{(\omega_s^2 + \omega_b^2) \pm \sqrt{(\omega_s^2 + \omega_b^2)^2 - 4(1-\gamma)(\omega_s^2\omega_b^2)}\right\} \tag{3.19}$$

Moreover, making the following position for the term under the square root:

$$\sqrt{(\omega_s^2+\omega_b^2)^2-4(1-\gamma)(\omega_s^2\omega_b^2)}=(\omega_s^2-\omega_b^2)\sqrt{1+\frac{4\gamma(\omega_s^2\omega_b^2)}{(\omega_s^2-\omega_b^2)^2}} \tag{3.20}$$

And then expanding the right-hand side of Eq. (3.20) using a binomial series it is possible to write:

$$\sqrt{(\omega_s^2+\omega_b^2)^2-4(1-\gamma)(\omega_s^2\omega_b^2)}\approx(\omega_s^2-\omega_b^2)\left(1+\frac{2\gamma\omega_s^2\omega_b^2}{(\omega_s^2-\omega_b^2)^2}\right) \tag{3.21}$$

Eq. (3.21) is then substituted into Eq. (3.19) such as to derive the expression for the two natural frequencies of the isolated system:

$$\omega_1^2=\frac{\omega_b^2}{(1-\gamma)}\left[1-\frac{\gamma\omega_s^2}{(\omega_s^2-\omega_b^2)}\right] \tag{3.22}$$

$$\omega_2^2=\frac{\omega_s^2}{(1-\gamma)}\left[1+\frac{\gamma\omega_b^2}{(\omega_s^2-\omega_b^2)}\right] \tag{3.23}$$

Since the following assumption is valid: $\omega_s >> \omega_b$, Eq.s (3.22)-(3.23) can be rewritten us:

$$\omega_1^2=\omega_b\sqrt{1-\gamma\varepsilon}\approx\omega_b \tag{3.24}$$

$$\omega_2^2=\frac{\omega_s^2}{\sqrt{(1-\gamma)}}\sqrt{\left[1+\frac{\gamma\omega_b^2}{(\omega_s^2)}\right]}\approx\frac{\omega_s}{\sqrt{(1-\gamma)}} \tag{3.25}$$

The first natural frequency ω_1 is the frequency of the isolation system, which is only slightly modified by the presence of the superstructure (the modification factor is of the order of ε).

The second natural frequency ω_2 is the superstructure's frequency which is on the contrary significantly affected by the presence of the base slab mass.

Once the natural frequencies are determined it is possible to derive the first $\{A^{(1)}\}$ and second $\{A^{(2)}\}$ mode shapes, which it is possible to demonstrate being equal to the following mathematical expressions:

$$\{A^{(1)}\}=\begin{Bmatrix}1\\ \varepsilon\end{Bmatrix} \tag{3.26}$$

$$\{A^{(2)}\}=\begin{Bmatrix}1\\ -\left(\dfrac{1-(1-\gamma)\varepsilon}{\gamma}\right)\end{Bmatrix} \tag{3.27}$$

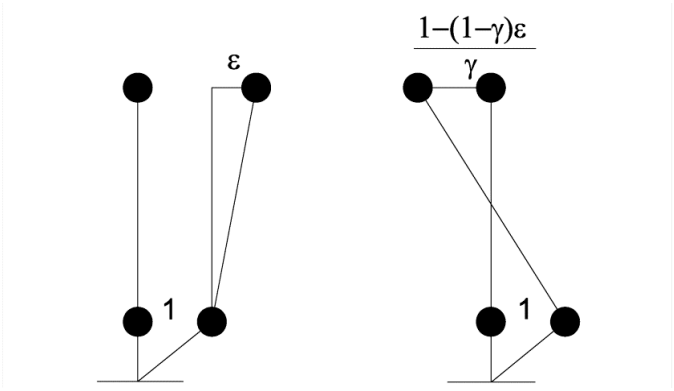

Figure 3.2. Mode shapes for a Base Isolated 2DOF system [40-41].

The first two mode shapes for the isolated structure are illustrated in Figure 3.2. It can be observed that the first mode shape is approximately the deformation of a rigid structure on a flexible isolation system placed at the base. The second mode shape determines deformations both in the isolation system and in the superstructure, with the displacement at the top of the structure that is out of phase and of the same order of magnitude as the isolation displacement.

The second mode appears to be the mode of vibration of two masses vibrating freely in space about the center of mass of the isolated system. The great result of this behavior is that the second mode is not responsible for a large base shear even for strong values of the acceleration.

By using the modal superimposition method, it is possible to rewrite the relative displacements v_s and v_b as follows:

$$v_b(t) = u_1(t)A_1^{(1)} + u_2(t)A_1^{(2)} \tag{3.28}$$

$$v_s(t) = u_1(t)A_2^{(1)} + u_2(t)A_2^{(2)} \tag{3.29}$$

Where $u_1(t)$ and $u_2(t)$ are the principal coordinates in the modal space that allow to rewriting Eq.s (3.16)-(3.17) in the following way:

$$\ddot{u}_1 + 2\xi_1\omega_1\dot{u}_1 + \omega_1^2 u_1 = -\alpha_1\ddot{u}_g \tag{3.30}$$

$$\ddot{u}_2 + 2\xi_2\omega_2\dot{u}_2 + \omega_2^2 u_2 = -\alpha_2\ddot{u}_g \tag{3.31}$$

Being ξ_1 and ξ_2 the modal damping ratios and α_1, α_2 the modal participation factors. Based on the hypothesis concerning the factor ε, it is possible to demonstrate that the following relations hold for the first mode:

$$\alpha_1 = 1 - \gamma\varepsilon \tag{3.32}$$

$$M_1^* \approx M \tag{3.33}$$

Where M_1^* is the modal mass in the first mode.

Similarly, for the second mode it is possible to derive the following:

$$\alpha_2 = \gamma\varepsilon \tag{3.34}$$

$$M_2^* = M\,\frac{(1-\gamma)[1-2\varepsilon(1-\gamma)]}{\gamma} \tag{3.35}$$

with M_2^* the modal mass in the second mode.

The last results explain why the seismic isolation system is effective in reducing the seismic effects on the superstructure: the participation factor α_2, associated with the second mode and as so involving structural deformation, is of the order of magnitude of ε and in general, could be very small if the original natural frequencies ω_s, ω_b are well separated. Additionally, the natural frequency of the second mode is shifted towards higher values than the original fixed-base frequency (Eq. (3.25)) which means that the isolated structure will be out of range of strong earthquake ground motion with large acceleration at the fixed-base structure.

Furthermore, an important feature related to the seismic isolation is the energy dissipation. A natural rubber isolation system provides a degree of damping typically in the range of 10-20% of the critical one, which, as is well known, is just of the order of 5% for a non-isolated structure.

It is possible to demonstrate that the following relations are valid for the computation of the first and second modal damping ratio ξ_1 and ξ_2:

$$\xi_1 \approx \xi_b\left(1-\frac{3}{2}\gamma\varepsilon\right) \tag{3.36}$$

$$\xi_2 \approx \frac{\xi_s}{\sqrt{1-\gamma}} + \frac{\gamma\xi_b\sqrt{\varepsilon}}{\sqrt{1-\gamma}} \tag{3.37}$$

It is therefore possible to infer that the first modal damping ratio practically coincides with the high value of the damping ratio of an isolator device. Conversely, the structural damping (second modal damping ratio) is increased by the damping in the isolation system by the term $\sqrt{\varepsilon}$. Particularly, the product $\xi_b\sqrt{\varepsilon}$ could have a high weight to the overall damping of the isolated system especially if the structural damping ξ_s is as small as it generally is.

Knowing $\alpha_1, \alpha_2, \xi_1, \xi_2$ the response of the 2DOF isolated structure under a ground acceleration time history $\ddot{u}_g$ can be calculated (in terms of modal displacements) through the Duhamel's integral:

$$u_1(t) = -\frac{\alpha_1}{\omega_1}\int_0^t \ddot{u}_g(t-\tau)e^{-\xi_1\omega_1\tau}\sin\omega_1(t-\tau)d\tau \tag{3.38}$$

$$u_2(t) = -\frac{\alpha_2}{\omega_2}\int_0^t \ddot{u}_g(t-\tau)e^{-\xi_2\omega_2\tau}\sin\omega_2(t-\tau)d\tau \tag{3.39}$$

Or is simply possible to obtain the maximum values of u_1 and u_2 by using the displacement response spectrum for the ground motion $\ddot{u}_g$ at the frequencies ω_1 and ω_2 and for damping ratios ξ_1 and ξ_2:

$$|u_1(t)|_{\max} = \alpha_1 S_d(\omega_1, \xi_1) \tag{3.40}$$

$$|u_2(t)|_{\max} = \alpha_2 S_d(\omega_2, \xi_2) \tag{3.41}$$

Once the maximum displacements are obtained in the principal coordinates notation, it is possible to estimate the corresponding maximum values of the relative displacements (in the geometric space) v_s and v_b, using the SRSS combination:

$$|v_s(t)|_{\max} = \sqrt{(A_2^{(1)}|u_1(t)|_{\max})^2 + (A_2^{(2)}|u_2(t)|_{\max})^2} \tag{3.42}$$

$$|v_b(t)|_{\max} = \sqrt{(A_1^{(1)}|u_1(t)|_{\max})^2 + (A_1^{(2)}|u_2(t)|_{\max})^2} \tag{3.43}$$

And recalling the most powerful results and approximations made in the previous equations:

$A_1^{(1)} = 1$ and $A_2^{(1)} = \varepsilon$;

$A_1^{(2)} = 1$ and $A_2^{(2)} = \left((1-\gamma)\varepsilon - 1\right)/\gamma$;

$\alpha_1 = 1 - \gamma\varepsilon$ and $\alpha_2 = \gamma\varepsilon$;

The following relations are derived:

$$|v_b(t)|_{\max} = \sqrt{(1-\gamma\varepsilon)^2[S_D(\omega_1, \xi_1)]^2 + \gamma^2\varepsilon^2[S_D(\omega_2, \xi_2)]^2} \tag{3.44}$$

and:

$$|v_s(t)|_{\max} = \sqrt{\varepsilon^2(1-\gamma\varepsilon)^2[S_D(\omega_1, \xi_1)]^2 + \gamma^2\varepsilon^2\frac{1}{\gamma^2}[(1-\gamma)\varepsilon - 1]^2[S_D(\omega_2, \xi_2)]^2} \tag{3.45}$$

Where generally the second term from Eq.s (3.44)-(3.45) can be neglected if the displacements at a higher frequency ω_2, are smaller than the ones at ω_1. Making this assumption it is finally possible to simplify Eq.s (3.44)-(3.45) accordingly:

$$|v_b(t)|_{\max} \approx (1-\gamma\varepsilon)[S_d(\omega_1, \xi_1)] \tag{3.46}$$

and:

$$|v_s(t)|_{\max} \approx \varepsilon\sqrt{[S_d(\omega_1, \xi_1)]^2 + [S_d(\omega_2, \xi_2)]^2} \tag{3.47}$$

Since the primary objective of this thesis is to apply the theoretical principles of base isolation systems, for those structures specifically equipped with friction pendulum devices, the next section will delve into the primary physical and dynamic characteristics of these devices.

3.2 Friction Pendulum devices

FPS devices, originally developed and manufactured by Earthquake Protection Systems in Richmond California [45], is a friction-type bearing that uses the physical law of the pendulum motion to increase the period of vibration of the structure (to 4 seconds or longer), independently of the isolated mass. The main components of friction pendulum bearings include a stainless-steel concave surface upon which an articulated friction slider moves, typically coated with a low-friction material such as PTFE (Figure 3.3).

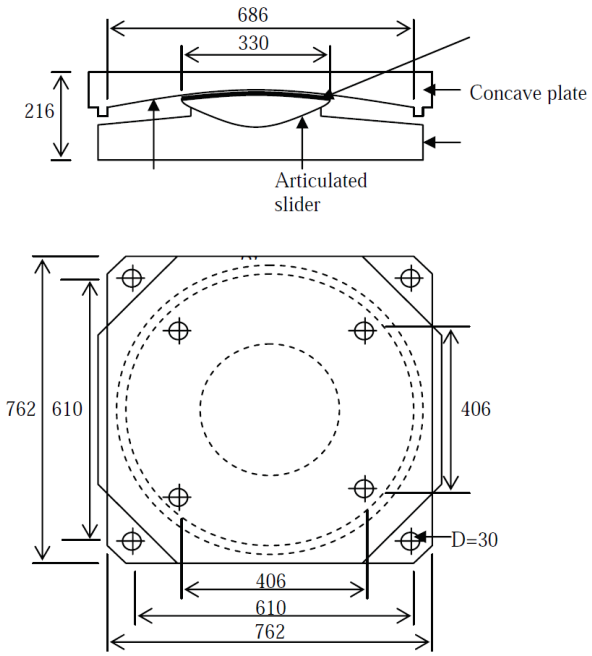

Figure 3.3. Friction pendulum isolator [37].

In the case it is required to accommodate large displacement demands without increasing the isolator's dimension, it is possible to use the double concave friction pendulum system [21-46-48], which consists of two facing concave stainless steel surfaces separated by an articulated double friction slider provided with a low-friction material. The upper and lower concave surfaces can have both different radii of curvature R_1, R_2 and different friction coefficients f_1, f_2. From Figure 3.4 it is evident that the articulated double friction slider is needed to accommodate differential movements along the two sliding concave surfaces. Particularly, when the friction resistance f_2 is exceeded at the bottom surface then the movement is started at the bottom first, while the top surface stays fixed

with respect to the slider (Figure 3.4 (b)). As soon as the friction resistance f_1 is reached also at the top sliding surface, the situation depicted in Figure 3.4(c) arises, with the isolator that can eventually displace a total distance of 2*d*.

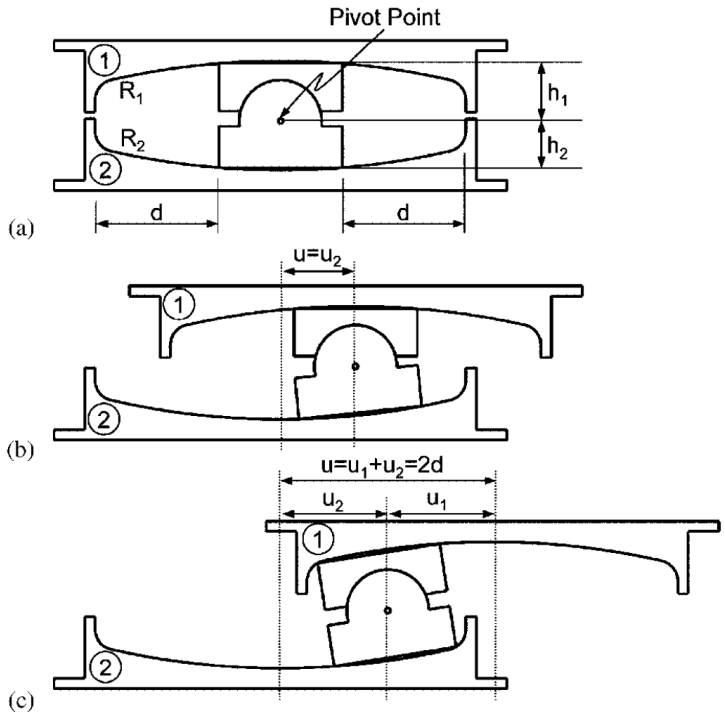

Figure 3.4. Double Concave Friction Pendulum isolator (DCFP) [46].

3.2.1 Formulation of the dynamic behavior

The principle of operation of the friction pendulum system, as originally developed by Zayas in 1990 [49] is presented next. It considers a rigid structure with weight W supported by an FPS device displaced horizontally by d on the spherical concave surface of radius R. In this configuration, the forces acting on the bearing, as illustrated in Figure 3.5 are the following:

- $W =$ weight of the superstructure;
- $F =$ lateral force acting on the slider;
- $F_f =$ friction force acting on the slider;
- $S =$ normal force acting on the slider and due to the superstructure weight;
- $t_1 =$ tensile forces acting on the slider surface which will not be explicitly modeled as they are a component of the friction forces F_f;

Considering the forces involved in the dynamic behavior, it is possible to write the equilibrium equations in both vertical and horizontal directions:

$$W - S\cos\vartheta + F_f \sin\vartheta = 0 \tag{3.48}$$

and:

$$F - S\sin\vartheta - F_f \cos\vartheta = 0 \tag{3.49}$$

Whereas the displacement d results equal to:

$$d = R\sin\vartheta \tag{3.50}$$

Being R the radius of curvature of the isolator, measured from the center of the sliding concave surface to the center of the slider.

Combining Eq.s (3.48)-(3.49)-(3.50), it is possible to obtain the horizontal force F required to displace the bearing:

$$F = W \cdot tg\vartheta + F_f \cos\vartheta = \frac{W}{R\cos\vartheta} d + F_f \cos\vartheta \tag{3.51}$$

Additionally, making the hypothesis of small pendulum oscillations, it is possible to assume that: $\cos\vartheta \cong 1$, $\sin\vartheta \cong \vartheta \cong tg\vartheta \cong 1/R$. Thus, the two components (normal and horizontal) of the vertical force W respectively become:

$$W\cos\vartheta \cong W \tag{3.52}$$

$$W\sin\vartheta \cong \frac{W}{R} \tag{3.53}$$

As a result, the expression for the horizontal force acting on the bearing simplifies to:

$$F = \frac{W}{R} d + F_f \tag{3.54}$$

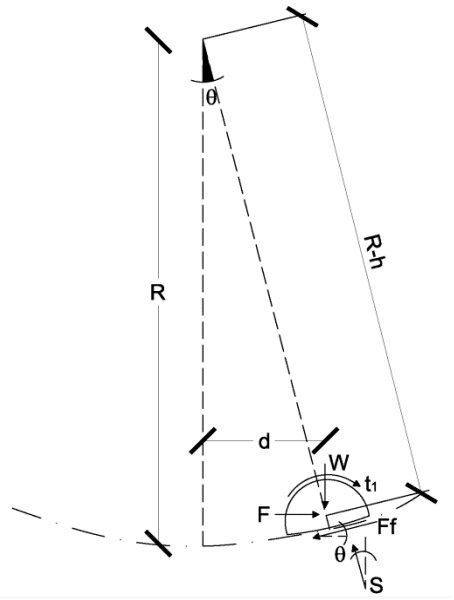

Figure 3.5. Dynamic isolation behavior of friction pendulum bearing expressed through the free body diagram of the forces involved during the motion.

The friction force F_f acting along the tangent direction of the sliding surface with a sign equal to the tangent component of the gravity force W is clearly a function of the friction coefficient f and the normal component of W, equal to $W\cos\vartheta \cong W$. Therefore, it is possible to write:

$$F_f = f \cdot W \tag{3.55}$$

Regarding the first term of Eq. (3.54), it is associated with the restoring force coming from the bearing pendulum movement:

$$F = \frac{W}{R} d \tag{3.56}$$

Therefore, the lateral stiffness of the isolator is equal to:

$$k = \frac{W}{R} \tag{3.57}$$

Consequently, the natural period T is given by:

$$T = 2\pi\sqrt{\frac{W}{gk}} = 2\pi\sqrt{\frac{R}{g}} \tag{3.58}$$

The expression derived for the isolatio period demonstrates how the natural frequency of a structure, isolated with FP devices, depends solely on the radius of curvature of the bearings. This is a significant insight because demonstrates that adopting an FP system it is possible to achieve a target-isolation period independent of the mass of the superstructure.

The idealized force-displacement hysteresis loop for the friction pendulum isolator provided with a generic amount of friction f is represented in Figure 3.6.

The system behaves nearly rigidly until the friction force F_f is overcome. Subsequently, the pendulum motion is triggered, and the force increases proportionally to the stiffness of Eq. (3.57). When the motion is reversed, the friction force suddenly drops to zero. To initiate motion in the opposite direction, the sliding surface must overcome the same friction force F_f, such that the vertical segment in Figure 3.6 at the reversal of the sliding motion is equal to $2f$.

Considering the case of the double-concave-friction-pendulum (DCFP) isolator, according to [46-47], it can be modeled as a serial combination of two single FP isolators. Additionally, if the inertial force related to the movement of the articulated slider mass is neglected, then the forces acting on the upper and lower surfaces, respectively equal to F_1 and F_2, result equal and can be obtained as follows:

$$F = F_1 = F_2 = \frac{M \cdot g}{R_1 + R_2} \cdot d + \frac{M \cdot g \cdot \left(R_1 f_1 + R_2 f_2\right)}{R_1 + R_2} \tag{3.59}$$

Where d represents the global bearing displacements and f_1, f_2 are the friction coefficients that characterize the upper and lower surface, while R_1 and R_2 refer to the radii of curvature of the concave sliding surfaces.

The first part of Eq. (3.59) represents the equivalent stiffness of the restoring force from the combined DCFP isolator, denoted as K_{comb}, which is equal to:

$$K_{comb} = \frac{M \cdot g}{R_1 + R_2} \tag{3.60}$$

Conversely, the second part of Eq. (3.59) aims at representing the equivalent friction coefficient of the DCFP, under the hypothesis that sliding occurs on both surfaces and in the same direction:

$$\mu_{eqv} = \frac{f_1 R_1 + f_2 R_2}{R_1 + R_2} \tag{3.61}$$

It will be demonstrated next that, being the behavior of the isolator affected by several factors such as the apparent pressure, sliding velocity, and temperature, its response is generally nonlinear, meaning that in the case an elastic method of analysis is used, it is necessary to introduce some equivalent linear properties that generally coincide with the effective bearing stiffness K_{eff} and the equivalent viscous damping ratio β_e.

Specifically, the effective stiffness is obtained by dividing the horizontal force F for the corresponding bearing displacement d:

$$K_{eff} = \frac{W}{R} + \frac{fW}{d} \tag{3.62}$$

Eq.(3.62) clearly demonstrates that the equivalent stiffness K_{eff} is higher than the pendulum stiffness of Eq. (3.57).

Then, since the area under the hysteresis loop is equal to:

$$A = 4fWd \tag{3.63}$$

By employing the equivalence established between the energy dissipated due to viscous damping and the energy dissipated by the generic hysteretic device, as discussed in Chapter 2, we obtain the following relationship:

$$\beta_e = \frac{E_D}{2\pi k_{eff} d^2} = \frac{4fWd}{2\pi\left(\frac{fW}{d} + \frac{W}{R}\right)d^2} = \frac{2}{\pi}\left(\frac{f}{f + \frac{d}{R}}\right) \tag{3.64}$$

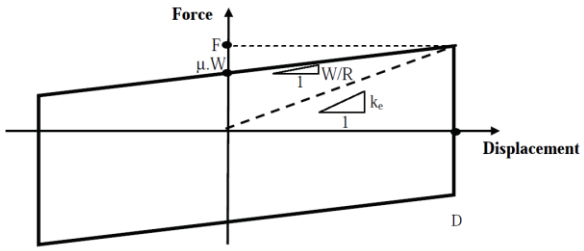

Figure 3.6. Idealized force-displacement hysteretic behavior of the FPS.

It is evident that the equivalent viscous damping is a function of the friction coefficient, of the radius of curvature, and function of the displacement demand. The displacement demand can be understood as the required displacement at the limit state of interest (*e.g.*, Life-Safety limit state (SLV)). It follows that the equivalent viscous damping to be adopted in an elastic analysis changes as a function of the demand parameter for the structure at the site of interest.

3.2.2 Frictional properties of the sliding surface

Friction is a dissipative force that restrains the relative motion between two sliding solids in contact, arising from tangential forces exchanged between the contact surfaces. The friction theory is based on three assumptions that have been validated experimentally [45]:

- The total friction force is independent of the apparent surface of contact;
- The total friction force is proportional to the total normal force acting on the sliding solids in contact;
- When the sliding relative velocity is slow, then the friction coefficient is independent of the sliding velocity.

During sliding, a relation is developed between the frictional force F_f arising along tangentially at the interface of sliding, opposite to the direction of motion, and the normal force *N*, according to the following relation:

$$F_f = f \cdot N \tag{3.65}$$

Where f is the friction coefficient and *N* is the normal force acting at the interface.

Two main kinds of frictional forces can be recognized: a static friction force, which occurs between solid surfaces at the beginning of the motion or at the reversal of it, and a dynamic friction force which occurs when the surfaces in contact are in relative movement.

At the macroscopic scale of interest for engineering purposes, three general phenomena can be recognized between two sliding surfaces:

- The adhesion component;
- The ploughing component at the bulk zone;
- The presence of contaminants or wearing debris that acts like a third body along the sliding surface:

3.2.2.1 Adhesion component

When two bodies are in contact, before the normal load is applied, their points of contact are represented by the asperities. After the load appliance, the asperities deform plastically and specific areas of contact, called junctions, are formed. The presence of a tangential force can increase the area at the junctions which can subsequently increase the shear stresses and decrease the normal force.

It follows that the frictional force due to adhesion can be written as [50]:

$$F_{fa} = sA_r \tag{3.66}$$

Where s is the shear strength of the junctions and A_r is the so called “true contact area”.

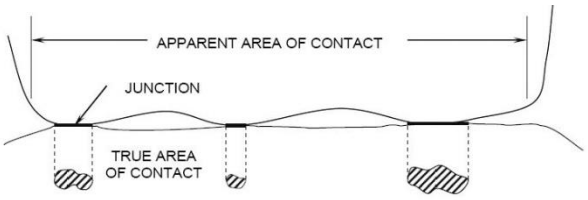

Figure 3.7. Asperities and junctions in sliding interface [50].

Understandably, the highest friction force develops in those cases where the true contact area is equal to the apparent contact area. The adhesion mechanism is at the base of the difference between static and dynamic friction coefficient: indeed, as soon as the sliding is triggered, the true contact area tends to reduce and the shear strength of the junctions does not exist anymore.

3.2.2.2 Ploughing component

All the surfaces are characterized by roughness and ploughing. During sliding, the roughness of each body undergoes elastic or plastic deformations. Nevertheless, summing up this phenomenon for all the contact points it can be inferred that the overall effect, and so the frictional force related to roughness, tends to cancel out. The phenomenon that concerns the ploughing can be easily explained by referring to a hard and non-spherical roughness over a soft and flat surface. If an axial force is applied, the asperities located on the harder surface dig into the softer surface, and contemporary junctions are formed in other softer asperities. Introducing a tangential force, it happens that the sharp edges on the hard surface, moving horizontally, drag with it part of the soft material producing scores or grooves along the traveled trajectory. The debris tend to accumulate at the ploughing edge and therefore a higher friction force is required to overcome the accumulated debris on the sliding path. The phenomenon tends to increase as much as the sliding length increases.

3.2.2.3 Third bodies component

This aspect is mainly related to contaminants or wearing debris that can affect the friction coefficient. It is not always a detrimental effect: for example contaminants can accumulate on very high roughness surfaces (ploughing) and reduce their asperity while increasing the true contact area. This would increase the static friction force.

On the other hand, if the contaminants are round in shape and made of strong material, they reduce the friction coefficient by facilitating the sliding.

3.2.2.4 Stick-slip motion

Stick-slip motion is a phenomenon that arises every time the dynamic friction coefficient is lower than the static one (Figure 3.8). Before reversal of motion the static friction force, which is generally larger than the dynamic one, is mobilized again. When this happens causes an irregular stick-slip motion with the frictional force that drops for increasing displacement and then increases again as the sliding velocity starts to rise up.

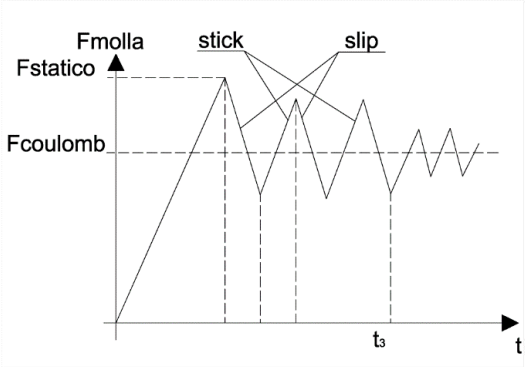

Figure 3.8. Stick-slip phenomenon.

3.2.3 Effects influencing frictional behavior

The determination of the friction coefficient is rather complex as it is influenced by several aspects such as apparent pressure, sliding velocity, temperature, history of loading, etc. For a comprehensive study of the experimental results that have highlighted this dependence refer to [38-39].

3.2.3.1 Effect of sliding velocity

At the initiation of motion, in quasi-static conditions, the interfaces exhibit a rather high value of the friction coefficient f due to the adhesion component mainly. Furthermore, the interface of the sliding surfaces is covered of a thin crystalline and oriented PTFE film that is easier to deform in shear than the frictional material itself. At very low velocities a small amount of force is enough to shear the film and this is the reason why the friction reduces to a minimum value $f_{\min}$. Nevertheless, the sliding friction coefficient increases as the sliding velocity increases and attains a constant maximum value $f_{\max}$ at velocities almost equal to 100mm/sec. This behavior is mainly due to the increasing true contact area during the movement, which happens at the level of the friction materials and not at the level of the thin film, while also the accumulation of debris from the softer material on the surface of the harder material contributes to the increasing of the friction.

Figure 3.9 [46] illustrates the dependence of the friction coefficient on the sliding velocity and on the apparent pressure: after the initial slip the coefficient of friction decreases until it reaches its minimum value $f_{\min}$ and then it increases again with increasing velocity, eventually reaching its maximum value $f_{\max}$, after which it remains about constant. Increasing the normal load has the effect of reducing the friction coefficient, with a degree of reduction that starts to decrease when the normal load reaches some limiting value.

For intermediate velocities, the sliding friction coefficient depends on the sliding velocity throughout the following relationship [38-39-50]:

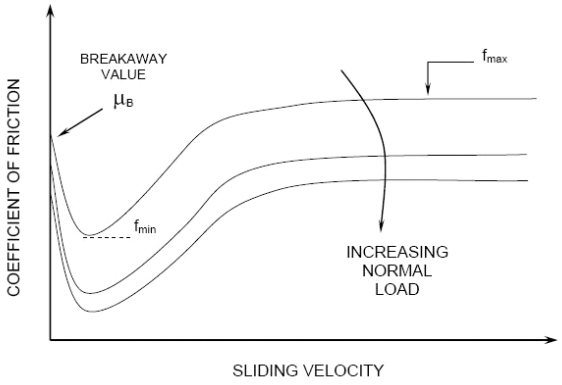

Figure 3.9. Relation between sliding velocity, pressure, and friction coefficient [46].

$$f = f_{\max} - (f_{\max} - f_{\min})e^{-\alpha|v|} \tag{3.67}$$

Where $f_{\max}$ and $f_{\min}$ are the already mentioned friction coefficients at high and low velocities, $|v|$ is the absolute value of the sliding velocity, and α is a coefficient typically ranging from 20 to 30 sec/m for devices using teflon-PTFE stainless steel interfaces. This coefficient regulates the transition from velocities minimum values to velocities maximum values.

Figure 3.10 shows two curves that are based on Eq. (3.67) for two different values of the ratio $\frac{f_{\max}}{f_{\min}} = 2.5$ and 5.0 and $\alpha = 100$ m/sec, and 20 m/sec.

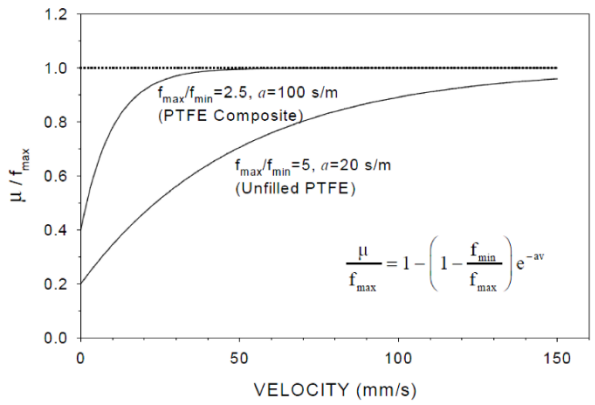

Figure 3.10. Effect of the α parameter on the variation of friction coefficient with velocity [50].

3.2.3.2 Effect of temperature

After sliding motion initiates, frictional heating occurs and the temperature increases abruptly and in proportion to sliding velocity. Elevated temperatures resulting from this heat can lead to the accumulation of debris and a modest reduction in the friction coefficient. This reduction occurs despite several components contributing to the friction force, each responding differently to increased temperature. As shown in Figure 3.11, as temperature decreases, the

friction value substantially increases at the beginning of motion but as the velocity goes up the degree of increase tends to diminish.

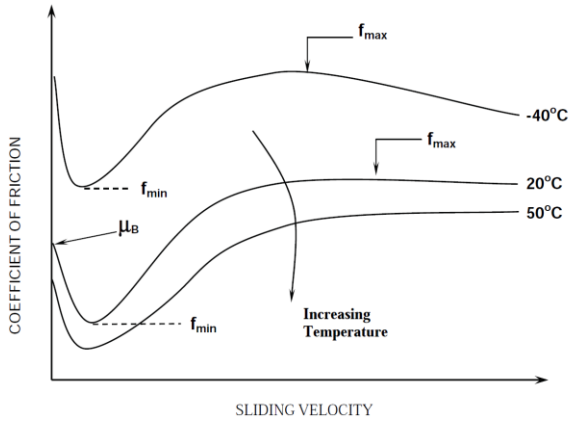

Figure 3.11. Influence of temperature on the friction coefficient [50].

3.2.3.3 Effects of loading history

Buckle in [37] has reported that for tests conducted on full-scale friction pendulum isolators, involving 3-5 cycles of displacement, the coefficient of friction related to the first cycle is generally 20% higher than the average friction coefficient from the other cycles. Consequently, the average friction coefficient is considered the target design value according to AASHTO specifications [51].

3.3 Elastic structural model of isolated bridges

Seismic isolation of bridges is an effective technique that decouples the bridge deck from horizontal earthquake components, significantly reducing deck acceleration and minimizing forces transferred to the substructure, while also providing efficient energy dissipation. These features have been demonstrated in many studies adopting both lead rubber bearings (LRBs) and frictional isolators (Friction pendulum system [FPS]) [43-44].

In the referenced literature [21-22-42-44], various numerical models are proposed for modeling multi-span continuous deck bridges seismically isolated with friction devices, either accounting for the presence of a rigid abutment [21-22] or neglecting it (*i.e.* isolated viaducts) [42].

One specific numerical model employed to represent the equivalent configuration of a continuous multi-span reinforced concrete (RC) deck bridge supported by the FP devices, as proposed in [22], is represented in Figure 3.12. It consists of an equivalent 6DOF model with 5DOF used to represent the behavior of the elastic RC pier, indeed discretized in 5 lumped masses, and 1 DOF for the RC deck mass equipped with FPS.

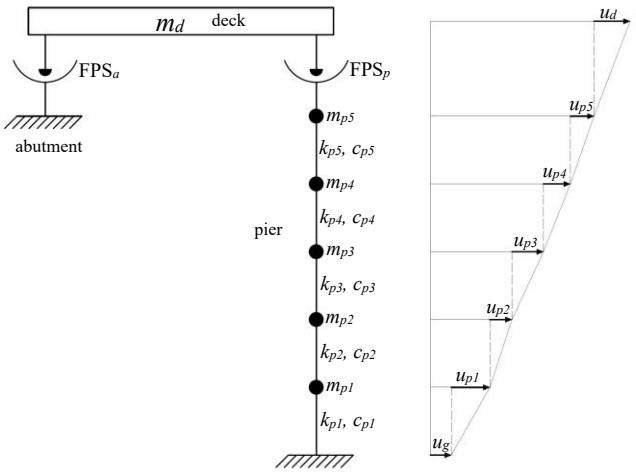

Figure 3.12. 6dof model of a bridge isolated by FP bearings considering pier-abutment-deck interaction [22].

Under these assumptions, the equations of motion, expressed in terms of drifts between the different degrees of freedom that govern the response of the system, when a ground motion $\ddot{u}_g$ is considered applied along the longitudinal bridge direction, are as follows:

$$
\begin{aligned}
&m_d\ddot{u}_d(t)+m_d\ddot{u}_{p5}(t)+m_d\ddot{u}_{p4}(t)+m_d\ddot{u}_{p3}(t)+m_d\ddot{u}_{p2}(t)+m_d\ddot{u}_{p1}(t)+c_d\dot{u}_d(t)+F_p(t)+F_a(t)=\\
&=-m_d\ddot{u}_g(t)\\
&m_{p5}\ddot{u}_{p5}(t)+m_{p5}\ddot{u}_{p4}(t)+m_{p5}\ddot{u}_{p3}(t)+m_{p5}\ddot{u}_{p2}(t)+m_{p5}\ddot{u}_{p1}(t)-c_d\dot{u}_d(t)+c_{p5}\dot{u}_{p5}(t)+k_{p5}u_{p5}(t)-F_p(t)=\\
&=-m_{p5}\ddot{u}_g(t)\\
&m_{p4}\ddot{u}_{p4}(t)+m_{p4}\ddot{u}_{p3}(t)+m_{p4}\ddot{u}_{p2}(t)+m_{p4}\ddot{u}_{p1}(t)-c_{p5}\dot{u}_{p5}(t)-k_{p5}u_{p5}(t)+c_{p4}\dot{u}_{p4}(t)+k_{p4}u_{p4}(t)=\\
&=-m_{p4}\ddot{u}_g(t)\\
&m_{p3}\ddot{u}_{p3}(t)+m_{p3}\ddot{u}_{p2}(t)+m_{p3}\ddot{u}_{p1}(t)-c_{p4}\dot{u}_{p4}(t)-k_{p4}u_{p4}(t)+c_{p3}\dot{u}_{p3}(t)+k_{p3}u_{p3}(t)=-m_{p3}\ddot{u}_g(t)\\
&m_{p2}\ddot{u}_{p2}(t)+m_{p2}\ddot{u}_{p1}(t)-c_{p3}\dot{u}_{p3}(t)-k_{p3}u_{p3}(t)+c_{p2}\dot{u}_{p2}(t)+k_{p2}u_{p2}(t)=-m_{p2}\ddot{u}_g(t)\\
&m_{p1}\ddot{u}_{p1}(t)-c_{p2}\dot{u}_{p2}(t)-k_{p2}u_{p2}(t)+c_{p1}\dot{u}_{p1}(t)+k_{p1}u_{p1}(t)=-m_{p1}\ddot{u}_g(t)
\end{aligned}
\tag{3.68}
$$

Where F_a and F_p are the reaction forces of the isolators placed over the abutment and over the pier, that can be evaluated according to Eq. (3.54); u_d denotes the horizontal displacement of the deck relative to the pier, $u_{p1,}u_{p2,}u_{p3,}u_{p4,}u_{p5}$ are the pier relative displacements, $m_d, m_{p1}, m_{p2}, m_{p3}, m_{p4}, m_{p5}$ are respectively the mass of the deck and each pier degree-of-freedom, $k_{p1,}k_{p2,}k_{p3,}k_{p4,}k_{p5}$ and $c_{p1,}c_{p2,}c_{p3,}c_{p4,}c_{p5}$ respectively the stiffness and inherent viscous damping coefficient of the same pier DOFs, c_d the bearing viscous damping factor.

It should be pointed out that, according to [43], the following hypotheses are considered within the context of the aforementioned equivalent representation of the multi-span continuous deck bridge isolated with FPS:

1. The bridge superstructure and piers are assumed to remain elastic during the seismic excitation;
2. The superstructure is supposed to move as a rigid body;

3. The abutments are assumed to be rigid;
4. The deck is supposed to be straight and representative of a large number of spans, supported at discrete locations by piers and abutments, while the skew angle is assumed to be zero;
5. Both pier and deck are modeled as a lumped mass system, divided into a certain number of elements connected by nodes;
6. The piers are assumed to be all of equal height and stiffness, fully restrained at their base.

4 Generation of spectrum-compatible seismic ground motion accounting for spatial variability (SVEGM)

This chapter explores the fundamental concepts of spatial variability of earthquake ground motion (SVEGM). It starts with a historical overview of the key studies and findings in the scientific literature regarding the topic. It is nowadays well established that SVEGM primarily arises from factors such as the loss of coherence, the so-called wave-passage effect, and the site-response effect. Given the complexity of the phenomenon, a deterministic analysis approach is impractical, requiring the use of probabilistic methods instead. Before delving into the adopted simulation techniques, a brief description of the equation of motions valid for a multi-degree-of-freedom (MDOF) system, subjected to different input ground motions, is provided. Following this, it discusses the main aspects of the spectral representation method used to simulate spatially variable earthquake ground motion. Within this method, particular attention is given to the specifically selected power spectral density (PSD), coherency function, and modulating function. Additionally, this study adopts a generation procedure that accounts for spectrum compatibility with the specific site of interest. Thus, this procedure is described along with its implementation to the case study, which refers to a friction pendulum seismically isolated multi-span reinforced concrete bridge located near the site of L'Aquila, in Italy.

Finally, the chapter presents a validation of the adopted procedure, which particularly compares the simulated coherency functions with the target ones initially integrated into the adopted procedure.

4.1 Introduction

Bridges are structures that are often required and designed to link areas separated by water and some geological marks, they often span over long distances with their support points being far away from each other. Differently to other structures, such as buildings, spatial variability of earthquake ground motion (SVEGM) is a critical factor in the seismic design of bridges due to the significant

differences in seismic waves characteristics such as amplitude, frequency content, and arrival time when travelling across successive piers separated by long distances. The first isolated studies date back to 1970s [52-53], even if only with the data recorded from dense seismographic arrays, installed in the late 1970s-early 1980s (e.g. El Centro differential array) [54-58], significant advancements in understanding the causes of spatial variability were made. Prior to the installation of these arrays, the variation of the earthquake ground motion between two consecutive points was primarily attributed to the time delay in the arrival of seismic waves. As specified in [54] the array that has been studied and analyzed the most by engineers and seismologists is the SMART-1 array, located in Taiwan, consisting of 37 triaxial accelerometers arranged on three concentric circles. Twelve equispaced stations were placed at each ring with an additional station at the center of the array, named C00. The array started being operative in 1980 and the data collected from the instruments quickly started to appear in literature. This disposal of collected seismic data allowed for significant advancements in the knowledge of spatial variability of ground motion.

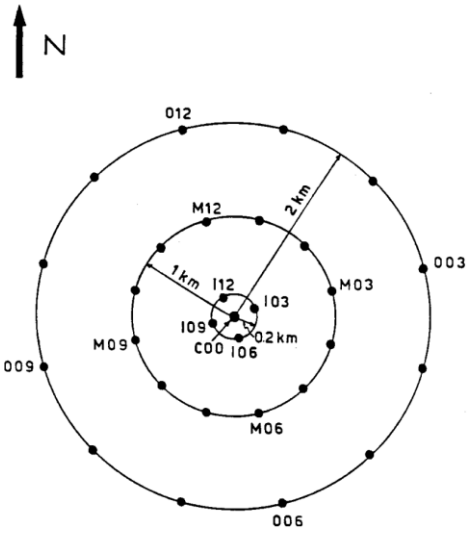

Figure 4.1. SMART-1 array in Taiwan.

Being the seismic response of bridges under SVEGM of great relevance for engineers due to the potential negative effects of the phenomenon on such structures, it has long been studied [55]. The detrimental effects of SVEGM on bridges started to become particularly clear following on-field evidence from past earthquakes such as 1989 Loma Prieta and 1995 Kobe earthquakes [56].

It is now a well-established convention as also specified in [57-58] to consider the phenomenon of spatial variability as coming from mainly three causes: the *loss of coherence* (*i.e.* loss of statistical correlation) of the motion as a function of distance caused by reflections and refractions of seismic waves, the so-called *wave-passage effect*, that is the time delay between the arrival of the wave trains when different support points (stations) are considered at different distances in space and finally, the *site-response effect* that takes into account the changing in

the motion properties assuming that each of the support points of interest is characterized by a specific soil stratigraphy.

Given the rather complex nature of the phenomenon, a deterministic analysis approach is impractical, requiring for probabilistic methods instead.

One such probabilistic approach is the Random Vibration Analysis (RVA) [59-60], which despite its statistical robustness and relevance for Performance-Based-Earthquake-Engineering it is unfortunately also too complex to be applied in the engineering practice [58].

An alternative approach, widely adopted in the scientific literature, consists of extending the response spectrum method to SVEGM by adopting the theoretical principles of the random vibration analysis [61-62]. The major drawback of this approach is that it deals with linear or linearized problems that make it inadequate for bridge assessment purposes.

On the other hand, although computationally demanding, simulation of non-synchronous ground motions in time history analysis can be used practically for all sources of nonlinearity (material and geometric) and are particularly appropriate in a Montecarlo framework. Within this context, different simulation techniques can be adopted, which describe stochastic processes through a combination of a power spectral density (PSD) model and an appropriate coherency model [63]. Spectral representation method is among the most frequently adopted methods for the simulation of stochastic process model [64] and has been further improved to simulate ergodic, multivariate stochastic processes [65].

Starting from simulated ground motions, different algorithms have been developed to satisfy the seismic codes requirements in terms of spectrum compatibility between the target spectrum of the considered site and the ensemble response spectra of the simulated motions [66-67-68].

Given the aforementioned methods different sensitivity analysis of structures under multiple support excitation have been presented by the scientific community.

Nonlinear time history analysis, in particular, have been used in several studies to analyze the response of different types and configurations of bridges under multiple support excitation [57-69-70-71-73-73], while only few contributions investigate the seismic response of base isolated bridges [74-75].

Neverthless, despite the extensive research on the topic discussed above most of the seismic codes worldwide, do not follow a common approach to spatial variability of ground motion while often preferring simplified methods or indirect provisions such as designing larger seating deck lengths. Currently, only two seismic codes address specifically the SVEGM in the seismic design and assessment of bridges, which are Eurocode 8-Part 2 [76] and the Italian Building Code [77], even if they are far from providing a code-oriented approach that can be easily implemented by the civil engineering community.

4.2 Equations of motion for Multiple Degree of Freedom (MDOF) subjected to SVEGM

Considering the case of a linear elastic structure with N unconstrained degrees-of-freedom and M degrees-of-freedom at the supports, subjected to different input ground motions, the formulation of the seismic response to each of the considered excitation components would be different from the case of uniform excitation. It is indeed widely accepted that the difference is that if the system supports are moving independently one of each other, they induce a pseudo-static response that needs to be sum up to the dynamic component resulting from inertial forces.

As already mentioned, for multi-support excitation the support motions at every time instant are different along the MDOFs at the supports and this requires that the total displacement of the superstructure (N unconstrained DOFs) should be expressed as the sum of the relative displacements of the superstructure with respect to the supports (u) and the quasi-static displacements (u_s), where the latter consist of the displacements generated at the superstructure due to a quasi-static motion at the supports. Thus the following relation is valid:

$$u_t(t) = u(t) + u_s(t) \tag{4.1}$$

It is convenient to express the quasi-static displacement (u_s) in the following way:

$$u_s(t) = \underline{\Gamma} u_g(t) \tag{4.2}$$

$$u_t(t) = u(t) + \underline{\Gamma} u_g(t) \tag{4.3}$$

Where $\underline{\Gamma}$ is an influence matrix of dimension [NxM] and has the same significance that has the influence vector for the case of uniform excitation, where each column $\{\Gamma_k\}$ represents the static displacements of the superstructure nodes when the *k*-th support is subjected to unit displacement while all the others are kept fixed.

According to [72-78] the equations of motion for an MDOF system under multiple support excitations have the following expression:

$$\begin{bmatrix} \underline{M} & \underline{M}_c \\ \underline{M}_c^T & \underline{M}_g \end{bmatrix} \begin{Bmatrix} \ddot{u}_t \\ \ddot{u}_g \end{Bmatrix} + \begin{bmatrix} \underline{C} & \underline{C}_c \\ \underline{C}_c^T & \underline{C}_g \end{bmatrix} + \begin{Bmatrix} \dot{u}_t \\ \dot{u}_g \end{Bmatrix} + \begin{bmatrix} \underline{K} & \underline{K}_c \\ \underline{K}_c^T & \underline{K}_g \end{bmatrix} \begin{Bmatrix} u_t \\ u_g \end{Bmatrix} = \begin{Bmatrix} 0 \\ P_g \end{Bmatrix} \tag{4.4}$$

Where:

$\underline{M}, \underline{C}, \underline{K}$ = mass, damping, and stiffness matrices [NxN] of superstructure with N unconstrained DOFs;

$\underline{M}_g, \underline{C}_g, \underline{K}_g =$ mass, damping, and stiffness matrices [MxM] associated with the MDOFs at the supports;

$\underline{M}_c, \underline{C}_c, \underline{K}_c =$ coupling mass, damping, and stiffness matrices [NxM] between the N unconstrained and the M constrained nodes;

$u_t =$ vector $\{Nx1\}$ of the total displacements corresponding to the superstructure/unconstrained DOFs;

$u_g =$ vector $\{Mx1\}$ of the input ground motion displacements at the support DOFs;

$P_g =$ vector $\{Mx1\}$ of forces generated at the support DOFs.

Furthermore, to write the equations of motion according to Eq. (4.3) and thus separate the total superstructure displacements into two components, the vector $\{u_t \quad u_g\}^T$ is exploited as follows:

$$\begin{Bmatrix} u_t \\ u_g \end{Bmatrix} = \begin{Bmatrix} u \\ 0 \end{Bmatrix} + \begin{Bmatrix} u_s \\ u_g \end{Bmatrix} = \begin{Bmatrix} u \\ 0 \end{Bmatrix} + \begin{Bmatrix} \underline{\Gamma} u_g \\ u_g \end{Bmatrix} \tag{4.5}$$

To find the quasi-static displacements u_s produced by the support displacements u_g the following equilibrium equation can be written according to [78]:

$$\begin{bmatrix} \underline{K} & \underline{K}_c \\ \underline{K}_c^T & \underline{K}_g \end{bmatrix} \begin{Bmatrix} u_s \\ u_g \end{Bmatrix} = \begin{Bmatrix} 0 \\ P^s{}_g \end{Bmatrix} \tag{4.6}$$

Where $P^s{}_g$ are the support forces that arise when displacements u_g is applied in a quasi-static way.

From Eq. (4.6) it derives that:

$$\underline{K} u_s + \underline{K}_c u_g = 0 \tag{4.7}$$

And so:

$$u_s = -\underline{K}^{-1} \underline{K}_c u_g \tag{4.8}$$

Where:

$$\underline{\Gamma} = -\underline{K}^{-1} \underline{K}_c \tag{4.9}$$

Such that:

$$u_s = \underline{\Gamma} u_g \tag{4.10}$$

Further, by substituting Eq. (4.10) into Eq. (4.7) the following relation is derived:

$$(\underline{K}\underline{\Gamma} + \underline{K}_c)u_g = 0 \tag{4.11}$$

Starting from the system of equations of motion expressed in Eq. (4.4) the following are derived:

$$\underline{M}\ddot{u}_t + \underline{M}_c\ddot{u}_g + \underline{C}\dot{u}_t + \underline{C}_c\dot{u}_g + \underline{K}u_t + \underline{K}_c u_g = 0 \tag{4.12}$$

$$\underline{M}\ddot{u}_t + \underline{C}\dot{u}_t + \underline{K}u_t = -\underline{M}_c\ddot{u}_g - \underline{C}_c\dot{u}_g - \underline{K}_c u_g \tag{4.13}$$

Substituting Eq. (4.3) into Eq. (4.13), together with the equally derived expression for acceleration:

$$\ddot{u}_t(t) = \ddot{u}(t) + \underline{\Gamma}\ddot{u}_g(t)$$

and velocity:

$$\dot{u}_t(t) = \dot{u}(t) + \underline{\Gamma}\dot{u}_g(t)$$

The equations of motion are expressed as follows:

$$\underline{M}\ddot{u} + \underline{C}\dot{u} + \underline{K}u = -(\underline{M}_c + \underline{\Gamma}\underline{M})\ddot{u}_g - (\underline{C}_c + \underline{\Gamma}\underline{C})\dot{u}_g - (\underline{K}_c + \underline{\Gamma}\underline{K})u_g \tag{4.14}$$

Following Eq. (4.11) the term $(\underline{K}_c + \underline{\Gamma}\underline{K})u_g$ is equal to zero; additionally, the coupling mass can be generally neglected for most structures; also the contribution of the damping term $(\underline{C}_c + \underline{\Gamma}\underline{C})\dot{u}_g$ is generally very small and can be neglected. Thus Eq. (4.14) is reduced as follows:

$$\underline{M}\ddot{u} + \underline{C}\dot{u} + \underline{K}u = -\underline{\Gamma}\underline{M}\ddot{u}_g \tag{4.15}$$

The above equation is the most general equation of motion for an MDOF system subjected to multiple support excitation and is consistent with the same equation that can be generally written for the case of uniform excitation.

The main difference in the calculation is that if in the uniform excitation case, the influence matrix Γ is obtained straightforwardly, for multiple support excitation it is obtained from a static analysis of the structure under relative movements.

In addition, expressing the displacements u in terms of modal contribution:

$$u = \underline{\Phi}q = \sum_{i=1}^{N} \varphi_i q_i \tag{4.16}$$

Being q the modal coordinates, substituting Eq. (4.16) into Eq. (4.15), under the hypothesis of modes' orthogonality, the N decoupled equations of motion are derived:

$$\ddot{q}_i + 2\omega_i\zeta_i\dot{q}_i + \omega_i^2 q_i = -\sum_{k=1}^{M}\gamma_{i,k}\ddot{u}_{g,k}\gamma_{i,k} = \frac{\varphi_i^T \underline{M}\{\Gamma_k\}}{\varphi_i^T \underline{M}\varphi_i} \tag{4.17}$$

Where $\gamma_{i,k}$ is the modal participation factor for mode i when the *k*-th support of the structure is excited and Γ_k is the *k*-th column of the influence matrix introduced above. It is worth noting that in the case of uniform excitation, the modal participation factor for mode i is defined as: $\gamma_i = \sum_{k=1}^{M} \gamma_{i,k}$.

The solution of the *i*-th (i=1,…,N) equation of motion is given by:

$$q_i = \sum_{k=1}^{M} q_{i,k} = \sum_{k=1}^{M} \gamma_{i,k} D_{i,k} \tag{4.18}$$

Where $D_{i,k}$ is the displacement related to the single-dof oscillator with dynamic properties given by mode i when the *k*-th support is excited.

Substituting into Eq. (4.16) the total displacement expressed in Eq. (4.1) can be rewritten as:

$$u_t = \sum_{k=1}^{M}\{\Gamma_k\}u_{g,k} + \sum_{i=1}^{N}\sum_{k=1}^{M}\varphi_i\gamma_{i,k}D_{i,k} \tag{4.19}$$

Eq. (4.19) shows how the response of a structure under different motions can differ from the uniform excitation one because if in the latter case, the first term of Eq. (4.19) represents a rigid body motion with no overstresses in the structure, the multiple support produces additional internal forces.

4.3 Simulations of spatially variable ground motions (SVEGM)

In the literature, various simulation techniques can be found for the generation of spatially variable ground motion time histories [79]. In this study, the Spectral representation method [64-65] has been adopted as it integrates well with the Montecarlo framework approach. Accordingly, the ground motion is considered to be a sample of a stochastic Gaussian process.

Particularly, following the algorithm explained in [65] it is possible to generate 1D-*m*V (one-dimensional, multi-variate) quasi-stationary (only the amplitude of the process is considered to vary with time) stochastic vector process with components $f_j(t), (j = 1,...,m)$ having zero mean:

$$E\left[f_j(t)\right] = 0 \text{ (j=1,…,m)} \tag{4.20}$$

And cross-correlation matrix given by:

$$R_f(t,t+\tau)=\begin{bmatrix} R_{11}(t,t+\tau) & R_{12}(t,t+\tau) & \dots & R_{1m}(t,t+\tau) \\ R_{21}(t,t+\tau) & R_{22}(t,t+\tau) & \dots & R_{2m}(t,t+\tau) \\ \vdots & \vdots & \ddots & \vdots \\ R_{m1}(t,t+\tau) & R_{m2}(t,t+\tau) & \dots & R_{mm}(t,t+\tau) \end{bmatrix} \tag{4.21}$$

Consistently, the corresponding cross-spectral density matrix is equal to:

$$S_f(\omega)=\begin{bmatrix} S_{11}(\omega) & S_{12}(\omega) & \dots & S_{1m}(\omega) \\ S_{21}(\omega) & S_{22}(\omega) & \dots & S_{2m}(\omega) \\ \vdots & \vdots & \ddots & \vdots \\ S_{m1}(\omega) & S_{m2}(\omega) & \dots & S_{mm}(\omega) \end{bmatrix} \tag{4.22}$$

Additionally, the cross-correlation matrix results a function of time lag τ only, whereas the cross-spectral density matrix is Hermitian and has off-diagonal elements expressed in the following form:

$$S_{jk}(\omega)=\sqrt{S_j(\omega)S_k(\omega)}\Gamma_{jk}(\omega), \quad j,k=1,2,...,m;\ j\neq k \tag{4.23}$$

Where $\Gamma_{jk}(\omega)$ is the complex coherence function between $f_j(t)$ and $f_k(t)$. It follows that the off-diagonal terms of $S_f(\omega)$ are complex functions of the frequency ω satisfying the following properties:

$$S_{jk}(\omega)=S_{jk}^{*}(-\omega), \qquad j,k=1,2,...,m;\ j\neq k \tag{4.24}$$

$$S_{jk}(\omega)=S_{kj}^{*}(\omega), \qquad j,k=1,2,...,m;\ j\neq k \tag{4.25}$$

Where the asterisk is assumed to represent the complex conjugate.

On the other hand, the diagonal elements are both real and non-negative:

$$S_{jj}(\omega)=S_{jj}(-\omega), \qquad j=1,2,..,m \tag{4.26}$$

For the special case of a uniformly modulated quasi-stationary vector process, it is possible to introduce the modulating functions $A_j(t)$, $j=1,2,..,m$ as a function of time only and relate the elements of the cross-correlation matrix to the corresponding elements of the cross-spectral density matrix through the following transformations:

$$R_{jj}(t,t+\tau)=A_j(t)A_j(t+\tau)\int_{-\infty}^{+\infty}S_j(\omega)e^{i\omega\tau}d\omega;\qquad j=1,2,...,m \tag{4.27}$$

$$R_{jk}(t,t+\tau)=A_j(t)A_k(t+\tau)\int_{-\infty}^{+\infty}\sqrt{S_j(\omega)S_k(\omega)}\Gamma_{jk}(\omega)e^{i\omega\tau}d\omega; \tag{4.28}$$

$$j=1,2,...,m;\ j\neq k$$

In such a case, the m-components of the quasi-stationary stochastic vector process with zero mean can be expressed as:

$$f_j(t)=A_j(t)g_j(t),\ j=1,2,...,m; \tag{4.29}$$

Where $g_j(t)$, $j=1,2,...,m$, are the m-components of a stationary stochastic vector process having mean value equal to zero.

4.3.1 Power Spectral Density (PSD)

The power spectral densities (PSD) $S_{jj}(\omega)$ of the motion at the station $j=1,2,...,m$ with $j=k$ are estimated from the Fourier analysis of the recorded data. Once the power spectra of the ground motion at the stations of interest is known, a parametric form is evaluated via a regression scheme and used to fit the estimates.

The most commonly used parametric power spectral density [80-83] is the Kanai-Tajimi PSD, further extended by Clough and Penzien. The physical meaning of the Kanai-Tajimi PSD is that it results from a filtered process whose input is a white-gaussian-noise at the bedrock and the filter is represented by the soil strata, resulting in the following expression:

$$S_a(\omega)=S_0\frac{1+4\zeta_g^2\left(\frac{\omega}{\omega_g}\right)^2}{\left[1-\left(\frac{\omega}{\omega_g}\right)^2\right]^2+4\zeta_g^2\left(\frac{\omega}{\omega_g}\right)^2} \tag{4.30}$$

In which S_0 is the amplitude of the white-gaussian-noise at the bedrock and ω_g and ζ_g are the frequency and damping coefficient of the soil filter. The major drawback of Eq. (4.30) is that it gives infinite variances for the ground velocity and displacement. Indeed, the power spectral velocity and displacement are related to that of the acceleration through the following:

$$S_v(\omega) = \frac{1}{\omega^2} S_a(\omega), \qquad S_d(\omega) = \frac{1}{\omega^4} S_a(\omega) \tag{4.31}$$

Such that as $\omega \to 0$ the velocity and displacement spectrum of Kanai-Tajimi go to infinity. The Clough and Penzien PSD [81] adds a second soil filter with parameter ω_f and ζ_f to the Kanai-Tajimi model to yield finite variances for velocities and displacements. The resulting power spectral density has the following expression:

$$S_a(\omega) = S_0 \frac{1 + 4\zeta_g^2 \left(\frac{\omega}{\omega_g}\right)^2}{\left[1 - \left(\frac{\omega}{\omega_g}\right)^2\right]^2 + 4\zeta_g^2 \left(\frac{\omega}{\omega_g}\right)^2} \cdot \frac{\left(\frac{\omega}{\omega_f}\right)^4}{\left[1 - \left(\frac{\omega}{\omega_f}\right)^2\right]^2 + 4\zeta_f^2 \left(\frac{\omega}{\omega_f}\right)^2} \tag{4.32}$$

Depending on the soil condition, the soil filter parameters can assume different values [65]:

Rock or stiff soil conditions:

$$\omega_g = 8\pi rad/\sec, \qquad \zeta_g = 0.6 \tag{4.33}$$

Medium soil conditions:

$$\omega_g = 5\pi rad/\sec, \qquad \zeta_g = 0.6 \tag{4.34}$$

Soft soil conditions:

$$\omega_g = 2.4\pi rad/\sec, \qquad \zeta_g = 0.85 \tag{4.35}$$

Whereas the filtering parameters ω_f is set generally equal to $0.10\omega_g$ and $\zeta_f = \zeta_g$ [65].

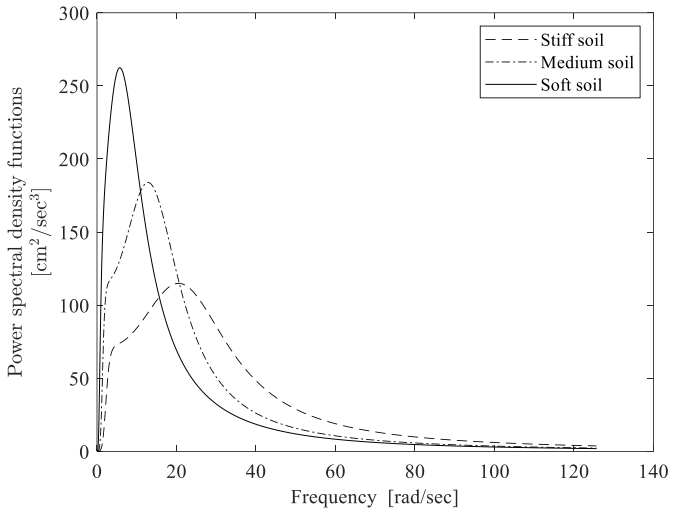

Figure 4.2. Power spectral density functions according to the Kanai-Tajimi modified model for stiff, medium, and soft soil.

It should be pointed out that the aforementioned power spectra model is only representative of the local soil conditions, since the excitation at the bedrock is modeled through a white-Gaussian-Noise. Because the seismic ground motion is the result of a complex phenomenon that starts with the rupture at the fault and is followed by the transmission of waves through the soil from the fault to the ground surface, alternatively seismological models that consider these effects can be uses in lieu of the Kanai-Tajimi model. One of the most adopted in literature is the Joyner and Boore model [82].

4.3.2 Coherency

The coherency of the seismic motion is obtained by inverting Eq. (4.23), it can be therefore expressed through the ratio between the cross power spectral density of the motion between station j and k and the corresponding power spectral density:

$$\Gamma_{jk}(\omega) = \frac{S_{jk}(\omega)}{\sqrt{S_{jj}(\omega) S_{kk}(\omega)}} \tag{4.36}$$

The so obtained coherency is a complex number while its absolute value squared, called coherence, is a real number bounded between zero and one.

$$\left|\Gamma_{jk}(\omega)\right|^2 = \frac{\left|S_{jk}(\omega)\right|^2}{S_{jj}(\omega) S_{kk}(\omega)} \tag{4.37}$$

An alternative way of expressing the coherency is the following:

$$\Gamma_{jk}(\omega) = \left|\Gamma_{jk}(\omega)\right| \exp\left[i\vartheta_{jk}(\omega)\right] \tag{4.38}$$

Being $\vartheta_{jk}(\omega)$ the phase spectrum expressed as:

$$\vartheta_{jk}(\omega) = \tan^{-1}\left(\frac{\mathrm{Im}[S_{jk}(\omega)]}{\mathrm{Re}[S_{jk}(\omega)]}\right) \tag{4.39}$$

The coherency is also a function of the separation distance ξ_{jk} between two further away stations j and k on the ground surface and can be alternatively expressed as:

$$\Gamma_{jk}(\xi,\omega) = \left|\Gamma_{jk}(\xi,\omega)\right| \exp\left[i\vartheta_{jk}(\xi,\omega)\right] \tag{4.40}$$

4.3.2.1 Wave passage effect

The complex term in the above equation $\exp\left[i\vartheta_{jk}(\xi,\omega)\right]$ represents the wave-propagation effect and so the delay in the time arrival of seismic waves at two separated stations. Under the hypothesis that waves propagate with constant velocity along a line connecting the stations of interest on the ground surface, $\vartheta_{jk}(\xi,\omega)$ is expressed as:

$$\vartheta_{jk}(\xi,\omega) = \frac{-\omega\xi_{jk}}{v_{app}} \tag{4.41}$$

Where v_{app} indicates the apparent propagation velocity of the motion along the line connecting the stations j and k with separation distance ξ_{jk}.

Based on the coherence estimates derived from recorded ground motions (e.g., SMART-1 array in Taiwan), various mathematical models have been proposed in the literature to fit the data points through regression analyses. In the following section, two of the most commonly used mathematical models for coherence will be presented. However, it's important to note that many other models, each with their own advantages and limitations, could also be utilized for this purpose.

4.3.2.2 Empirical coherency models

Most of the empirical expressions for the coherency were proposed based on the analyses of data collected at the SMART-1 array. One of these is the Harichandran and Vanmarcke model [52], whose expression is specifically based on the fitting of data related to the SMART-1 array event 20:

$$\left|\Gamma_{jk}(\omega)\right| = A\exp\left[-\frac{2\left|\xi_{jk}\right|}{\alpha\theta(\omega)}(1-A-\alpha A)\right] + (1-A)\exp\left[-\frac{2\left|\xi_{jk}\right|}{\alpha\theta(\omega)}(1-A-\alpha A)\right] \tag{4.42}$$

$$\theta(\omega) = k\left[1+\left(\frac{\omega}{\omega_0}\right)^b\right]^{-0.5} \tag{4.43}$$

This coherency model makes use of the parameters derived by Harichandran and Wang [85]: $A = 0.606$, $\alpha = 0.0222$, $k = 19700m$, $\omega_0 = 12.692 rad/\sec$, $b = 3.47$.

Figure 4.3 presents the decay of the coherency with frequency ω at three different separation distances equal to 100, 300, and 500m according to the Harichandran and Vanmarcke model.

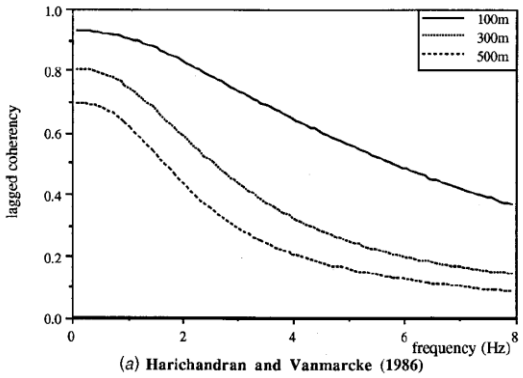

Figure 4.3. Harichandran and Vanmarcke Coherency model [79].

4.3.2.3 Semi-empirical models

Semi-empirical models are those that employ an analytical function to describe data, using parameters that are calibrated based on recorded data.

The wider-used semi-empirical coherency model is the one introduced by Luco and Wong in 1986 [53] and is based on the following expression:

$$\left|\gamma_{jk}(\omega)\right| = \exp\left[\left(\frac{-\alpha\omega\xi_{jk}}{v_s}\right)^2\right] \tag{4.44}$$

Where v_s is the shear-wave velocity of the soil strata and α is a constant empirically calibrated; according to the observation of field data, Luco and Wong [53] suggested for the ratio α / v_s a value comprised between $2.5x10^{-4} \le \alpha / v_s \le 3.0x10^{-4}$. The coherency, according to this model, decays exponentially with the frequency ω, the separation distance between two stations ξ_{jk}, and the inverse of the mechanical property of the soil (Figure 4.4).

Zanardo et al. [71] proposed to adopt different correlation patterns for the ground motion time history simulation, depending on the value of the ratio α / v_s as summarized below:

- $\alpha / v_s = 0$ meaning the ground motions are perfectly coherent;
- $\alpha / v_s = 2.5x10^{-5}$ the ground motions are strongly correlated;
- $\alpha / v_s = 2.5x10^{-4}$ the ground motions are intermediately correlated;
- $\alpha / v_s = 2.5x10^{-3}$ the ground motions are weakly correlated;
- $\alpha / v_s = 2.5x10^{-2}$ meaning that the ground motions are totally incoherent.

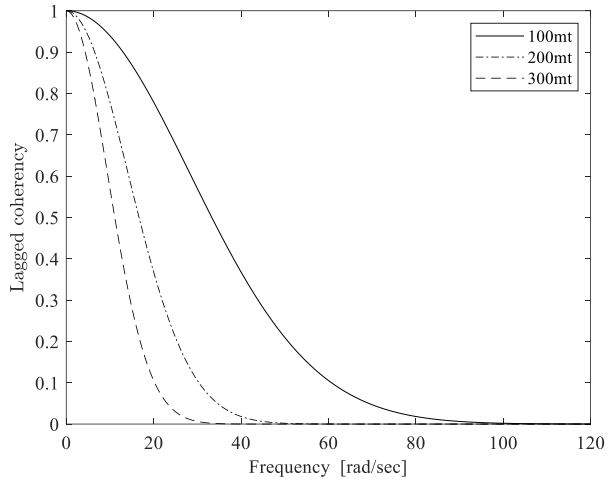

Figure 4.4. Luco and Wong coherency model for three separation distances and for a value of $\alpha / v_s = 2.5x10^{-4}$.

4.3.3 Simulation formula of spatially variable ground motions (SVEGM)

To simulate the 1D-*m*V quasi-stationary ground motion vector process $f_j(t), (j = 1,...,m)$, according to [65], the first step of the procedure involves decomposing the cross-spectral density matrix $S_f(\omega)$ at every time instant *t* using the Cholesky's method as follows:

$$S_f(\omega) = H(\omega)H^{T^*}(\omega) \tag{4.45}$$

Where $H(\omega)$ is a lower triangular matrix written as:

$$H(\omega)=\begin{bmatrix} H_{11}(\omega) & 0(\omega) & \dots & 0(\omega) \\ H_{21}(\omega) & H_{22}(\omega) & \dots & 0(\omega) \\ \vdots & \vdots & \ddots & \vdots \\ H_{m1}(\omega) & H_{m2}(\omega) & \dots & H_{mm}(\omega) \end{bmatrix} \tag{4.46}$$

Once the cross-spectral density matrix $S_f(\omega)$ has been decomposed according to Eqs. (4.45) and

(4.46) it is possible to generate the quasi-stationary ground motion vector process $f_j(t),(j=1,...,m)$ through the following series as $N\to\infty$ and being $j=1,2,....,m$:

$$f_j(t)=A_j(t)\cdot 2\sum_{r=1}^{m}\sum_{s=1}^{N}\left|H_{jr}(\omega_s)\right|\sqrt{\Delta\omega}\cos[\omega_s t-\vartheta_{jr}(\omega_s)+\phi_{rs}] \tag{4.47}$$

Where:

$$\vartheta_{jr}(\omega)=\tan^{-1}\left(\frac{\mathrm{Im}[H_{jr}(\omega)]}{\mathrm{Re}[H_{jr}(\omega)]}\right) \tag{4.48}$$

In which Im and Re denote respectively the imaginary and real part of a complex number, whereas:

$$\omega_s=s\Delta\omega,\quad s=1,2,...,N,\qquad \Delta\omega=\frac{\omega_C}{N} \tag{4.49}$$

In Eq. (4.49) ω_C represents an upper cut-off frequency beyond which the elements of the cross-spectral density matrix $S_f(\omega)$ can be considered equal to zero. In addition, inside Eq.

(4.47) m sequences of N independent random phase angles ϕ_{rs}, uniformly distributed over the interval $[0,2\pi]$, are introduced.

Additionally, the simulated quasi-stationary stochastic vector process $f_j(t),(j=1,...,m)$ is asymptotically Gaussian as $N\to\infty$ invoking the central limit theorem.

In order to generate multiple sample function $f_j^{(i)}(t)$ of the quasi-stationary stochastic vector process $f_j(t),(j=1,...,m)$, each of the m sequences of the random phase angles ϕ_{rs} can be substituted with their respective realizations $\phi^{(i)}{}_{rs}$. Following this approach, the generic sample function $f_j^{(i)}(t),(j=1,...,m)$ can be written as follows:

$$f_j^{(i)}(t)=A_j(t)\cdot 2\sum_{r=1}^{m}\sum_{s=1}^{N}\left|H_{jr}(\omega_s)\right|\sqrt{\Delta\omega}\cos[\omega_s t-\vartheta_{jr}(\omega_s)+\phi^{(i)}{}_{rs}] \tag{4.50}$$

4.4 Spectrum-compatible quasi-stationary ground motion vector process

Given the importance of generating simulated time histories for the design or the assessment of structures according to the international seismic codes, and considering that the elastic response spectrum is the most widely used tool for the seismic design of structures and infrastructures, it is crucial for the simulated ground motion to be spectrum-compatible. Accordingly, in this work of thesis, the method proposed by Cacciola in 2010 [66] for the generation of fully non-stationary, spectrum-compatible earthquake motions and further extended by Cacciola and Deodatis [67] for the case of multi-variate simulation, is adopted.

The method assumes that the average response spectrum derived from the simulated time histories, closely matches the target response spectrum provided by the code within a code-specified tolerance and over a certain frequency range:

$$\left|\frac{RSA^{j}(\omega)-RSA^{f_j}(\omega)}{RSA^{j}(\omega)}\right| \le \varepsilon \qquad (j=1,....,m) \tag{4.51}$$

Where $RSA^{j}(\omega)$ is the *j*-th target response spectrum associated with the *j*-th station and $RSA^{f_j}(\omega)$ the *j*-th ensemble-averaged response spectrum of the simulated ground motion vector process $f_j(t),(j=1,...,m)$ that superimposes to the target spectrum, satisfying a constant ε code-specified tolerance.

Given a target pseudo-acceleration response spectrum $RSA(\omega_0,\zeta)$ for a given natural frequency ω_0 and damping ratio ζ, the procedure requires for the simulated time histories to have a power spectral density matrix whose response spectrum matches (within the aforementioned tolerance ε) the target one.

The first crossing problem defined by Vanmarcke and Gasparini [84] is essential to accomplish this task as it provides a relationship between the response-spectrum and the ground motion power spectral density. In this problem, the ground motion acceleration process is assumed to be a zero-mean Gaussian stationary process. The pseudo-acceleration response-spectrum, $RSA(\omega_0,\zeta)$, given a damping ratio ζ and the natural circular frequency ω_0, is associated through the following expression to the median value of the maximum peak of the response of a single degree of freedom system:

$$RSA(\omega_0,\zeta)=\omega_0^2\eta_U(T_S,p=0.5,\lambda_{0,U}(\omega_0,\zeta),\lambda_{1,U}(\omega_0,\zeta),\lambda_{2,U}(\omega_0,\zeta))\cdot\sqrt{\lambda_{0,U}(\omega_0,\zeta)} \tag{4.52}$$

Where η_U is the peak factor given by the following expression:

$$\eta_U = \sqrt{2\ln\left\{2N_U[1-\exp[-\delta_U^{1.2}\sqrt{\pi\ln(2N_U)}]\right\}} \tag{4.53}$$

With:

$$N_U = \frac{T_S}{2\pi}\sqrt{\frac{\lambda_{2,U}(\omega_0,\zeta)}{\lambda_{0,U}(\omega_0,\zeta)}} - (\ln p)^{-1} \tag{4.54}$$

And:

$$\delta_U = \sqrt{1-\frac{\lambda_{1,U}(\omega_0,\zeta)^2}{\lambda_{0,U}(\omega_0,\zeta)\lambda_{2,U}(\omega_0,\zeta)}} \tag{4.55}$$

In Eq. (4.53) the term T_S is the observing time window whereas p is the not-exceeding probability.

Additionally, the terms $\lambda_{i,U}(\omega_0,\zeta)$, with (i=0,1,2) represent the response spectral moments expressed as:

$$\lambda_{i,U}(\omega_0,\zeta) = \int_0^\infty \omega^i \left|H(\omega,\omega_0,\zeta)\right|^2 G_j(\omega)d\omega \tag{4.56}$$

In which $\left|H(\omega,\omega_0,\zeta)\right|^2 = \left(\left(\omega_0^2-\omega^2\right)^2 + 4\zeta^2\omega_0^2\omega^2\right)^{-1}$ is the energy transfer function of the system and $G_j(\omega)$ is the unilateral power spectral density to be determined as a property of the seismic acceleration process. Specifically, the unilateral power spectral density $G_j(\omega) = (2S_j(\omega), \omega \geq 0; = 0 \ elsewhere)$, compatible with a given response spectrum, has the following recursive expression:

$$G_j(\omega) = 0,\ 0 \leq \omega \leq \omega_l \tag{4.57}$$

$$G_j(\omega) = \frac{4\zeta}{\omega_i\pi - 4\zeta\omega_{i-1}}\left(\frac{RSA(\omega_i,\zeta)^2}{\eta_U^2(\omega_i,\zeta)} - \Delta\omega\sum_{r=1}^{i-1}G_j(\omega_r)\right) \qquad \omega > \omega_l \tag{4.58}$$

To determine the peak factor η_U and the parameter δ_U it is possible to make the assumption that the input PSD features a smooth shape and $\zeta \ll 1$. Accordingly, the following simplified relations are valid:

$$N_U = \frac{T_S}{2\pi}\omega_i - (\ln p)^{-1} \tag{4.59}$$

and:

$$\delta_U = \left[1 - \frac{1}{1-\zeta^2} \left(1 - \frac{2}{\pi} \arctan \frac{\zeta}{\sqrt{1-\zeta^2}} \right)^2 \right]^{1/2} \tag{4.60}$$

In Eq. (4.58) ω_l has the significance of a lower bound in the frequency domain for η_U and is assumed to be $\omega_l \cong 1 rad/\sec$.

Having determined the unilateral spectrum-compatible power spectral density function it is then possible to evaluate the elements of the cross-spectral density matrix $S_f^{SC}(\omega)$ defined as for Eq. (4.22). Particularly, the elements on the diagonal are specified by the following relation between $G_j(\omega)$ and $S_j^{SC}(\omega)$:

$$S_j^{SC}(\omega) = G_j(\omega)/2, \; j = 1,2,...,m \tag{4.61}$$

Whereas the off-diagonal terms are defined in perfect analogy with Eq. (4.23) as:

$$S_{jk}^{SC}(\omega) = \sqrt{S_j^{SC}(\omega) S_k^{SC}(\omega)}\,\Gamma_{jk}(\omega), \quad j,k = 1,2,....,m, \; j \neq k \tag{4.62}$$

where the superscript "SC" stands for "spectrum-compatible".

At the end of the procedure, it is possible to generate at each station or support points of the ground surface quasi-stationary ground motion time histories that make use of a certain coherence function $\Gamma_{jk}(\omega)$ and are spectrum-compatible.

4.5 Generation of input ground motion accounting for spatial variability for the case study

In this section, the adopted methodology for generating quasi-stationary and spectrum-compatible ground motion vector process is further detailed for the case study, where the seismic response under spatially variable earthquake ground motion of respectively 5-span and 7-span isolated bridges (testbed bridges) is investigated.

The acceleration time histories at six (two abutments + four piers) and eight (two abutments + six piers) support points on the ground surface of the two testbed bridges are considered as 6-variate and 8-variate quasi-stationary, spectrum-compatible input motions. The wave train is assumed to propagate along the bridge's longitudinal axis from left to right.

The 5-span bridge is located in Central Italy, near the city of L'Aquila, known for its high seismic hazard. As for NTC2018 [77], a total of 9 intensity measure levels, corresponding to a mean return period ranging from 30 to 2475 years are considered to evaluate the structural response under increasing seismic intensity levels.

The soil underneath the support points is assumed to be either of Category A (rock or other rock-like geological formation) or of Category B (very dense sand, gravel, or very stiff clay) as defined in [77]. This classification allows the evaluation of the target elastic response spectrum for the site of interest and for the specific soil category. In this study, the following combination of local soil conditions for the 5-span bridge and the 7-span bridge is adopted:

5-span bridge- Soil condition at support points					
Ab1	**P1**	**P2**	**P3**	**P4**	**Ab2**
Soil A	Soil B	Soil B	Soil B	Soil B	Soil A

Table 4.1. Soil condition combination for the 5-span bridge.

7-span bridge- Soil condition at support points							
Ab1	**P1**	**P2**	**P3**	**P4**	**P5**	**P6**	**Ab2**
Soil A	Soil B	Soil B	Soil B	Soil B	Soil B	Soil B	Soil A

Table 4.2. Soil condition combination for the 7-span bridge.

The first and the last letters indicate the soil type underneath the abutments, which are assumed to be founded on soil of Category A, differently from the piers that rest on a soil B Category, according to the soil type combinations proposed in [57].

The acceleration time histories at the abovementioned support points are considered partially correlated according to the Harichandran and Vanmarcke coherency model [52] (Figure 4.5), which makes use of the parameters that Harichandran and Wang [85] obtained by analyzing the data from the SMART-1 array: $A = 0.606$, $\alpha = 0.0222$, $k = 19700m$, $\omega_0 = 12.692 rad/\sec$, $b = 3.47$:

$$\left|\Gamma_{jk}(\omega)\right| = A\exp\left[-\frac{2\left|\xi_{jk}\right|}{\alpha\theta(\omega)}(1-A-\alpha A)\right] + (1-A)\exp\left[-\frac{2\left|\xi_{jk}\right|}{\alpha\theta(\omega)}(1-A-\alpha A)\right] \tag{4.63}$$

$$\theta(\omega) = k\left[1+\left(\frac{\omega}{\omega_0}\right)^b\right]^{-0.5} \tag{4.64}$$

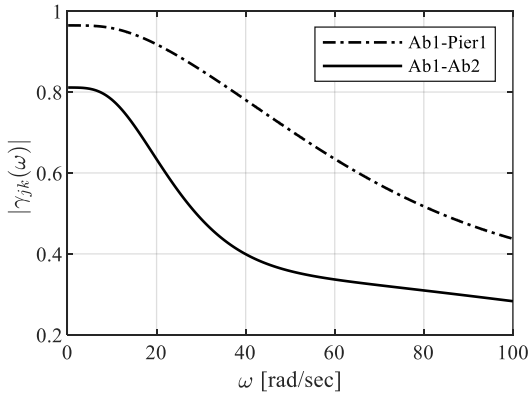

Figure 4.5. Harichandran and Vanmarcke loss of coherency between the ground motion time series for station at Abutment 1 and Pier#1 (32m) and Abutment 1 - Abutment 2 (229m), for the 7-span bridge configuration.

The model used here differs from other mathematical expressions, such as the semi-empirical models by Luco and Wong [53], because it avoids a sharp exponential decay with distance and frequency. This allows for a greater contribution coming from the dynamic component (and not just the pseudo-static component) of the seismic bridge response. This dynamic contribution has been demonstrated to be particularly crucial for isolated bridges. Alternatively, any other model can be adopted straightforwardly.

The wave propagation effect as defined in §4.3.2.1 is also taken into account assuming an apparent wave propagation velocity equal to $v_{app} = 900 m/s$ [74].

As such, the complex coherence function $\Gamma_{jk}(\omega)$ defined in Eq. (4.23) must include the wave propagation term expressed as:

$$\gamma_{wp} = \exp\left[-i\frac{\omega\xi_{jk}}{v_{app}}\right] \tag{4.65}$$

in which ξ_{jk} is the distance between points j and k and v_{app} is the abovementioned apparent velocity. Including the wave propagation term the coherency can be written as follows:

$$\Gamma_{jk}(\xi,\omega) = \left|\Gamma_{jk}(\xi,\omega)\right| \exp\left[-i\frac{\omega\xi_{jk}}{v_{app}}\right] \tag{4.66}$$

Based on the previous comments, it is possible to simulate time histories that are at the same time spatially correlated, that incorporate the wave propagation effect, and that are representative of different local soil conditions.

Such ground motion time histories $f_j(t)$, modeled as quasi-stationary stochastic vector process, need for the definition of a modulating function $A_j(t)$ $j = 1,2,...,m$ as per Eq. (4.29).

In this study the modulating function proposed by Jennings, Housner, and Tsai [86], (Figure 4.6), is selected. Its mathematical expression is as follows:

$$A_j(t) = \begin{Bmatrix} \left(\frac{t}{t_1}\right)^2 & t < t_1 \\ 1 & t_1 \le t \le t_2 = T_s \\ \exp[-\beta(t-t_2)] & t > t_2 \end{Bmatrix} \qquad (4.67)$$

$j = 1, 2, ...m$

In Eq. (4.67), named $T_S = t_2 - t_1$ the duration of the stationary part of the ground motion time history (*i.e.* the duration of the strong motion S-wave observing window) and based on the requirements of Eurocode 8 ($T_s \ge 10\,\text{sec}$) [76], the constant segment of the Jennings et al. function has been extended over a time length $T_S = 15s$.

Regarding the values of β, t_1 and t_2, they are evaluated by ensuring that the energy of the stochastic ground motion reaches the values of 5% and 95% respectively at times t_1 and t_2. This assumption extends the well-known Husid function (Eq. (4.68)) to the stochastic process [66]; accordingly, it is possible to evaluate the values of $H(t_1) = 0.05$ and $H(t_2) = 0.95$.

$$H(t) = \frac{\int_0^t \int_0^\infty a(t)^2 G_j(\omega) dt}{\int_0^{tf} \int_0^\infty a(t)^2 G_j(\omega) dt} \qquad (4.68)$$

Eq. (4.68) permits to derive the following relationship [68] between the parameters β and t_1, t_2, once defined the strong motion stationary duration T_S:

$$\beta = \frac{9}{T_S}; \qquad t_1 = \frac{2.5}{\beta}; \qquad t_2 = \frac{11.5}{\beta} \tag{4.69}$$

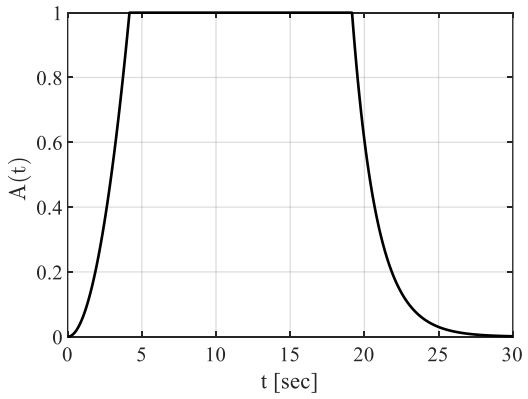

Figure 4.6. Modulating function $A_j(t)$ according to the Jennings, Housner, and Tsai model [86].

In (Figure 4.7) the power spectral density functions defined according to Eq.s (4.57)-(4.58) and related to the pseudo-acceleration response spectrum $\mathrm{RSA}(\omega_0,\zeta=2\%)$ for the specific site of interest, a mean return period $T_R = 2475 years$, PGA=0.452g, and for Soil Category A and Soil Category B is presented:

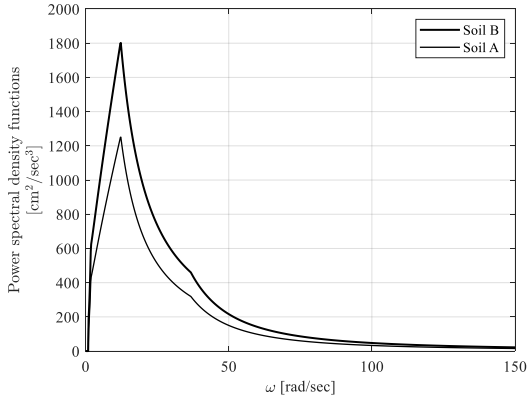

Figure 4.7. Power spectral density functions spectrum-compatible with the pseudo-acceleration response spectrum $\mathrm{RSA}(\omega_0,\zeta=2\%)$ for the site of L'Aquila (Italy), mean return period $T_R = 2475 yrs$, Soil Category A, and Soil Category B.

The i-*th* sample of the spectrum-compatible acceleration time histories $f_j^{(i)}(t)$, generated according to Eq. (4.50), is then presented in (Figure 4.8) for each station or bridge support, for the case of the 7-span testbed bridge, $T_R = 2475 years$, PGA=0.452g and $v_{app} = 900 m/\sec$. For the simulation of $f_j^{(i)}(t)$, in both cases of 6-variate and 8-variate vector processes, the upper cut-off frequency ω_C has been set equal to 157rad/sec whereas the frequency step is defined as $\Delta\omega = \frac{\omega_C}{N}$, being N=1000. Simulation of acceleration time histories is performed at 3000-time instances with a time step equal to 0.01s.

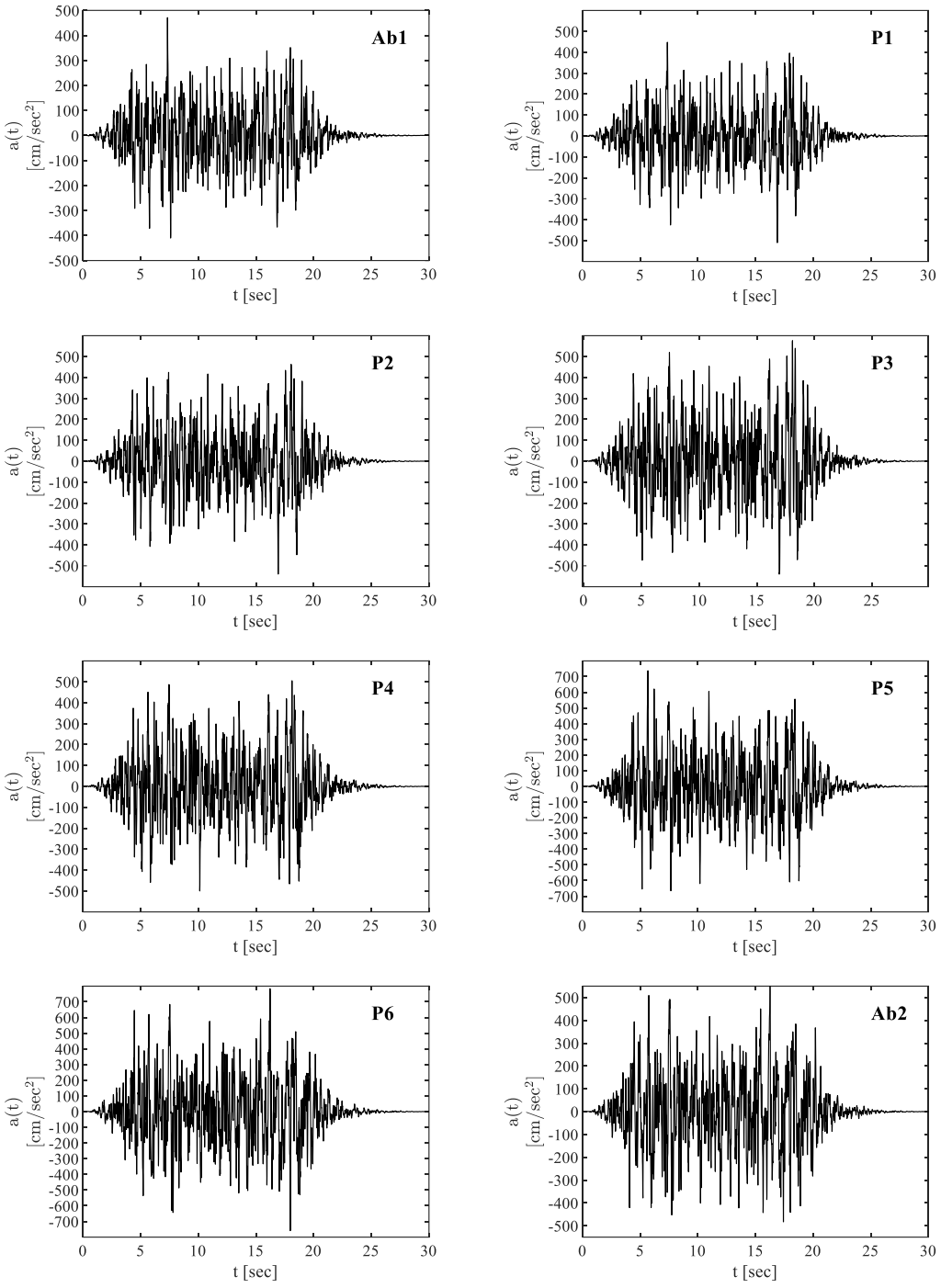

Figure 4.8. Set of accelerograms along the 7-span bridge supports for the case of PGA=0.452g, v_{app}=900m/sec .

In this study, a total of 30 realizations (sample functions) are generated for each bridge support to express the uncertainty related to the seismic input and to reach convergence between the mean spectra of the realizations and the targeted pseudo-spectral acceleration response spectrum for the site of interest $RSA(\omega_0,\zeta=2\%)$. In (Figure 4.9) a comparison between the ensemble-averaged simulated response spectrum and the target one, for the specific case of a mean return period $T_R = 2475 years$, PGA=0.452g, is shown, and the effectiveness of the followed procedure is demonstrated.

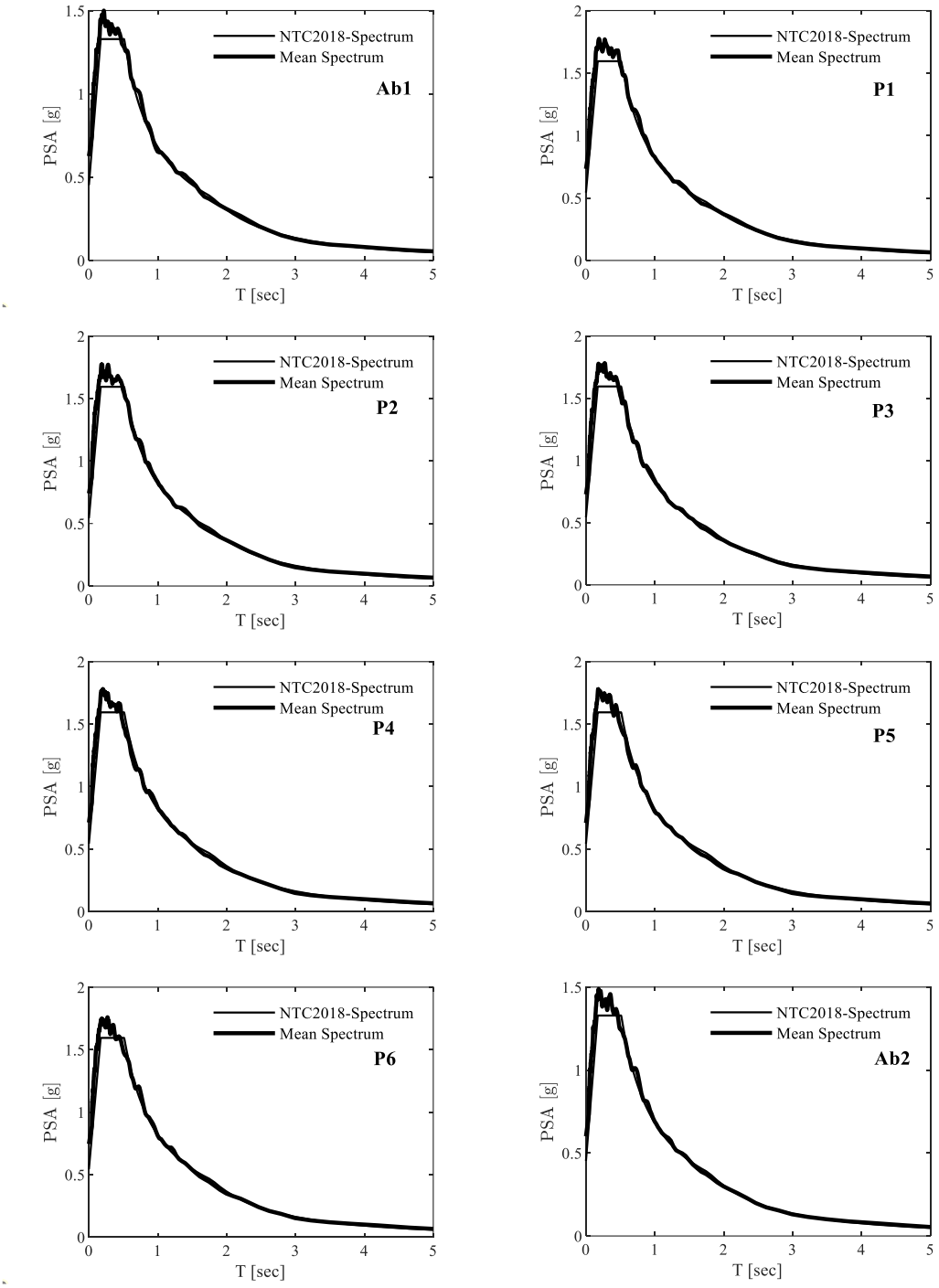

Figure 4.9. Comparison of mean response spectrum (30 realizations) of the *i*-th generated motions for the case of PGA=0.452g, T_R=2475yrs, $v_{app} = 900m/\sec$.

4.6 Validation of the adopted procedure

To numerically validate the adopted procedure for the 5-span testbed bridge, it is possible to compare the ensemble-averaged coherence functions with the prescribed ones defined in Eq. (4.63) [65].

For the 5-span, 6 support points bridge, (6-variate quasi-stationary stochastic vector process) the elements of the 6x6 spectrum-compatible cross-spectral density matrix (Eq.

(4.22)) are defined as follows:

$$S_f^{SC}(\omega)=\begin{bmatrix} S_1^{SC}(\omega) & S_{12}^{SC}(\omega) & S_{13}^{SC}(\omega) & S_{14}^{SC}(\omega) & S_{15}^{SC}(\omega) & S_{16}^{SC}(\omega) \\ S_{21}^{SC}(\omega) & S_2^{SC}(\omega) & S_{23}^{SC}(\omega) & S_{24}^{SC}(\omega) & S_{25}^{SC}(\omega) & S_{26}^{SC}(\omega) \\ S_{31}^{SC}(\omega) & S_{32}^{SC}(\omega) & S_3^{SC}(\omega) & S_{34}^{SC}(\omega) & S_{35}^{SC}(\omega) & S_{36}^{SC}(\omega) \\ S_{41}^{SC}(\omega) & S_{42}^{SC}(\omega) & S_{43}^{SC}(\omega) & S_4^{SC}(\omega) & S_{45}^{SC}(\omega) & S_{46}^{SC}(\omega) \\ S_{51}^{SC}(\omega) & S_{52}^{SC}(\omega) & S_{53}^{SC}(\omega) & S_{54}^{SC}(\omega) & S_5^{SC}(\omega) & S_{56}^{SC}(\omega) \\ S_{61}^{SC}(\omega) & S_{62}^{SC}(\omega) & S_{63}^{SC}(\omega) & S_{64}^{SC}(\omega) & S_{65}^{SC}(\omega) & S_6^{SC}(\omega) \end{bmatrix} \quad (4.70)$$

Where the diagonal terms are computed as half of the unilateral power spectral density $G_j(\omega)$: $S_j^{SC}(\omega)=G_j(\omega)/2$, $(j=1,2,..,m)$, whereas the off-diagonal terms are defined as for Eq. (4.62): $S_{jk}^{SC}(\omega)=\sqrt{S_j^{SC}(\omega)S_k^{SC}(\omega)}\Gamma_{jk}(\omega)$.

The 6 diagonal elements of the spectrum-compatible cross-spectral density matrix will reflect the aforementioned soil combinations.

The first step of the validation involves the computation of the ensemble-averaged time autocorrelation and cross-correlation for stochastic processes:

$$\tilde{R}_{jj}(\tau)\triangleq E_X\left\{f^{SC(i)}{}_j(t)f^{SC(i)}{}_j(t-\tau)\right\}=E_X\left\{\hat{R}_{jj}(\tau)\right\} \quad (4.71)$$

, with $j=1,2,...6$

$$\tilde{R}_{jk}(\tau)\triangleq E_X\left\{f^{SC(i)}{}_j(t)f^{SC(i)}{}_k(t-\tau)\right\}=E_X\left\{\hat{R}_{jk}(\tau)\right\} \quad (4.72)$$

with $j,k=1,2,...6$, $j\neq k$

Where $E_X\{\bullet\}$ is the expectation operator, τ indicates the time lag, the accent $\sim$ in Eq.s (4.71)-(4.72) indicates ensemble averages while the accent ^ stands for the time average. Indeed, $\hat{R}_{jj}(\tau)$ and $\hat{R}_{jk}(\tau)$ are the time averages of the autocorrelation and cross-correlation functions based on the *i*-th sample defined as:

$$\hat{R}_{jj}(\tau)=\lim_{T\to\infty}\frac{1}{T}\int_0^{T+|\tau|}f^{SC(i)}{}_j(t)f^{SC(i)}{}_j(t+\tau)dt \quad (4.73)$$

$$\hat{R}_{jk}(\tau)=\lim_{T\to\infty}\frac{1}{T}\int_0^{T+|\tau|}f^{SC(i)}{}_j(t)f^{SC(i)}{}_k(t+\tau)dt \quad (4.74)$$

The components of the spectrum-compatible cross-spectral density matrix of the stochastic process are then linked to the ensemble-averaged time autocorrelation and cross-correlation functions through the Wiener-Kintchin-Einstein formula:

$$S^{SC}{}_{j}(\omega) = F\left\{\tilde{R}_{jj}(\tau)\right\} \tag{4.75}$$

with $j = 1,2,...6$

$$S^{SC}{}_{jk}(\omega) = F\left\{\tilde{R}_{jk}(\tau)\right\} \tag{4.76}$$

with $j,k = 1,2,...6, j \neq k$

It is also important to highlight the following properties of the autocorrelation function:

$$\tilde{R}_{jj}(0) = E_X\left\{\left(f_j^{SC(i)}\right)^2\right\} = P_X \tag{4.77}$$

$$\left|\tilde{R}_{jj}(\tau)\right| \leq \tilde{R}_{jj}(0) \tag{4.78}$$

$$\tilde{R}_{jj}(\tau) = \tilde{R}_{jj}{}^{*}(-\tau) \tag{4.79}$$

Where $P_X = \int_{-\infty}^{+\infty} S_j^{SC}(\omega) d\omega$ coincides with the average power of the process, such that, by differentiation:

$$\frac{dP_X}{d\omega} = S_j^{SC}(\omega)$$

it is possible to obtain the power spectral density of the average power P_X, $S_j^{SC}(\omega)$.

Moreover, assuming that the stochastic process is stationary inside the time interval defined by the time values t_1 and t_2 during which the Jenning modulation function remains constant at $A_j(t) = 1$, it is reasonable to assume that the process is ergodic within this interval of time. A stochastic process is said to be ergodic for a specific average if the statistical and the temporal averages coincide for each and all the realizations of the process. For example, a process is said to be ergodic for the autocorrelation if:

$$E_X\left\{f^{SC(i)}{}_{j}(t) f^{SC(i)}{}_{j}(t-\tau)\right\} = \langle f_j^{SC}(t; f^{SC(i)}{}_{j}) f_j^{SC}(t-\tau; f^{SC(i)}{}_{j})\rangle_{\mathbb{R}} \tag{4.80}$$

, $\forall f_j^{SC(i)}$

Where the right-hand side of Eq. (4.80) coincides with the time average of the autocorrelation $\hat{R}_{jj}(\tau)$ for the specific i-*th* sample function given in Eq. (4.73).

The assumption of ergodicity implies that the statistical of a single realization over its stationary duration are representative of the ensemble statistical property. This implication has herein been used for the computation of the ensemble-averaged time autocorrelation and cross-correlation to increase the number of sample functions up to 8000 samples.

In Figure 4.10 the spectrum-compatible cross-spectral density matrix components, $S^{SC}{}_{1}(\omega)$ and $S^{SC}{}_{2}(\omega)$, calculated according to Eq. (4.75) by Fourier

transforming the ensemble-averaged time autocorrelation function $\tilde{R}_{11}(\tau)$ and $\tilde{R}_{22}(\tau)$ are compared with the target ones calculated according to Eq. (4.61).

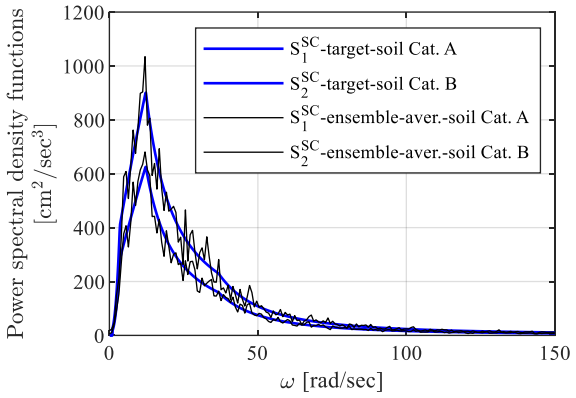

Figure 4.10. Comparison between the target spectrum-compatible cross-spectral density matrix components $S^{SC}{}_1(\omega)$ and $S^{SC}{}_2(\omega)$, and the corresponding ones calculated throughout Eq. (4.75).

Once the cross-correlation matrix and the corresponding cross-spectral density matrix are calculated according to Eq.s (4.71) to (4.76) it is possible to evaluate the ensemble-averaged coherence functions, comprehensive of the wave propagation complex term, between two different support points $j=1,2,..,6$ and $k=1,2,...,6$ with $j\neq k$, as obtained from 8000 sample functions.

Specifically, the ensemble-averaged coherence function has been computed by inverting Eq. (4.62):

$$\Gamma_{jk}(\omega)=\frac{S^{SC}_{jk}(\omega)}{\sqrt{S^{SC}_{j}(\omega)S^{SC}_{k}(\omega)}}, \qquad (4.81)$$
$$j,k=1,2,....,m;,\ j\neq k$$

To show the effectiveness of the adopted methodology the following Figure 4.11 compares the ensemble-averaged coherence functions $\Gamma_{1k}(\omega)$, $j=1$, $k=1,2,...6$ with the corresponding prescribed ones calculated starting from Eq. (4.63).

The same comparison could be made for $j=2,..,6$.

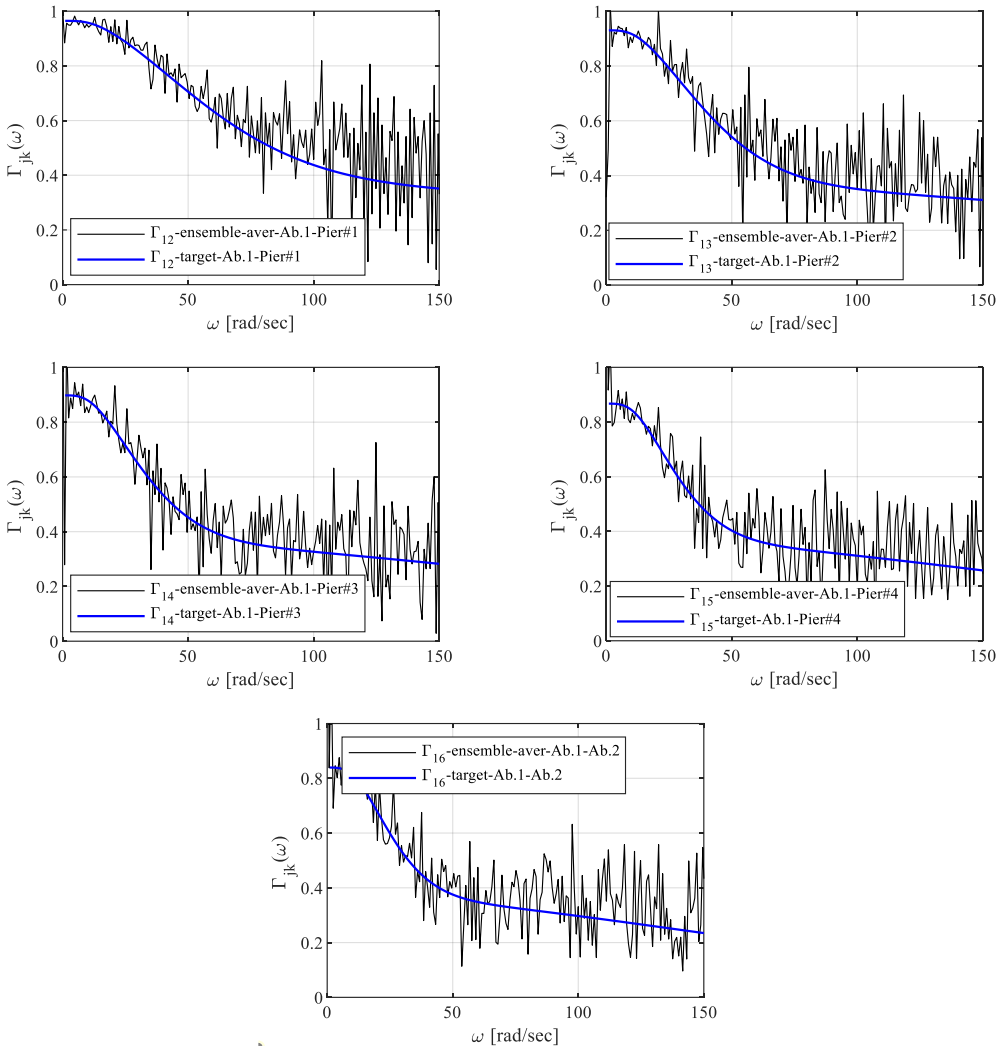

Figure 4.11. Comparison between the ensemble-averaged coherence functions $\Gamma_{1k}(\omega)$ $j=1$, $k=2,...6$ and the corresponding prescribed ones calculated as for Eq. (4.63) using 8000 sample functions.

5 Numerical modeling and structural analysis

This chapter describes the testbed bridge adopted in the analysis: an existing simply supported reinforced concrete (RC) bridge located in central Italy, near the site of L'Aquila.

Due to the lack of design seismic details, primarily in the pier component, the bridge will be retrofitted with a seismic isolation system using friction-type devices (*i.e.*, FP system).

The chapter includes an in-depth focus on the numerical model of each bridge component implemented in *Opensees*, the open-source software for structural and geotechnical problems. The model uses a three-dimensional spine line approach with elastic beam-column elements for the deck and fiber-section, force-based beam-column elements for the piers. Additionally, the FP devices are modeled through the built-in element of *Opensees*, while the soil-structure interaction at the abutments is implemented through a *zero-length* element with specific stiffnesses assigned along the longitudinal and transverse bridge directions.

Furthermore, details are provided regarding the parametric analysis carried out, which encompasses a wide range of bridge properties (*i.e.*, the total number of spans and the isolation period), different seismic intensity levels along with two incidence angle conditions. Additionally, the friction coefficient at large velocities and the uncertainties related to the seismic input (both for the SVEGM condition and the uniform one) are treated as random variables relevant to the problem.

Finally, the chapter illustrates the procedure for implementing multiple-support excitation in *Opensees*.

5.1 Description of the Case-Study Bridge

The bridge used as analysis testbed [87] is an existing straight, simply supported reinforced concrete (RC) bridge (Figure 5.1) constructed in 1979 and located in central Italy, at the border between the regions of Marche and Abruzzo, in an area where the design peak ground acceleration that corresponds to a Return Period $T_R = 475 years$ (SLV limit state as for NTC18) is 0.3 [g] .

The layout information and material properties of the testbed bridge were retrieved as courtesy of Dr. Volkan Ozsarac from Scuola Universitaria Superiore

IUSS Pavia [33]; they have to be considered as expected material strength values which are obtained via laboratory tests.

a) b)

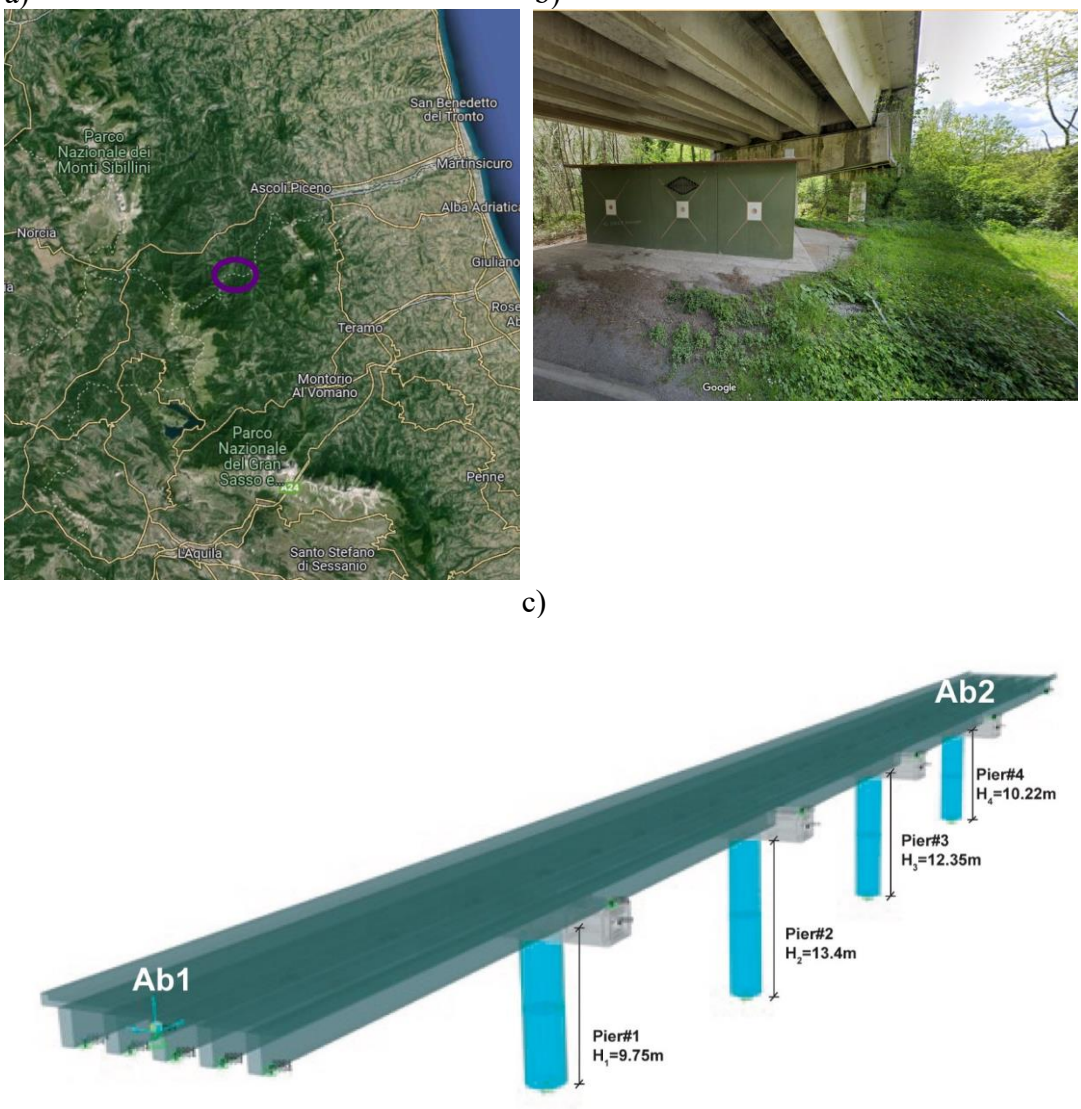

Figure 5.1. Bridge site location a); Bridge Street-view photograph b); 5-span bridge model - extrude view in SAP2000 [91] c).

The superstructure spans over a total length of 163.0m and consists of five simply-supported spans with an average length of 32.0m and a deck section that is 12.5m wide, including five reinforced concrete I-shaped girders and a superior reinforced concrete slab of 27.0cm (Figure 5.2).

a)

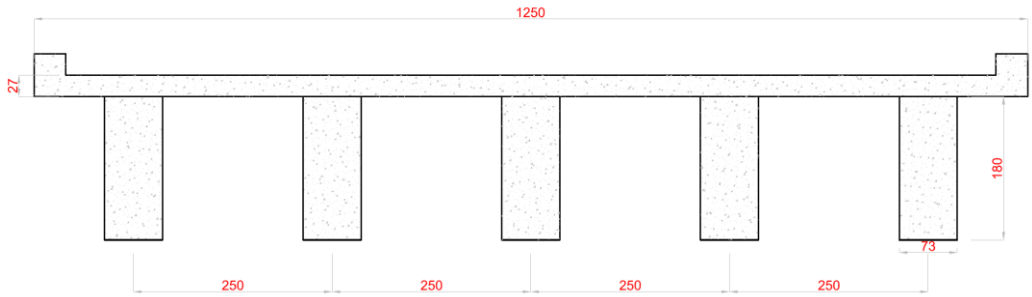

b)

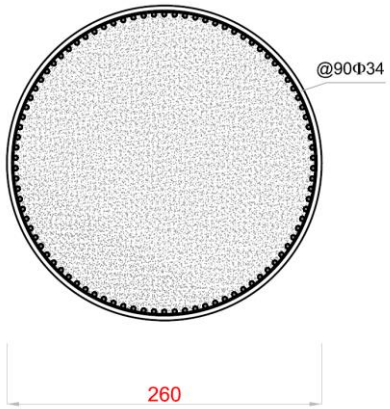

Figure 5.2. Deck geometry a); Pier section geometry b).

The substructure of the bridge comprises thin un-reinforced elastomeric bearings (70x50x2cm) placed on each of the girder beams, a cap beam with a hollow rectangular section and a width of 11.0m and four reinforced concrete piers with different heights of H_1=9.75m, H_2=13.4m, H_3=12.35m, and H_4=10.22m, all characterized by an equal circular section of 2.6m diameter with a compressive concrete strength of 29.1MPa and a longitudinal reinforcement ratio of 1.6% (90Φ34), with a yield strength of 420.MPa (Figure 5.2). Transverse steel reinforcement consists of hoops with a clear distance of 44cm for a total transverse steel ratio of 0.055%.

The bridge at each end is supported by a seat-type, zero skew-angle abutment with five elastomeric bearings placed on the abutment stemwall. The abutment is 12m wide and 3.5m high as provided in [33].

Two monolithic nonisolated shear keys are present both on the cap beams and on the abutments stemwall in order to restrain the movement of the bridge in the transverse direction by a gap of 5cm. In the longitudinal direction, the bridge is restrained at each end by the abutments backwall.

As far as the foundation system is concerned, both piers and abutments are sustained on pile foundations even though no further details regarding the geometric pile features are provided in [87], and as such they are considered fully restrained at the base.

Given the main mechanical and geometrical properties of the testbed bridge, because of the absence of seismic details, the lack of confinement provided by the hoops, it is assumed that a retrofit intervention has been carried over providing the

bridge with an isolation system through friction-type devices. Specifically, friction pendulum bearings (FPS), are considered installed in place of the un-reinforced elastomeric bearings, maintaining their same number and spacing, both on the abutments stemwall and on the cap beams.

Furthermore, in the context of the retrofit intervention with friction pendulum isolators, it is essential to allow for unrestrained bearing displacements along the transverse direction. To achieve this, the shear keys are removed from both the cap beams and the abutments. In the next section, an overview of the numerical model adopted for all the structural components of the FPS seismically isolated testbed bridge is presented. This model will enhance to analyze the bridge seismic response under spatial variability of earthquake ground motion.

5.2 Computational model of the bridge system

A three-dimensional nonlinear finite element (FE) model of the considered testbed isolated bridge is implemented using *OpenseesPy* [89], a *Python* library for *Opensees* [90], the open-source software for creating FE models both in structural and geotechnical engineering. The adopted numerical model is depicted in (Figure 5.3) and a detailed description of the modeling approach employed for each of the bridge components is illustrated in the following sections.

To take advantage of a better visualization environment, the model geometry is initially implemented in SAP2000 [91] and then the connectivity data (frames and structural nodes) imported in *OpenseesPy* to assign to each component the specific properties.

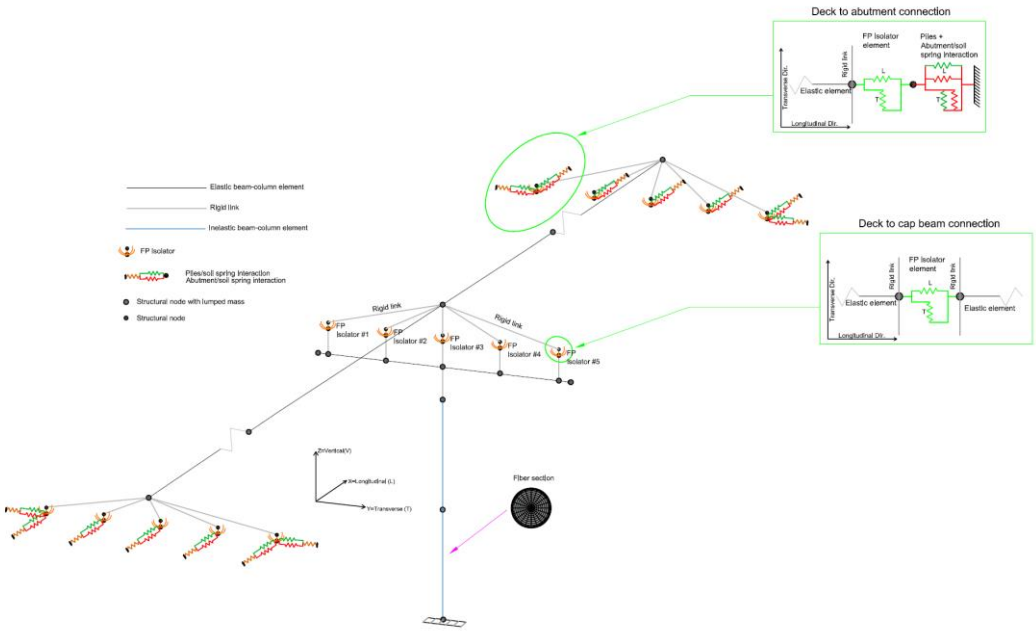

Figure 5.3. Illustration of the adopted numerical modeling approach for the testbed bridge.

5.2.1 Deck modeling

The bridge superstructure is generally designed to remain elastic under seismic actions. According to this, the deck of the isolated bridge is modeled using five elastic beam-column elements per span. The section properties depicted in Figure 5.2 are assigned to the elements together with the mean material properties provided in [87]. The deck mass density (per unit length) is considered and assigned to each element for the determination of the lumped mass matrix.

5.2.2 Pier modeling

In the adopted modelling approach the bridge inelasticity is considered solely for pier elements and FP isolator devices. Accordingly, two Euler-Bernoulli fiber-section, force-based beam-column elements [92] are used for each pier (Figure 5.4 a).

Geometric nonlinearity is included in the pier elements model via *P-Delta* effects.

This kind of element permits the definition of a detailed fiber-section that can be discretized into unconfined concrete fibers, confined concrete fibers and individual fibers to model each of the steel reinforcing bars. Specifically, for the adopted fiber-section, 90 fibers are used for the steel reinforcing bars, whereas the confined area is discretized into 200 fibers (Figure 5.4 b).

The behavior of concrete fibers is defined using *Concrete 02* [93] material in *Opensees* that implements a uniaxial Kent-Scott-Park [94] concrete material with the addition of a tensile stress strength and a linear tension softening behavior (Figure 5.4 d). In the case of the unconfined concrete, the mean compressive strength is equal to $f_c = 29.1 MPa$ and the corresponding strain is equal to $\varepsilon_c = 0.002$. According to the *Concrete 02* material definition, the initial slope in compression is equal to:

$$E_c = 2 f_c / \varepsilon_c \tag{5.1}$$

The concrete unconfined compressive strength at crushing f_u is assumed equal to $0.2 f_c = 5.82 MPa$ whereas the concrete unconfined crushing strain is set equal to $\varepsilon_u = 0.006$.

The parameter λ required in the *Concrete 02* material definition that refers to the unloading and reloading loops in compression is set equal to a value of 0.1.

As far as the concrete tensile strength is concerned, it is calculated using the relation proposed by Collins and Mitchell in 1991 [95]:

$$f_{ct} = 0.56\sqrt{f_c} \tag{5.2}$$

The stiffness E_{ts} of the tension softening branch is approximately equal to the concrete tensile strength divided by the strain at which zero stress is reached in

tension. The latter is assumed equal to the strain ε_c at which the maximum compressive strength is reached, equal to 0.002.

In the case of confined concrete fibers, the mean compressive strength and strain is obtained by the following Eq.s (5.9-(5.4):

$$f_{cc} = k_{fc,Mander} \cdot f_c \tag{5.3}$$

$$\varepsilon_{cc} = k_{fc,Mander} \cdot \varepsilon_c \tag{5.4}$$

Where $k_{fc,Mander}$ is the amplification factor proposed by Mander in 1988 [96] to take into account the confinement effect on the concrete stress-strain response. SpecificallyIt is equal to:

$$k_{fc,Mander} = \left(2.254\sqrt{1+7.94\frac{f_e}{f_c}} - 2\frac{f_e}{f_c} - 1.254 \right) \tag{5.5}$$

Where f_e is the confining pressure which can be obtained as:

$$f_e = 0.5 k_e \rho_v f_{yh} \tag{5.6}$$

In which f_{yh} is the yield strength of transverse reinforcements and k_e is the so-called confinement effectiveness coefficient calculated as per Eq. (5.7):

$$k_e = \left(1 - \frac{s_h}{2D_0} \right)^2 \cdot \left(1 - \frac{A_{sl}}{\pi D_0^2 / 4} \right) \tag{5.7}$$

With D_0 being the concrete core diameter, s_h the spacing of transverse reinforcements and A_{sl} the total area of longitudinal reinforcements.

As far as ρ_v is concerned, it is the ratio of the volume of transverse reinforcements to the volume of confined concrete core (Eq. (5.8)):

$$\rho_s = \frac{A_{sh} \cdot \pi \cdot D_0}{\frac{\pi}{4} \cdot D_0^2 \cdot s_h} = \frac{4A_{sh}}{D_0 \cdot s_h} \tag{5.8}$$

Regarding the material definition for the steel fibers, a uniaxial stress-strain law (*Steel01* in *Opensees*) is selected for modeling both the longitudinal and trasnverse reinforcements (Figure 5.4 c). In the material definition, the yield strength has a value $f_y = 420MPa$, with an initial elastic tangent stiffness equal to $E_s = 200000MPa$ and a strain-hardening ratio $b = 0.001$. The ultimate strain is limited to 0.1 through the *MinMax Opensees* material, as recommended by Prestley [97].

When it comes to the quadrature rule adopted in the force-based formulation, considering that the commonly used *Gauss-Lobatto* beam integration scheme can lead to a loss of objectivity in the case of softening section behavior (the element response is not unique as it depends on the number of integration points) [98] in this study the modified two-point *Gauss-Radau* integration scheme [99] is preferred for the pier mathematical model definition. According to this model, the integration points location and weight are the following:

$$\begin{aligned} \xi &= \left\{0, 8l_{pI}/3, L-8l_{pJ}/3, L\right\} \\ \omega &= \left\{l_{pI}, 3l_{pI}, 3l_{pJ}, l_{pJ}\right\} \end{aligned} \tag{5.9}$$

Where l_{pI} and l_{pJ} are the plastic hinge lengths at the element ends I and J, that are the regions where the plastic behavior is assumed to be confined.

With the adopted two-point modified *Gauss-Radau* integration scheme it is possible to integrate exactly linear curvature distributions and the characteristic length for softening plastic hinges is equal to the model-related plastic hinge length.

It is worth pointing out that within the context of the two-point modified *Gauss-Radau* quadrature rule, for the interior element it is used the same inelastic fiber section adopted for the plastic hinge regions.

Plastic hinge length is specified according to the empirically validated relation given in Eq. (5.10) as proposed by Paulay and Priestley in 1992 [100]:

$$L_p = 0.08L + L_{sp} \ \ (kN, mm) \tag{5.10}$$

Being $L_{sp} = 0.022 f_y d_l$ the strain penetration length and f_y, d_l respectively the yield strength and diameter of the longitudinal reinforcement bars, whereas L= length of the member.

A further modeling detail is represented by the rigid element attached to the top node of the force-based beam-column element. This is done with the scope of modeling the portion of the pier embedded in the cap beam and has a length equal to the distance between the cap-beam centroid and the pier top (Figure 5.4 a).

The pier mass density (per unit length) is considered and assigned to each element for the determination of the lumped mass matrix.

In (Figure 5.5-Figure 5.6) the moment-curvature relation is calculated according to the previously defined pier section mechanical properties. Coherently with a moment-curvature analysis, the axial force P acting on each pier is retrieved employing a linear elastic static analysis under gravity load.

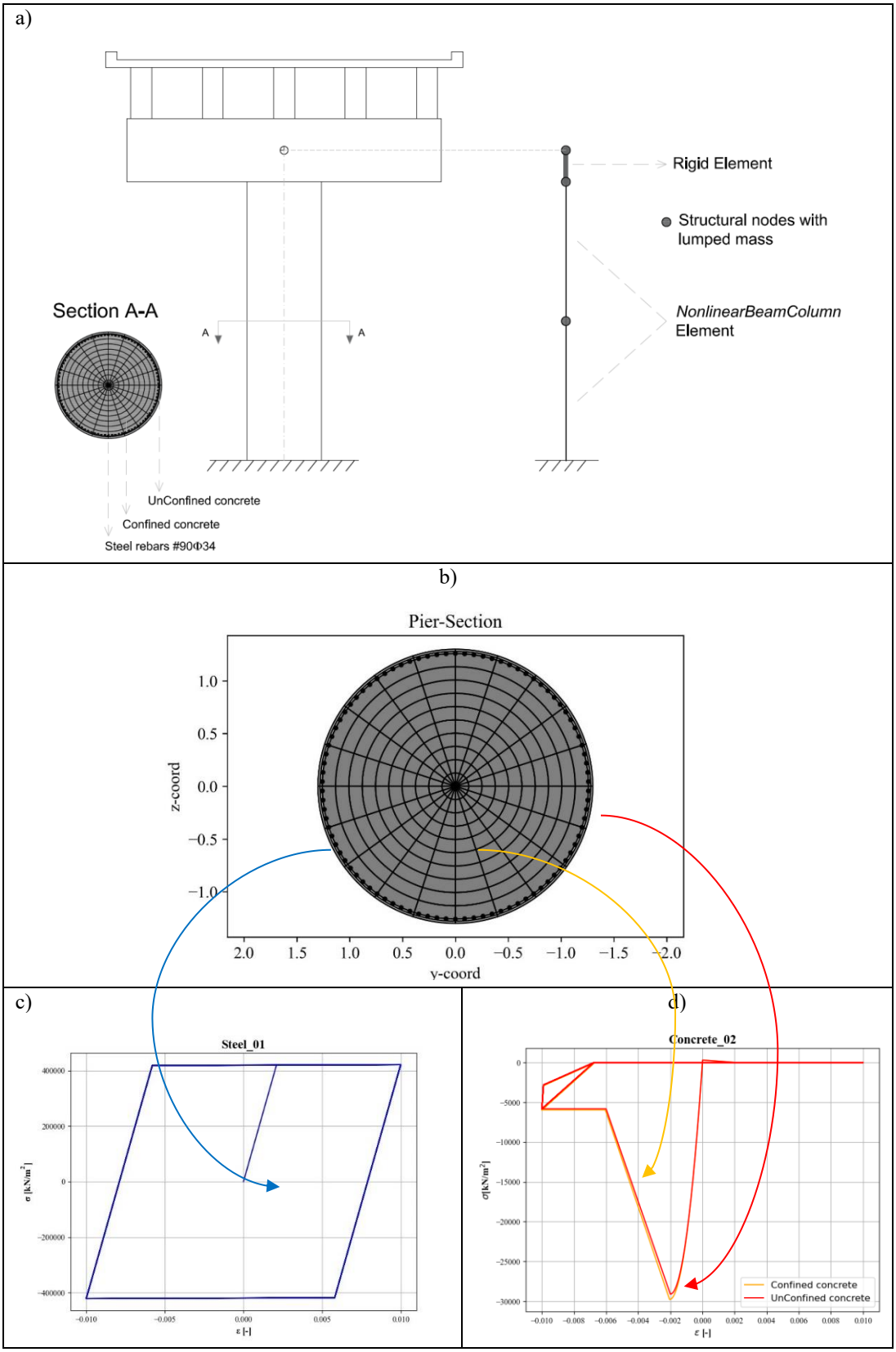

Figure 5.4. Bridge column model: a) Modelling details; b) pier section fiber discretization; c) Material hysteretic stress-strain law for reinforcing steel fibers; d) Material hysteretic stress-strain laws for unconfined (red) and confined (orange) concrete fibers.

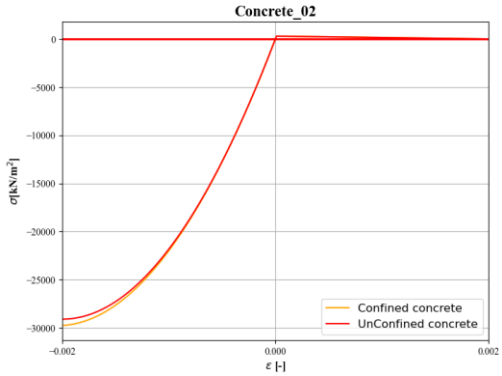

Figure 5.5. Tensile branch detail of the unconfined (red) and confined (orange) concrete fibers.

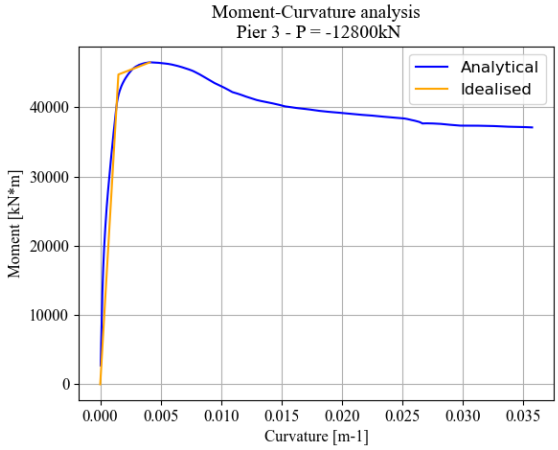

Figure 5.6. Moment curvature analysis for Pier #3 section.

5.2.3 Abutment modeling

The abutment modeling approach is consistent with Caltrans guidelines and recommendations [101]. Accordingly, they are considered to contribute to the bridge stiffness in both longitudinal and transverse directions.

In detail, the abutment resistance in the longitudinal direction is provided by the passive earth pressure offered by both embankment fill-backwall interaction and piles-soil interaction. On the other hand, it is assumed that if the abutment is pulled away from the backfill soil, no resistance is offered, meaning that no active soil pressure is taken into account. Therefore, in the active direction the sole contribution is the one provided by piles.

In the transverse direction it is assumed that the stiffness is coming from the backfill-wingwall and piles-soil interaction resistance.

In the bridge numerical model (Figure 5.3), the abutment/soil interaction at the two bridge endpoints in both longitudinal and transverse direction is modeled through the adoption of a *ZeroLength* element in *Opensees* connected to each deck end at one extreme, and fully restrained at the other. The piles-soil interaction and the abutment backwall/abutment wingwall-soil interaction are

assumed to act as springs in parallel both in the longitudinal and in the transverse direction and as so, assigned separately to the *ZeroLength* element. To model this double parallel spring interaction, a *parallel* uniaxial material in *Opensees* is assigned to each one of the two springs with the scope of considering in each direction the contribution offered from piles and from the abutment components (backwall and wingwall).

The abutment backwall-soil interaction is accounted for using an elastic perfectly plastic backbone curve with zero tension strength, *i.e. ElasticPPGap* material in *Opensees* with zero compression gap. The stiffness and the ultimate strength needed for the material definition are obtained according to the guidelines provided by Caltrans [101] and expressed in the following two Eq.s:

$$k_{abut/backwall-soil} = w_{backwall} \cdot (5.5 \cdot h_{backwall} + 20) \cdot R_{sk} \quad (kips/in) \tag{5.11}$$

$$F_{abut/backwall-soil} = w_{backwall} \cdot (\frac{5.5 \cdot h^{2.5}_{backwall}}{1 + 2.37 h_{backwall}}) \cdot R_{sk} \quad (kips) \tag{5.12}$$

Where $w_{backwall}$, $h_{backwall}$ are respectively width and height of the abutment backwall, with $h_{backwall}$ having a lower boundary of 2ft and an upper boundary of 10ft. The third term, R_{sk}, is the skew reduction factor given by Eq. (5.13):

$$R_{sk} = e^{-\vartheta_{sk}/45} \text{ with } \vartheta_{sk} \le 66° \tag{5.13}$$

Where ϑ_{sk} is the skew angle, equal to zero for the testbed isolated bridge.

According to the geometrical features of the testbed bridge abutments ($w_{backwall} = 12.0mt$ and $h_{backwall} = 3.5mt$), the backwall-soil stiffness and ultimate strength calculated according to Eq.s (5.11-(5.12) are respectively equal to $k_{abut/backwall-soil} = 517106 \ kN/m$ and $F_{abut/backwall-soil} = 12331kN$.

As far as the transverse direction is concerned, to the abutment wingwall-soil interaction is assigned an elastic perfectly plastic backbone curve. Stiffness and strength are computed starting from the corresponding ones in longitudinal direction $k_{abut/backwall-soil}$ and $F_{abut/backwall-soil}$, properly modified using factors corresponding to wall effectiveness ($C_L = 2/3$) and participation coefficients ($C_w = 4/3$) according to Maroney and Chai [102] assuming the wingwall length being 50% of the backwall width. As such, an *ElasticPP* material in *Opensees* is selected for the transverse direction with stiffness and ultimate strength given by Eqs. (5.14(5.15):

$$k_{abut/wingwall-soil} = c_L \cdot c_w \cdot 0.5 \cdot k_{abut/backwall-soil} \tag{5.14}$$

$$F_{abut/wingwall-soil} = c_L \cdot c_w \cdot 0.5 \cdot F_{abut/backwall-soil} \tag{5.15}$$

and respectively equal to $229824kN/m$ and $5480kN$. This time, for the transverse direction, the backbone curve is defined both in tension and compression.

As noted before, the abutment piles are assumed to act in either the active or passive direction. Again an *ElasticPP* material in *Opensees* is used and the recommendations from Caltrans [101] of using 40 kip/in/pile for the pile stiffness denoted as $k_{pile-soil}$, and an ultimate strength value of 199kN/pile are followed.

a)

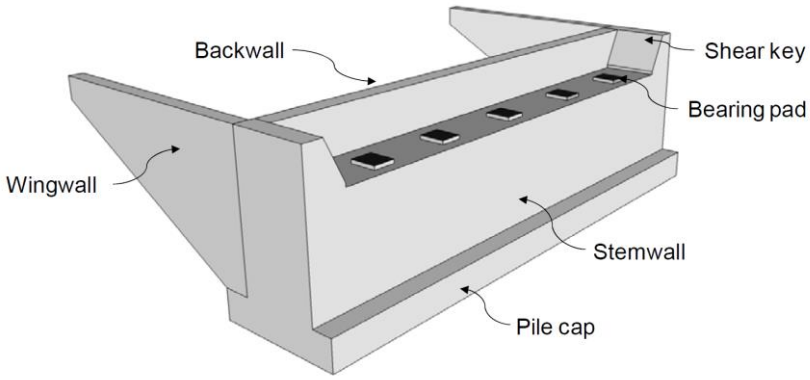

b)

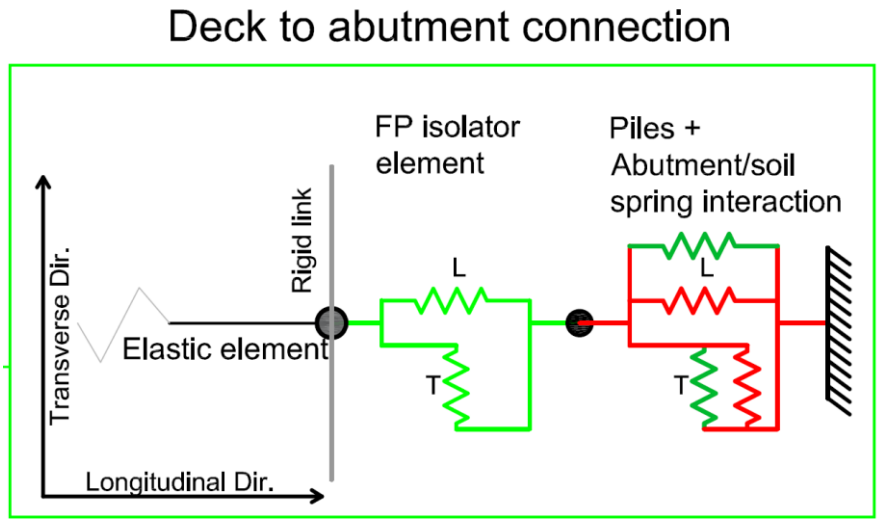

Figure 5.7 Geometry of a typical seat-type abutment a); abutment numerical modeling b).

5.2.4 Friction pendulum isolator modeling

Regarding the friction pendulum isolator elements, as previoulsy mentioned they are introduced in place of the elastomeric bearings to seismically isolate the bridge. Five FPS are modeled both at the cap beams and at the two abutments.

The numerical model of such elements has been implemented by adopting the built-in *SingleFrictionPendulumBearing* element from the *Opensees* library (Figure 5.10). According to the element definition, the i-node represents the concave sliding surface and the j-node the articulated slider. In a 3D space, the

isolator definition assumes a shear force-deformation relationship both in the longitudinal direction and in the transverse direction. Along the vertical direction, in order to capture the uplift behavior an *Elastic-NoTension* material in *Opensees* is adopted. In addition, three *Elastic Uniaxial Material* are properly defined to model the moments along longitudinal and transverse directions (flexural moments) and along the vertical direction (torsional moment). Specifically, a very low value of 1kN is assigned to the initial elastic stiffness in order to describe the mechanical behavior of the friction pendulum isolators with no flexural resistance.

The distance between i-node and j-node coincides with the isolator's height and is assumed equal to 25cm [103]. In order to fully define the shear-deformation behavior of the isolator element it is necessary to enter the initial elastic stiffness k_{init} and the effective radius of curvature R of the concave sliding surface.

Additionally, an appropriate sliding-friction model must be provided. As specified in §3.2.3, this model could be assumed to follow a velocity-dependent law based on the value of the friction coefficient at high velocities $f_{\max}$ and at low velocities $f_{\min}$ [80].

The initial elastic stiffness along the two horizontal directions is defined as follows:

$$k_{init} = \frac{f \cdot W_{iso}}{d_y} \tag{5.16}$$

Where f is the friction coefficient evaluated accordingly to the adopted velocity-dependent model, W_{iso} is the weight acting on the single isolator and d_y is the FPS displacement at which the isolator changes its behavior from a friction dependent law to a pendulum dependent law; in this study d_y is assumed equal to 1mm.

A typical force-deformation response along the longitudinal direction of the testbed bridge is provided in Figure 5.8-Figure 5.9 for an FPS with a Radius of curvature R of respectively 1.0m ($T_1 = 2\,\text{sec}$) and 4.0m ($T_1 = 4\,\text{sec}$).

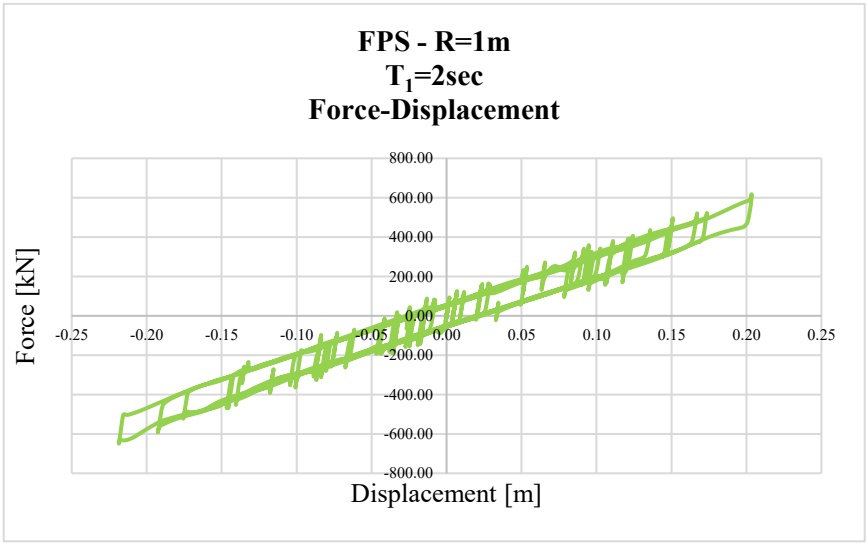

Figure 5.8. FPS Force-Displacement relationship for R=1m.

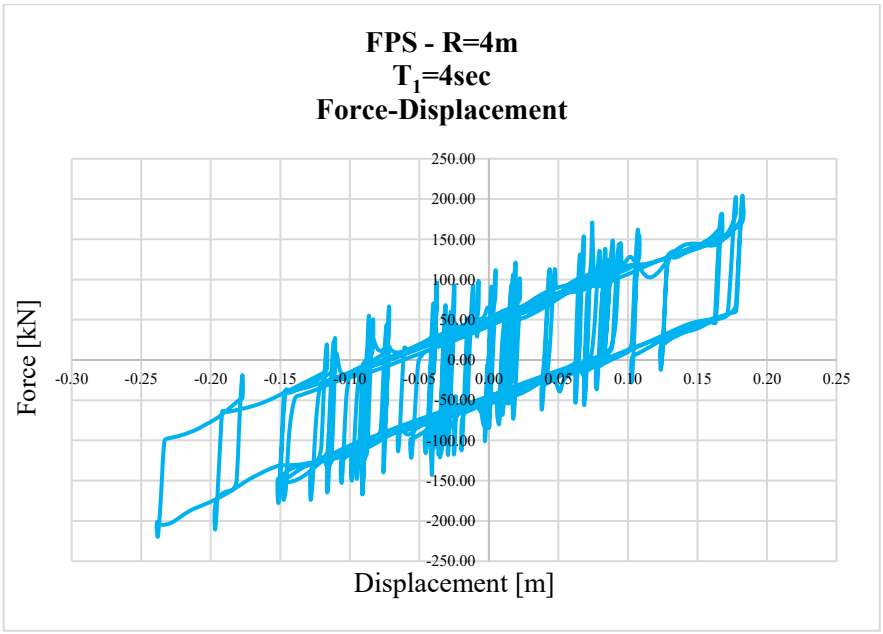

Figure 5.9. FPS Force-Displacement relationship for R=4m.

Regarding the isolator connection with the rest of the bridge components, a distinction needs to be made between isolators at the cap beams and those at the abutments. At the cap beam, the j-node of each isolator is connected to the end of the deck span by means of five rigid links (Figure 5.11). Meanwhile, at the abutments, an additional rigid link connection between the i-node and the non-restrained extreme of the abutment spring is provided. This kind of modeling approach assumes that the isolator stiffness along transverse and longitudinal directions are in series with the abutment/soil springs as illustrated in detail in (Figure 5.12).

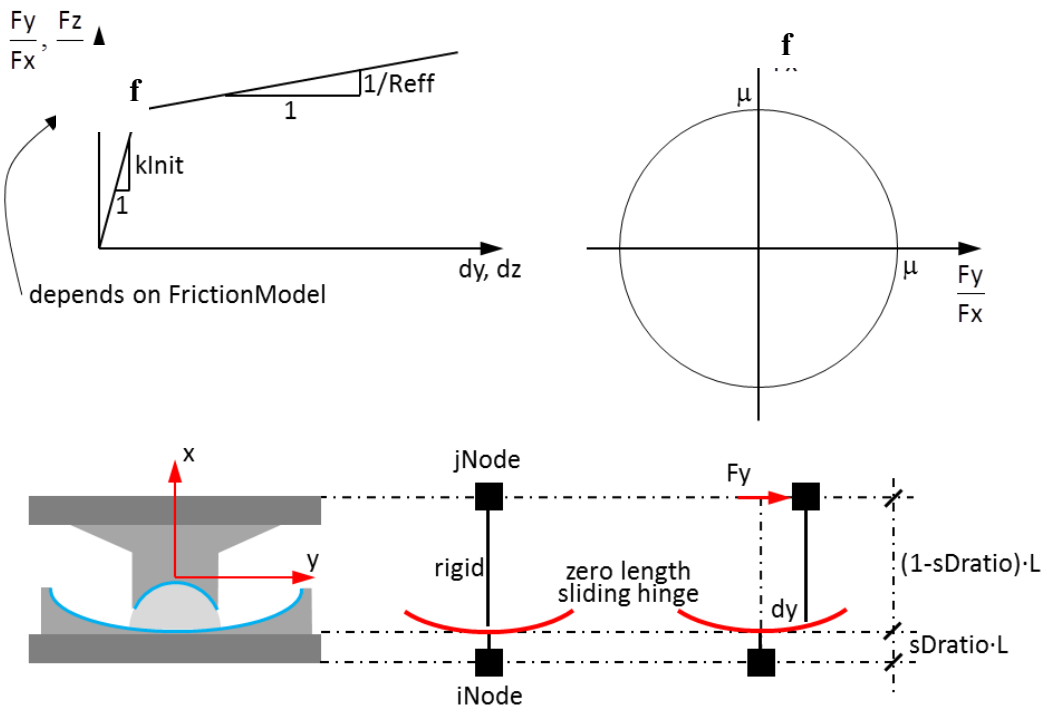

Figure 5.10. FPS isolator object in *Opensees* (Figure taken from OpenseesWiki).

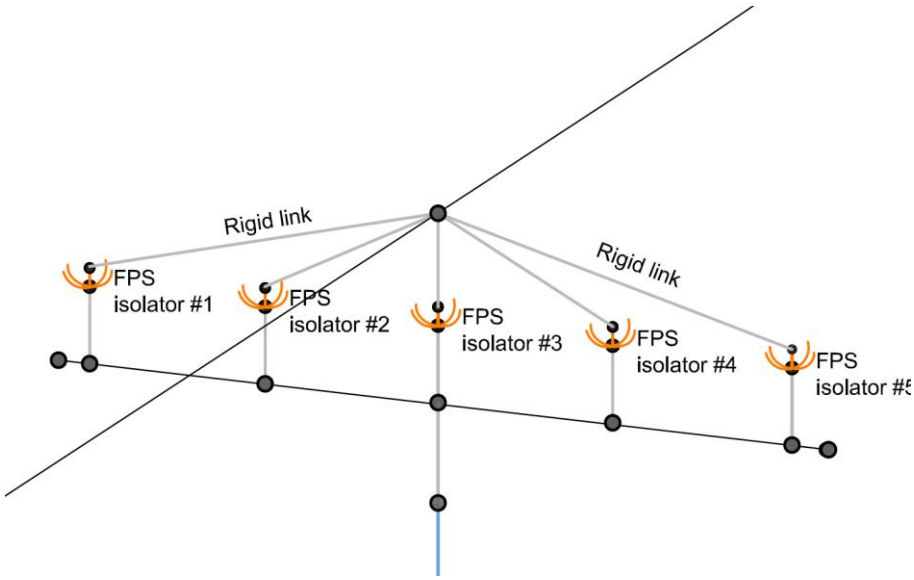

Figure 5.11. FPS isolator modeling details at the generic cap beam.

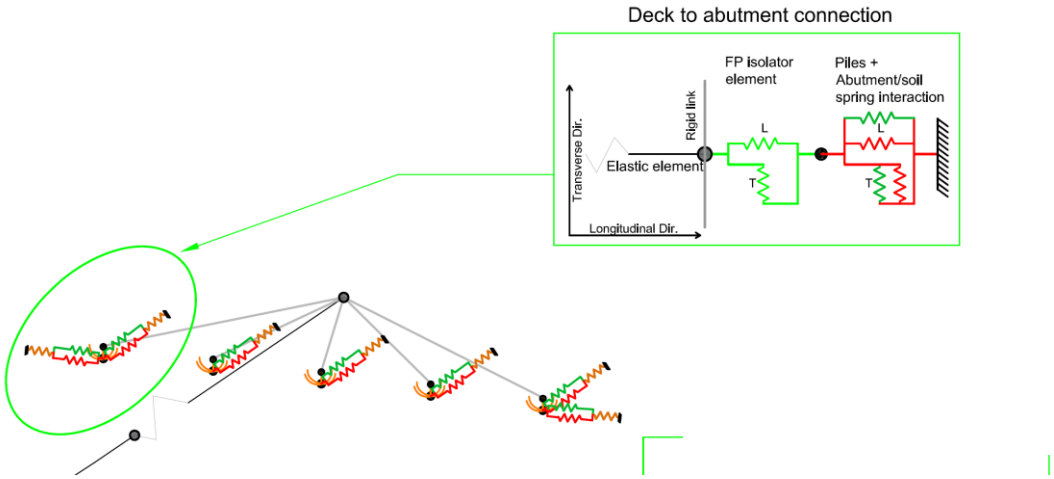

Figure 5.12. FPS isolator modeling details at the abutments.

5.2.5 Modal analysis

After defining the bridge model and completing the static analysis under gravitational loads, a modal analysis is performed to derive eigenvectors and eigenperiods.

The natural periods and frequencies for the 5-span testbed isolated bridge with R=1m ($T_1 = 2\,\text{sec}$), are summarized in Table 5.1 with the first three mode shapes shown in Figure 5.13. The first mode is along the transverse direction (Global axis Y), the second mode is along the longitudinal direction (Global axis X) whereas the third mode is a torsional mode.

Mode	**Modal participation masses [%]**	**Natural period (sec)**	**Natural Frequency (Hz)**
1	85.367	0.849	1.177
2	91.634	0.70	1.427
3	92.885	0.58	1.1719

Table 5.1. Natural periods and frequencies for the testbed bridge, with R=1m ($T_1 = 2\,\text{sec}$).

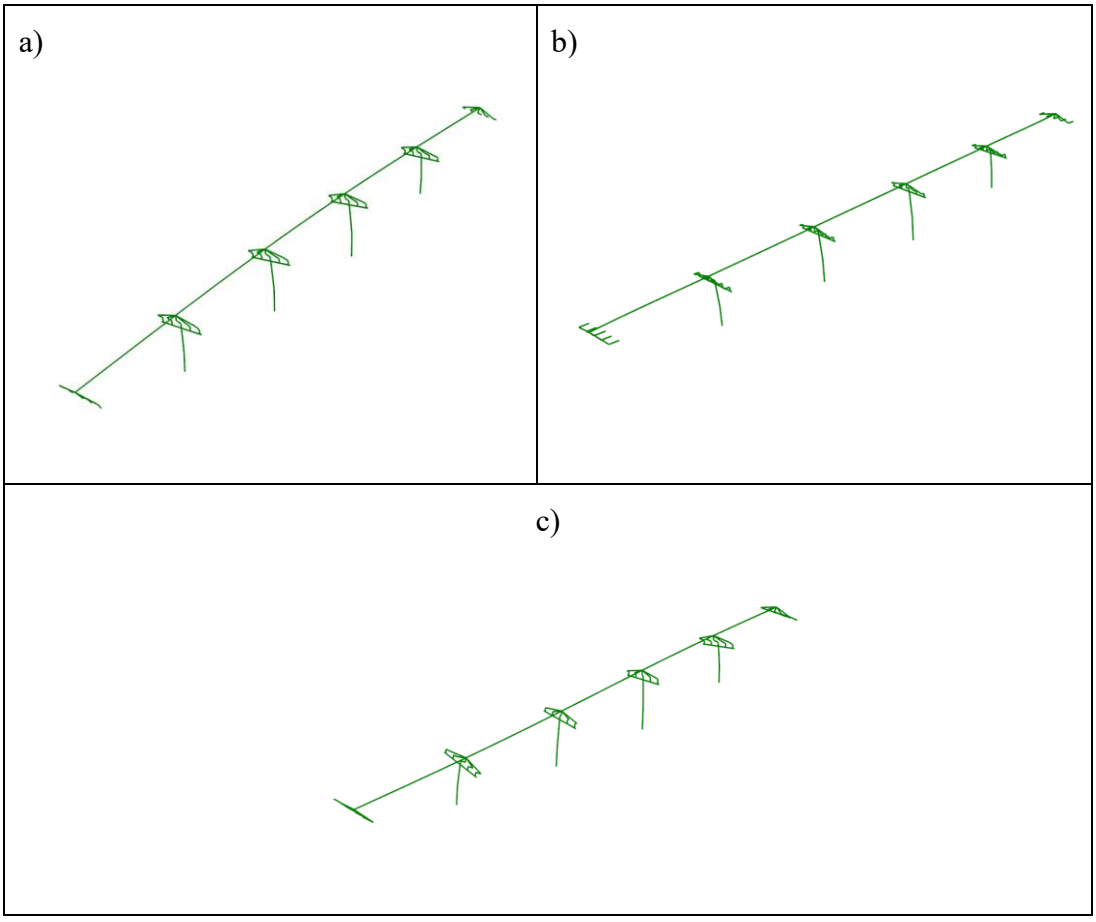

Figure 5.13. Mode shapes for the testbed isolated bridge, with R=1m (T_1=2sec): first mode a); second mode b); third mode c).

5.3 Parametric analysis

Since the main goal of this work of thesis is to assess the seismic response of bridges equipped with FPS considering spatial variability of earthquake ground motion, the same testbed isolated bridge described above is considered with a larger number of spans (*i.e.*, 7 spans). In addition, the most influential properties of the friction pendulum isolators (*i.e.*, radius of curvature and friction coefficient) are treated as deterministic and random parameters, respectively.

5.3.1 Deterministic structural parameters

Two different overall lengths of the testbed bridge are considered: the existing 5-span, 163m long bridge and a longer 7-span bridge spanning a total length of 229m. In addition, three FPS isolation periods $T_1 = 2,3,4\,\text{sec}$ (*i.e.*, radii of curvature) are selected, resulting in a total of 6 bridge structural deterministic models with the aim of performing a comprehensive parametric analysis.

	5-Span	**7-Span**
BridgeID		
T_1=2sec	5SP-T_1=2sec	7SP-T_1=2sec
T_1=3sec	5SP-T_1=3sec	7SP-T_1=3sec
T_1=4sec	5SP-T_1=4sec	7SP-T_1=4sec

Table 5.2. Bridge model IDs.

5.3.1.1 Number of spans

It is well known that spatial variation of seismic ground motions particularly affects those bridges that extend over long distances, as their pier foundations are more likely to undergo earthquake with differences in amplitude and phase [52]. Considering this aspect, a second structural configuration of the testbed isolated bridge has been considered for the analysis by duplicating the fourth span with a length of 33.0m and its left-support pier (12.35m) twice, such as to obtain a 7-span isolated bridge with an overall length of 229m. This choice strikes a good balance between the model of a sufficiently longer bridge than the real one, to explore to what extent it is much more affected by SVEGM, and the time demanded by the generation of different artificial records at each bridge supports.

An extruded view of the so-modelled bridge in SAP2000 (as for the 5-span bridge the first-phase of the modeling procedure is the implementation in SAP2000) is shown in Figure 5.14 reporting also piers' dimension. Spans' dimension are detailed in Table 5.3.

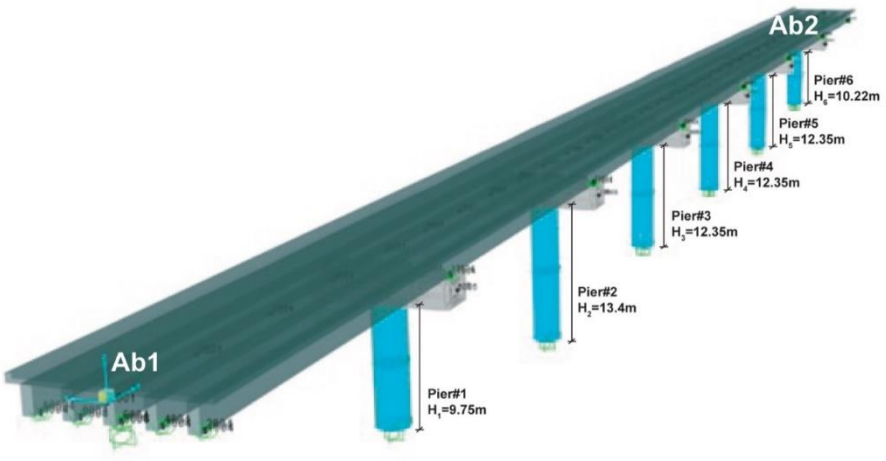

Figure 5.14. 7-Span bridge model - extrude view.

Span 1	Span 2	Span 3	Span 4	Span 5	Span 6	Span 7
32m	33m	33m	33m	33m	33m	32m

Table 5.3. 7-Span bridge dimensions – span lengths and pier heights.

5.3.1.2 FPS radius of curvature R

As already pointed out earlier, one of the key parameters of friction pendulum isolator is the radius of curvature of the sliding surface as it governs the isolated bridge period T_1 throughout the well-known expression $T_1 = 2\pi\sqrt{R/g}$.

It is straightforward that the radius of curvature is a key design parameter to reach the desired level of seismic isolation degree. In this study, three different values of the radius of curvature, meaning three different values of the isolation period are considered for both the 5-span and 7-span testbed bridge configurations considered for the analysis (Table 5.4):

R [m]	T_1 [sec]
1.0	2.0
2.25	3.0
4	4.0

Table 5.4. Radii of curvature of the FPS sliding surface and corresponding values of the isolation period used in the analysis for each bridge configuration.

5.3.2 Random parameters

The behavior of the FPS isolator is strongly influenced by the friction coefficient. As mentioned in §3.2.2 the friction phenomenon does not necessarily follow the Coulomb friction law (friction constant during sliding) but rather depends on several mechanisms that can influence its magnitude value such as pressure, temperature, and sliding velocity. Following the experimental results from Mokha *et al*. [38] and Constantinou *et al*. [39], in this study the sliding friction coefficient is assumed velocity-dependent, according to Eq. (3.67):

$$f = f_{\max} - (f_{\max} - f_{\min})e^{-\alpha|v|}$$

In this context, the maximum value of the friction coefficient $f_{\max}$ (*i.e.*, the friction coefficient related to large velocities) is assumed to be a random parameter due to the uncertainty in its statistical value especially under dynamic conditions as demonstrated in [38]- [39]. To model such uncertainty a standard normal distribution ranging from 2% to 8% is selected and 10 different samples of the friction coefficient $f_{\max}$ are extracted with the *Latin Hypercube Sampling Method* [29]. According to [21-22-80] the value α from Eq. (3.67) is set equal to $\alpha = 30$, whereas the friction coefficient at low velocities $f_{\min}$ is related to $f_{\max}$ via the following ratio: $\frac{f_{\max}}{f_{\min}} = 3$.

5.4 Seismic action

Following the procedure described in §4.5, thirty different realizations of multi-variate quasi-stationary and spectrum-compatible acceleration time histories $f_j^{(i)}(t)$, $j=1,2,...,6$, in the case of the 5-span, 6-supports bridge and $j=1,2,...,8$ for the 7-span, 8-supports bridge are generated according to Eq. (4.50).

As mentioned earlier in Chapter 4, the ensemble-averaged spectra of the thirty generated sample functions are matched according to the adopted procedure to the target elastic response spectra of L'Aquila (Italy). L'Aquila is selected as the reference site for the evaluation of the seismic hazard due to its proximity to the testbed bridge and its high seismicity. Particularly, following the april 6, 2009, L'Aquila Earthquake (M_w=6.3), this site has been extensively investigated in terms of geotechnical characterization. In this study the data collected by [105] are used given the absence of specific soil properties information at the bridge site [33]. Accordingly, a subsoil profile of Category B ($360m/s \le V_s \le 800m/s$) is assumed under each bridge piers.

Additionally, following the study by Lupoi [74] on isolated bridges accounting for spatial variability of ground motion, the soil beneath the abutments is assumed to be of Category A [77] ($V_s > 800m/s$). This assumption accounts for the third main cause of spatial variability: the difference in soil conditions between two different support points.

The elastic response spectra are then calculated for the site of L'Aquila and for two different soil categories (A and B) and the ensemble-averaged spectra of the thirty generated sample functions is matched to these spectra at each bridge supports (abutments and piers). Within the context of the PEER's PBEE methodology, the structural response under increasing intensity levels needs to be determined. To this purpose, 9 different Intensity Measure Levels (*IM*Ls) are considered according to NTC2018 [77], which correspond to a return period ranging from 30 years to 2475 years with a probability of exceedance in 50 years that goes from 81% to 2%. In Table 5.5 the nine values of PGA for the site of L'Aquila (outcrop stiff soil of category A) corresponding to the abovementioned nine different values of the return periods are reported:

T_R [yrs]	***POE* in 50 yrs [%]**	**PGA [g]**
2475	2	0.4526
975	5	0.3343
475	10	0.2610
201	22	0.1908
140	30	0.1640
101	39	0.1424
72	50	0.1226
50	63	0.1041
30	81	0.0789

Table 5.5. PGA values for the site of L'Aquila (soil A) for 9 IMLs.

Then, in (Figure 5.15) the Uniform Hazard Spectrum for the site of L'Aquila (soil A and $\xi = 2\%$) corresponding to nine different *IM*Ls according to the NTC2018 [77] are shown:

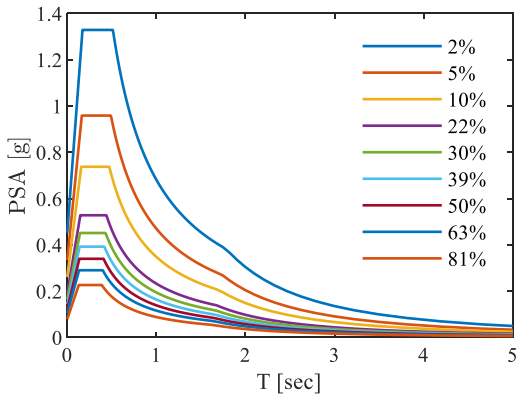

Figure 5.15. Uniform Hazard Spectrum for the site of L'Aquila (soil A) corresponding to nine return periods.

Once the acceleration time histories for each bridge support (abutments and piers) are generated including spatial variability effects and satisfying the spectrum compatibility for each return period and soil category, they are scaled such that their corresponding elastic spectrum is equal to the target spectral acceleration at the isolated bridge period and for the *i*-th intensity level $S^{i}_{a,target}(T_1)$, being $T_1 = 2,3,4\,\text{sec}$ and i=1:9. The spectral acceleration $S_a(\xi_1, T_1)$ at the isolation period T_1 and for the inherent damping ratio $\xi_1 = 2\%$ is chosen as intensity measure (*IM*) due to its characteristics of sufficiency, efficiency and scaling robustness [15]. The scaled response spectrum $S_a(\xi_1 = 2\%, T_1)$ for $T_1 = 2\,\text{sec}$ and $T_1 = 3\,\text{sec}$, for the thirty sample acceleration time histories generated at right abutment (Ab2) of the 7-span bridge (Figure 5.14) for the case of soil category A and for $T_R = 2475 yrs$ are presented in (Figure 5.16):

a) b)

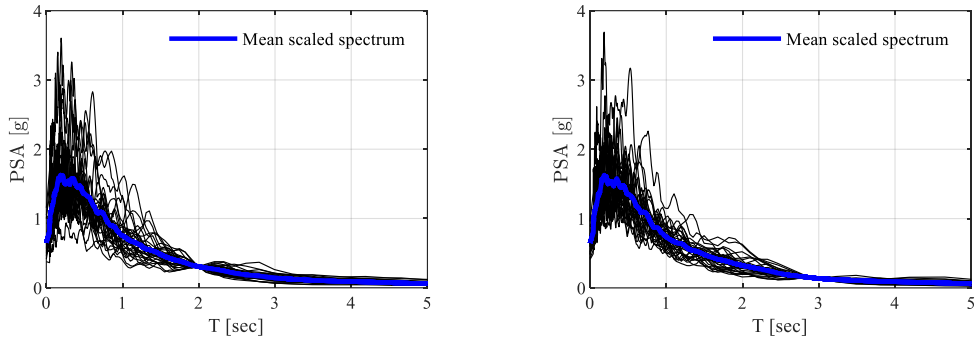

Figure 5.16. Generated time histories response spectrum (soil A and T_R=2475yrs) scaled to $S_a(T_1)$: response spectrum scaled to $S_a(\xi_1 = 2\%, T_1)$ with $T_1 = 2\,\mathrm{sec}$ a); response spectrum scaled to $S_a(\xi_1 = 2\%, T_1)$ with $T_1 = 3\,\mathrm{sec}$ b).

5.4.1 Incidence angle

In the proposed procedure, the acceleration time histories are supposed to be representative of a far-field ground motion characterized by a seismic waves front that arrives at the bridge site with a certain incidence angle that remains constant with respect to the different bridge supports (abutments and piers) as schematically drawn in Figure 5.17-Figure 5.18.

Two different incidence angles (i.a.) of 30° and 60° are assumed for the case of study and subsequentially two components of the seismic action along the longitudinal and transverse direction of the bridge are obtained by multiplying the generated acceleration time histories once for cos/sin (30°) and once for cos/sin (60°).

Summarizing, two different sets of analyses will be performed for each bridge structural configuration and isolation period, depending on the incidence angle (i.a.) considered (30° and 60°).

For an incidence angle equal to 30°, the seismic action results nearly aligned to the longitudinal bridge axis whereas a seismic action with an incidence angle of 60° is representative of a quasi-orthogonal acceleration time history.

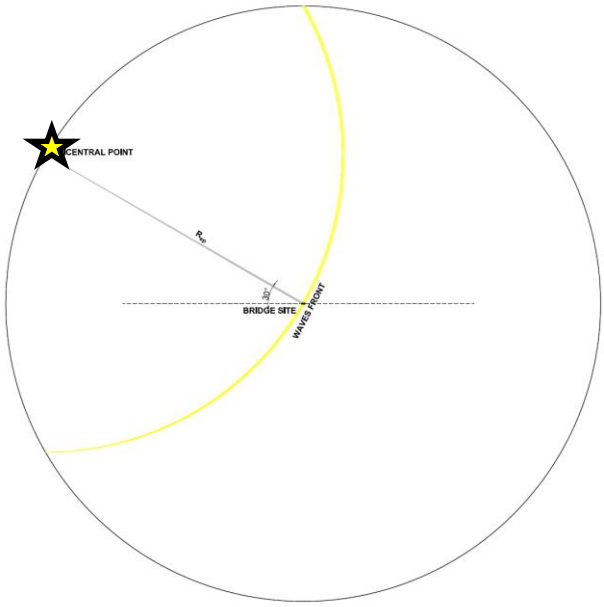

Figure 5.17. Seismic wave front for the case of an incidence angle (i.a.) = 30°.

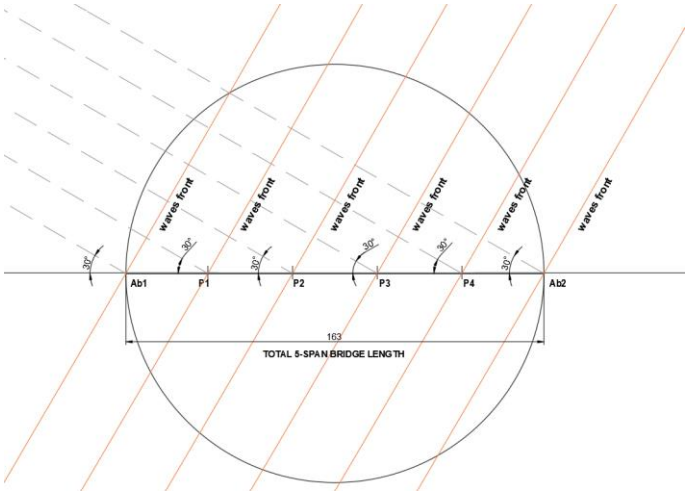

Figure 5.18. Seismic waves front for the case of an incidence angle (i.a.) = 30°.

5.4.2 Displacement time histories

In the analysis to be performed and following the recommendation from the *Opensees* manual, the multiple support excitation is applied to the different bridge supports in the form of displacement time histories; these are calculated from their respective acceleration time series by means of the necessary baseline correction (Figure 5.19).

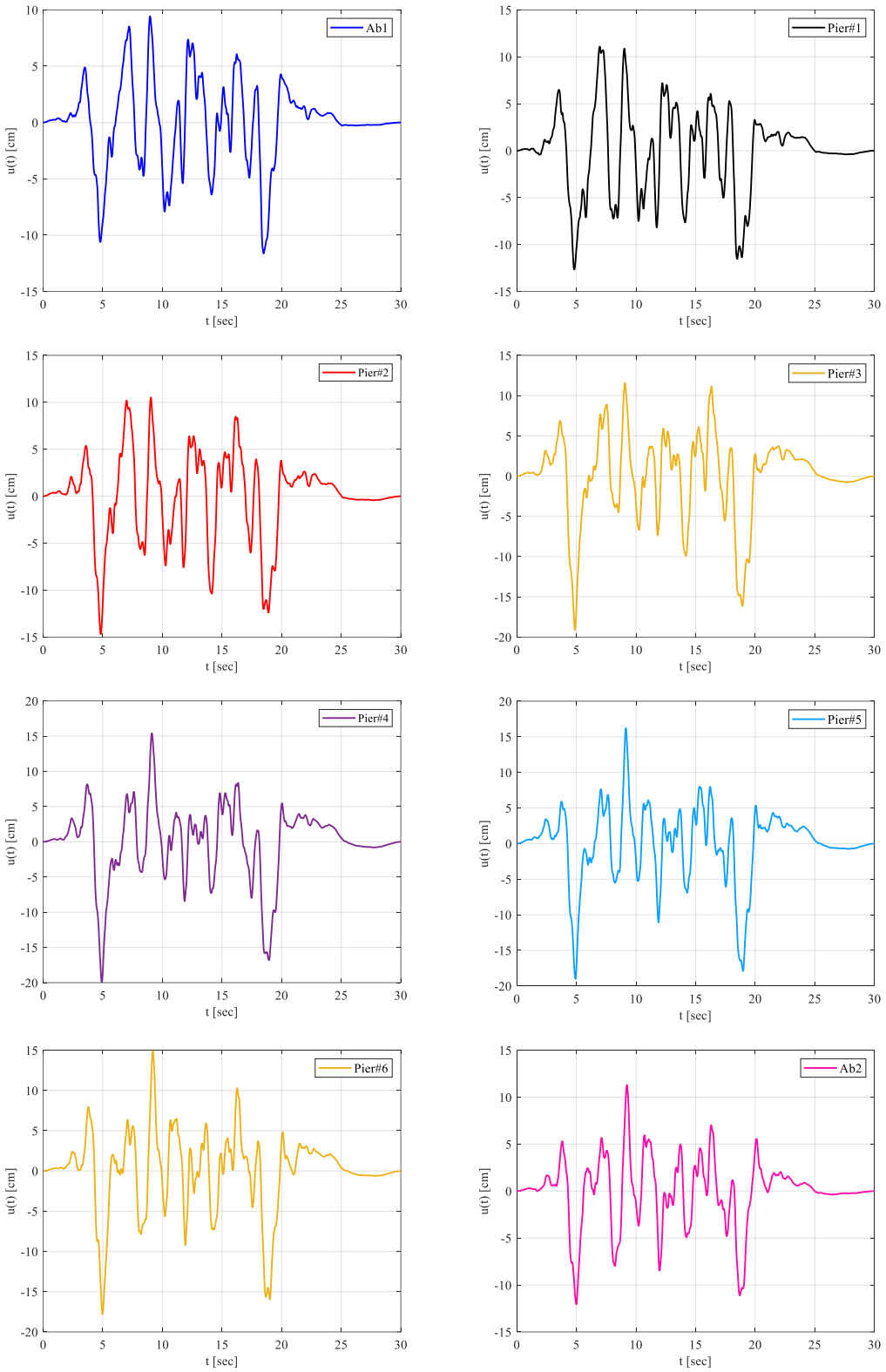

Figure 5.19. Displacement time histories at the eight supports of the 7-span bridge for T_1=2s and for a mean return period T_R=2475yrs.

In order to appreciate the combined effects of the three main causes that determine the spatial variability of ground motion along the bridge supports (*i.e.*, the loss of coherence, the time lag of the wave trains, and the local soil conditions), the 7-span bridge displacement time histories are plotted all together in Figure 5.20. Additionally,

Figure 5.21 to Figure 5.23 show the displacement time histories to highlight the time lag between different supports: Abutment 1-pier#1 (32m apart), pier#1-pier#6 (165m apart), and Abutment1 (Ab1)-Abutment2 (Ab2) (230m apart).

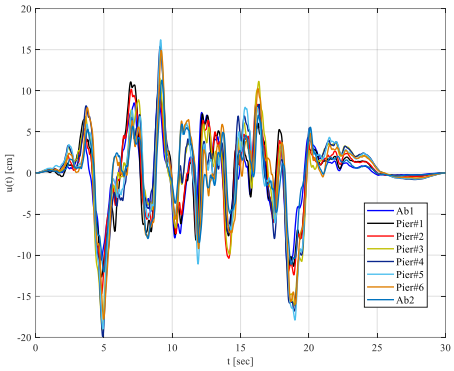

Figure 5.20. Displacement time histories at the eight supports of the 7-span bridge for T_1=2s and for a mean return period T_R=2475yrs.

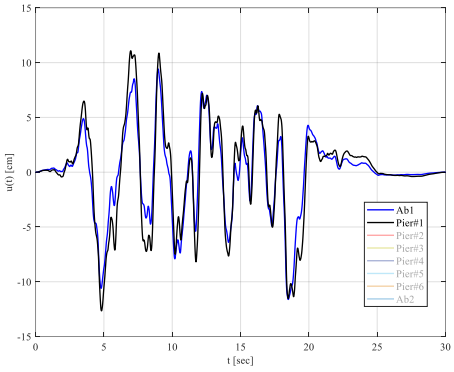

Figure 5.21. Displacement time histories at the Abutment 1 support and pier #1 support of the 7-span bridge for T_1=2s and for a mean return period T_R=2475yrs.

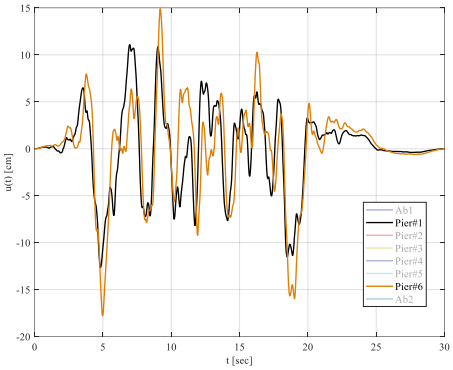

Figure 5.22. Displacement time histories at the pier #1 and pier #6 of the 7-span bridge for T_1=2s and for a mean return period T_R=2475yrs.

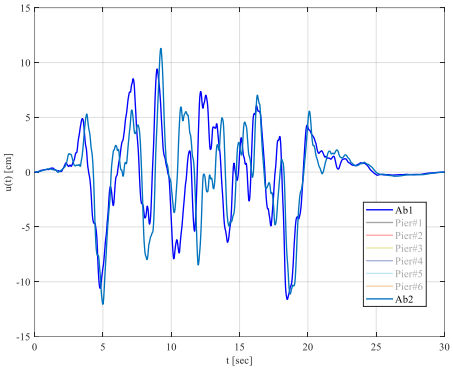

Figure 5.23. Displacement time histories at the Abutment 1 support and Abutment 2 support of the 7-span bridge for T_1=2s and for a mean return period T_R=2475yrs.

5.5 Multiple-support excitation in *Opensees*

Spatial variability of ground motion is implemented in *Opensees* through the *Multisupport Excitation* pattern that allows for similar or different ground motions to be applied to each constrained node (supports of the bridge structure). The pattern, differently from the mostly used *Uniform Excitation* one, requires the ground motion preferably be input as displacement ground motion rather than acceleration. Furthermore, in the case of *Multisupport Excitation* pattern the responses at the nodes are provided in terms of absolute values and not relative values as is the case of *Uniform Excitation.*

In more details, the *Multisupport Excitation* pattern depends on a series of additional commands required from *Opensees* that are the *Imposed motion command* and the *Ground Motion command.* The first one is used to specify the ground motion to be applied to each constrained node (supports of the bridge) whereas the second one is used to specify the ground motion time history.

In the case of study, for each analyzed testbed bridges, a *Multisupport Excitation* pattern is created where the *Imposed motion* command applies to the abutment and pier supports, that are enforced to move in the transverse and longitudinal direction according to the ground motion specified through the *Ground Motion command.* This ground motions refer to the time series along the longitudinal and transverse direction obtained as explained earlier for the two different incidence angles (i.a.).

In order to compare the response of the testbed bridges in the case of uniform excitation input motion, an additional scheme is employed. This scheme adopts the *Multisupport Excitation* pattern in *Opensees* as well, with the difference that the ground motion specified through the *Ground Motion command* is always the same for all the supports (abutments and piers) and specifically it is the one generated at the first left abutment (Ab1) either for the case of the 5-span testbed bridge or the 7-span one.

6 Seismic reliability analysis of isolated bridges equipped with FPS accounting for spatial variability of earthquake ground motion (SVEGM)

This chapter focuses on the seismic reliability assessment of two configurations of isolated bridges equipped with friction pendulum devices. It examines both 5-span and 7-span bridge configurations across three different isolation periods, analyzing their seismic response under both uniform input conditions and spatially variable earthquake ground motion (SVEGM). The friction coefficient is treated as a random variable in the analysis. To ensure convergence between the target response spectrum for the reference site of L'Aquila and the ensemble-averaged spectra derived from simulations, 30 ground motions are artificially generated for each bridge support station. Two different incidence angle conditions (30° and 60° relative to the bridge longitudinal axis) are also considered. The reliability assessment begins with the Incremental Dynamic Analysis (IDA), involving a total of 3600 tridimensional (3D) simulations for each of the 9 Intensity Measure Levels (IMLs) considered in the IDA. Engineering demand parameters (EDPs), chosen to evaluate the response statistics related to both bridge piers and bridge isolation system, are presented next. Subsequent steps in the seismic reliability estimation include the derivation of fragility curves for the bridge piers and friction pendulum devices, assuming different damage levels and limit state thresholds.

Finally, considering the seismic hazard curves at different isolation periods related to the reference site of L'Aquila (Italy), the seismic reliability of both bridge piers and friction pendulum devices is evaluated in the time frame of interest through the convolution integral between seismic fragility and seismic hazard.

Additionally, SRBD (Seismic Reliability-Based Design) abacuses are derived and proposed with a twofold objective:

c) to define the radius in plan of the FP bearings, accounting for both uniform excitation and spatial variability of earthquake ground motion (SVEGM), as a function of the bridge configuration, isolation period and expected reliability level.
d) To establish specific design safety factors for the seismic design of FP isolators adopted to retrofit conventional highway bridges, implicitly considering the adverse effects of SVEGM.

6.1 Nonlinear response time history analysis (NRHA)

Based on the deterministic structural parameters considered and presented in the previous chapter (*i.e.* number of spans and isolation periods) it follows that 6 different testbed bridges are properly defined by combining two different structural configurations (*i.e.* bridge with different number of spans) with three values of the radius of curvature (see Table 5.2). The response of the abovementioned six bridge structural models, considering 10 sampled values of the friction coefficient, using as input 30 simulated ground motions accounting for SVEGM, with two different incidence angle conditions, is computed. A total set of 3600 3D simulations (nonlinear response time history analysis [NRHA]) are specifically performed for each of the 9 *IM*Ls within the context of incremental dynamic parametric analysis (IDA) as will be detailed later.

In addition, the same set of 3600 simulations is carried out for the case of uniform excitation, assuming that the input ground motion coincides with the time history generated at the first bridge support, which is coincident with the first left abutment (Ab1). This approach allows for a direct comparison of the bridge response under uniform excitation and spatial variability of ground motion.

Nonlinear response time history analyses are performed in *Opensees* by means of a *transient analysis* that adopts an implicit time-stepping integration scheme as developed by Newmark in 1959 [106]. The method is second-order accurate and unconditionally stable if the constant average acceleration algorithm is used. Additionally, to solve the nonlinear equations of structural equilibrium the iteration algorithm of Krylov-Newton as proposed by [107] is used. At each analysis time step the convergence is checked via the norm of the displacement increment, with a tolerance of 1.0^{-8} m and 200 iterations per analysis step. The latter is performed at a time equal to 0.01 sec while the analysis duration is set equal to 30 sec, as much as the time length of the simulated ground motion time histories.

As far as the damping model is concerned, the classical proportional *Rayleigh damping* model is adopted in the analysis, which is a combination of mass proportional and stiffness proportional damping as per the following equation:

$$\underline{\underline{C}} = a_0 \underline{\underline{M}} + a_1 \underline{\underline{K}} \tag{6.1}$$

Where $\underline{\underline{C}}$, $\underline{\underline{M}}$ and $\underline{\underline{K}}$ are respectively the damping, mass and stiffness matrix of the bridge system and a_0, a_1 are two coefficients that can be determined once the damping ratios ξ_m and ξ_n have been assigned to two generic modes *m* and *n* with circular frequencies ω_m, ω_n through the following equation:

$$\begin{Bmatrix} a_0 \\ a_1 \end{Bmatrix} = 2\frac{\omega_m \omega_n}{\left(\omega_n^2 - \omega_m^2\right)} \begin{vmatrix} \omega_n & \omega_m \\ -\frac{1}{\omega_n} & \frac{1}{\omega_m} \end{vmatrix} \begin{Bmatrix} \xi_m \\ \xi_n \end{Bmatrix} \tag{6.2}$$

Finally, having determined the coefficients a_0, a_1 it is possible to evaluate the damping ξ_i at the i-*th* mode with circular frequency ω_i based on the relation presented below:

$$\xi_i = \frac{a_0}{2}\frac{1}{\omega_i} + \frac{a_1}{2}\omega_i \tag{6.3}$$

Eq. (6.3) shows how the damping coefficient according to the Rayleigh model is the sum of two terms, the first one is the mass-proportional term, which decreases as the circular frequency ω increases and the second one is the stiffness-proportional counterpart which increases linearly against frequency.

Nevertheless, following the approach proposed by [108] only the tangent-stiffness proportional damping is considered, as it seems to be a more realistic approach in the case of a system subjected to large inelasticity demand.

Given this assumption, in Eq. (6.3), only the stiffness-proportional term survives:

$$\xi_i = \frac{a_1}{2}\omega_i \tag{6.4}$$

The coefficient a_1 is calculated by inverting Eq. (6.4) assuming that an inherent viscous damping of 2% is assigned at the first vibration period of the isolated bridge.

6.2 Engineering Demand Parameters (EDPs)

Various response parameters are registered while running nonlinear analysis to quantify the damage at a bridge component level. These components include the abutments, deck, reinforced concrete piers, and friction pendulum (FP) isolators.

In more detail, the response of the FP bearings (five in total) placed at the two abutments and at each of the bridge cap beams is registered by computing the maximum in absolute terms of the relative displacement between the bearing j-node and the bearing i-node, $u_{b,\max} = \max_t\left(\left|u_b(t)\right|\right)$ (Figure 5.10), in both the

bridge longitudinal direction (X-direction) $u_{b,x,\max} = \max_t \left(\left| u_{b,x}(t) \right| \right)$ and transverse direction (Y-direction) $u_{b,y,\max} = \max_t \left(\left| u_{b,y}(t) \right| \right)$. In addition, the vectorial sum of X and Y displacements is calculated for each analysis time step through the following equation:

$$u_{b,vet}(t) = \sqrt{u_{b,x}^2(t) + u_{b,y}^2(t)} \tag{6.5}$$

The maximum vector displacement over time $u_{b,vet,\max} = \max_t \left(u_{b,vet}(t) \right)$ is then registered and adopted as an additional demand parameter concerning the friction pendulum devices.

Moreover, only the maximum of the displacements $u_{b,x,\max}$, $u_{b,y,\max}$ and $u_{b,vet,\max}$ among the five FP bearings placed at each bridge support (piers and abutments) is registered and assumed as an engineering demand parameter (EDP).

Regarding the bridge RC piers, the monitored response parameters encompass both element-level metrics (*i.e.*, pier drift ratio) and section-level metrics (*i.e.*, pier curvature ductility).

Specifically, the curvature ductility μ_φ of the pier section at the element base, which coincides with the integration point closest to the fully restrained node, is calculated during the nonlinear time history analysis. This parameter is calculated both in the longitudinal and transverse direction as for the following ratio:

$$\left(\mu_\varphi(t) \right)_{x,y} = \frac{\varphi(t)}{\varphi_y} = \frac{\left(\varphi(t) \right)_{x,y}}{\varphi_y} \tag{6.6}$$

Where $\varphi(t) = \left(\varphi(t) \right)_{x,y}$ is the section curvature in either the X-direction or Y-direction and φ_y is the reference nominal yield curvature defined as [109]:

$$\varphi_y = \frac{2.25\varepsilon_y}{D} \tag{6.7}$$

Where ε_y is the longitudinal steel reinforcement yield strain and *D* is the pier section diameter.

As for the case of the FPS displacements also the curvature ductility is registered as the maximum over time of the absolute value of the response:

$$\left(\mu_{\varphi,\max} \right)_{x,y} = \max_t \left(\left| \frac{\left(\varphi(t) \right)_{x,y}}{\varphi_y} \right| \right) \tag{6.8}$$

The curvature ductility in terms of the vectorial sum of the curvatures along the longitudinal and transverse directions is also retrieved using the following relation:

$$\mu_{\varphi,vet}(t) = \sqrt{\mu^2{}_{\varphi,x}(t) + \mu^2{}_{\varphi,y}(t)} \tag{6.9}$$

The maximum over time of this quantity is registered as a pier demand parameter:

$$\mu_{\varphi,vet,\max} = \max_t \left(\mu_{\varphi,vet}(t) \right) \tag{6.10}$$

In line with this approach, drift ratios in both longitudinal and transverse directions are monitored for each bridge pier. The drift ratios are registered as the maximum absolute value during the time history analysis:

$$(\delta_{\max})_{x,y} = \max_t \left(\left| \frac{\left(u_p(t)\right)_{x,y}}{H_i} \right| \right) \tag{6.11}$$

with $i = 1,..,N_{pier}$, being N_{pier} the number of piers.

The monitored response parameter $\left(u_p(t)\right)_{x,y}$ is the relative displacement between the pier top node and the pier bottom node, expressed as a function of time in either the X or Y direction. Meanwhile, H_i is the height of the i-*th* bridge piers, where i ranges from one to the number of piers N_{pier}, which is equal to four in the case of the 5-span bridge configuration and six in the case of the 7-span configuration.

The drift vectorial sum is again calculated as:

$$\delta_{vet}(t) = \sqrt{\delta^2{}_x(t) + \delta^2{}_y(t)} \tag{6.12}$$

The maximum value is then registered over time to be adopted as an additional pier demand parameter:

$$\delta_{vet,\max} = \max_t \left(\delta_{vet}(t) \right) \tag{6.13}$$

Other monitored response parameters are the maximum absolute values of the deck acceleration response over time, in both X and Y directions or in terms of the vectorial sum. The abutment spring forces and deformations are also monitored in the X and Y direction.

6.3 Incremental Dynamic Analysis (IDA)

The initial phase of seismic reliability assessment involves performing Incremental Dynamic Analysis (IDA) [10], where the structural response of the bridge system under consideration is evaluated across increasing *IM* levels (*IM*Ls). The results of the (IDA) can be summarized by reporting in a 2D plot, the structural response parametrized versus the seismic intensity level, (*i.e.*, IDA curves).

In this study, regarding the reference site of L'Aquila (Italy), for a soil category A [77], the spectral displacement $S_d(\xi_1, T_1)$ at the isolation period T_1 and for the inherent damping ratio $\xi_1 = 2\%$ is assumed as intensity measure (*IM*). Since in the implemented parametric analysis three different isolation periods are considered as a function of the FPS radius of curvature *R*, the following *IM*= $S_d(\xi_1, T_1)$, with $\xi_1 = 2\%$ and $T_1 = 2,3,4$ sec, are considered:

	*IM*L$_1$	*IM*L$_2$	*IM*L$_3$	*IM*L$_4$	*IM*L$_5$	*IM*L$_6$	*IM*L$_7$	*IM*L$_8$	*IM*L$_9$
$S_d(\xi_1, T_1 = 2\,\text{sec})$	0.04	0.057	0.069	0.0813	0.096	0.1156	0.173	0.234	0.339
$S_d(\xi_1, T_1 = 3\,\text{sec})$	0.042	0.058	0.072	0.088	0.109	0.137	0.23	0.344	0.51
$S_d(\xi_1, T_1 = 4\,\text{sec})$	0.038	0.053	0.065	0.08	0.099	0.124	0.21	0.312	0.57

Table 6.1. $S_d(\xi_1, T_1)$ *IM* values for the adopted *IM*Ls and isolation period T_1.

The intensity measure levels (*IM*Ls) reported in Table 6.1 are assumed coherently with the NTC2018 [77] corresponding to a mean return period ranging between 30 and 2475 years, as already reported in Table 5.5.

After performing incremental dynamic analysis (IDA) according to the nonlinear time history analysis specifications, cartesian planes are constructed for each of the abovementioned engineering demand parameters (EDPs). These cartesian planes illustrate the relationship between the pertinent intensity measure (*IM*) values on the horizontal axis and the corresponding values of the Engineering Demand Parameters (EDPs) on the vertical axis. They depict the bridge structural response, depending on the isolation period and bridge configuration as well as on the ground motion scenario, including the two ground motion incidence angles and considering both spatial variability of earthquake ground motion and uniform.

Among the Engineering Demand Parameters (EDPs) presented in the previous section, only the results in terms of vectorial sum ($u_{b,vet,\max}$, $\mu_{\varphi,vet,\max}$, $\delta_{vet,\max}$) for the FPS bearings displacements, the piers section curvature ductility, and the piers drift ratio are further analyzed and used for the seismic fragility assessment of both bridge piers and FP isolators.

For a fixed value of the *IM* level and for the specific bridge structural model and earthquake ground motion scenario (uniform or spatially variable), 300 values of the monitored EDPs are obtained considering thirty simulated time histories combined with 10 sampled values of the friction coefficient; these points are

assumed to follow a lognormal distribution according to [111-112-113]. The assumption of lognormality is especially useful for seismic reliability assessment because it allows obtaining the response at different percentile levels even with a limited number of samples.

The lognormal distribution can be fitted to the assumed EDPs, $u_{b,vet,\max}$, $\mu_{\varphi,vet,\max}$, $\delta_{vet,\max}$, after estimating the sample geometric mean $GM(EDP)$, and the sample lognormal standard deviation $\sigma_{\ln}(EDP)$, or dispersion $\beta(EDP)$ defined as follows:

$$GM(EDP) = \sqrt{d_1 \cdot ..... \cdot d_N}^{N} \tag{6.14}$$

$$\beta(EDP) = \sqrt{\frac{\left(\ln d_1 - \ln[GM(EDP)\right)^2 + ... + \left(\ln d_N - \ln[GM(EDP)\right)^2}{N-1}} \tag{6.15}$$

Where d_i refers to the i-*th* sample value of the considered EDP while *N*=300 is the total number of samples.

The sample geometric mean *GM* serves as an estimator of the median of the structural response, and its logarithm coincides with the lognormal sample mean $\mu_{\ln}(EDP)$. Under the lognormality assumption, the relationship between *GM*, $\beta(EDP)$ and the k-*th* percentile [111] is expressed as:

$$d_k = GM(EDP)\exp[f(k)\beta(EDP)] \tag{6.16}$$

Being d_k the i-*th* sample value of the considered EDP at the k-*th* percentile and $f(k)$ is a function of the percentile itself that assumes the following values $f(50) = 0$, $f(84) = 1$, and $f(16) = -1$. The 84-*th* and 16-*th* percentiles are computed because indicate the dispersion of the results with respect to the 50-*th* percentile under the aforementioned lognormality assumption.

It is worth underlying that the following results from incremental dynamic analysis are presented without considering the collapse cases. Indeed, as will be discussed later, data characterized by dynamic collapses will be incorporated in the seismic fragility assessment.

Figure 6.1-Figure 6.3 show the IDA curves of the peak (absolute maximum) value of the vectorial sum for the piers drift ratio $\delta_{vet,\max}$, for the three isolation periods considered in the parametric analysis: $T_1 = 2,3,4$ sec. Each row is referred to a different bridge pier whereas the two columns include the response for an incidence angle (i.a.) of 30° (first column) and 60° (second column).

Each plot presents the IDA for the three percentiles (16-*th*,50-*th*,84-*th*) of the drift ratios, reporting a comparison between the two bridge structural configurations (7-span and 5-span) and for the case of uniform excitation and spatial variability of earthquake ground motion.

Figure 6.1 a) and b) display the IDA curves in terms of $\delta_{vet,\max}$ for an isolation period equal to $T_1 = 2\,\text{sec}$, corresponding to the first left pier, which has the lowest height (9.75m) among both the 5-span and 7-span configurations. These curves are shown for incidence angles of 30° and 60°, respectively.

The 50-*th* percentile of $\delta_{vet,\max}$ is approximately 0.7% at the highest *IM* level for an incidence angle of 30° and 0.65% for an incidence angle of 60°, in the case of spatially variable earthquake ground motion. Under the uniform ground motion input condition, the drift ratio $\delta_{vet,\max}$ is lower and specifically equal to 0.5% for both incidence angles.

On the other hand, the response is only slightly affected by the two structural configurations considered in the analysis, showing slightly greater drift ratios for the 5-span configuration at the highest intensity measure level and under the SVEGM condition. Conversely, the 7-span configuration exhibits higher drifts in the case of uniform excitation.

As expected, the dispersion increases with higher intensity measure levels, particularly noticeable under spatially variable earthquake ground motion (SVEGM), for both incidence angle conditions.

The presented results provide the opportunity to quantify the effect of the spatial variation of ground motion on current the EDP, $\delta_{vet,\max}$, in terms of the ratio $\rho_i^{\delta vet,\max}$ defined as follows:

$$\rho_i^{\Delta vet,\max} = \frac{\left(\max^{\delta vet,\max}{}_{asyn}\right)_i}{\left(\max^{\delta vet,\max}{}_{syn}\right)_i} \tag{6.17}$$

This ratio is defined for each bridge configuration, isolation period, incidence angle, and considering the specific pier.

Specifically, the numerator, $\max^{EDP}{}_{asyn}$, indicates the maximum of the response computed under spatial variability of earthquake ground motion, whereas $\max^{EDP}{}_{syn}$ at the denominator represents the corresponding quantity for the uniform excitation input.

For the case of $T_1 = 2\,\text{sec}$ and of pier 1 (height 9.75m), the maximum $\rho_i^{P1-\delta vet,\max}$ among the two structural configurations and the two incidence angles $\rho_{\max}^{P1-\delta vet,\max} = \max_i(\rho_i^{P1-\delta vet,\max})$ results equal to $\rho_{\max}^{P1-\delta vet,\max} = 1.344$.

Figure 6.1 c) and d) present the drift results $\delta_{vet,\max}$ for the highest pier of the two bridge structural configurations, which is pier 2 with a height of 13.4m. Consequently, the drift ratios are greater than those for pier 1, with a mean value for the SVEGM input condition of 0.85% and 0.73% for the uniform case at the highest IM level. These values are nearly the same for both incidence angles.

The response related to pier 2 does not differ at all between the 7-span and 5-span testbed bridge, with an overall trend that is similar also with respect to the incidence angle.

The maximum ratio $\rho_i^{\delta vet,\max}$ used to quantify the spatial variability effect on the drift response, for pier 2 is equal to $\rho_{\max}^{P2-\delta vet,\max}=1.22$.

The dispersion is higher under spatially variable earthquake ground motion (SVEGM) and for an incidence angle of 60°.

Figure 6.1 e) and f) depict the drift $\delta_{vet,\max}$ for pier 3, which is 12.35m high.

The 50-*th* percentile is equal to 0.87% for the SVEGM scenario combined with the 7-span bridge configuration and a 30° incidence angle. For the 5-span configuration under the same conditions, the corresponding drift is 0.78%. The spatial variability ground motion case for pier 3 presents slightly different results as the incidence angle changes: the drift is equal to 0.82% in the case of 60°, regardless of the number of spans. For the uniform excitation case, the drift results are not affected by the structural configuration and are equal to 0.67% for the two incidence angle conditions.

The maximum ratio $\rho_i^{\delta vet,\max}$ for pier 3 is equal to $\rho_{\max}^{P3-\delta vet,\max}=1.29$.

The dispersion is higher under spatially variable earthquake ground motion (SVEGM) and for an incidence angle of 30°.

Finally, figure 6.1 g) and h) refer to the rightmost pier in both structural configurations (pier 4/6) with a height of 10.22m.

The results for the 50-*th* percentile show a drift of 0.72% for spatially variable earthquake ground motion with a 30° incidence angle. The drift increases to 0.84% for an incidence angle of 60°.

Conversely, the drift results for the uniform input condition are nearly the same for both incidence angles and equal to 0.57%.

These results remain consistent for both the 5-span and 7-span bridges, independent of the seismic input condition or the incidence angle.

The maximum ratio $\rho_i^{\delta vet,\max}$ is equal for pier 4/6 to $\rho_{\max}^{P4/6-\delta vet,\max}=1.48$.

The overall trend observed in the incremental dynamic analysis, concerning the drift ratios vectorial sum related to an isolation period $T_1=2\sec$, manifests a pronounced nonlinear behavior with an upward concavity.

The difference between uniform and spatially variable ground motion can reach a value of $\rho_{\max}^{P4/6-\delta vet,\max}=1.48$, notably impacting the last bridge pier. In addition, the incidence angle slightly affects the results, either in terms of mean values or dispersion. An incidence angle of 60° exhibits results that are up to 1.15 times compared to those at an incidence angle of 30°, under spatial variability of earthquake ground motion.

Figure 6.2 presents the same results in terms of drift ratios vectorial sum $\delta_{vet,\max}$, for an isolated bridge period equal to $T_1=3\sec$.

Increasing the isolation period allows to reduce the drift ratios by two-thirds across all bridge piers as will be detailed below.

Figure 6.2 a) and b) present the drift vectorial sum results $\delta_{vet,\max}$ related to pier 1, with a height of 9.75m.

The drift ratios are equal to 0.25% for the SVEGM case and for both the incidence angles. In the case of uniform excitation, the drift ratios remain unaffected by the input incidence angle, and they result equal to 0.20%. The drift ratios exhibit the same trend as far as the structural configuration is concerned, with the 7-span bridge showing higher results only at the highest *IM* across all the input conditions (*i.e.*, incidence angle and earthquake ground motion scenario).

The maximum ratio $\rho_i^{\delta vet,\max}$ used to quantify the spatial variability effect on the drift response, for pier 1 and for an isolation period $T_1 = 3\,\text{sec}$ is equal to $\rho_{\max}^{P1-\delta vet,\max} = 1.35$.

Figure 6.2 c) and d) focus on pier 2. As previously mentioned, the drift results indicate a reduction compared to $T_1 = 2\,\text{sec}$. The peak of the response at the highest intensity measure is indeed equal to 0.50% for the SVEGM, 7-span, 30° incidence angle combination and equal to 0.40% for the 5-span bridge configuration under the same earthquake input conditions. Under uniform excitation condition, the drifts are equal to 0.35% for the 7-span bridge, 30° incidence angle combination, and to 0.29% for the 5-span bridge, 30° incidence angle combination. Similar results are observed for the 60° incidence angle condition, regardless of the bridge configuration, and for both input scenarios of uniform and spatially variable earthquake ground motion.

The maximum ratio $\rho_i^{\delta vet,\max}$ for pier 2 is equal to $\rho_{\max}^{P2-\delta vet,\max} = 1.40$.

The results associated with pier 3 are shown in Figure 6.2 e) and f) and can be compared to those for pier 2, although they are somewhat lower in magnitude.

The maximum ratio $\rho_i^{\delta vet,\max}$, for pier 3, is equal to $\rho_{\max}^{P3-\delta vet,\max} = 1.47$.

Figure 6.2 g) and h) pertain to pier 4 or 6 depending on the bridge configuration (5-span or 7-span). For the case of an isolation period $T_1 = 2\,\text{sec}$. This pier exhibits a trend nearly identical for both incidence angle conditions, with a drift of 0.29% at the highest *IM* level for the SVEGM, 7-span configuration and equal to 0.25% for the SVEGM, 5-span configuration. Under the uniform case, the drift decreases to 0.22% for the 7-span configuration and to 0.18% for the 5-span one.

The maximum ratio $\rho_i^{\delta vet,\max}$ is equal for pier 4/6 to $\rho_{\max}^{P4/6-\delta vet,\max} = 1.38$.

As the isolation period increases, dispersion also increases, with spatial variability of input ground motion always yielding higher variability in results.

As in the previous case with a lower isolation period, the IDA curves follow a nonlinear behavior although there is a tendency for the curves to approach a more linear relationship. Even here, the difference between uniform and spatially variable ground motion, represented by the ratio $\rho_{\max}^{\delta vet,\max}$, can reach a value of around 1.47.

Figure 6.3 presents the piers drift results related to an isolation period $T_1 = 4\,\text{sec}$. Each of the plots shows a further reduction of the drifts demonstrating

the increasing effectiveness of the friction pendulum isolation system for larger values of the radius of curvature.

The bridge response at the highest isolation period considered in the analysis is roughly the same either in the case of different structural configurations and for different incidence angles. Nevertheless, the negative effect of spatial variability is still evident especially for pier 3, as the associated ratio $\rho_i^{\delta vet,\max}$ results equal to $\rho_{\max}^{P3-\delta vet,\max} = 1.48$.

Consistent with the results shown for the other isolation periods, dispersion stays higher for the spatial variability of earthquake ground motion input condition, though only slightly higher than that observed for $T_1 = 3\,\text{sec}$.

In addition, it is worth underlying as the IDA curves tend to exhibit an almost linear relation against IM levels, for all the considered parametric cases.

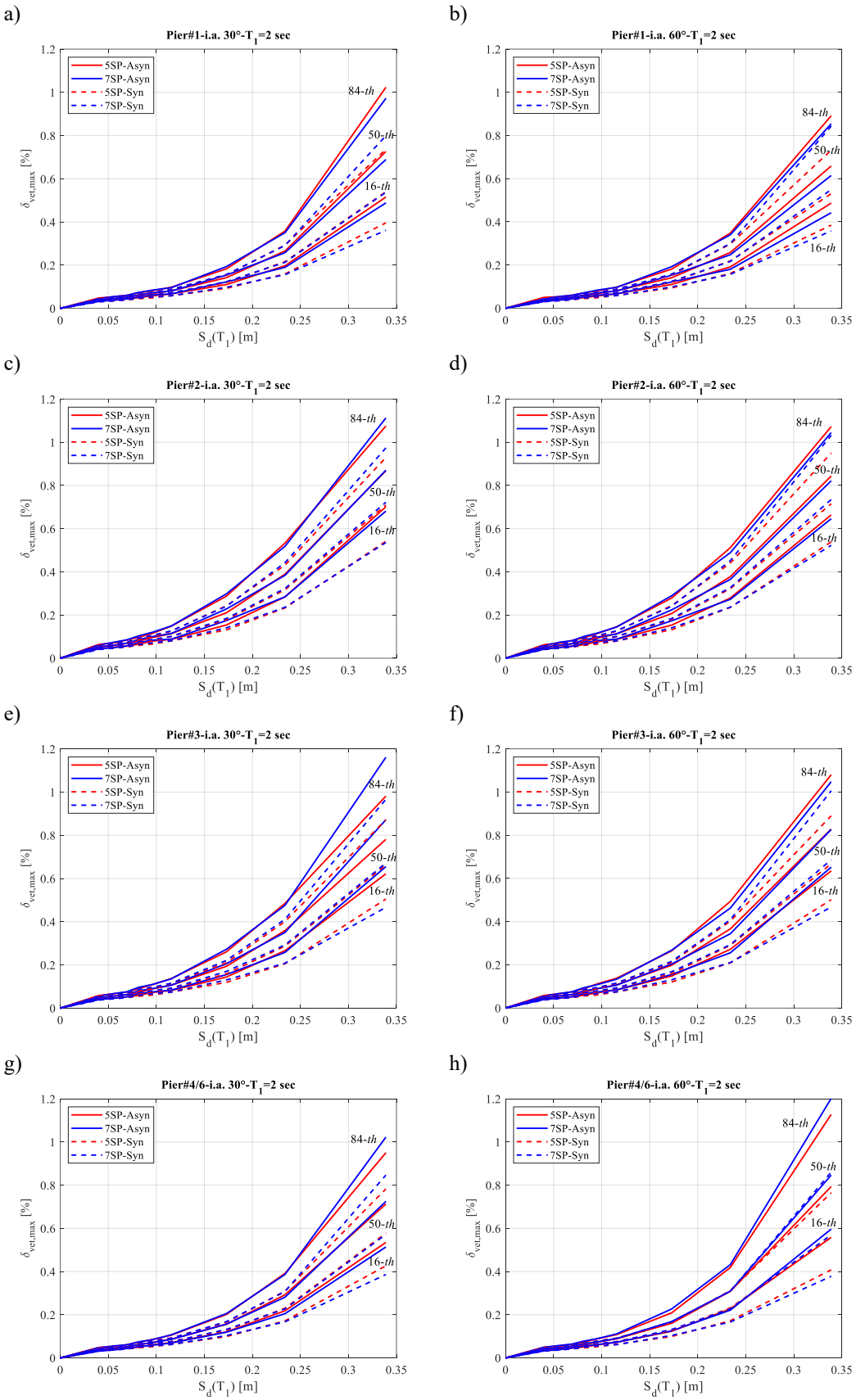

Figure 6.1. IDA curves for piers drift [%] for $T_1 = 2\,\text{sec}$; a) Pier 1, i.a. 30°; b) Pier 1, i.a. 60°; c) Pier 2, i.a. 30°; d) Pier 2, i.a. 60°; e) Pier 3, i.a. 30°; f) Pier 3, i.a. 60°; g) Pier 4/6, i.a. 30°; h) Pier 4/6, i.a. 60°.

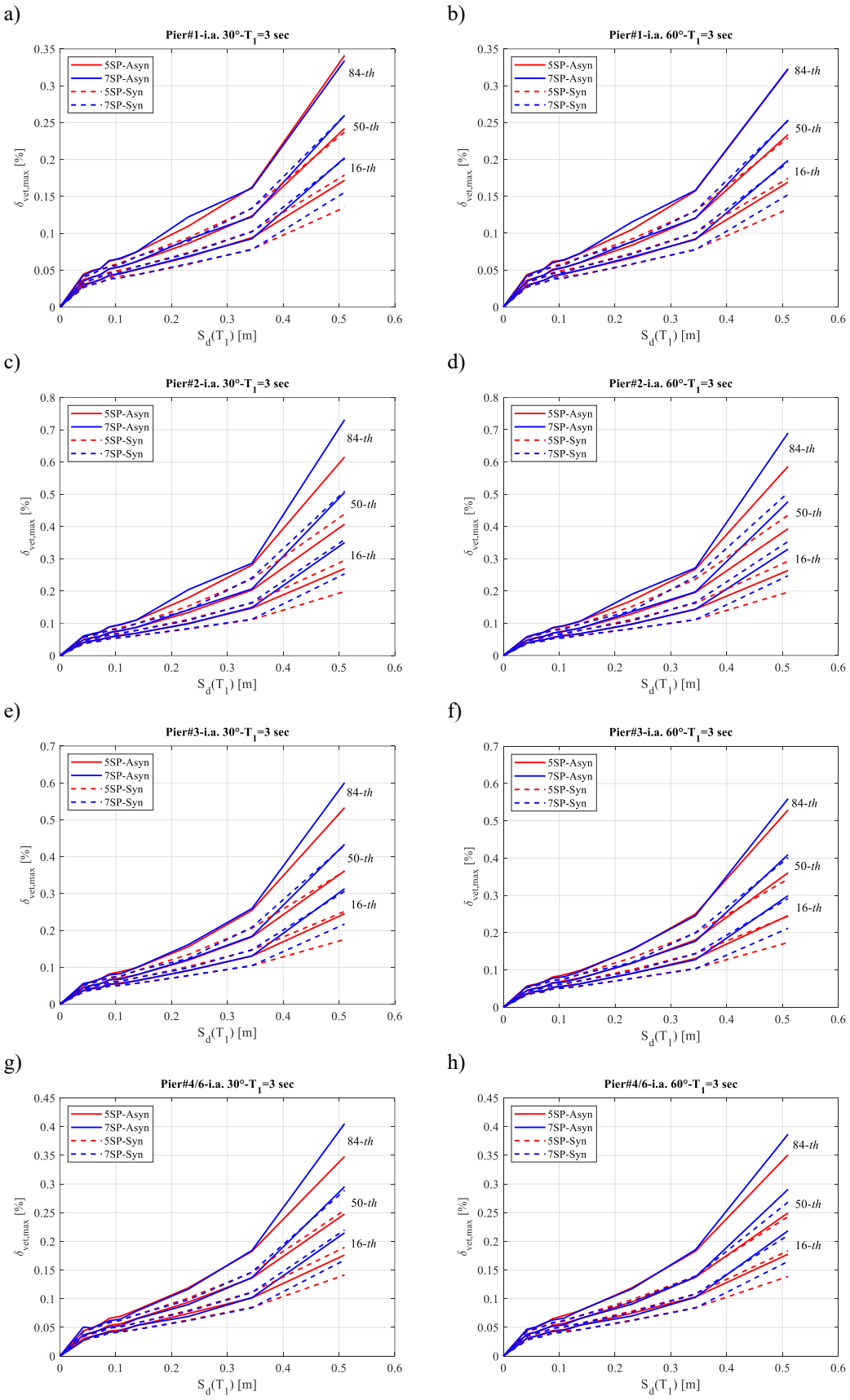

Figure 6.2. IDA curves for piers drift [%] for $T_1 = 3\,\text{sec}$; a) Pier 1, i.a. 30°; b) Pier 1, i.a. 60°; c) Pier 2, i.a. 30°; d) Pier 2, i.a. 60°; e) Pier 3, i.a. 30°; f) Pier 3, i.a. 60°; g) Pier 4/6, i.a. 30°; h) Pier 4/6, i.a. 60°.

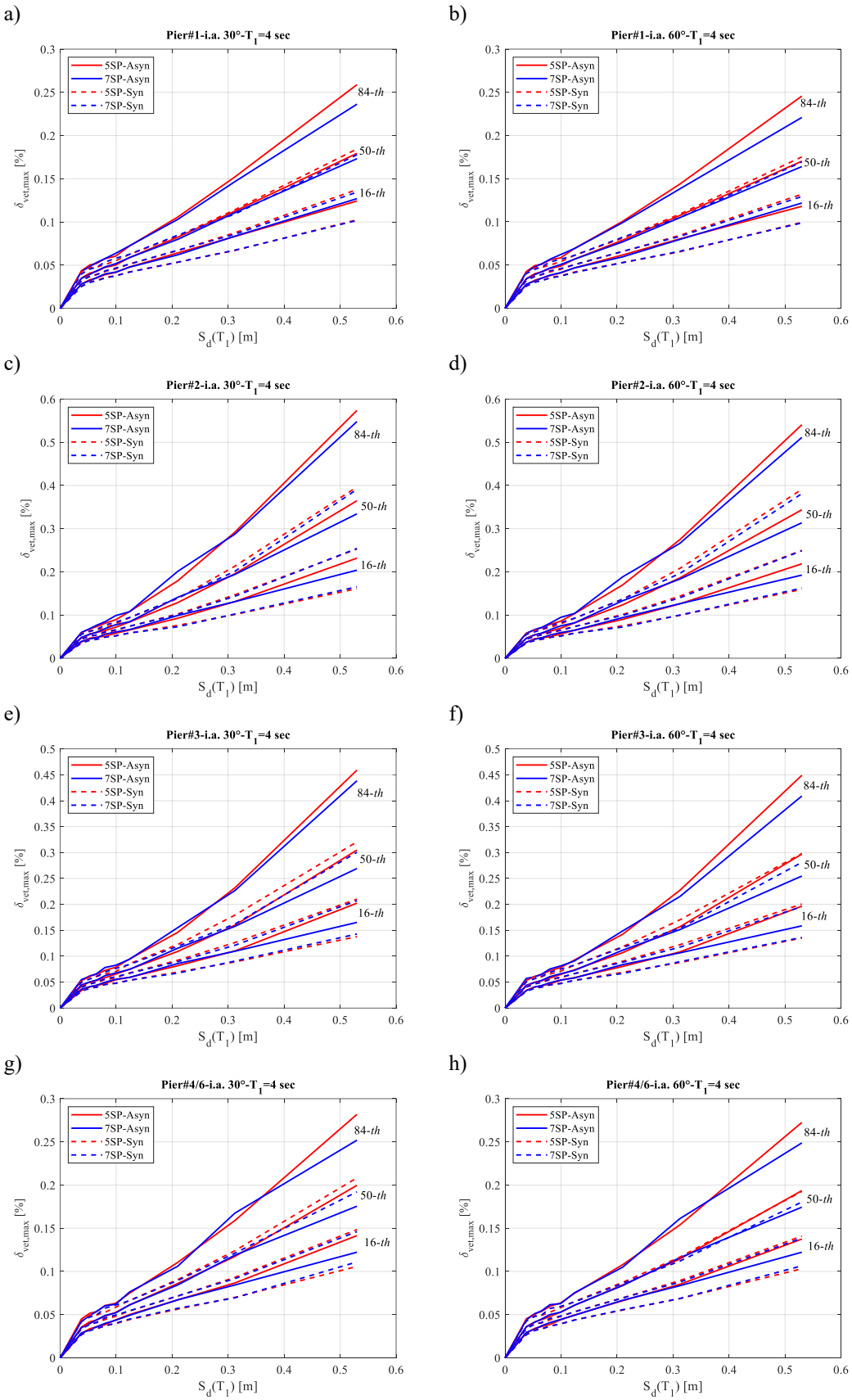

Figure 6.3. IDA curves for piers drift [%] for $T_1 = 4\,\text{sec}$; a) Pier 1, i.a. 30°; b) Pier 1, i.a. 60°; c) Pier 2, i.a. 30°; d) Pier 2, i.a. 60°; e) Pier 3, i.a. 30°; f) Pier 3, i.a. 60°; g) Pier 4/6, i.a. 30°; h) Pier 4/6, i.a. 60°.

Figure 6.4-Figure 6.6 present the IDA curves in terms of piers curvature ductility (vectorial sum along longitudinal and transverse direction) $\mu_{\varphi,vet,\max}$, using the same framework used for the piers drift ratio. The columns divide the IDA curves based on the incidence angle (30° and 60°) while the rows correspond to the same bridge piers already shown for the drift ratio EDP. Each figure corresponds to a different isolation period considered in the parametric analysis, $T_1 = 2,3,4\,\text{sec}$. Again, the results are reported for three different percentiles (16-*th*,50-*th,* and 84-*th*) under the hypothesis of lognormal distribution.

Figure 6.4 a) and b) report the curvature ductility $\mu_{\varphi,vet,\max}$ results, related to the first left bridge pier (9.75m high) for both the 5-span or 7-span configurations, for an incidence angle of respectively 30° and 60°.

The 50-th percentile of $\mu_{\varphi,vet,\max}$ is approximately 2.25 [-] at the highest *IM* level for an incidence angle equal to 30° and 1.95 [-] for an incidence angle of 60°, under spatial variability of earthquake ground motion. Considering the uniform ground motion input condition, the curvature ductility decreases to a value of 1.45 [-] for both incidence angles.

On the other hand, when it comes to the effect of the structural configuration, the results are much higher for the 5-span at the highest intensity measure level and under the SVEGM condition, regardless of the incidence angles. Conversely, for the case of uniform excitation, the IDA curves are nearly the same regardless of the structural configuration.

The dispersion is higher under spatially variable earthquake ground motion (SVEGM) and for an incidence angle condition of 30°.

The negative effect of spatial variability is still quantified by the ratio between the SVEGM response and uniform excitation response, $\rho_i^{P1-\mu_\varphi,vet,\max}$, which for pier 1 results equal to $\rho_{\max}^{P1-\mu_\varphi,vet,\max} = 1.54$.

Figure 6.4 c) and d) which pertain to pier 2, show slightly lower results in terms of curvature ductility compared to those for pier 1.

The 50-*th* percentile of the SVEGM response reaches a peak at the highest intensity level equal to 1.92 [-] for an incidence angle of 30° and 1.80 [-] for a 60° incidence angle. Lower results are always observed under the uniform excitation condition, being the curvature ductility equal to 1.42 [-] for the two incidence angles.

The responses are the same for the 5-span and 7-span configurations while the ratio $\rho_i^{P2-\mu_\varphi,vet,\max}$ for pier 2 results equal to $\rho_{\max}^{P2-\mu_\varphi,vet,\max} = 1.42$.

Dispersion remains higher under spatial variability of earthquake ground motion, whereas it is approximately the same for both incidence angles.

Pier 3 (12.35m high) in Figure 6.4 e) and f) show curvature ductility results comparable to pier 1, with similar mean values and levels of dispersion.

Finally, Figure 6.4 g) and h), which describe the response of pier 4 or 6 depending on the bridge configuration (5-span or 7-span), highlight greater results for an incidence angle of 60°, even if solely for the SVEGM input condition. The

curvature ductility is indeed equal to 2.07 [-] for the SVEGM, 30° incidence angle combination, and 2.61 [-] for the SVEGM, 60° incidence angle combination. In contrast, for the uniform excitation case, the results are almost identical among the two incidence angles and again equal to 1.42 [-]. Moreover, the response is unaffected by the bridge configuration, especially if a uniform excitation input motion is applied.

The dispersion is notably high for an incidence angle of 60° and for the spatially variable earthquake ground motion.

The negative effect of spatial variability is particularly evident for pier 4/6, as the associated ratio $\rho_i^{P4/6-\mu_\varphi,vet,\max}$ results equal to $\rho_{\max}^{P4/6-\mu_\varphi,vet,\max}=1.75$.

In summary, the IDA curves in terms of curvature ductility related to an isolation period $T_1=2\sec$, exhibit a strong nonlinear behavior with an upward concavity. The negative effect of spatial variability of earthquake ground motion, quantified through the ratio $\rho_i^{\mu_\varphi,vet,\max}$, is even more pronounced than that expressed in terms of piers drift ratio. Moreover, being the reinforced concrete section the same for all the piers, the results in terms of curvature ductility do not change significantly across different piers, especially for the uniform excitation case, with a curvature ductility always equal to 1.4 [-] independently of the specific bridge configuration and ground motion incidence angle.

Figure 6.5 identifies the results in terms of curvature ductility for an isolation period equal to $T_1=3\sec$. As already underlined for the piers drift ratio, increasing the isolation period from 2 to 3 seconds reduces the piers response by two-thirds.

The curvature ductility $\mu_{\varphi,vet,\max}$ at the 50-*th* percentile and at the highest *IM* is about 0.8 [-] for the SVEGM case and 0.6 [-] for the uniform excitation condition. The results are indeed only slightly affected by the incidence angle, whereas the 7-span bridge always presents greater results at the largest intensity measure.

The IDA curves tend to exhibit a less marked nonlinear behavior compared to an isolation period $T_1=2\sec$.

As previously observed for the pier drift ratio engineering demand parameter, the dispersion tends to increase with an increasing isolation period, while remaining higher under SVEGM input condition.

The maximum ratio $\rho_i^{\mu_\varphi,vet,\max}$ is associated with pier 3 and is equal to $\rho_{\max}^{P3-\mu_\varphi,vet,\max}=1.49$.

The last case depicted in Figure 6.6 refers to an isolation period $T_1=4\sec$. Regardless of the incidence angle, the curvature ductility is equal to 0.65 [-] for pier 2 (Figure 6.6 c) and d)) and pier 3 (Figure 6.6 e) and f)) and for SVEGM input condition. For uniform excitation, the curvature ductility for these piers is reduced to 0.45 [-].

Pier 1 (Figure 6.6 a) and b)) and pier 4/6 (Figure 6.6 g) and h)) show slightly lower curvature ductility under both SVEGM (0.55 [-]) and uniform input

conditions (0.4 [-]). Structural configuration shows effects only at the highest intensity level, being the 7-span bridge always more demanding in terms of curvature ductility.

Given the enhanced effectiveness of the isolation system resulting from the longer isolation period, the response in terms of curvature ductility at the three percentiles shows an almost linear relationship with the intensity measure.

The maximum ratio $\rho_i^{\mu_\varphi,vet,\max}$ is associated again with pier 3 and is equal to $\rho_{\max}^{P3-\mu_\varphi,vet,\max}=1.53$.

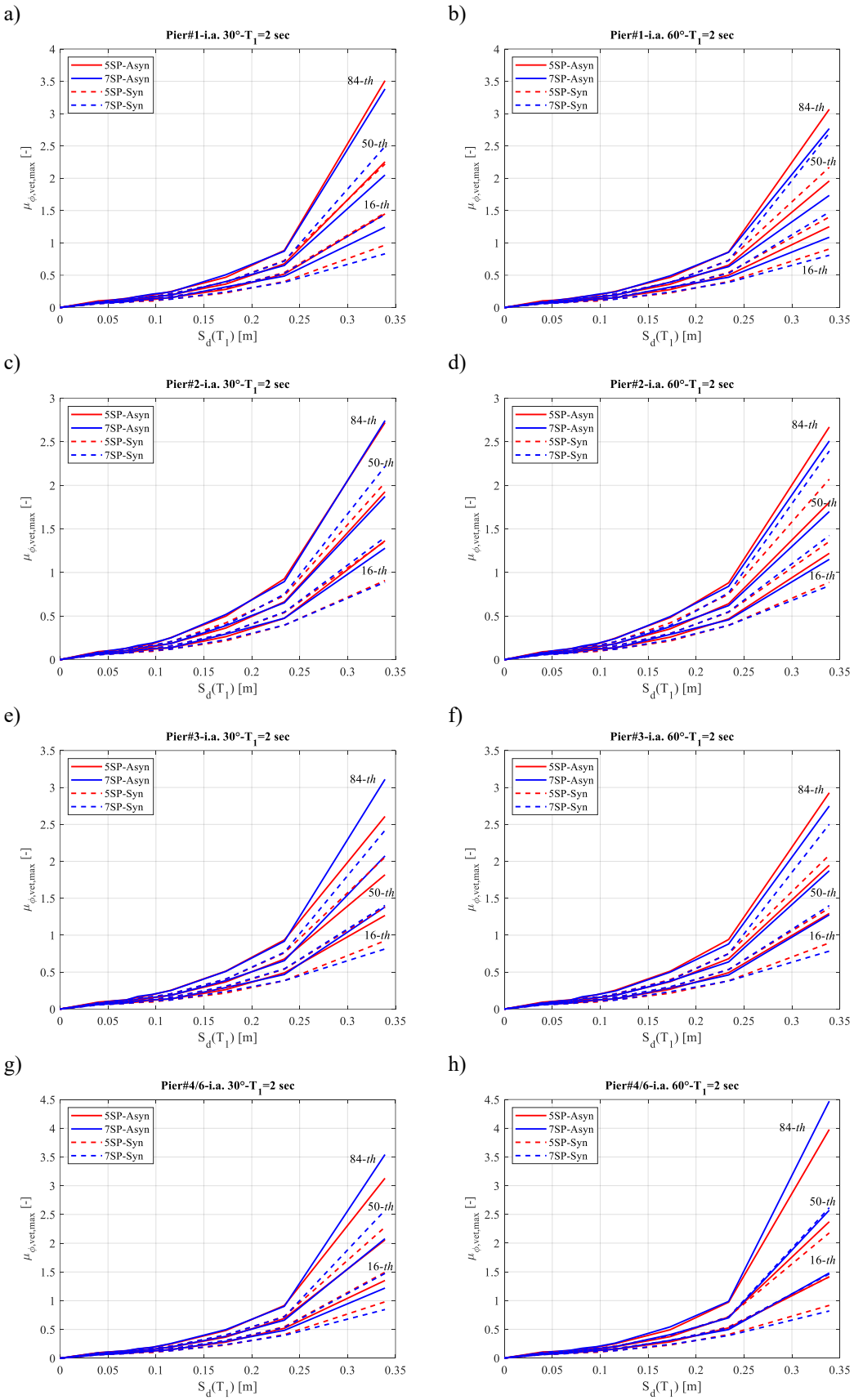

Figure 6.4. IDA curves for piers curvature ductility [-] for T_1=2sec; a) Pier 1, i.a. 30°; b) Pier 1, i.a. 60°; c) Pier 2, i.a. 30°; d) Pier 2, i.a. 60°; e) Pier 3, i.a. 30°; f) Pier 3, i.a. 60°; g) Pier 4/6, i.a. 30°; h) Pier 4/6, i.a. 60°.

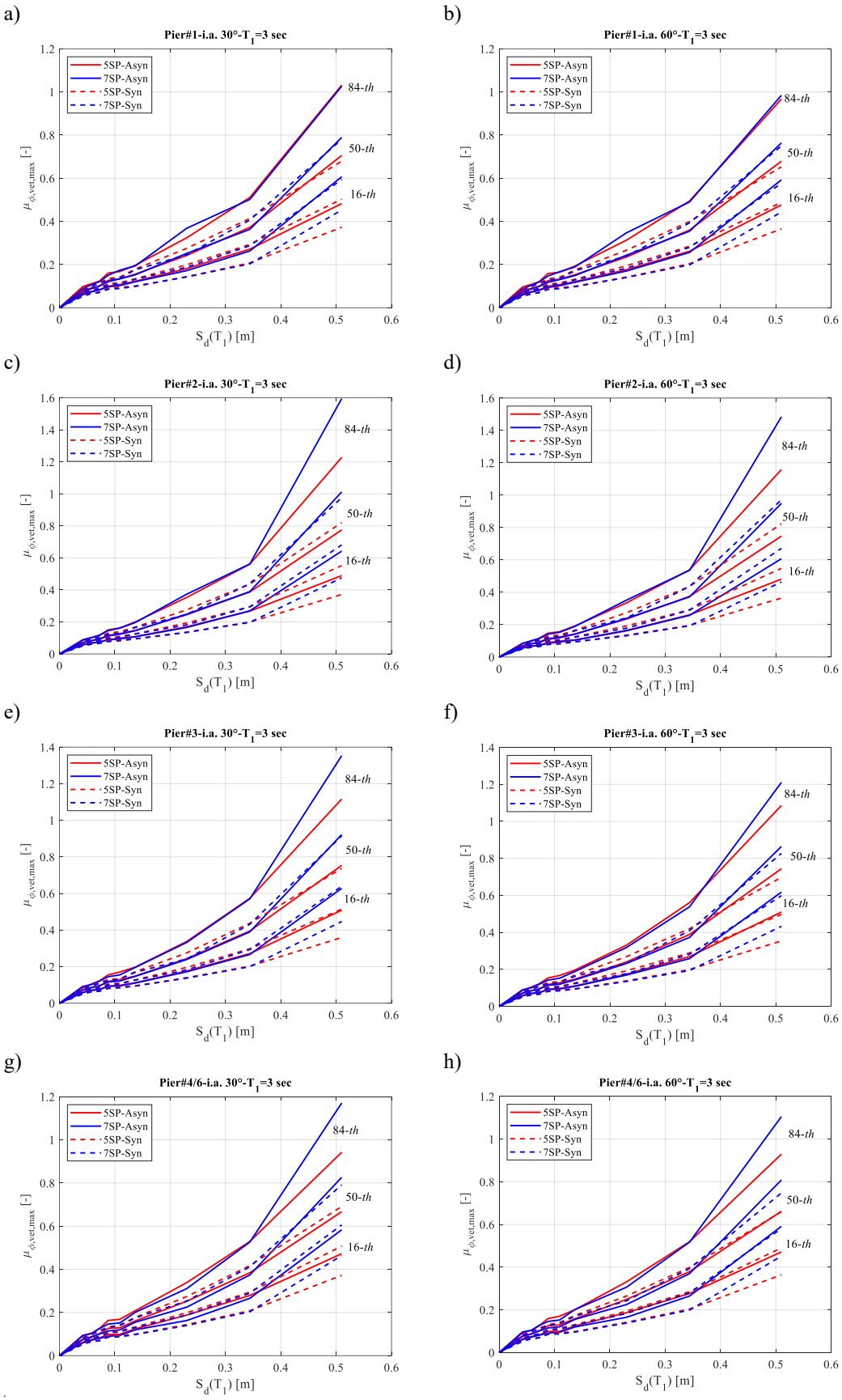

Figure 6.5. IDA curves for piers curvature ductility [-] for T_1=3sec; a) Pier 1, i.a. 30°; b) Pier 1, i.a. 60°; c) Pier 2, i.a. 30°; d) Pier 2, i.a. 60°; e) Pier 3, i.a. 30°; f) Pier 3, i.a. 60°; g) Pier 4/6, i.a. 30°; h) Pier 4/6, i.a. 60°.

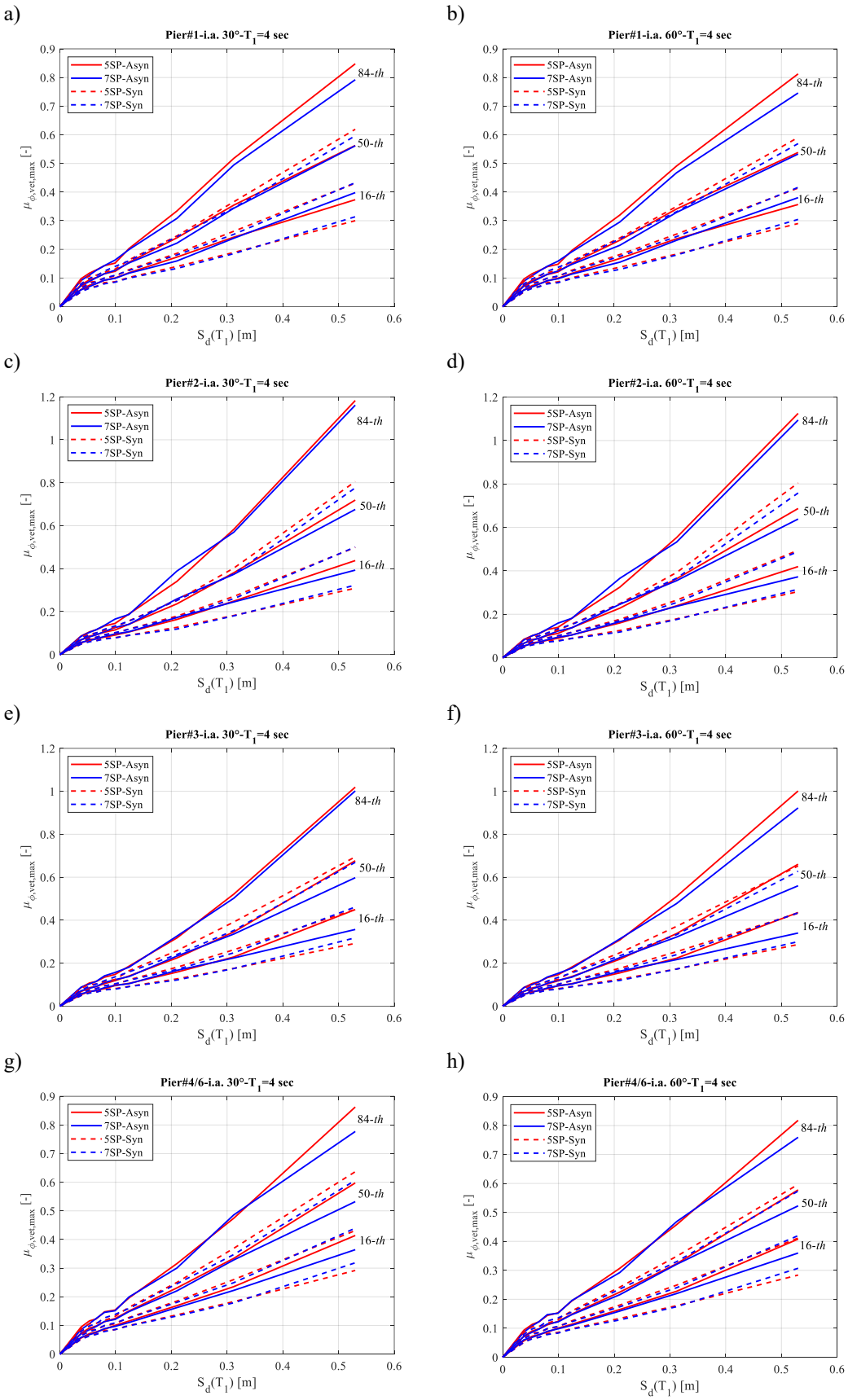

Figure 6.6. IDA curves for piers curvature ductility [-] for T_1=4sec; a) Pier 1, i.a. 30°; b) Pier 1, i.a. 60°; c) Pier 2, i.a. 30°; d) Pier 2, i.a. 60°; e) Pier 3, i.a. 30°; f) Pier 3, i.a. 60°; g) Pier 4/6, i.a. 30°; h) Pier 4/6, i.a. 60°.

Ultimately, the IDA curves for the FPS displacements as vectorial sum along the longitudinal and transverse direction, $u_{b,vet,\max}$, are computed at both the abutments and at the highest pier 2, and reported in Figure 6.7-Figure 6.9.

In the case of an isolation period $T_1 = 2\,\text{sec}$ (Figure 6.7), the FPS bearings placed at the two abutments (Figure 6.7 a) and b) - Figure 6.7 e) and f)) exhibit greater displacements than the ones placed at the highest bridge pier. Indeed, at the abutments, the FPS displacement under SVEGM input condition is close to 0.35m (50-*th* percentile at the highest *IM*), regardless of the structural configuration and the incidence angle. The displacements under uniform excitation are not significantly lower being equal to 0.32m; furthermore, the isolators' response under uniform input ground motion remains constant across both bridge configurations and incidence angle conditions.

As far as the FP bearings response is concerned, the detrimental impact of the spatial variability of ground motion is considerably less pronounced compared to its effects on the piers' response. This observation is supported by the usual coefficient $\rho_i^{u_b,vet,\max}$, which peaks at the abutments and results equal to $\rho_{\max}^{u_b,vet,\max} = 1.25$.

The IDA curves exhibit a linear relationship even at the lowest isolation period, which is something expected at the isolation level. Unlike the piers' response, the demand on the FPS is substantially independent of the structural configuration and incidence angle.

The dispersion consistently remains higher under the SVEGM input condition.

The same trend is also followed at the other two isolation periods $T_1 = 3\,\text{sec}$ and $T_1 = 4\,\text{sec}$ (Figure 6.8-Figure 6.9) with slightly higher demand for those FP bearings placed at the pier as the isolation period elongates.

Specifically, the friction pendulum displacement is equal to 0.26m at pier 2 (50-*th* percentile at the highest *IM*) for an isolation period of $T_1 = 2\,\text{sec}$ and under spatial variability of earthquake ground motion, whereas it increases to 0.28m for an isolation period of $T_1 = 4\,\text{sec}$. The spatial variability effect is quantified through the usual parameter $\rho_i^{u_b,vet,\max}$ that is at the most equal to $\rho_{\max}^{u_b,vet,\max} = 1.26$, for $T_1 = 3\,\text{sec}$ and equal to $\rho_{\max}^{u_b,vet,\max} = 1.29$, for $T_1 = 4\,\text{sec}$.

The dispersion increases for increasing isolation periods.

The greater the isolation period, the more linear the FP response becomes, as observed from the IDA curves in Figure 6.8-Figure 6.9.

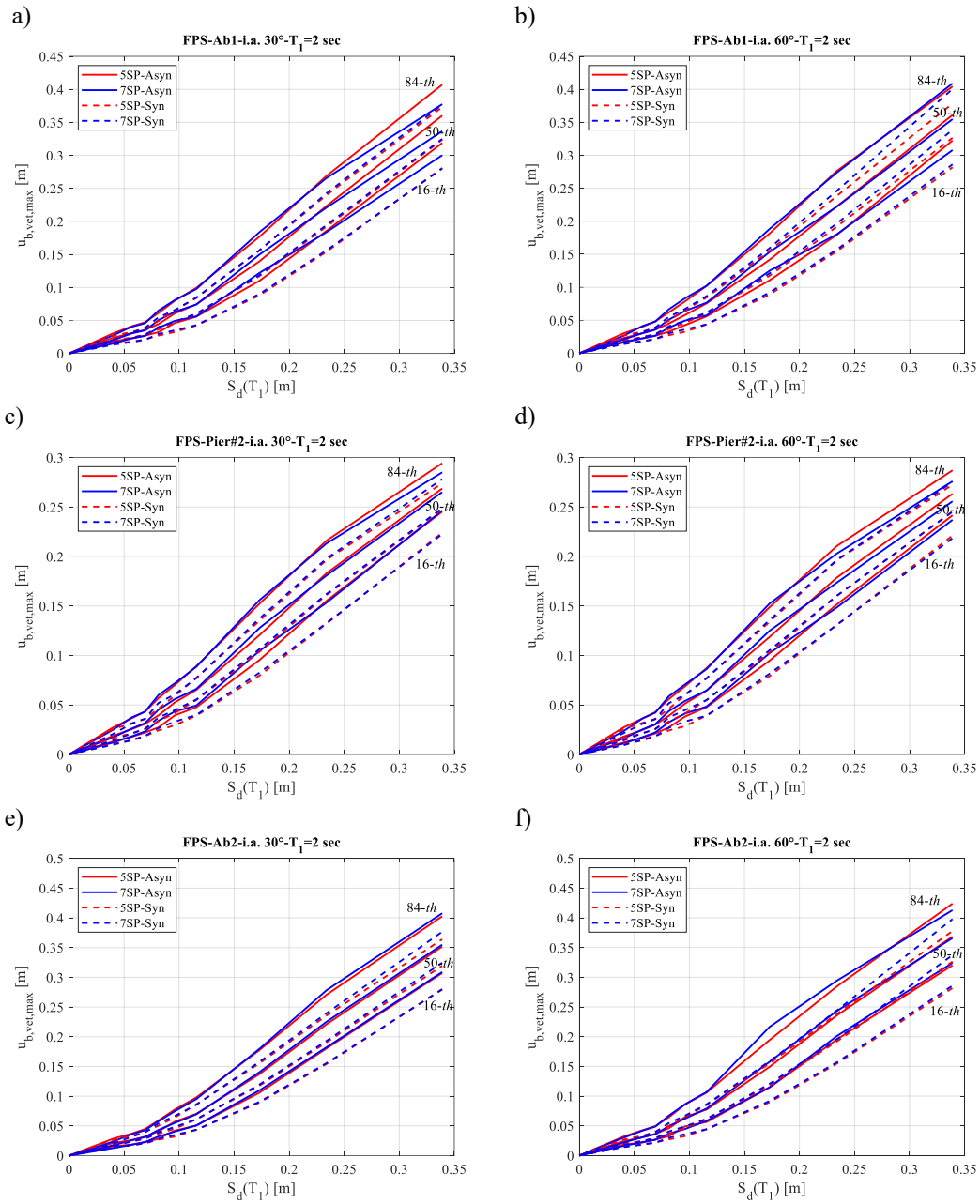

Figure 6.7. IDA curves for the FPS displacements [m] for T_1=2sec; a) Ab1, i.a. 30°; b) Ab1, i.a. 60°; c) Pier 2, i.a. 30°; d) Pier 2, i.a. 60°; e) Ab2, i.a. 30°; f) Ab2, i.a. 60°.

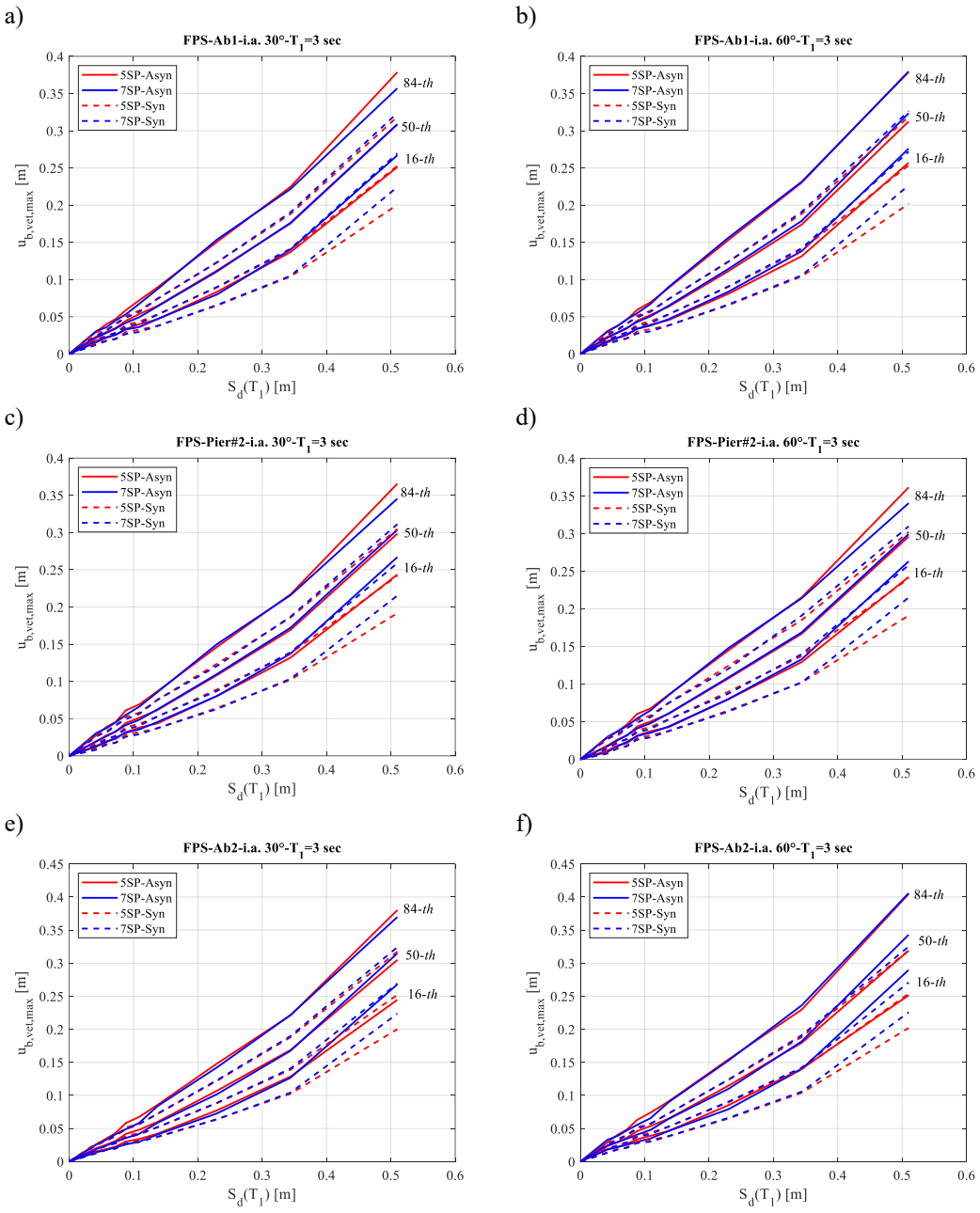

Figure 6.8. IDA curves for the FPS displacements [m] for T_1=3sec; a) Ab1, i.a. 30°; b) Ab1, i.a. 60°; c) Pier 2, i.a. 30°; d) Pier 2, i.a. 60°; e) Ab2, i.a. 30°; f) Ab2, i.a. 60°.

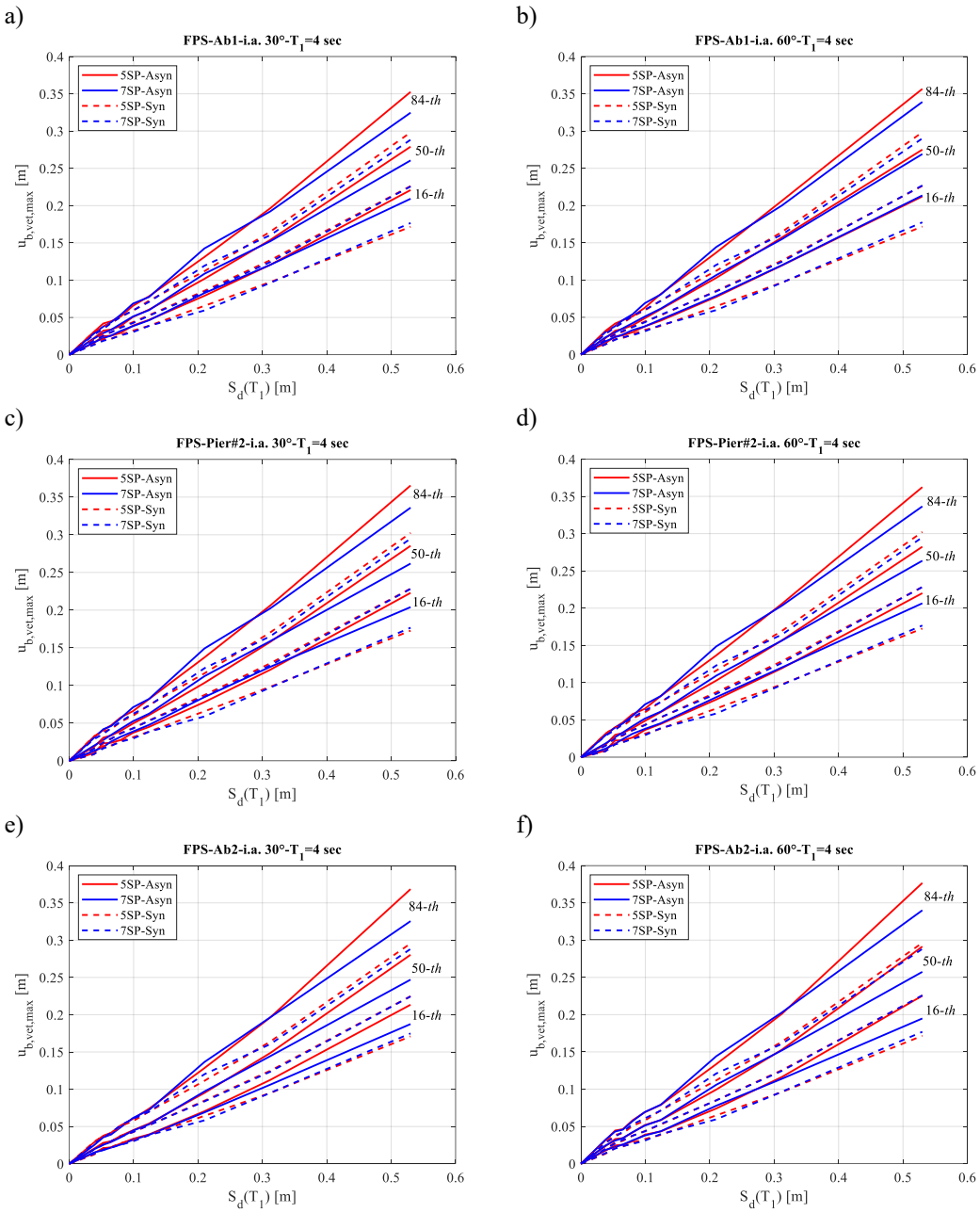

Figure 6.9. IDA curves for the FPS displacements [m] for T_1=4sec; a) Ab1, i.a. 30°; b) Ab1, i.a. 60°; c) Pier 2, i.a. 30°; d) Pier 2, i.a. 60°; e) Ab2, i.a. 30°; f) Ab2, i.a. 60°.

6.4 Seismic fragility analysis

This section aims to describe the computation of seismic fragility, defined as the probabilities P_f of structural systems of exceeding different damage limit states or limit state thresholds at each level of the *IM*. The seismic vulnerability and the following reliability of the testbed bridges will be assessed by focusing on two main bridge components, which are the bridge pier and the friction pendulum isolation system (FP bearings).

6.4.1 Damage limit states definition

To measure the vulnerability of a structural system or component it is essential to define physical damage limit states and the corresponding LS thresholds.

6.4.1.1 Piers damage limit states

As far as the pier is concerned, according to [115] four damage limit states are defined: slight, moderate, extensive, and complete.

As explained in [115] the abovementioned limit states reflect a different physical condition in the pier:

i. Slight (*DLS-1*): it is related to the yielding of the longitudinal steel bar reinforcements and as such only minor damage is expected, but could be in any case necessary to provide a repair action to avoid further deterioration (*e.g.* corrosion);
ii. Moderate (*DLS-2*): it is associated with the spalling of concrete cover. In this case repair actions need to be carried on, particularly focusing on the affected concrete area;
iii. Extensive (*DLS-3*): it is related to the onset of buckling of the longitudinal steel reinforcements or the fracture of transverse reinforcements. In this case it may be necessary to replace the longitudinal/transverse damaged reinforcements and the affected surrounding concrete volume;
iv. Complete (*DLS-4*): severe damage is expected at this stage, typically related to the crushing of the concrete core or the fracture of the longitudinal reinforcements. While piers may still bear gravity loads, their resistance to horizontal loads (*e.g.*, seismic action) is compromised. This damage state is generally associated with a collapse limit state.

In this research, the abovementioned damage limit states for the piers will be expressed in terms of the associated curvature ductility and drift ratios. Following the methodology presented in [116] the definition of both curvature ductilities and drift ratios at each damage limit state is settled on a strain-based criterion.

6.4.1.1.1 Curvature at different damage limit states

Defining the curvature (and consequently the curvature ductility) at the abovementioned damage limit states requires initially performing a moment-curvature analysis of the pier section defined in §5.2.2. The output from this analysis is then used to identify the curvature corresponding to the onset of each damage limit state.

6.4.1.1.1.1 Curvature at DLS-1

The curvature at the slight damage state is calculated according to the following equation, as also recommended by Priestley et al. in [109]:

$$\varphi_{DLS-1} = \varphi_y \frac{M_N}{M_y} \tag{6.18}$$

Where φ_y and M_y are the yield curvature and moment related to the first occurrence of a concrete strain equal to $\varepsilon_c = 0.002$ or of a reinforcement strain of $\varepsilon_s = \varepsilon_{s,y} = \frac{f_y}{E_s}$, being $f_y = 420MPa$ the longitudinal reinforcement yield strength and $E_s = 200000MPa$ the initial elastic tangent stiffness. M_N is the so-called nominal moment corresponding to first occurrence among a concrete strain of $\varepsilon_c = 0.004$ or of a reinforcement strain equal to $\varepsilon_s = 0.015$.

Based on the output of the moment-curvature analysis, the curvature at the slight damage state φ_{DLS-1} computed according to Eq. (6.18) results equal to:

$$\varphi_{DLS-1} = 0.0015 \tag{6.19}$$

6.4.1.1.1.2 Curvature at DLS-2

According to the recommendations of Priestley et al. in [109], the curvature corresponding to the onset of concrete cover spalling is given by:

$$\varphi_{DLS-2} = \varphi(\varepsilon_c = 0.004) \tag{6.20}$$

and for the pier section of interest results equal to:

$$\varphi_{DLS-2} = 0.0055 \tag{6.21}$$

6.4.1.1.1.3 Curvature at DLS-3

As mentioned above the extensive damage limit state can be associated either with the fracture of transverse reinforcements or with the buckling of the steel longitudinal bars.

According to Priestley et al. [109] the concrete compressive strain of the extreme fiber at the onset of steel reinforcement fracture is equal to:

$$\varepsilon_{c,DLS-3} = 0.004 + 1.4\frac{\rho_v f_{yh}\varepsilon_{su}}{f_{cc}} \tag{6.22}$$

In Eq. (6.22), $f_{yh} = 415.2MPa$ represents the transverse reinforcement yield strength, $\varepsilon_{su} = 0.10$ is the ultimate transverse reinforcement strain, $f_{cc} = 29.78MPa$ is the mean compressive strength of the confined concrete and ρ_v is the transverse reinforcement ratio given by the following relation:

$$\rho_v = \frac{4A_{sh}}{D_0 \cdot s_h} \tag{6.23}$$

Where D_0 is the diameter of the confined concrete core section, s_h is the transverse reinforcement spacing, and A_{sh} is the transverse reinforcement bar area.

Consequently, it is straightforward to evaluate the curvature corresponding to the concrete strain at the onset of the steel transverse reinforcement fracture as:

$$\varphi_{DLS-3\_h} = \varphi(\varepsilon_{c,DLS-3}) \tag{6.24}$$

The so-evaluated curvature, considering the geometrical, material, and reinforcement characteristics of the circular pier section is equal to:

$$\varphi_{DLS-3\_h} = 0.007 \tag{6.25}$$

Because the examined piers are provided with poorly confined sections, featuring a clear vertical spacing between hoop bars equal to 44cm, it is crucial to consider the potential buckling of the longitudinal reinforcements. Following the formulation recommended by Priestley et al. [109], the curvature at the onset of the buckling is given by:

$$\varphi_{DLS-3\_buck} = \varphi_{ser} + \left(\frac{16d_l - s_h}{16d_l - s_{\max}}\right)\left(12\varphi_{DLS-1} - \varphi_{ser}\right) \tag{6.26}$$

Where $\varphi_{ser} = 0.00135$ is the curvature corresponding to the yield reinforcement strain $\varepsilon_{s,y}$, $d_l = 34mm$ is the longitudinal bar diameter, φ_{DLS-1} is the curvature at the slight damage state expressed in Eq.s (6.18)-(6.19), and s_h is again the vertical spacing between hoop bars. Finally, $s_{\max}$, is given by the following equation:

$$s_{\max} = 3 + 6\left(\frac{f_u}{f_y} - 1\right) d_l \le 6 d_l \tag{6.27}$$

Where f_u is the transverse reinforcement ultimate strength.

The curvature at the buckling for the section of interest, calculated according to Eq. (6.26) is equal to:

$$\varphi_{DLS-3\_buck} = 0.0064 \tag{6.28}$$

The curvature at the extensive damage limit state will be then the minimum between φ_{DLS-3_h} and φ_{DLS-3_buck} and based on the above calculations it results equal to φ_{DLS-3_buck}:

$$\varphi_{DLS\text{-}3} = \min\left\{\varphi_{DLS\text{-}3\_h}, \varphi_{DLS\text{-}3\_buck}\right\} = \varphi_{DLS\text{-}3\_buck} = 0.0064 \tag{6.29}$$

6.4.1.1.1.4 Curvature at DLS-4

The curvature at the complete damage state is given by the following equation:

$$\varphi_{DLS-3} = \varphi_{\max} \tag{6.30}$$

Being $\varphi_{\max}$ the curvature corresponding to concrete core crushing $\varphi_{\max} = \varphi(\varepsilon_{ccu} = 0.00605)$. Consequently, the curvature at the complete damage state results equal to:

$$\varphi_{DLS-4} = 0.0081 \tag{6.31}$$

6.4.1.1.2 Curvature ductility at different damage limit states

The curvature ductility at different damage limit states is calculated according to the following relation [115]:

$$\mu_{\varphi_{DLS-i}} = \frac{\varphi_{DLS-i}}{\varphi_{y,N}} \tag{6.32}$$

Where $\varphi_{y,N}$ is the reference nominal yield curvature [109] equal to:

$$\varphi_{y,N} = \frac{2.25\varepsilon_y}{D_0} \tag{6.33}$$

It follows that the thresholds for the curvature ductility corresponding to the aforementioned damage limit states assumed for the seismic fragility assessment of the bridge piers at a section level, and calculated accordingly to Eq. (6.32) are the ones reported in Table 6.2:

Damage limit states in terms of curvature ductility		$LS\mu$	$LS\mu_{IB}$
DLS-1	Slight damage	$\mu_{\varphi_{DLS-1}} = 0.72$	$\mu_{\varphi_{DLS-1\_IB}} = 0.24$
DLS-2	Moderate damage	$\mu_{\varphi_{DLS-2}} = 2.96$	$\mu_{\varphi_{DLS-2\_IB}} = 0.99$
DLS-3	Extensive damage	$\mu_{\varphi_{DLS-2}} = 3.44$	$\mu_{\varphi_{DLS-3\_IB}} = 1.15$
DLS-4	Complete damage	$\mu_{\varphi_{DLS-4}} = 4.37$	$\mu_{\varphi_{DLS-4\_IB}} = 1.46$

Table 6.2. Damage limit states for the piers section in terms of curvature ductility.

Moreover, according to FEMA 274 provisions [80-117], which requires higher performance standards for base isolated bridges, the damage limit state thresholds are assumed to be about one-third of the corresponding limit state thresholds for non-isolated bridges. It follows that the adopted curvature ductility $LS\mu$ thresholds for the base-isolated bridge are the ones indicated as $LS\mu_{IB}$ and reported in the last column of Table 6.2.

6.4.1.1.3 Drifts at different damage limit states

The drift ratios corresponding to the specific damage limit state and to the specific pier's height are calculated as follows:

$$\delta_{DLS-i} = \frac{\Delta_{DLS-i}}{H} \tag{6.34}$$

Where Δ_{DLS-i} is the lateral displacement at the attainment of each of the aforementioned limit states and H is the pier's height.

The lateral displacement can be calculated according to the following relationship:

$$\Delta = \begin{cases} \Delta_y \dfrac{\varphi}{\varphi_y} & for \quad \varphi \le \varphi_y \\ \Delta_y \dfrac{M}{M_y} + \left(\varphi - \varphi_y \dfrac{M}{M_y}\right) L_p H & for \quad \varphi > \varphi_y \end{cases} \tag{6.35}$$

Where φ and M are the outputs of the moment-curvature analysis, M_y is the first yield moment already presented in Eq. (6.18), L_p is the plastic hinge length calculated according to Eq. (5.10), and Δ_y is the yield displacement defined as follows:

$$\Delta_y = \varphi_y \frac{\left(H + L_{sp}\right)^2}{3} \tag{6.36}$$

It follows then that the lateral displacements at the attainment of each damage limit states (Δ_{DLS-i}) can be retrieved by substituting the curvature limit states calculated in §6.4.1.1.1 in Eq.

(6.35).

Following the abovementioned procedure, the drift ratios corresponding to each different pier's height at the different damage limit states are presented in the following tables:

Damage limit states - pier with height H_1 (H_1=9.75m)		LS_δ	$LS_{\delta_{IB}}$
DLS-1	Slight damage	$\delta_{P1\_\delta_{DLS-1}} = 0.54\%$	$\delta_{P1\_\delta_{DLS-1\_IB}} = 0.18\%$
DLS-2	Moderate damage	$\delta_{P1\_\delta_{DLS-2}} = 1.06\%$	$\delta_{P1\_\delta_{DLS-2\_IB}} = 0.35\%$
DLS-3	Extensive damage	$\delta_{P1\_\delta_{DLS-3}} = 1.16\%$	$\delta_{P1\_\delta_{DLS-3\_IB}} = 0.39\%$
DLS-4	Complete damage	$\delta_{P1\_\delta_{DLS-4}} = 1.33\%$	$\delta_{P1\_\delta_{DLS-4\_IB}} = 0.44\%$

Table 6.3. Damage limit states for the pier with height H_1 (H_1=9.75m) in terms of drift ratios.

Damage limit states - pier with height H_2 (H_2=13.4m)		LS_δ	$LS_{\delta_{IB}}$
DLS-1	Slight damage	$\delta_{P2\_\delta_{DLS-1}} = 0.73\%$	$\delta_{P2\_\delta_{DLS-1\_IB}} = 0.24\%$
DLS-2	Moderate damage	$\delta_{P2\_\delta_{DLS-2}} = 1.40\%$	$\delta_{P2\_\delta_{DLS-2\_IB}} = 0.47\%$
DLS-3	Extensive damage	$\delta_{P2\_\delta_{DLS-3}} = 1.52\%$	$\delta_{P2\_\delta_{DLS-3\_IB}} = 0.51\%$
DLS-4	Complete damage	$\delta_{P2\_\delta_{DLS-4}} = 1.74\%$	$\delta_{P2\_\delta_{DLS-4\_IB}} = 0.58\%$

Table 6.4. Damage limit states for the pier with height H_2 (H_2=13.4m) in terms of drift ratios.

Damage limit states - pier with height H_3 (H_3=12.35m)		LS_δ	$LS_{\delta_{IB}}$
DLS-1	Slight damage	$\delta_{P3\_\delta_{DLS-1}} = 0.68\%$	$\delta_{P3\_\delta_{DLS-1\_IB}} = 0.23\%$
DLS-2	Moderate damage	$\delta_{P3\_\delta_{DLS-2}} = 1.30\%$	$\delta_{P3\_\delta_{DLS-2\_IB}} = 0.43\%$
DLS-3	Extensive damage	$\delta_{P3\_\delta_{DLS-3}} = 1.42\%$	$\delta_{P3\_\delta_{DLS-3\_IB}} = 0.47\%$
DLS-4	Complete damage	$\delta_{P3\_\delta_{DLS-4}} = 1.62\%$	$\delta_{P3\_\delta_{DLS-4\_IB}} = 0.54\%$

Table 6.5. Damage limit states for the pier with height H_3 (H_3=12.35m) in terms of drift ratios.

Damage limit states - pier with height H_4 or H_6 (H_4= H_6=10.22m)		LS_δ	$LS_{\delta_{IB}}$
DLS-1	Slight damage	$\delta_{P4\_\delta_{DLS-1}} = 0.57\%$	$\delta_{P4\_\delta_{DLS-1\_IB}} = 0.19\%$
DLS-2	Moderate damage	$\delta_{P4\_\delta_{DLS-2}} = 1.11\%$	$\delta_{P4\_\delta_{DLS-2\_IB}} = 0.37\%$
DLS-3	Extensive damage	$\delta_{P4\_\delta_{DLS-3}} = 1.20\%$	$\delta_{P4\_\delta_{DLS-3\_IB}} = 0.40\%$
DLS-4	Complete damage	$\delta_{P4\_\delta_{DLS-4}} = 1.39\%$	$\delta_{P4\_\delta_{DLS-4\_IB}} = 0.46\%$

Table 6.6. Damage limit states for the pier with height H_4 -H_6 (H_4=H_6=10.22m) in terms of drift ratios.

Coherently with the approach followed for the curvature ductility limit states thresholds, also the drift ratios limit states LS_δ for isolated bridges, are assumed to be one-third of the corresponding ones for non-isolated bridges, and indicated as $LS_{\delta_{IB}}$.

6.4.1.2 FPS limit states

As for the FP isolators, limit state thresholds are primarily defined in terms of radius in plan, r[m], which is a key design parameter for the FP bearings, specifically adopted within this study because it is a function of the required maximum displacement demand for the FPS isolator.

In the following table different *LS* thresholds are considered with the aim of providing reliable recommendations for the design of the FP isolation system:

	LS1	*LS2*	*LS3*	*LS4*	*LS5*	*LS6*	*LS7*	*LS8*	*LS9*
$r[m]$	0.10	0.15	0.20	0.25	0.30	0.35	0.40	0.45	0.50

Table 6.7. Limit states thresholds for the FP isolation system in terms of radius in plan r[m].

6.4.2 Seismic fragility curves

Once the damage limit states have been defined, it is possible to proceed with the seismic fragility assessment through the calculation of the probability of exceeding those *LS* thresholds, (*i.e.* probability of failure P_f) expressed in terms of the aforementioned engineering demand parameters (EDP*s*) and as a function of the i-*th* intensity measure (IM) level. This probability of failure is mathematically expressed as the complement to 1 of the cumulative distribution function $F_{EDP|IM_i=im}\left(LS_{j,EDP}\right)$ evaluated at the i-*th* IM level and for the j-*th* limit state threshold with reference to the EDP of interest. In the context of seismic fragility assessment, both the collapse and non-collapse results for a given structural configuration, isolation period, and seismic input scenarios considered in the analysis at each IM level have been considered employing the total probability theorem [118]. It follows that the implemented relation for computing the probability of failure P_f at the j-*th* limit state threshold and for a given EDP is expressed as:

$$P_{LSj}(IM_i = im) = \left(1 - F_{EDP|IM_i=im}\left(LS_{j,EDP}\right)\right)\frac{N_{non-collapse}}{N} + 1\cdot\left(1 - \frac{N_{non-collapse}}{N}\right) \tag{6.37}$$

Where $N = 300$ is the total number of analyses at each IM level for a given structural configuration, isolation period, and seismic input scenario, and $N_{non-collapse}$ is the number of numerical simulations where no collapse/numerical instability has been observed. The first term of Eq. (6.37) is associated with the probability of exceeding the j-*th* limit state threshold corresponding to a non-collapse case whereas the second part accounts for the probability of exceeding the j-*th* limit state given that the structural system has experienced collapse.

The following tables report the number of non-collapse cases for each intensity measure level and for each of the analyzed structural configuration, isolation period, and seismic input scenarios.

	5-span bridge configuration-SVEGM input condition					
	$T_1 = 2\,\text{sec}$		$T_1 = 3\,\text{sec}$		$T_1 = 4\,\text{sec}$	
$N_{non-collapse}$	i.a.=30°	i.a.=60°	i.a.=30°	i.a.=60°	i.a.=30°	i.a.=60°
IM1	300	300	300	300	300	300
IM2	300	300	300	300	300	300
IM3	300	300	300	300	300	300
IM4	300	300	300	300	300	300
IM5	300	300	300	300	300	300
IM6	300	300	300	300	300	300
IM7	300	300	300	300	300	300
IM8	300	300	300	300	300	300
IM9	290	293	300	300	300	300

Table 6.8. Number of non-collapse $N_{non-collapse}$ cases for the 5-span bridge configuration and under SVEGM input condition.

	5-span bridge configuration-uniform input condition					
	$T_1 = 2\,\text{sec}$		$T_1 = 3\,\text{sec}$		$T_1 = 4\,\text{sec}$	
$N_{non-collapse}$	i.a.=30°	i.a.=60°	i.a.=30°	i.a.=60°	i.a.=30°	i.a.=60°
IM1	300	300	300	300	300	300
IM2	300	300	300	300	300	300
IM3	300	300	300	300	300	300
IM4	300	300	300	300	300	300
IM5	300	300	300	300	300	300
IM6	300	300	300	300	300	300
IM7	300	300	300	300	300	300
IM8	300	300	300	300	300	300
IM9	299	299	300	300	300	300

Table 6.9. Number of non-collapse $N_{non-collapse}$ cases for the 5-span bridge configuration and under uniform input condition.

	7-span bridge configuration-SVEGM input condition					
	$T_1 = 2\,\text{sec}$		$T_1 = 3\,\text{sec}$		$T_1 = 4\,\text{sec}$	
$N_{non-collapse}$	i.a.=30°	i.a.=60°	i.a.=30°	i.a.=60°	i.a.=30°	i.a.=60°
IM1	300	300	300	300	300	300
IM2	300	300	300	300	300	300
IM3	300	300	300	300	300	300
IM4	300	300	300	300	300	300
IM5	300	300	300	300	300	300
IM6	300	300	300	300	300	300
IM7	300	300	300	300	300	300
IM8	300	300	300	300	300	300
IM9	291	290	300	300	300	300

Table 6.10. Number of non-collapse cases for the 7-span bridge configuration and under SVEGM input condition.

	7-span bridge configuration-uniform input condition					
	$T_1 = 2\,\text{sec}$		$T_1 = 3\,\text{sec}$		$T_1 = 4\,\text{sec}$	
$N_{non-collapse}$	i.a.=30°	i.a.=60°	i.a.=30°	i.a.=60°	i.a.=30°	i.a.=60°
IM1	300	300	300	300	300	300
IM2	300	300	300	300	300	300
IM3	300	300	300	300	300	300
IM4	300	300	300	300	300	300
IM5	300	300	300	300	300	300
IM6	300	300	300	300	300	300
IM7	300	300	300	300	300	300
IM8	300	300	300	300	300	300
IM9	294	296	300	300	300	300

Table 6.11. Number of non-collapse $N_{non-collapse}$ cases for the 7-span bridge configuration and under uniform input condition.

Once the probability of failures are calculated at all the intensity measure levels and for each of the limit states, the points that define the fragility at the j-*th* limit state can be approximated by a lognormal distribution through the following procedure:

i. For each limit state, the standard normal variable u_r associated to the i-*th* point of the fragility is computed;

ii. In a semilogarithmic plane, where the value of u_r is reported on the vertical axis and the logarithm of the intensity measure on the horizontal axis, a linear regression of the type $u_r = a \cdot \ln(S_d) + b$ is performed. Considering that, given a lognormal variable x its logarithm y=ln(x) is normally distributed with mean λ_y and standard deviation σ_y, then, by imposing that $u_r = \dfrac{y - \lambda_y}{\sigma_y}$, it is possible to compute the following relations:

$$\lambda_y = \frac{-b}{a} \tag{6.38}$$

$$\sigma_y = \frac{1}{a} \tag{6.39}$$

iii. With the so-obtained parameter, the fragility curve associated to the j-*th* limit state, mathematically expressed through the lognormal cumulative distribution function, is computed.

Figure 6.10-Figure 6.12 present the fragility curves for the peak vectorial sum of the piers' drift ratio $\delta_{vet,\max}$, across the four damage limit states presented in the previous section. These figures are shown similarly to the IDA curves, with each figure corresponding to a different isolation period. Within each figure, rows are representative of the specific bridge piers, while the two columns compare the response for an incidence angle of 30° (first column) and 60° (second column).

Each subplot includes a comparison between the two bridge structural configurations (7-span and 5-span) and the two input conditions of uniform excitation and spatial variability of earthquake ground motion. The plots display the probability of failure on the vertical axis against seismic intensity measure $S_d(T_1)$ on the horizontal axis.

In terms of drift ratio $\delta_{vet,\max}$, the fragility decreases as the isolation period increases, resulting in very low probabilities of exceeding especially the third and fourth damage limit states at the highest isolation period equal to $T_1 = 4\,\text{sec}$.

From the fragility curves and according to the IDA results, it is possible to observe that the spatial variability of earthquake ground motion leads to higher probabilities of failure with respect to the uniform input condition. This trend is a general result regardless of the structural configuration, of the incidence angle, and of the isolation period. Due to their geometrical properties, the most vulnerable piers result to be pier 2 and pier 3, among all the isolation periods and for the two incidence angle conditions.

Regarding the incidence angle, it has only a slight influence on the pier's fragility. It is generally observed that an incidence angle of 60° reduces the probability of exceeding damage limit states, especially at the lowest isolation period of $T_1 = 2\,\text{sec}$.

When it comes to the structural configuration it is not possible to draw a clear trend: at the lowest isolation period slightly higher probabilities of exceedance for all the damage limit states are due to the 5-span configuration and this is even more evident when combined with the uniform input condition; contrarily, for an isolation period equal to 3 sec the most vulnerable configuration is the 7-span combined with SVEGM input condition. At the highest isolation period the 5-span configuration becomes again the most vulnerable, especially under uniform conditions of input ground motion.

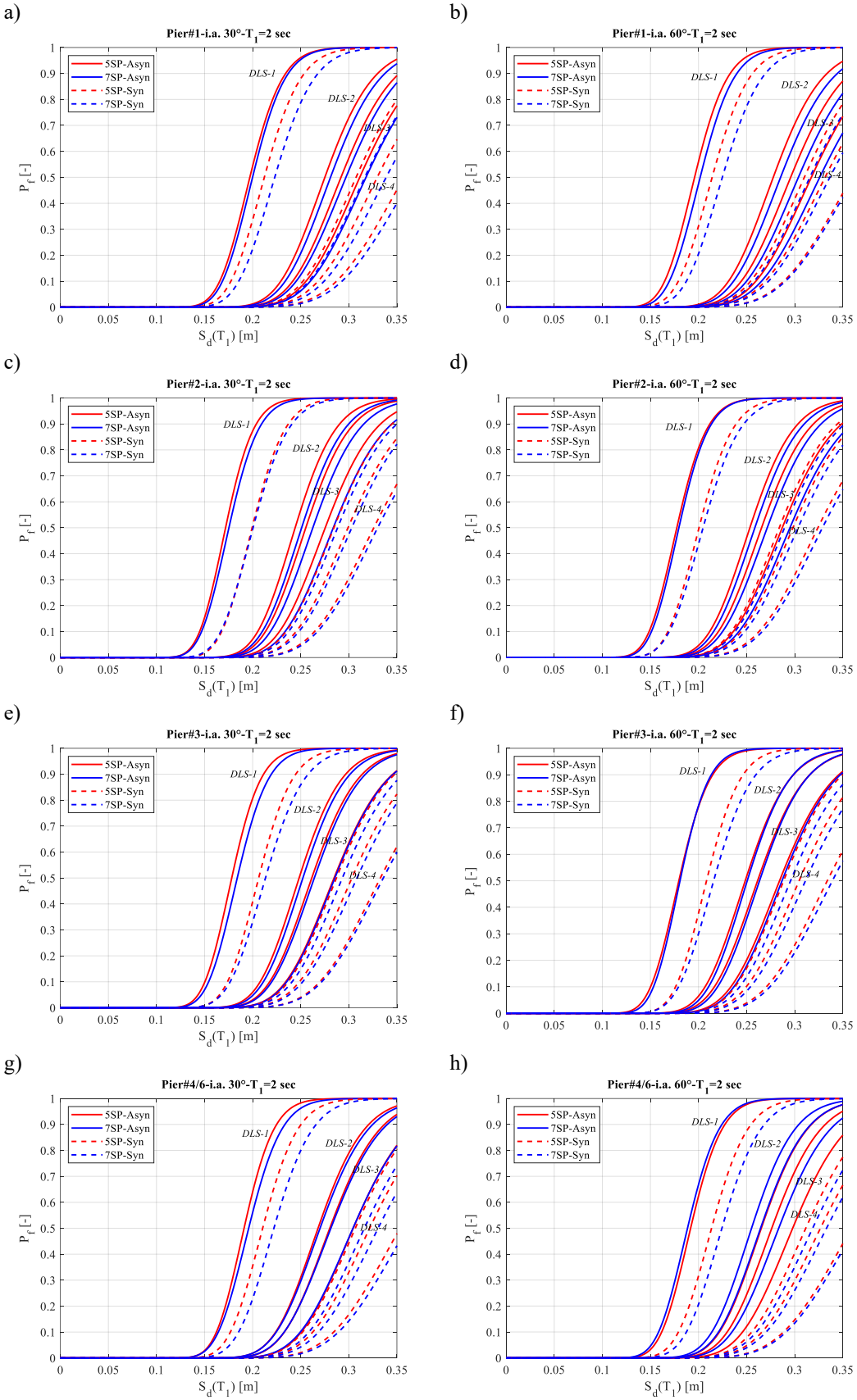

Figure 6.10. Fragility curves for the piers drift [%] for $T_1 = 2\,\text{sec}$, for damage limit states from *DLS*-1 to *DLS*-4 ; a) Pier 1, i.a. 30°: b) Pier 1, i.a. 60°; c) Pier 2, i.a. 30°; d) Pier 2, i.a. 60°; e) Pier 3, i.a. 30°; f) Pier 3, i.a. 60°; g) Pier 4/6, i.a. 30°; h) Pier 4/6, i.a. 60°.

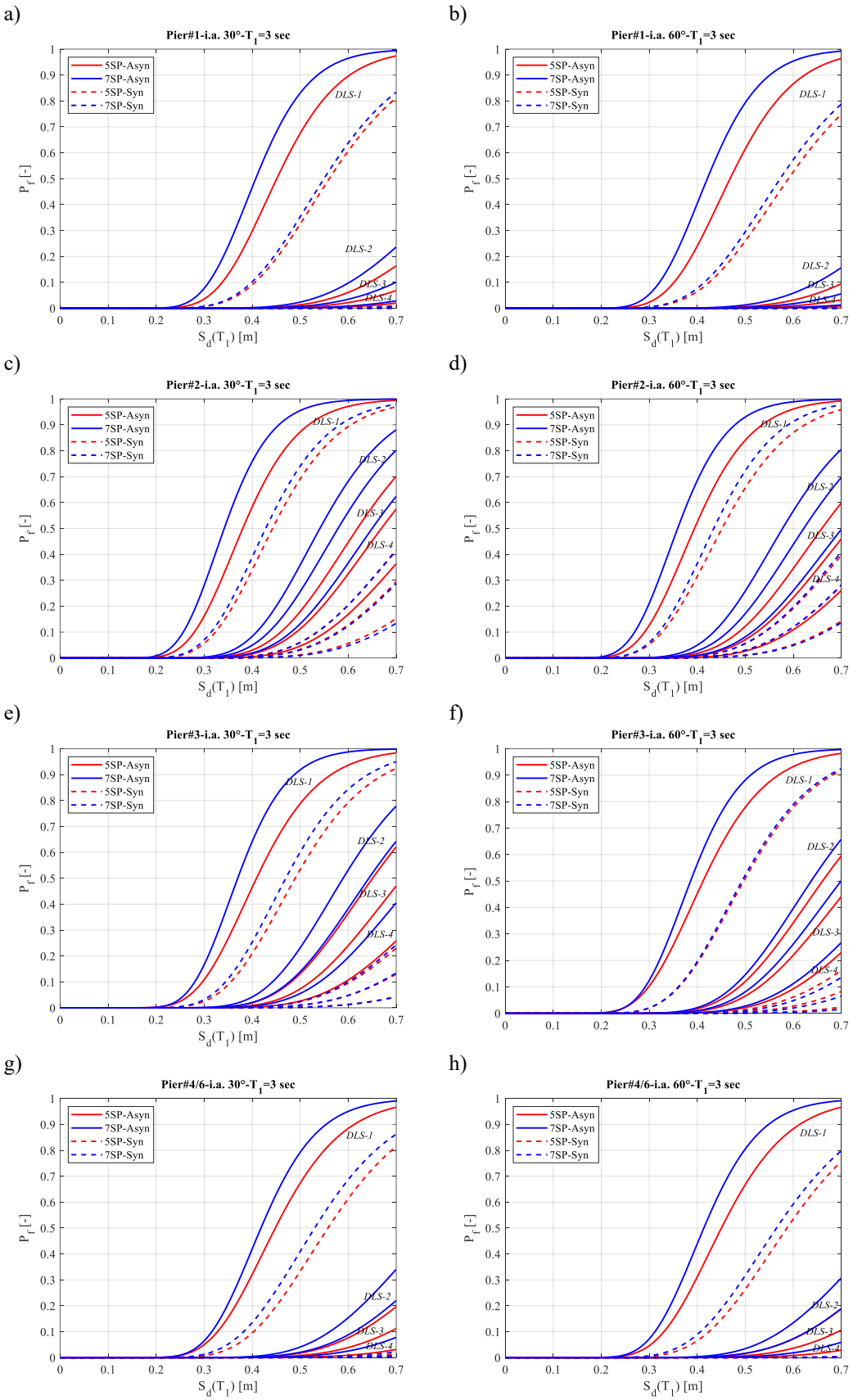

Figure 6.11. Fragility curves for the piers drift [%] for T_1=3sec, for damage limit states from DLS-1 to DLS-4 ; a) Pier 1, i.a. 30°: b) Pier 1, i.a. 60°; c) Pier 2, i.a. 30°; d) Pier 2, i.a. 60°; e) Pier 3, i.a. 30°; f) Pier 3, i.a. 60°; g) Pier 4/6, i.a. 30°; h) Pier 4/6, i.a. 60°.

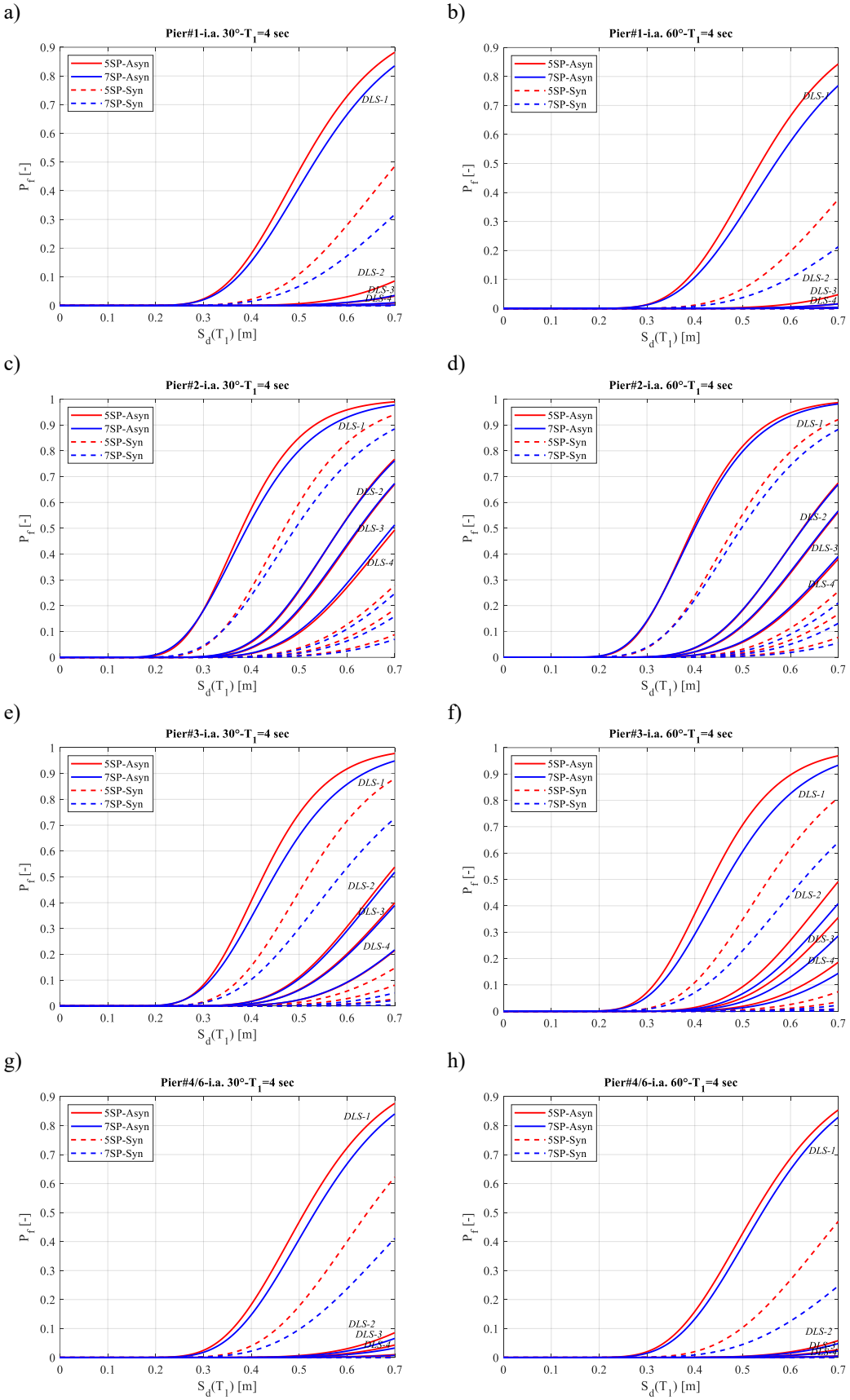

Figure 6.12. Fragility curves for the piers drift [%] for $T_1 = 4\,\text{sec}$, for damage limit states from *DLS*-1 to *DLS*-4 ; a) Pier 1, i.a. 30°: b) Pier 1, i.a. 60°; c) Pier 2, i.a. 30°; d) Pier 2, i.a. 60°; e) Pier 3, i.a. 30°; f) Pier 3, i.a. 60°; g) Pier 4/6, i.a. 30°; h) Pier 4/6, i.a. 60°.

Figure 6.13-Figure 6.15 present fragility in terms of piers curvature ductility $\mu_{\varphi,vet,\max}$. The probabilities of exceeding each of the assumed damage limit states follow the same decreasing trend for increasing isolation periods, as already observed for the piers drift ratios. The greater evidence is again the differences in results among the uniform input condition and the spatially variable one, with the latter consistently showing higher probabilities of failure for all damage limit states. Structural configuration affects the fragility mainly at an isolation period equal to $T_1 = 3\,\text{sec}$ combined with SVEGM condition, where higher probabilities of failure result from the 7-span testbed bridge. Differences can still be appreciated at the other isolation periods of 2 and 4 sec, though there is no clear preference for one configuration over the other.

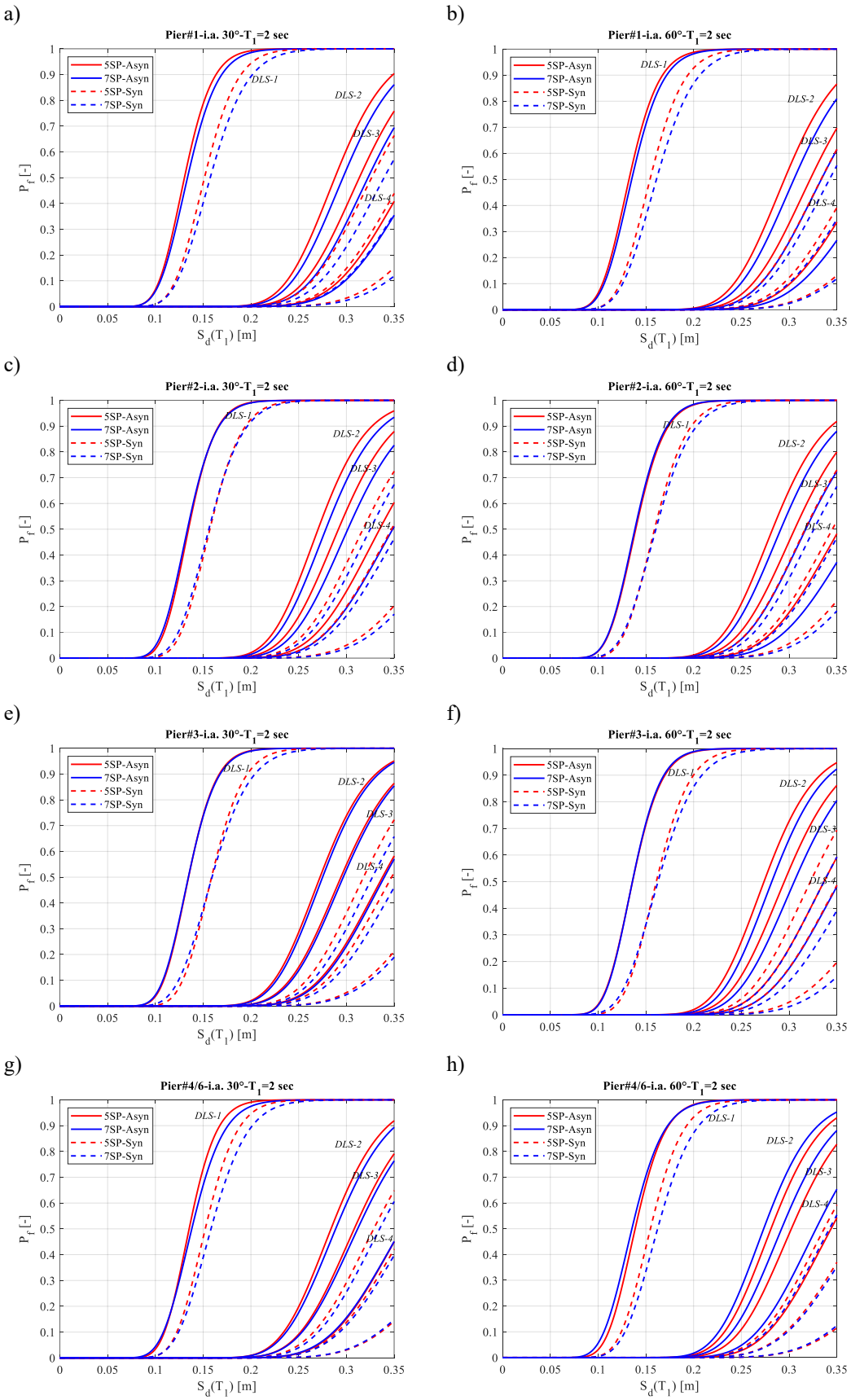

Figure 6.13. Fragility curves for piers curvature ductility [-] for $T_1 = 2\,\text{sec}$, for damage limit states from DLS-1 to DLS-4; a) Pier 1, i.a. 30°; b) Pier 1, i.a. 60°; c) Pier 2, i.a. 30°; d) Pier 2, i.a. 60°; e) Pier 3, i.a. 30°; f) Pier 3, i.a. 60°; g) Pier 4/6, i.a. 30°; h) Pier 4/6, i.a. 60°.

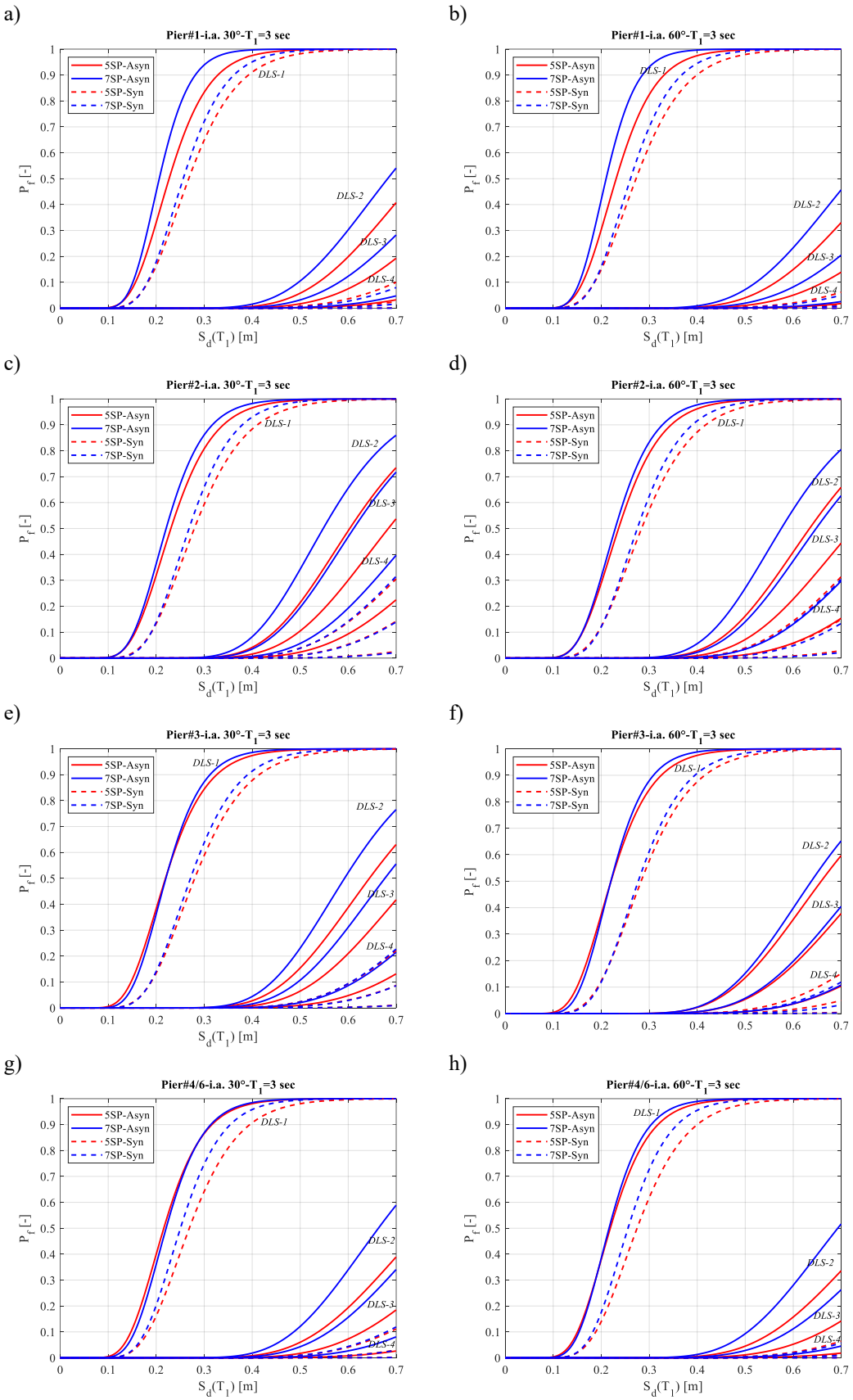

Figure 6.14. Fragility curves for piers curvature ductility [-] for $T_1 = 3\,\text{sec}$, for damage limit states from DLS-1 to DLS-4; a) Pier 1, i.a. 30°; b) Pier 1, i.a. 60°; c) Pier 2, i.a. 30°; d) Pier 2, i.a. 60°; e) Pier 3, i.a. 30°; f) Pier 3, i.a. 60°; g) Pier 4/6, i.a. 30°; h) Pier 4/6, i.a. 60°.

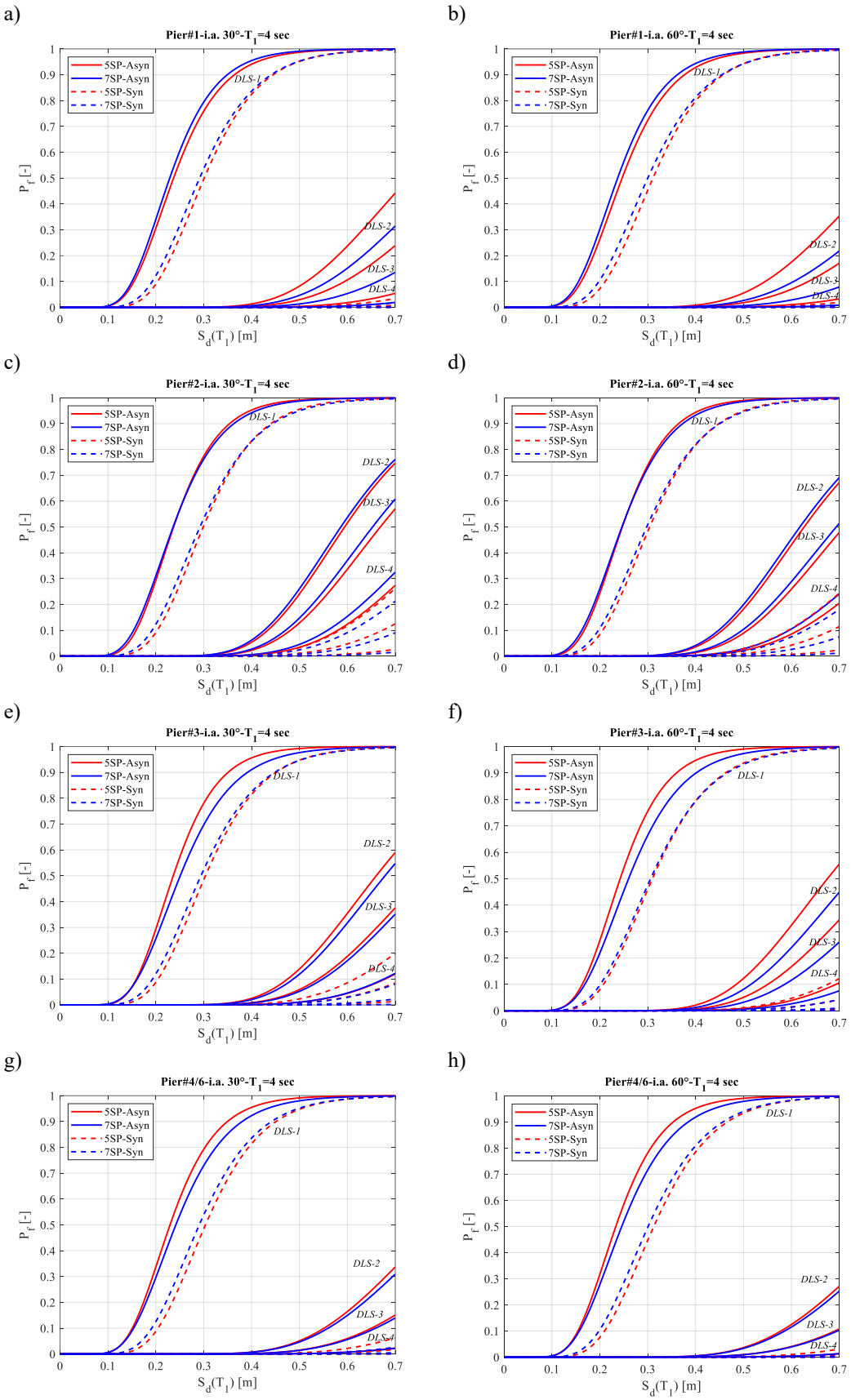

Figure 6.15. Fragility curves for piers curvature ductility [-] for $T_1 = 4\,\text{sec}$, for damage limit states from DLS-1 to DLS-4; a) Pier 1, i.a. 30°; b) Pier 1, i.a. 60°; c) Pier 2, i.a. 30°; d) Pier 2, i.a. 60°; e) Pier 3, i.a. 30°; f) Pier 3, i.a. 60°; g) Pier 4/6, i.a. 30°; h) Pier 4/6, i.a. 60°.

Finally, Figure 6.16-Figure 6.18 show the structural fragility for the isolation level. According to the IDA results presented beforehand, the seismic fragility is higher for the isolators placed at the two abutments compared to the those placed at the highest pier.

The general trend already drawn for the bridge piers is also observed for the isolation system: the seismic fragility decreases for higher values of the isolation period as well as for increasing limit state thresholds.

As for the bridge piers, higher probabilities of exceedance are due to spatially variable input ground motion, while the incidence angle only slightly affects the fragility, mainly at the lowest isolation period. Specifically, an incidence angle of 60° results in lower probabilities of exceeding all the limit state thresholds.

At the lowest isolation period and especially for lower limit state thresholds, the fragility for the two structural configurations is about the same, with only slightly higher probabilities for the 7-span bridge. Differences become more pronounced for the last three *LS* thresholds, but with an increasing fragility due to the 5-span configuration. This behavior is observed both in case of uniform excitation and spatially variable ground motion conditions. At an isolation period of $T_1 = 3\,\mathrm{sec}$ similar observations can be made. Starting from the last three *LS* thresholds the 5-span bridge results to be more vulnerable than the 7-span one. This trend is mainly observed for the isolators at the abutment 1 and at the pier 2. At the highest isolation period the difference among the structural configurations becomes almost negligble especially at the lowest *LS*. Only a small difference can still be observed for the uniform input case at the highest *LS*, with higher probabilities exhibiting from the 5-span bridge case.

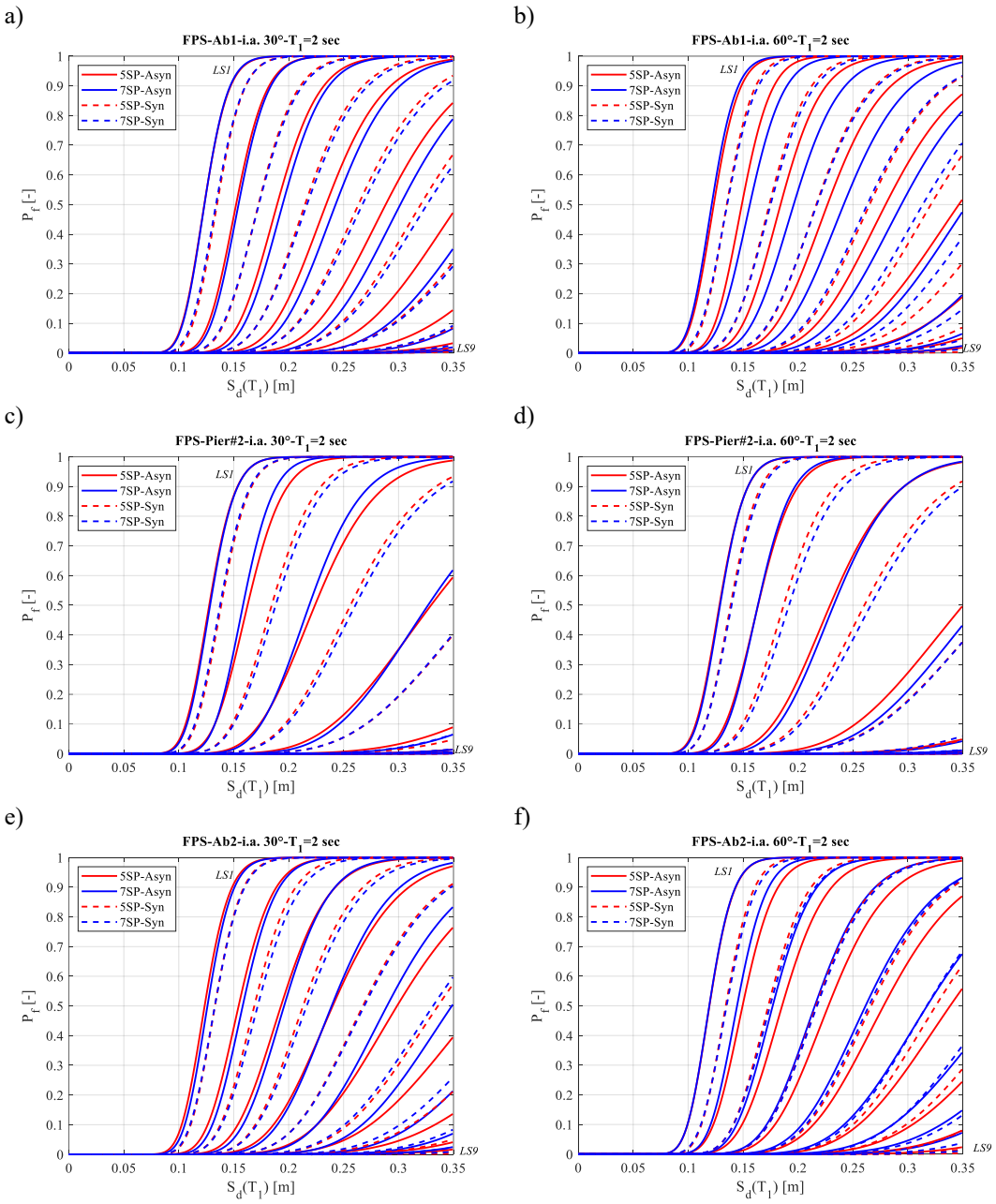

Figure 6.16. Fragility curves of the FPS displacements [m] for $T_1 = 2\,\text{sec}$; a) Abutment 1, i.a. 30°; b) Abutment 1, i.a. 60°; c) Pier 2, i.a. 30°; d) Pier 2, i.a. 60°; e) Abutment 2, i.a. 30°; f) Abutment 2, i.a. 60°.

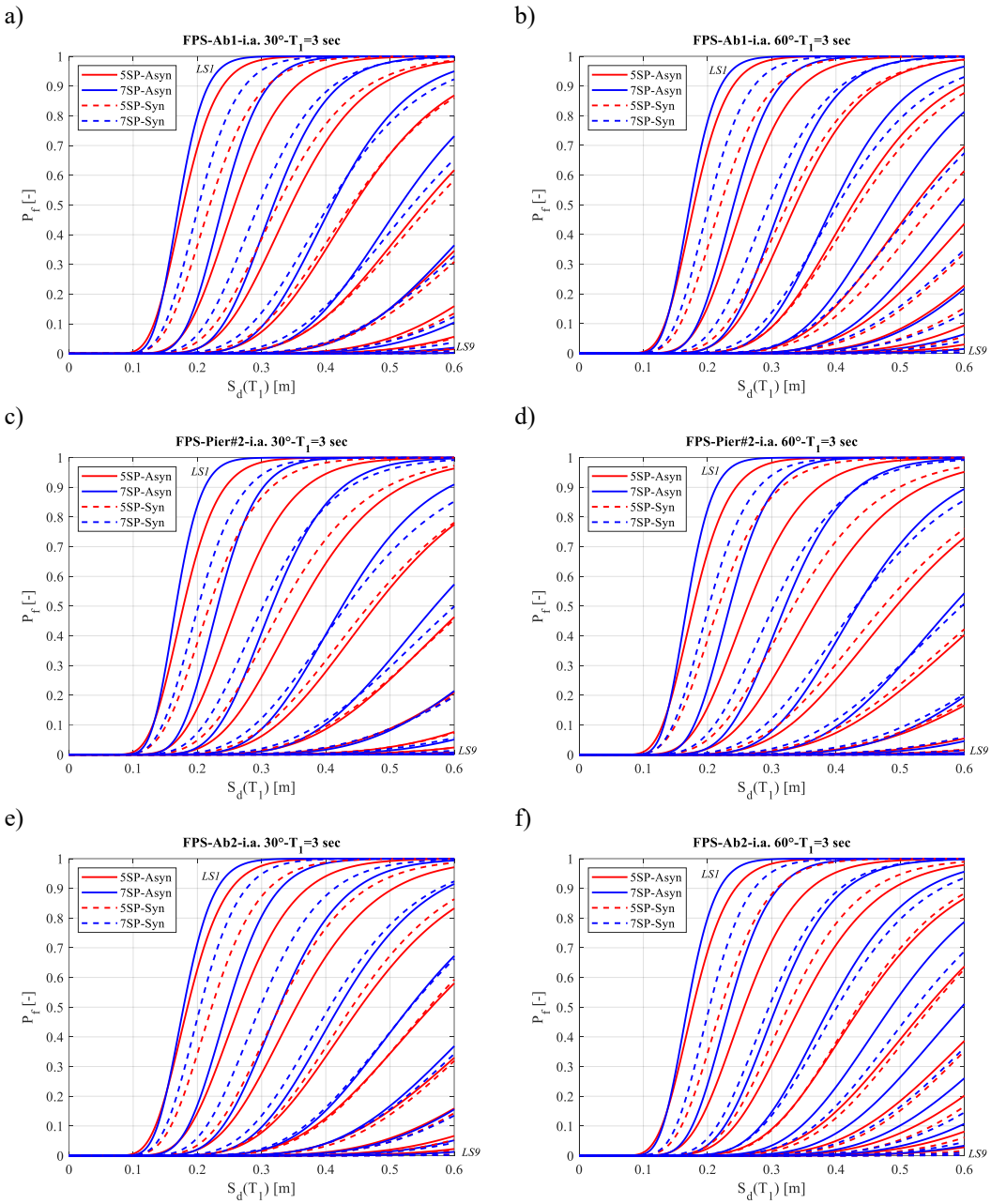

Figure 6.17. Fragility curves of the FPS displacements [m] for $T_1 = 3\text{sec}$; a) Abutment 1, i.a. 30°; b) Abutment 1, i.a. 60°; c) Pier 2, i.a. 30°; d) Pier 2, i.a. 60°; e) Abutment 2, i.a. 30°; f) Abutment 2, i.a. 60°.

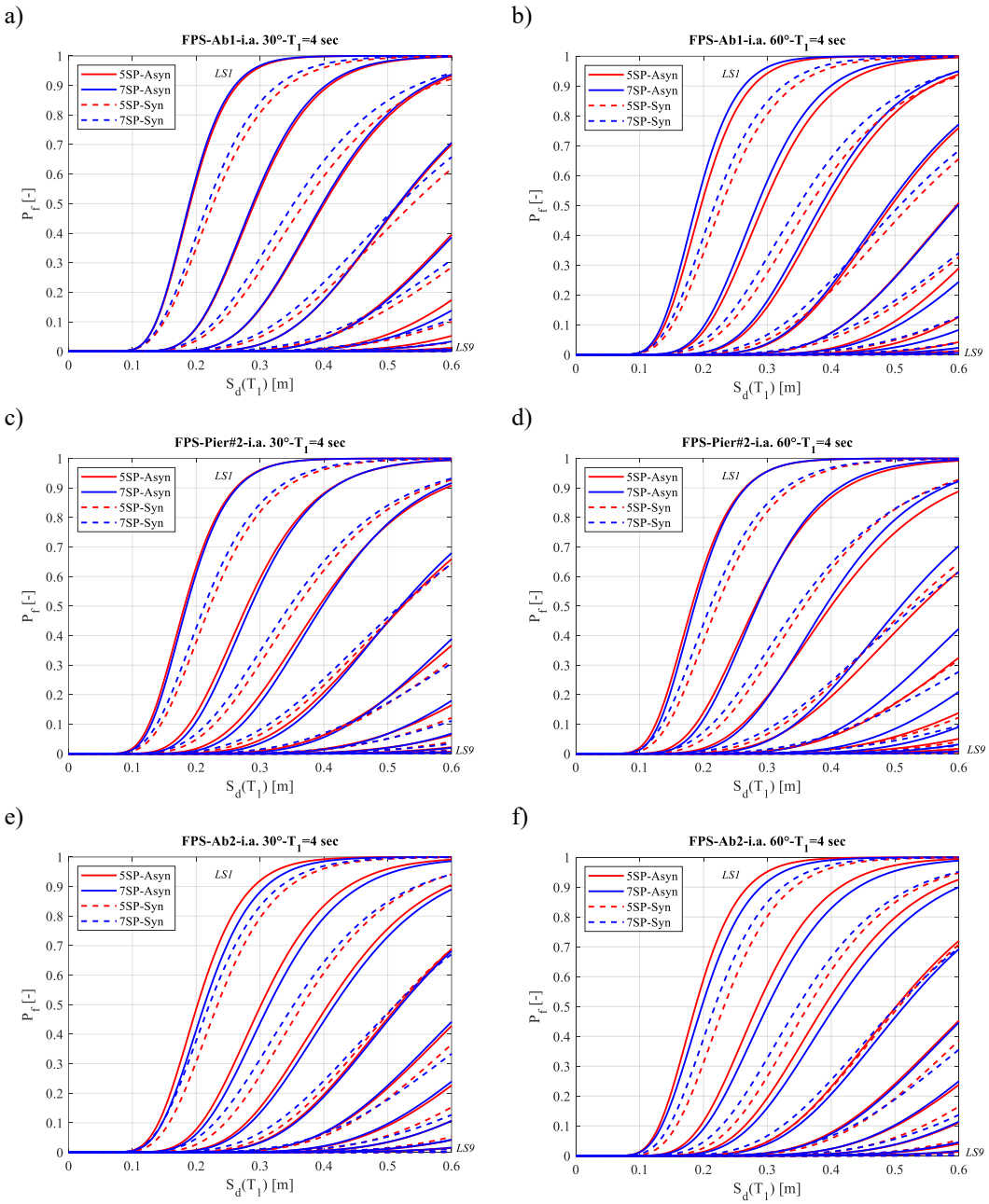

Figure 6.18. Fragility curves of the FPS displacements [m] for $T_1 = 4\,\text{sec}$; a) Abutment 1, i.a. 30°; b) Abutment 1, i.a. 60°; c) Pier 2, i.a. 30°; d) Pier 2, i.a. 60°; e) Abutment 2, i.a. 30°; f) Abutment 2, i.a. 60°.

6.5 Seismic hazard

Integrating the previously defined fragility curves with the seismic hazard curves for the reference site of L'Aquila, expressed in terms of the same intensity measure *IM*, $S_d(\xi_1, T_1)$, allows for the calculation of the mean annual rates of exceeding the damage limit states. As will be detailed later, these latter ones can be transformed into probabilities of exceeding the damage limit state in the time frame of interest (*e.g.*, 50 years), by adopting a Poisson distribution such as to evaluate the seismic reliability of the analyzed bridge components (*i.e.*, piers and FP bearings).

As already mentioned, the reference site considered for the evaluation of the seismic hazard is L'Aquila (Italy), with geographic coordinates 42°38'49''N 13°42'25''E, ID:26306.

Taking advantage of the information elaborated by the Italian INGV (Istituto Nazionale di Geofisica e Vulcanologia) through the *INPV DPC-INGV-S1* project [119], it is possible to retrieve nine different values of the peak ground acceleration (PGA), adopted by the INGV as representative parameter of the local seismicity, for as many mean annual frequencies of exceeding λ_s, and corresponding to three different percentiles $(16-th, 50-th, 84-th)$.

Each value of the PGA is associated with the probability of exceeding that value (POE) in 50 years. Using the well-known relation $\lambda_S = 1/T_{R,S}$, nine different mean values of the return periods are also identified, as summarized in Table 6.12.

$T_R[yrs]$	POE in 50 yrs [%]	$\lambda_s[years^{-1}]$	$PGA(16-th)[g]$	$PGA(50-th)[g]$	$PGA(84-th)[g]$
2475	2	0.0004	0.410	0.452	0.523
975	5	0.001	0.303	0.334	0.367
475	10	0.0021	0.238	0.261	0.284
201	22	0.005	0.174	0.190	0.204
140	30	0.0071	0.151	0.164	0.175
101	39	0.0099	0.131	0.142	0.153
72	50	0.0139	0.113	0.123	0.132
50	63	0.0199	0.098	0.104	0.111
30	81	0.0332	0.087	0.078	0.087

Table 6.12. PGA values for the reference site of L'Aquila (Italy) for soil category A, corresponding to three different percentiles and 9 *IM*Ls.

Starting from the hazard curves expressed in terms of PGA, the elastic pseudo-acceleration response spectrum is derived for the reference site and at the aforementioned return periods, corresponding to three different percentiles. Consequently, the spectral displacement at the three bridge isolation periods $T_1 = 2, 3, 4\,\text{sec}$ is calculated as:

$$S_d(T_1) = \frac{S_{pa}(T_1)}{\omega_1^2} \tag{6.40}$$

Being ω_1 the circular frequency expressed as $\omega_1 = 2\pi / T_1$.

The spectral displacements are calculated for each of the return periods such as to obtain the median curve of λ_s, indicated as $\bar{\lambda}_s$ and defined at nine different points.

Starting from the median curve it is possible to evaluate the mean hazard curve λ_s, by means of an amplification factor β_H, through the following relationship:

$$\lambda_S(S_d) = \bar{\lambda}_S(S_d) \exp\left(\frac{1}{2}\beta_H^2\right) \tag{6.41}$$

Where the amplification factor β_H is evaluated as:

$$\beta_H = \frac{\ln(S_{d,84-th}) - \ln(S_{d,16-th})}{2} \tag{6.42}$$

This accounts for the epistemic uncertainty hidden in the seismic hazard evaluation.

$S_{d,16-th}$ and $S_{d,84-th}$ are respectively the spectral displacements calculated for the isolation periods of interest and at nine different return periods, starting from the values of the PGA at the 16-*th* and 84-*th* percentiles.

The mean hazard curve defined at nine points is further processed in the logarithmic space, by means of an interpolating quadratic function of the type:

$$\ln\left(\lambda_s(S_d)\right) = k_1 \cdot \ln\left(S_d\right)^2 + k_2 \cdot \ln\left(S_d\right) + k_3 \tag{6.43}$$

Where k_1, k_2, k_3 are the regression parameters. By means of Eq.(6.43) it is straightforward to move in the linear space.

In Figure 6.19, considering the site of L'Aquila (Italy) and with reference to soil category A [77], the seismic hazard curves expressed in terms of $IM = S_d(T_1)$ with T_1 equal to the isolation period, are plotted in a semilogarithmic scale. Each curve, corresponding to a different isolation period T_1, expresses the average values of the annual rates λ_s of exceeding the $IM = S_d(T_1)$. It can be observed that the seismic hazard increases as the isolated period increases from 2 to 4 sec.

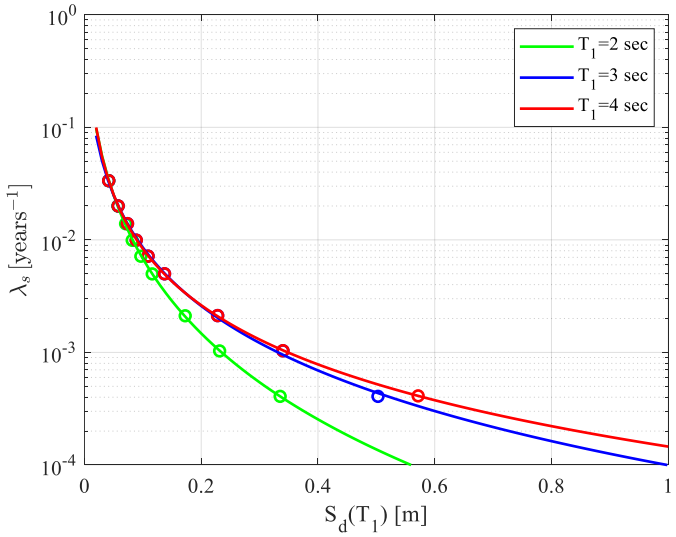

Figure 6.19. Seismic hazard curves for the reference site of L'Aquila, in terms of spectral displacement $S_d(T_1)$, for three different isolation periods.

6.6 Seismic reliability analysis

Performance-based earthquake engineering (PBEE) assumes that if seismic damage accumulation is not considered, not only the occurrence of earthquakes at the reference site follows a homogeneous Poisson process (HPP), but it also does the process of earthquakes causing structural failure. Following this assumption the probability of exceeding a generic damage limit state in the time frame of interest is one-parameter dependent, that is the mean annual rate of exceeding the corresponding damage limit state $\lambda_{f,LS}$. This must be evaluated for both the FPS bearings and bridge piers by means of a convolution integral between the beforehand calculated seismic fragilities and seismic hazard curves, expressed in terms of the same *IM*, as for the following relationship:

$$\lambda_{f,LS} = \int_s P_{f,LS}[s] \cdot |d\lambda_s| \tag{6.44}$$

Where $d\lambda_s = d(s) \cdot d\lambda_s / d(s)$ is obtained from the derivative of the seismic hazard curve and $P_{f,LS}[s]$ is the probability of exceeding the generic damage limit state conditional to the *i*-th value *s* of the ground motion intensity measure *IM* (*i.e.* $s = S_{d,i}(T_1)$).

Then, the mean annual rate of exceeding the corresponding damage limit state $\lambda_{f,LS}$ is converted into probability of exceeding the same damage limit state in the time frame of interest (*e.g.*, 50 years), taking advantage of the abovementioned Poisson distribution, through the well-known expression:

$$P_f(50yrs) = 1 - e^{\lambda_{f,LS} \cdot 50yrs} \tag{6.45}$$

Eq. (6.45) permits to evaluate the seismic reliability curves for both the FP bearings and the bridge piers, for each limit state, in the time frame of interest, chosen equal to 50 years, as will be illustrated in the next section. The so computed probability of exceeding the generic damage limit state are also compared with acceptable probabilities of failure P_f^* (target probabilities of failure) as provided in [80] and reported in Table 6.13-Table 6.14:

Damage limit states for bridge piers		P_f^*
DLS-1	Slight damage	$5 \cdot 10^{-1}$
DLS-2	Moderate damage	$1.6 \cdot 10^{-1}$
DLS-3	Extensive damage	$2.2 \cdot 10^{-2}$
DLS-4	Complete damage	$1.5 \cdot 10^{-3}$

Table 6.13. Acceptable probabilities of failure P_f^* for bridge piers.

Limit states for the FPS bearing									
	LS1	*LS2*	*LS3*	*LS4*	*LS5*	*LS6*	*LS7*	*LS8*	*LS9*
$r[m]$	0.10	0.15	0.20	0.25	0.30	0.35	0.40	0.45	0.50
P_f^*									
$1.5 \cdot 10^{-3}$									

Table 6.14. Acceptable probabilities of failure P_f^* for FP bearings.

6.6.1 Seismic reliability curves

Figure 6.20-Figure 6.22 depict the probabilities of exceeding the damage limit state in the time frame of interest (50 years) valid for the bridge piers and derived from the seismic fragility assessment expressed in terms of drift ratios. The plots, that compare the two structural bridge configurations and the uniform and spatially variable input conditions, are presented in a semilogarithmic scale in the range $10^{-5}:10^{0}$, depending on the specific pier and on the isolation period considered.

The horizontal axis represents the damage limit state thresholds in terms of drift ratios. The results are further compared with the performance objective curve constructed based on the target probabilities of failure. The curves highlight a generally increasing trend of the seismic reliability (lower probabilities of failure) for increasing values of the isolation period T_1. This trend reaffirms the effectiveness of the seismic isolation in enhancing structural performances.

In the uniform input condition, consistently higher levels of seismic reliability are achieved compared to the spatially variable earthquake ground motion (SVEGM) condition. These differences are particularly evident at the highest isolation period and at the highest damage limit states threshold, specifically for those piers of lower height. Conversely, a smaller influence is noted concerning

the incidence angle, some changes in results are more evident only for the highest isolation period; in this case, an incidence angle of 60° generally increases seismic reliability.

Irrespective of the isolation period and across all the considered piers and structural configurations, the fourth damage limit state, which imposes the lowest target probability of failure, is always exceeded. This outcome primarily arises due to the very stringent limite state thresholds adopted for the base-isolated bridge structure [117]. However, exceptions to this trend are observed in cases involving piers with lower height, combined with the uniform ground motion input condition and isolation periods greater than 2 seconds.

Structural configuration has practically no effects at the lowest isolation period, whereas, in line with the seismic fragility findings, tends to affect the response at an isolation period T_I=3sec, where the seismic reliability decreases in the case of the 7-span configuration.

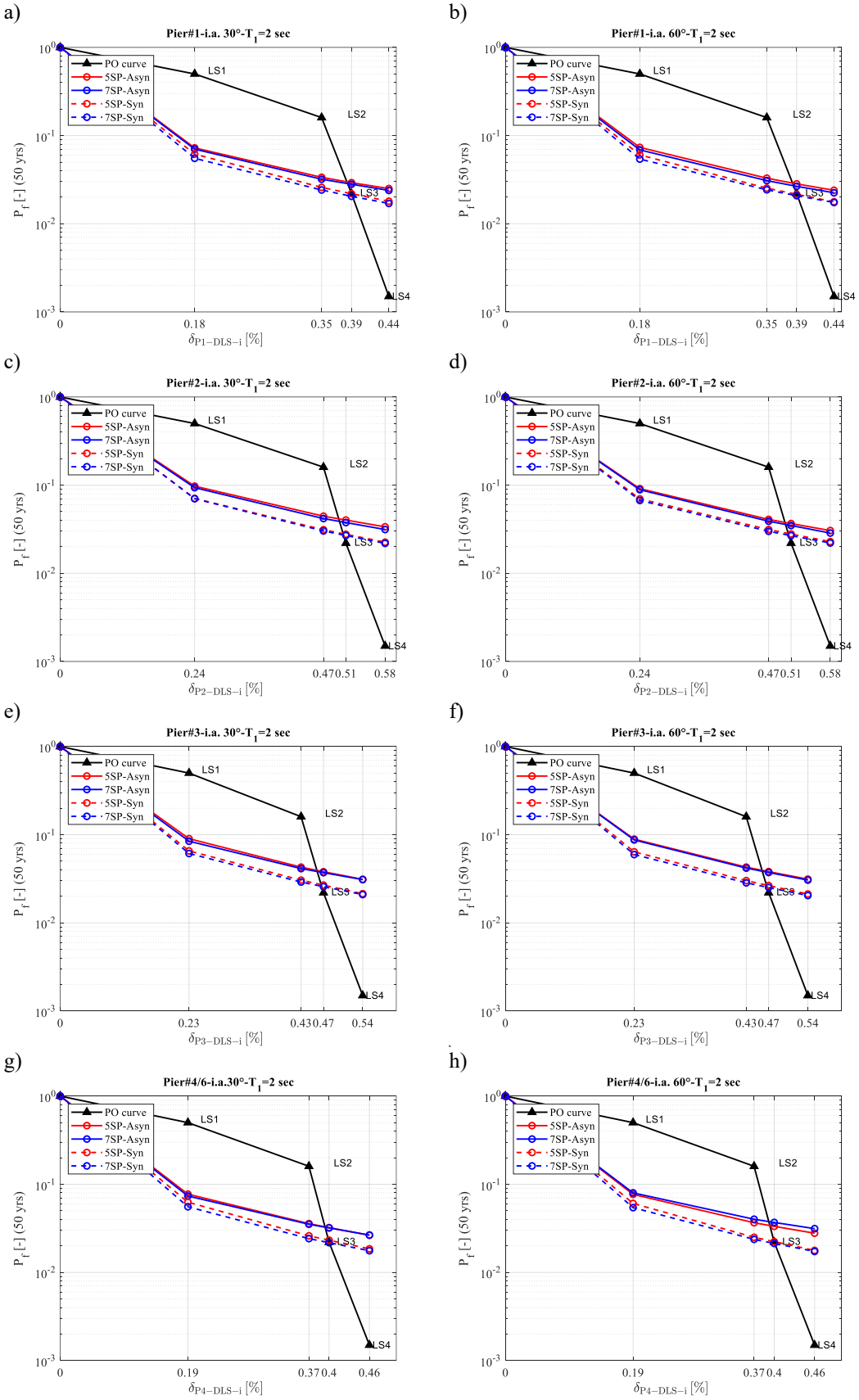

Figure 6.20. Reliability curves for piers drift [%] for T_1=2sec; a) Pier 1, i.a. 30°; b) Pier 1, i.a. 60°; c) Pier 2, i.a. 30°; d) Pier 2, i.a. 60°; e) Pier 3, i.a. 30°; f) Pier 3, i.a. 60°; g) Pier 4/6, i.a. 30°; h) Pier 4/6, i.a. 60°.

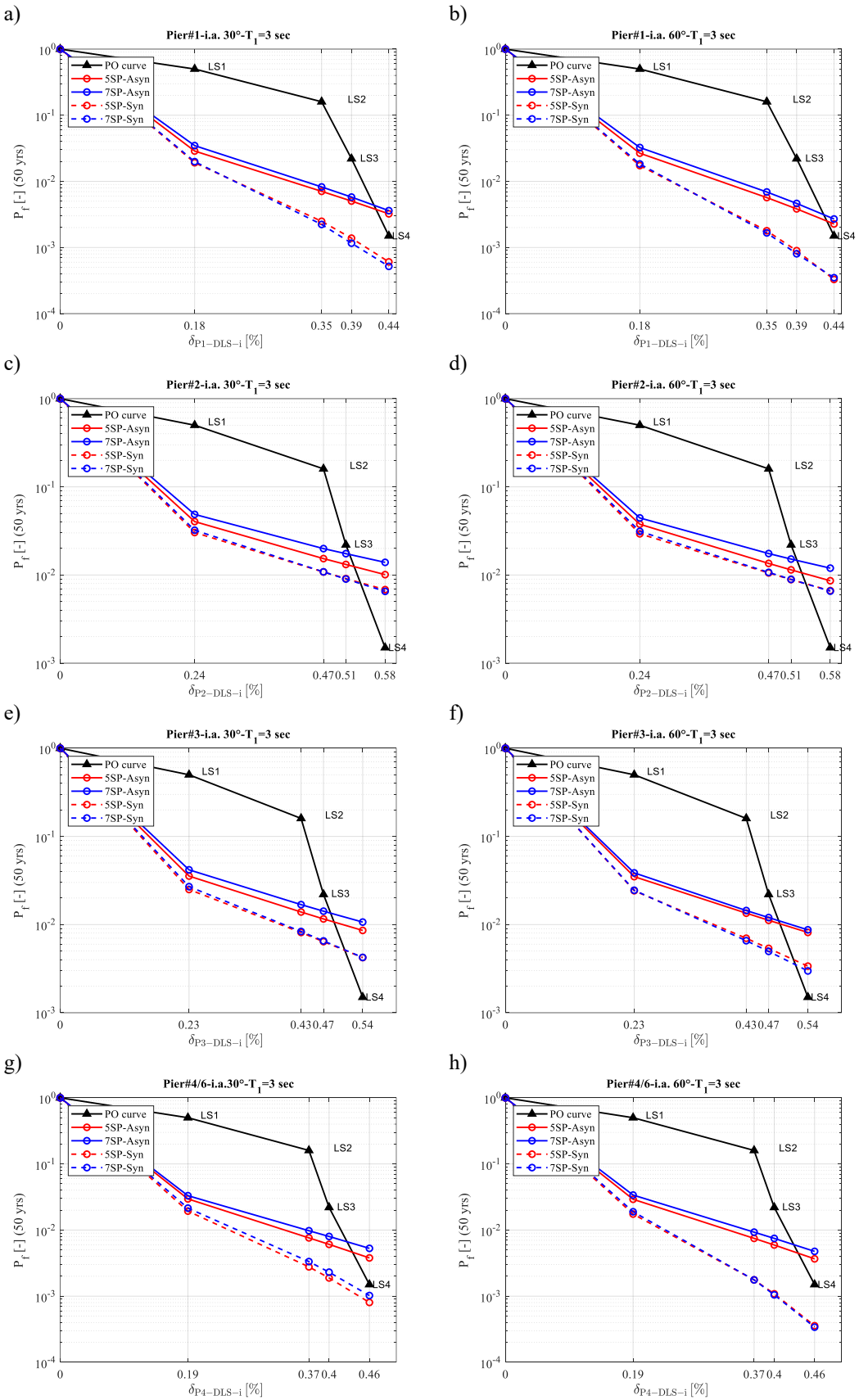

Figure 6.21. Reliability curves for piers drift [%] for $T_1 = 3\,\text{sec}$; a) Pier 1, i.a. 30°; b) Pier 1, i.a. 60°; c) Pier 2, i.a. 30°; d) Pier 2, i.a. 60°; e) Pier 3, i.a. 30°; f) Pier 3, i.a. 60°; g) Pier 4/6, i.a. 30°; h) Pier 4/6, i.a. 60°.

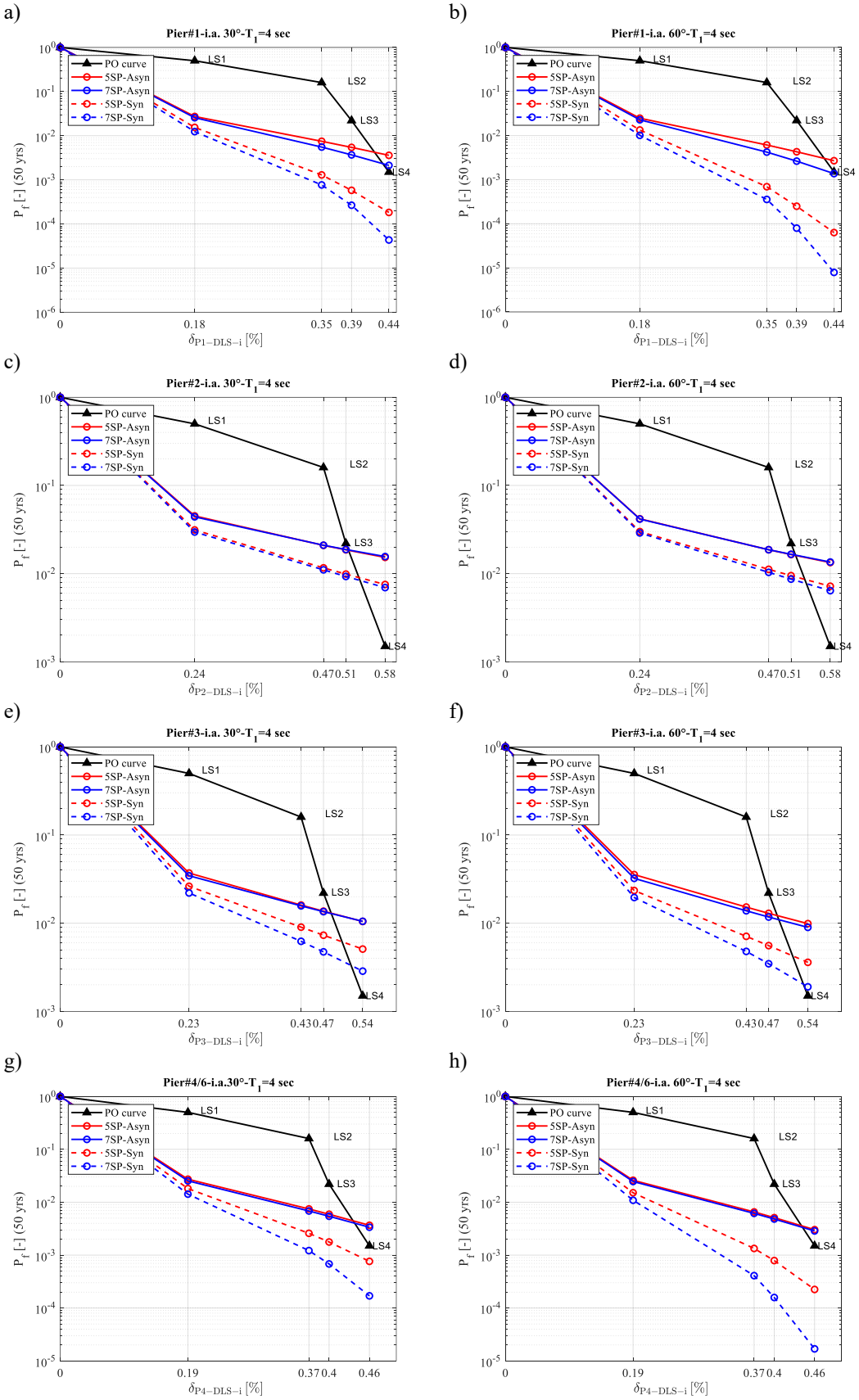

Figure 6.22. Reliability curves for piers drift [%] for T_1=4sec; a) Pier 1, i.a. 30°; b) Pier 1, i.a. 60°; c) Pier 2, i.a. 30°; d) Pier 2, i.a. 60°; e) Pier 3, i.a. 30°; f) Pier 3, i.a. 60°; g) Pier 4/6, i.a. 30°; h) Pier 4/6, i.a. 60°.

Figure 6.23-Figure 6.25 show the reliability curves associated with the pier's curvature ductility $\mu_{\varphi,vet,\max}$.

In terms of seismic reliability evaluated through curvature ductility, it is possible to draw the same conclusions already stated for the seismic reliability expressed in terms of drift ratios $\delta_{vet,\max}$. Spatial variability of earthquake ground motion worsens seismic performances, resulting in a lower seismic reliability.

Additionaly, there is an increasing reliability as the isolation period increases particularly under an incidence angle condition of 60°. In terms of ductility, the fourth damage limit state is practically never respected under SVEGM conditions, even at the highest isolation period. The third damage limit state is overcome only under SVEGM and at the lowest isolation period T_I=2sec. Indeed, increasing the isolation period has the effect to reduce the probability of exceeding damage limit states, permitting to satisfy limit states up to *DLS*-3.

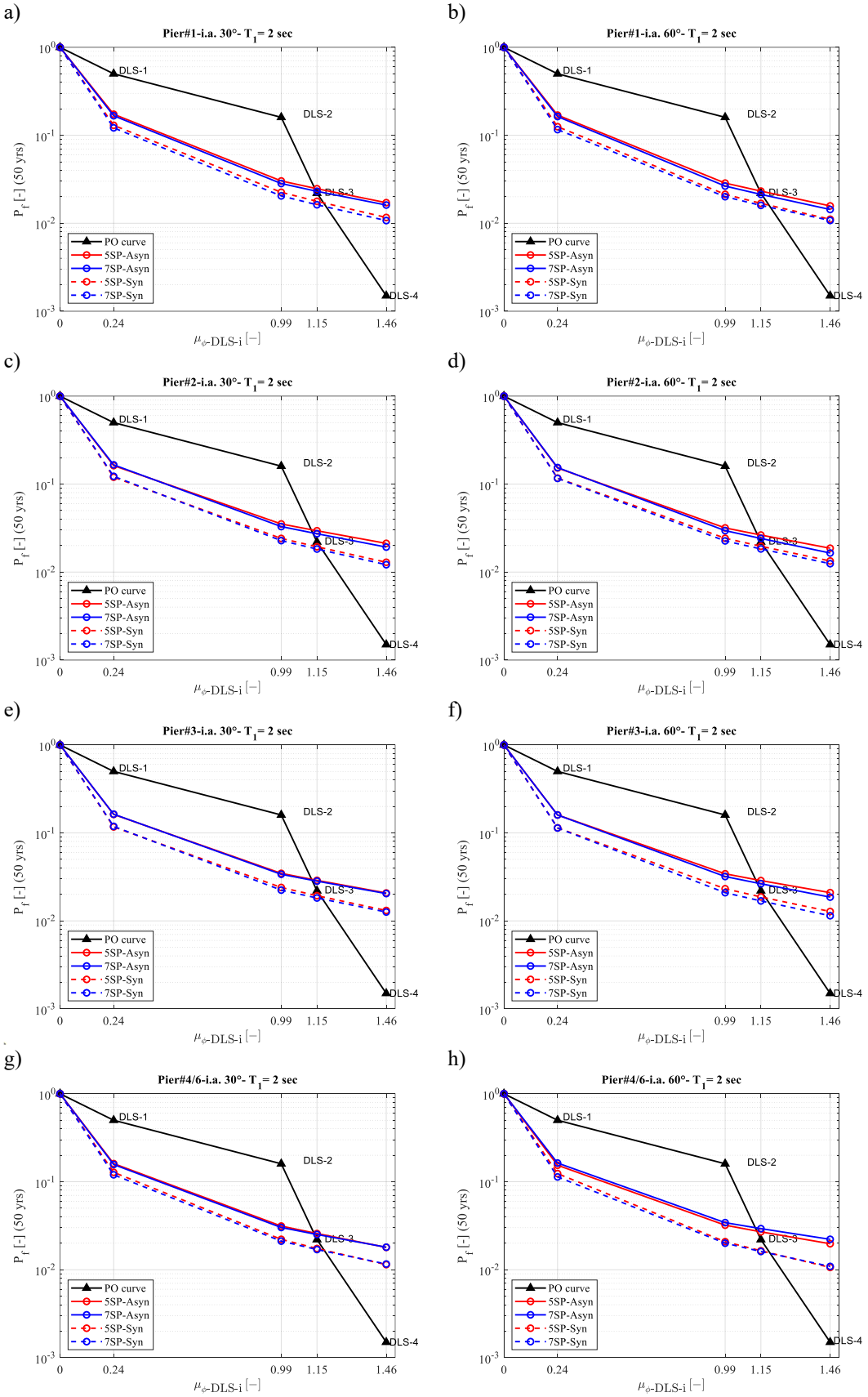

Figure 6.23. Reliability curves for piers curvature ductility [-] for $T_1 = 2\,\text{sec}$; a) Pier 1, i.a. 30°; b) Pier 1, i.a. 60°; c) Pier 2, i.a. 30°; d) Pier 2, i.a. 60°; e) Pier 3, i.a. 30°; f) Pier 3, i.a. 60°; g) Pier 4/6, i.a. 30°; h) Pier 4/6, i.a. 60°.

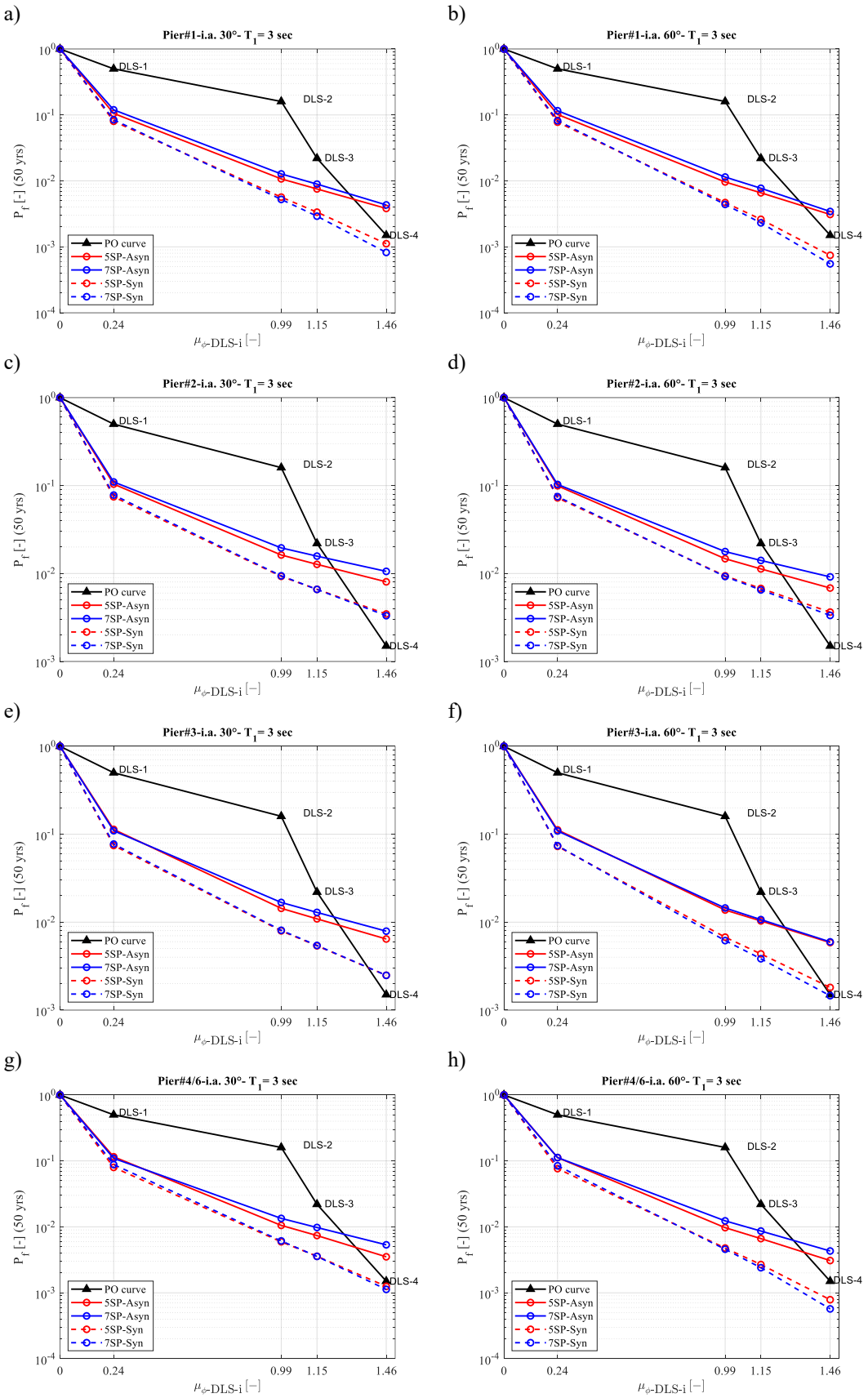

Figure 6.24. Reliability curves for piers curvature ductility [-] for T_1=3sec; a) Pier 1, i.a. 30°; b) Pier 1, i.a. 60°; c) Pier 2, i.a. 30°; d) Pier 2, i.a. 60°; e) Pier 3, i.a. 30°; f) Pier 3, i.a. 60°; g) Pier 4/6, i.a. 30°; h) Pier 4/6, i.a. 60°.

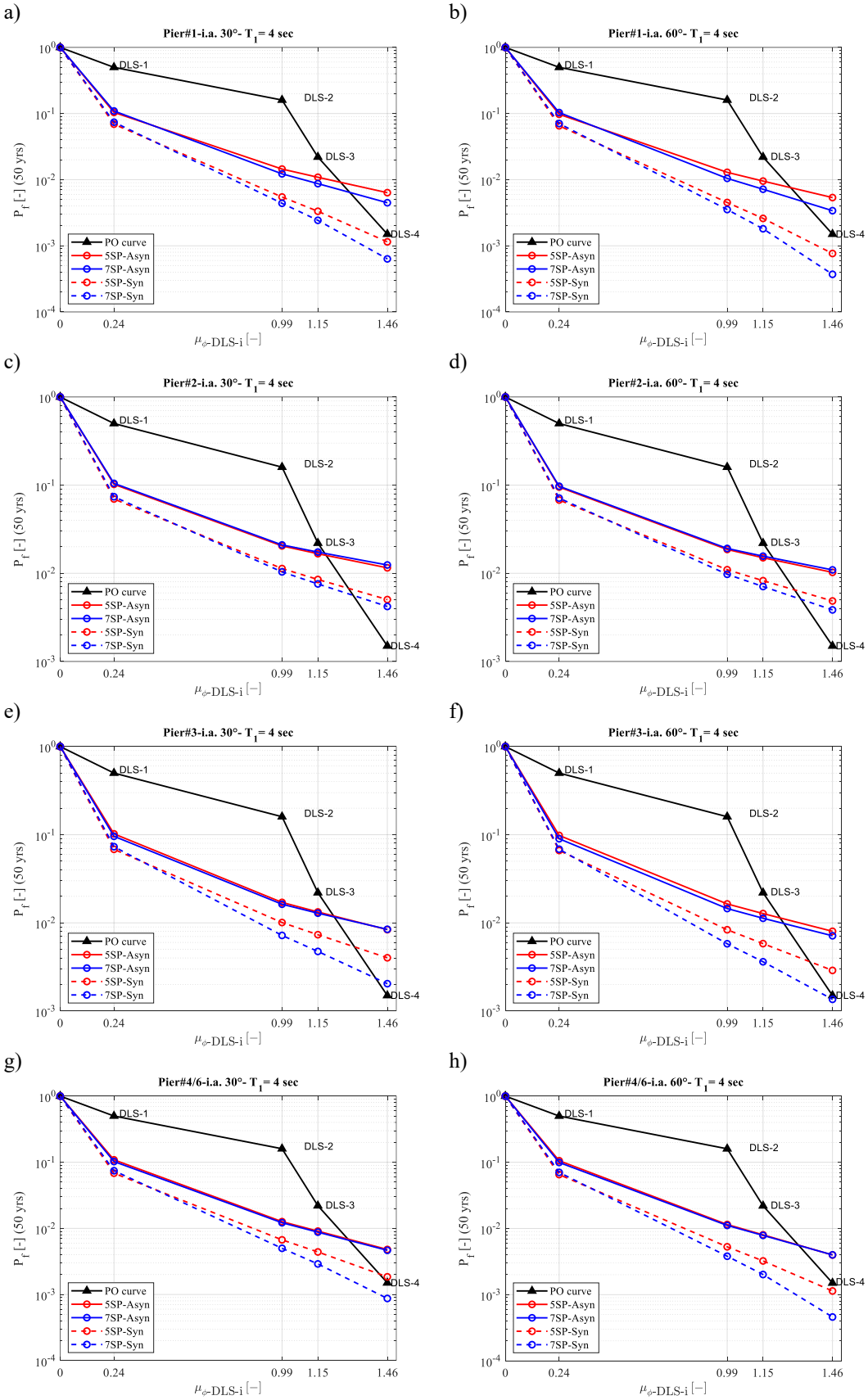

Figure 6.25. Reliability curves for piers curvature ductility [-] for T_1=4sec; a) Pier 1, i.a. 30°; b) Pier 1, i.a. 60°; c) Pier 2, i.a. 30°; d) Pier 2, i.a. 60°; e) Pier 3, i.a. 30°; f) Pier 3, i.a. 60°; g) Pier 4/6, i.a. 30°; h) Pier 4/6, i.a. 60°.

Finally, Figure 6.26-Figure 6.28 show the seismic reliability with reference to the isolation level. The curves are presented in a semilogarithmic plane in the range range $10^{-4}:10^{0}$ depending on the specific isolator's position and on the isolation period. The seismic reliability of the friction devices is plotted against the different FP displacement thresholds, as presented in Table 6.7, ranging from 0.10 m to 0.50m. It is possible to observe an increasing trend of the seismic reliability as the isolation period increases while it is always evident that the worst scenario is associated with the SVEGM condition with respect to the uniform case, particularly noticeable at the highest isolation period and for higher *LS*s thresholds.

Regarding structural configuration, it can be stated that they result in almost the same reliability levels concerning the friction devices, with slightly higher probabilities of exceedance for the 7-span configuration, even if some inverting trend can be highlighted at isolation period T_1 equal to 3 sec and 4 sec for the last three limit states thresholds.

The main outcome concerning the incidence angle condition is that a 60° angle has the main effect of magnifying the difference between SVEGM and uniform input conditions, especially at the highest isolation period.

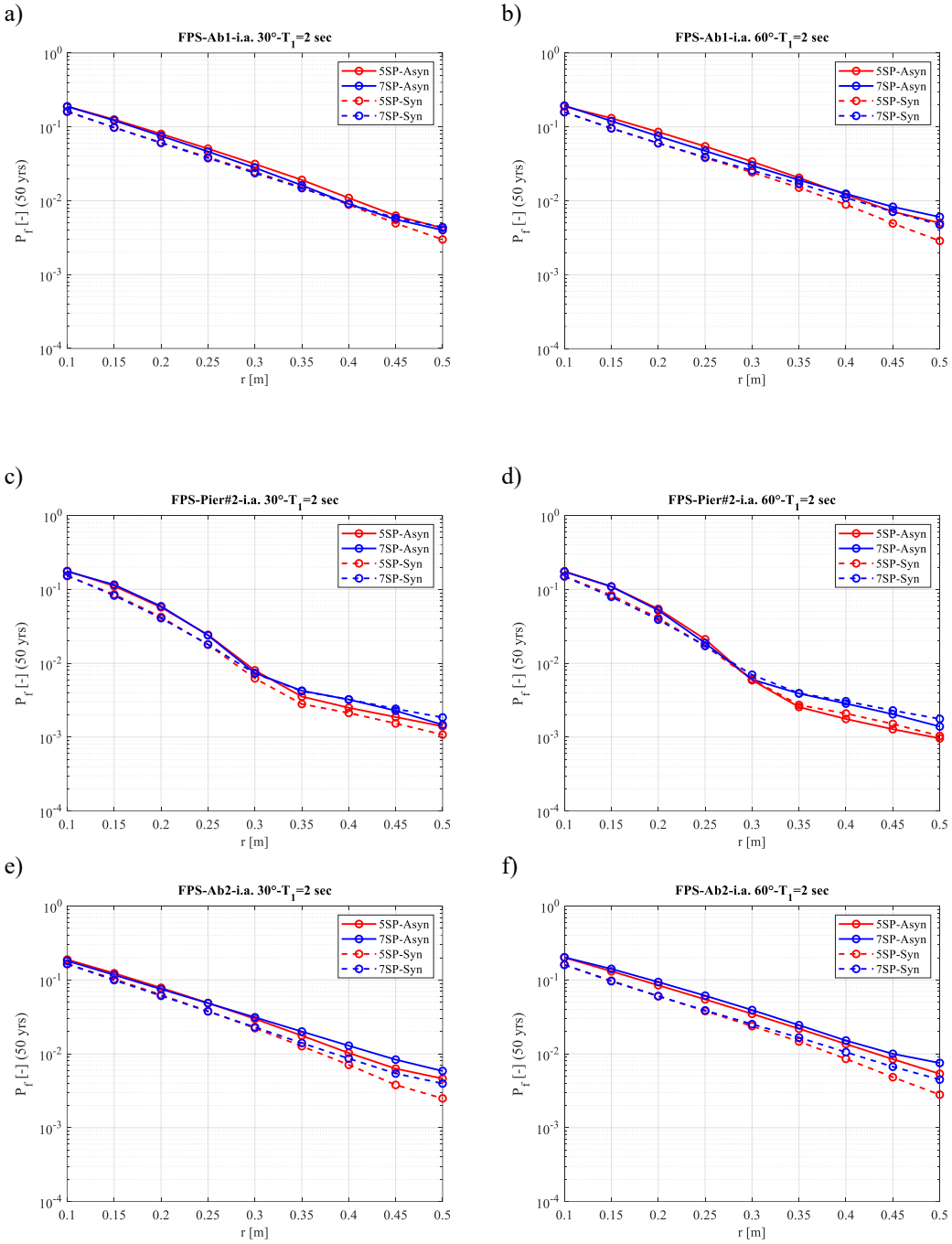

Figure 6.26. Reliability curves for the FPS displacements [m] for $T_1 = 2\text{sec}$; a) Abutment 1, i.a. 30°; b) Abutment 1, i.a. 60°; c) Pier 2, i.a. 30°; d) Pier 2, i.a. 60°; e) Abutment 2, i.a. 30°; f) Abutment 2, i.a. 60°.

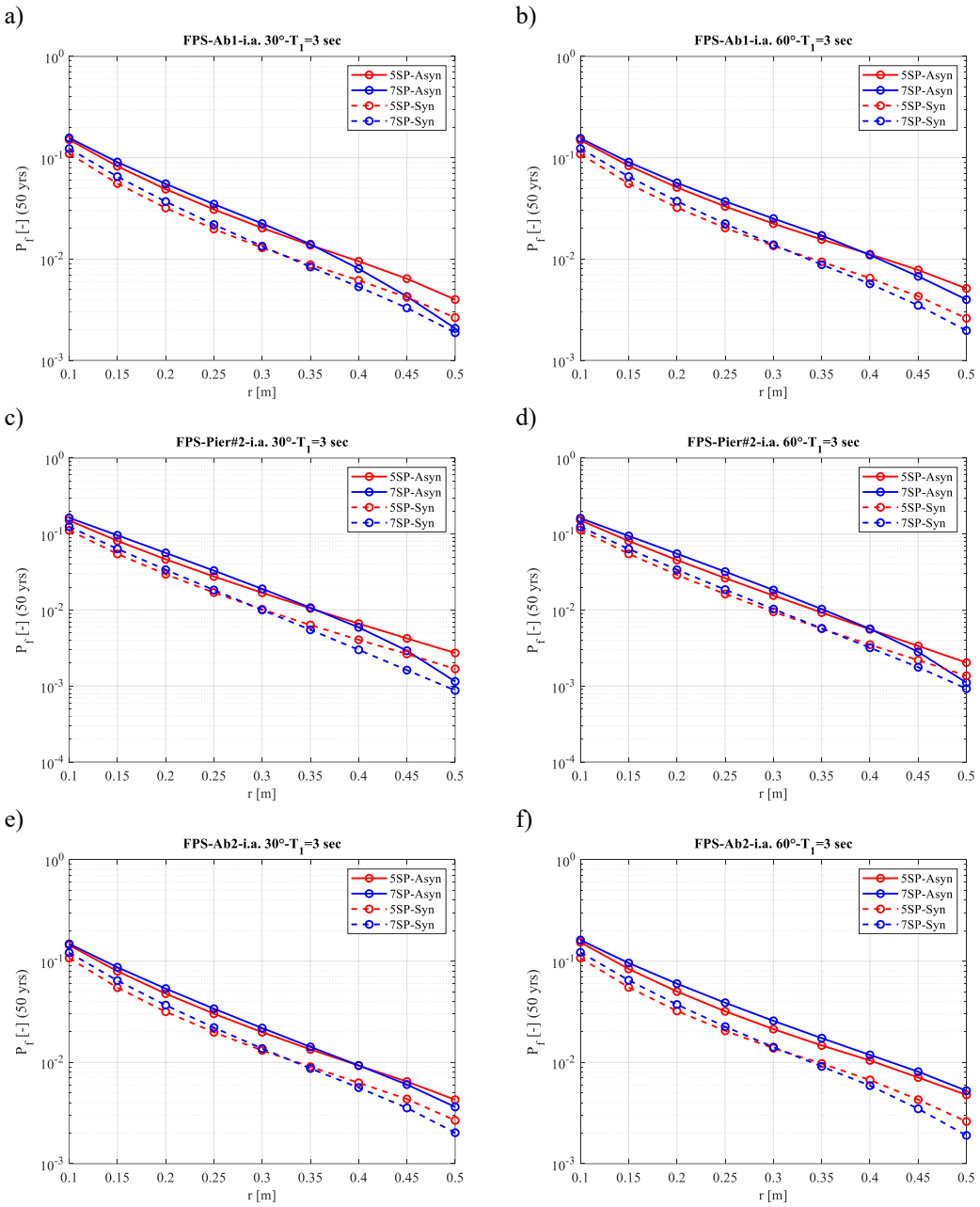

Figure 6.27. Reliability curves for the FPS displacements [m] for $T_1 = 3\text{sec}$; a) Abutment 1, i.a. 30°; b) Abutment 1, i.a. 60°; c) Pier 2, i.a. 30°; d) Pier 2, i.a. 60°; e) Abutment 2, i.a. 30°; f) Abutment 2, i.a. 60°.

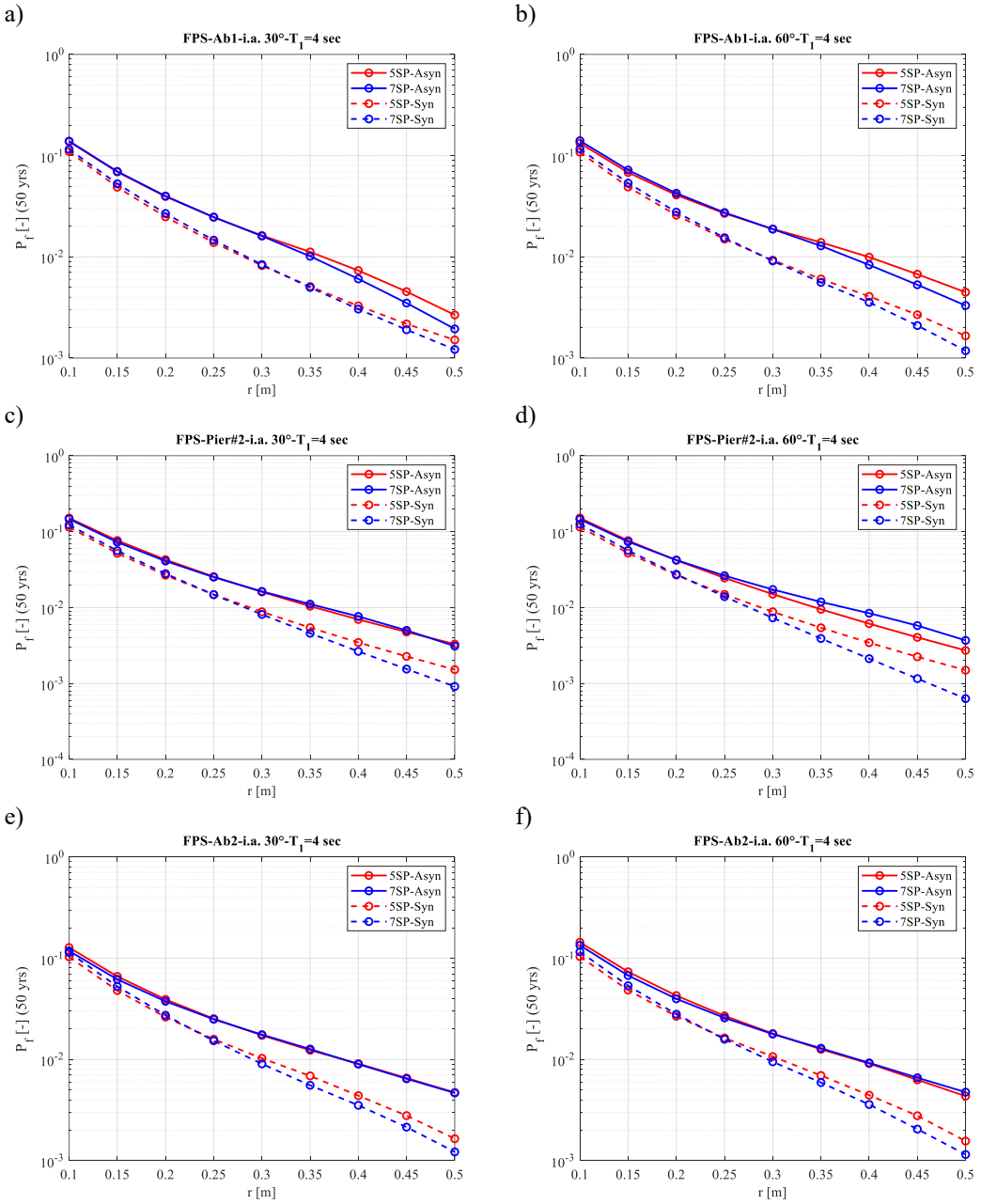

Figure 6.28. Reliability curves for the FPS displacements [m] for $T_1 = 4\text{sec}$; a) Abutment 1, i.a. 30°; b) Abutment 1, i.a. 60°; c) Pier 2, i.a. 30°; d) Pier 2, i.a. 60°; e) Abutment 2, i.a. 30°; f) Abutment 2, i.a. 60°.

6.6.2 Seismic Reliability-Based Design (SRBD) abacuses

The seismic reliability curves related to the FP bearing devices are further processed in the same semilogarithmic plane by means of a linear regression law, in order to obtain seismic reliability-based design (SRBD) abacuses for a preliminary design of the plan dimension of the isolator (*i.e.* radius in plan r of the FP concave surface) as a function of the selected target reliability and of the other structural parameters considered in the analysis, for a geographical area with a seismic hazard similar to the one considered in this study (*i.e.* L'Aquila).

The lowest value of *R*-square is equal to 0.97 confirming the effectiveness of the regression.

From the linear regression results, it is possible to observe that across all the isolation periods and structural configurations, the target probability of failure equal to $P_f = 1.5 \cdot 10^{-3}$ is reached through a radius in plan that ranges from a minimum value of 0.43m, referred to the uniform input condition to 0.68m under SVEGM input condition.

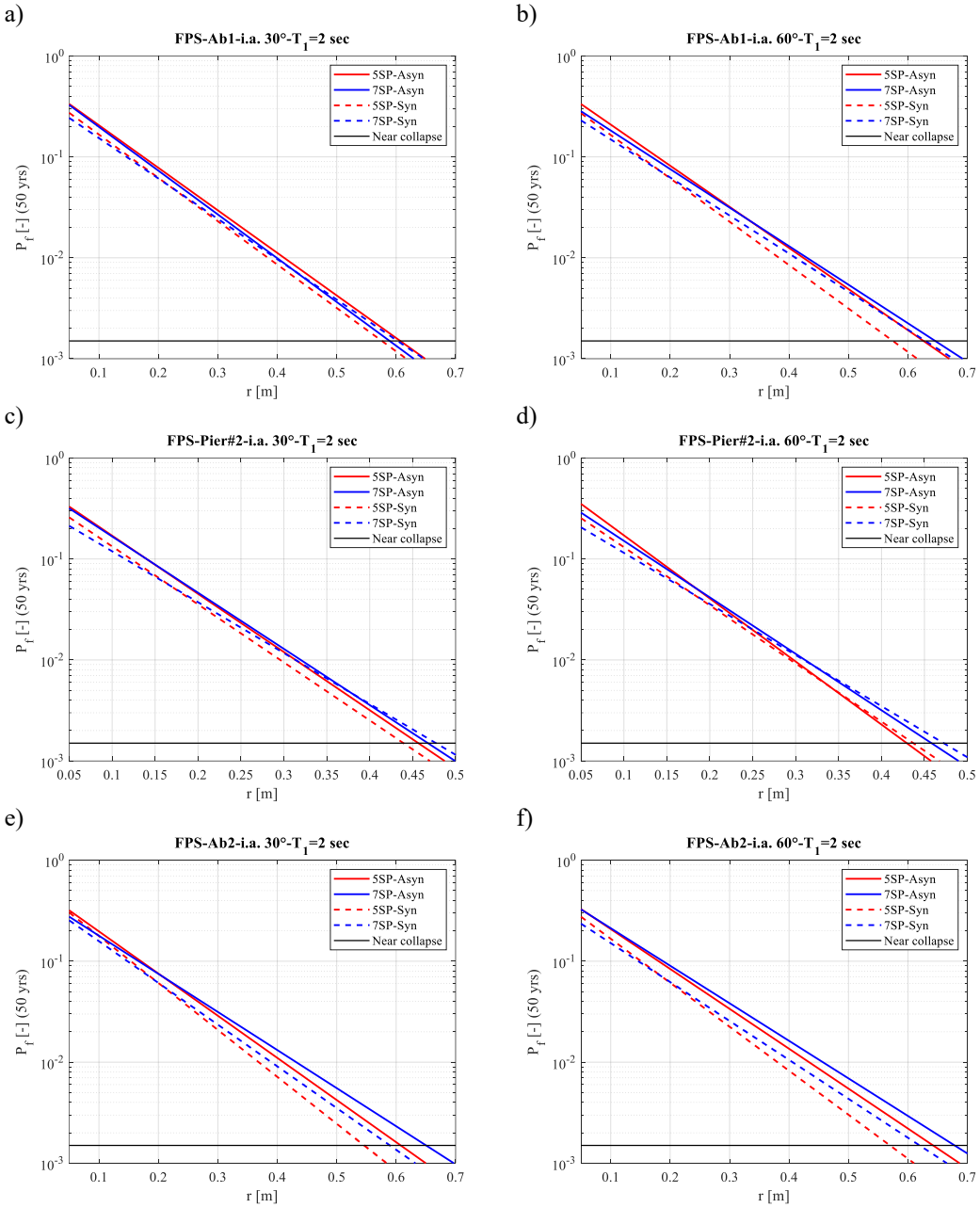

Figure 6.29. Design abacuses of the FPS for $T_1 = 2\,\text{sec}$; a) Abutment 1 and i.a. 30°, b) Abutment 1 and i.a. 60°, c) Pier 2 and i.a. 30°, d) Pier 2 and i.a. 60°, e) Abutment 2 and i.a. 30°, f) Abutment 2 and i.a. 60°.

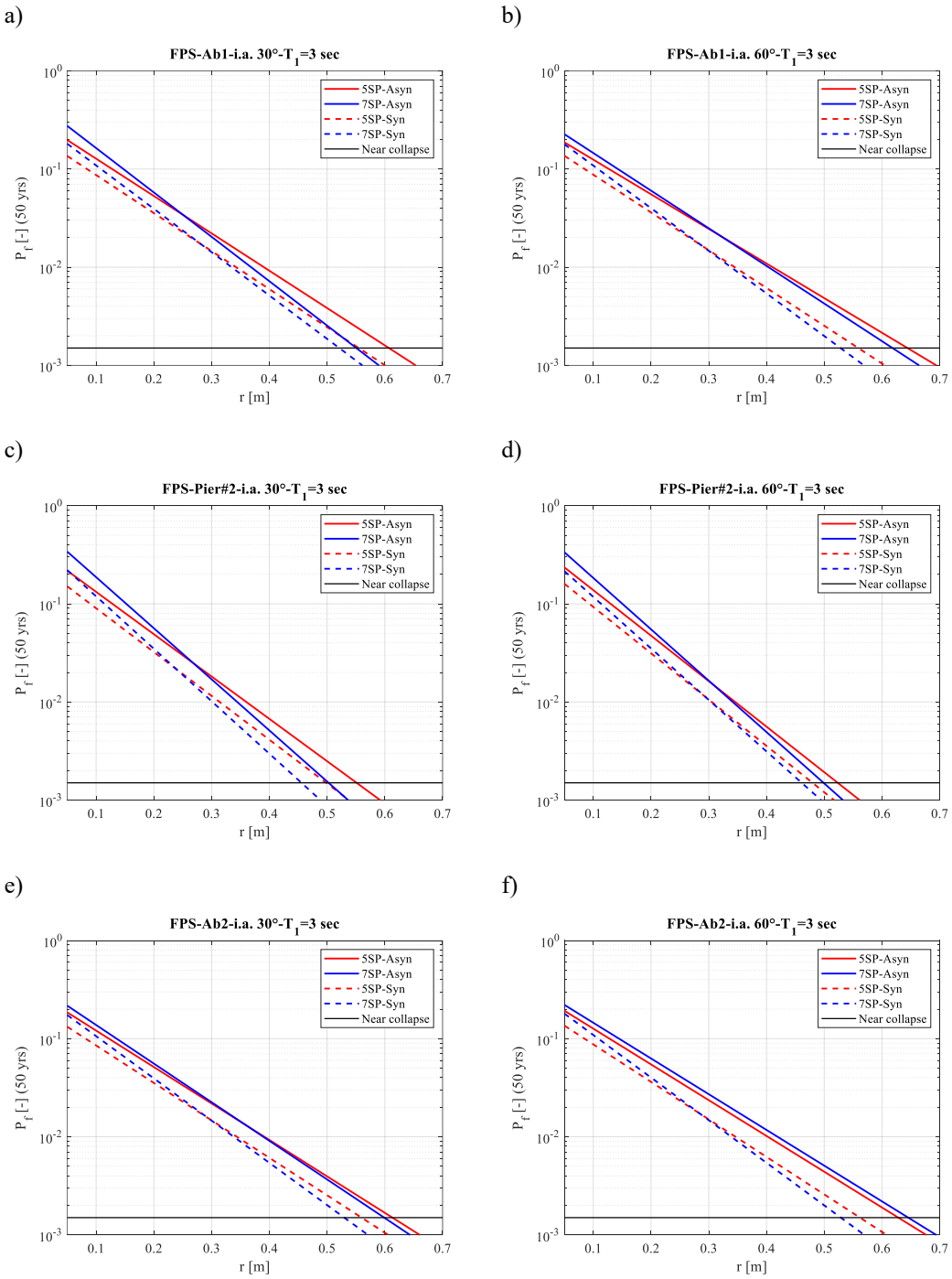

Figure 6.30. Design abacuses of the FPS for $T_1 = 3\,\text{sec}$; a) Abutment 1 and i.a. 30°, b) Abutment 1 and i.a. 60°, c) Pier 2 and i.a. 30°, d) Pier 2 and i.a. 60°, e) Abutment 2 and i.a. 30°, f) Abutment 2 and i.a. 60°.

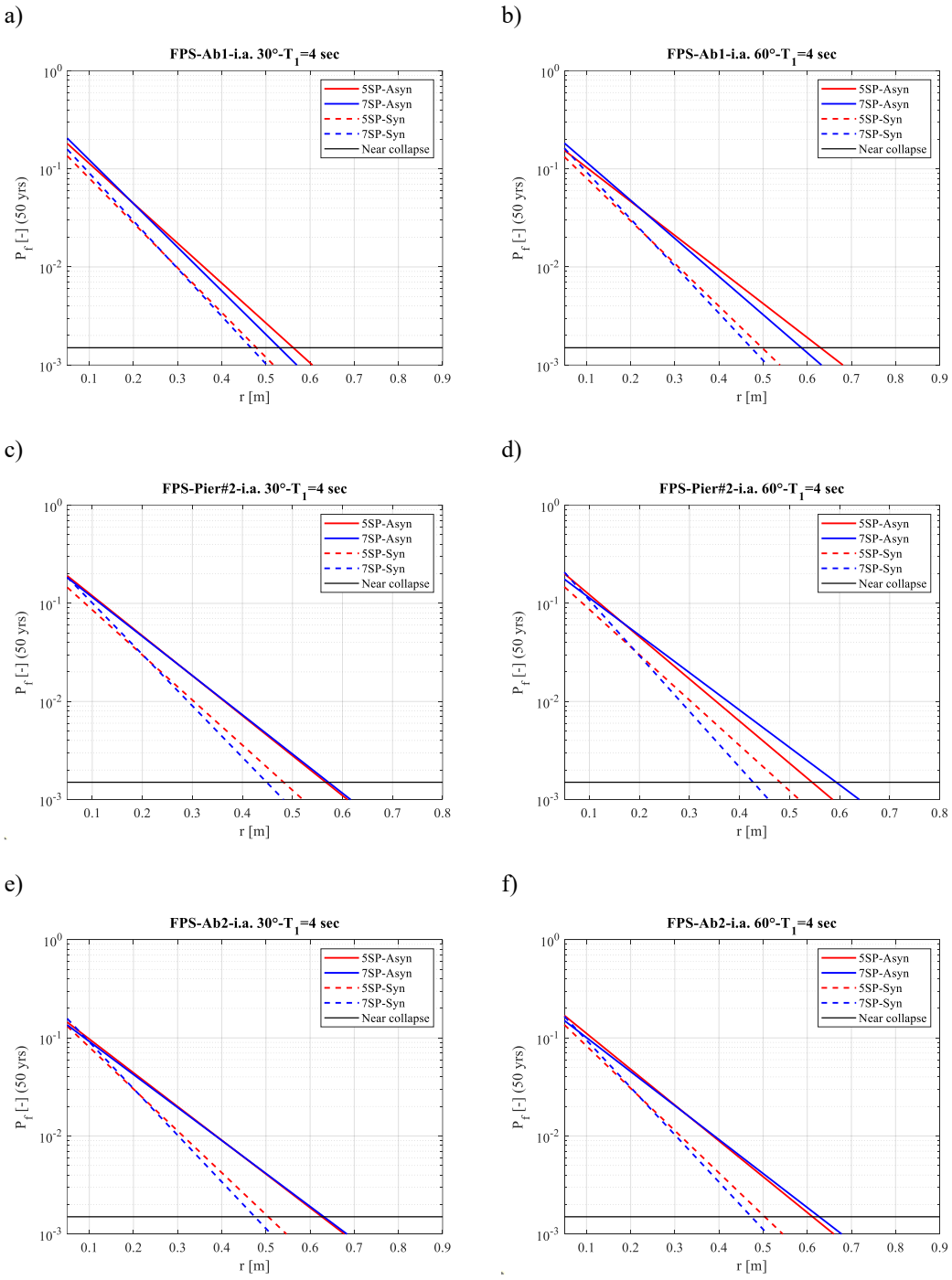

Figure 6.31. Design abacuses of the FPS for $T_1 = 4\text{sec}$; a) Abutment 1 and i.a. 30°, b) Abutment 1 and i.a. 60°, c) Pier 2 and i.a. 30°, d) Pier 2 and i.a. 60°, e) Abutment 2 and i.a. 30°, f) Abutment 2 and i.a. 60°.

Based on the design abacuses, *design safety factors* for friction type bearing devices used in base isolation of typical highway bridges can be derived to account for the spatial variability of input ground motion in bridges' seismic design.

The following figures report the design safety factors for the two incidence angles of 30° and 60°. These are plotted as a function of the isolation period for the two structural configurations (5-span and 7-span). The overall trend demonstrates that higher safety factors are needed for increasing values of the isolation period or FP radius of curvature, and for the case of a larger number of bridge spans. Additionally, regarding the i.a., it is possible to observe that an incidence angle of 60° requires slightly higher safety factors. Summarizing the results from

Figure 6.32-Figure 6.33, it can be stated that, for an incidence angle of 30°, combined with the 7-span bridge configuration, and an isolation period equal to $T_1 = 4\,\text{sec}$, the maximum design safety factor is equal to $SF_{30^\circ} = 1.32$, whereas in the case of an i.a. of 60° and for the same combination of structural configuration and isolation period, $SF_{60^\circ} = 1.39$. These design safety factors are in line with the ones provided by Lupoi in 2009 [57] for a generic elastoplastic isolation system and with the recommended value of $\gamma_{IS} = 1.5$ provided by EC8-Part 2: Bridges [76]. It is worth underlying that the amplification factor suggested by EC8 it is applied to the isolator displacements computed by means of a response-spectrum-analysis. This value of the amplification factor is consistently on the side of safety when compared with the slightly lower values of the design safety factors resulting from the presented reliability assessment, which are indeed in line with the use of the more sophisticated tool of analysis. Nevertheless, the application of a simplified design procedure regarding the FP devices, using the displacement response spectrum for the reference site of L'Aquila, while calculating the equivalent damping ratio as for Eq. (3.64), yields smaller design displacements for the isolator, as a function of the isolation period and in the case of SVEGM condition, compared to those derived in this study. Indeed, when the spectral displacements along the two bridge directions X and Y are combined using the approach proposed in EC8, $E_x + 0.3E_y$, and the recommended value $\gamma_{IS} = 1.5$ is applied to implicitly consider the SVEGM, the results are not on the side of safety. The ratio of displacements calculated according to the response-spectrum-analysis and displacements calculated through the full probabilistic reliability assessment presented in this study, are of the order of:

$$\frac{FPS_{displacement}^{Full-probabilistic-analysis}}{FPS_{displacement}^{\text{Re}sponse-spectrum-analysis}} = 1.2$$

The following outcome suggests that would be more conservative, to account for the spatial variability of earthquake ground motion (SVEGM) and in the case a

response-spectrum-analysis is adopted, to recommend a 20% higher value of γ_{IS} than the one proposed by EC8 (*i.e.*, using $\gamma_{IS} = 1.5 \times 1.2 = 1.8$).

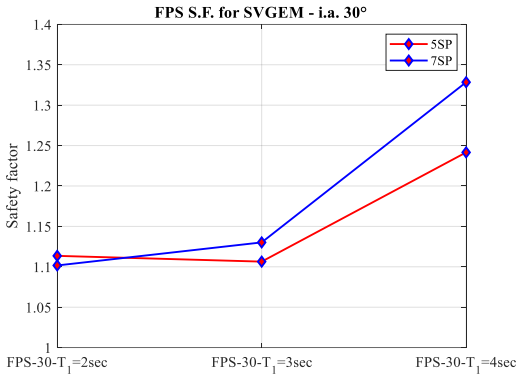

Figure 6.32. Safety factors for the FPS design to be accounted for when the spatial variability of ground motion (SVEGM) is considered (Case i.a.=30°).

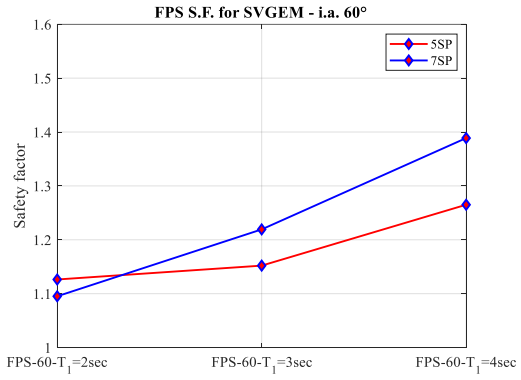

Figure 6.33. Safety factors for the FPS design to be accounted for when the spatial variability of ground motion (SVEGM) is considered (Case i.a.=60°).

7 Conclusions

This PhD thesis investigates the effects of the spatial variability of earthquake ground motion (SVEGM) on the seismic response of conventional highway bridges isolated with FP devices. Specifically, the input ground motion has been simulated using the spectral representation method, employing a spectrum-compatible power spectral density. In the simulation process, spatial variability has been accounted for by means of the introduction of a complex coherency function. In addition, different local soil conditions have been considered at the bridge supports. The testbed bridge, situated near the city of L'Aquila (Italy), is an existing 5-span simply supported bridge supposed to have been seismically retrofitted with friction pendulum devices. To assess the impact of SVEGM to the overall bridge length, an additional bridge configuration has been introduced by increasing of two the total number of spans. Both configurations have been implemented in the finite element software *Opensees*, adopting a three-dimensional spine line model, incorporating both elastic and non elastic 3D frame elements. Within *Opensees* a comprehensive set of nonlinear time history analysis (NRHA) has been conducted considering the FP friction coefficient as a random parameter alongside to three different radii of curvature (*i.e.* isolation periods). These analyses have been performed for both the case of uniform input condition and spatial variability of ground motion. Two different incidence angles of 30° and 60° have been also considered with respect to the bridge longitudinal axis. Finally, the simulated time histories have been scaled to different levels of the selected intensity measure *IM* (*i.e.* spectral acceleration at the isolation period) to subject the structural models to increasing levels of seismic demand. Incremental dynamic analyses (IDA) have been conducted to assess the seismic fragility of both the bridge piers and the isolation system that has required for the definition of specific damage limit states or limit state thresholds. Integrating the seismic fragility curves with the seismic hazard curves for the reference site of L'Aquila (Italy), the seismic reliability curves have been derived. These curves represent the probability of exceeding the damage limit state in a design life of 50 years for both the bridge piers and the friction pendulum (FP) devices.

The objective of this work of thesis is twofold:

1) Explore the influence of SVEGM on the seismic response of seismically isolated bridges employing FP devices. While the influence of SVEGM on

simply supported bridges has been extensively studied, its effect on seismically isolated bridges, particularly those equipped with FP devices, remains underexplored. Seismic isolation is crucial for protecting bridge piers and this raises questions regarding its effectiveness when asynchronous effects of earthquake ground motion are taken into consideration. To address this task, full probabilistic analyses have been conducted, incorporating both deterministic parameters (*i.e.* the number of bridge spans and the isolation period) and random variables (*i.e.* the FP friction coefficient at large velocities). These analyses have compared the seismic reliability of bridge piers under uniform and spatially variable input conditions, considering two different incidence angle conditions.

2) Provide specific design safety factors for the seismic design of FP isolators adopted to retrofit conventional highway bridges, implicitly considering the adverse effects of SVEGM. This was achieved by deriving seismic reliability-based (SRBD) design abacuses and comparing the outcomes for different input ground motion scenarios (uniform and spatially variable input conditions), isolation periods, number of span configurations and incidence angles.

The main findings of this study can be summarized as follows:

- The effectiveness of the seismic isolation applied to highway RC bridge structures is confirmed by the results related to the bridge piers. This effectiveness increases as the isolation period provided by FPS increases. It has been derived that increasing the FP radius of curvature from 1.00m to 2.25m (*i.e.* the isolation period from $T_1 = 2\,\text{sec}$ to $T_1 = 3\,\text{sec}$) leads to a reduction in piers drift of about two-thirds while only slightly higher displacements are demanded to the FP isolators;
- The worst seismic input scenario is always represented by the spatial variability of earthquake ground motion (SVEGM). This holds true for both the bridge piers and bridge FP isolators, with differences in results becoming more pronounced as the isolation period increases and at the highest levels of the intensity measure *IM*. Seismic fragility curves related to the bridge piers show that under SVEGM input condition, the bridge tends to exhibit a more fragile seismic response compared to uniform input ground motion, especially for the extensive (*DLS-3*) and complete (*DLS-4*) damage limit states.
- The bridge structural configuration (*i.e.* number of spans) is a critical parameter in assessing the seismic response of a bridge under spatial variability of ground motion. This study has highlighted that increasing the number of spans, even though not significantly, has determined a magnification of the seismic effects coming from the SVEGM input condition. This amplification is particularly evident in

the case of isolation periods equal to $T_1 = 3,4\,\text{sec}$ and concerning the FPS response.

- The incidence angle with respect to the bridge longitudinal axis (*i.e.*, 30° and 60°) has revealed that as seismic waves travel along paths closer to the bridge transverse direction then the SVEGM condition worsens compared to the uniform condition. However, analyses for both incidence angle conditions show differences in magnitude of only a small percentage.
- Seismic reliability analysis performed for both the bridge piers and the friction pendulum devices, have highlight that under the SVEGM input condition, there are higher probabilities of exceeding all the limit state thresholds, compared to the uniform condition. This is in line with the results coming from the fragility analysis. As mentioned earlier, these detrimental effects can become even more pronounced for a more orthogonal incidence angle and for increasing isolation periods and number of bridge spans.

  Accordingly, regarding friction pendulum devices, the proposed seismic reliability-based regressions in a semilogarithmic space show that under the combination of an incidence angle equal to 60° and for the case of 7-span bridge configuration, the radius in plan necessary to satisfy probabilities of failure of $P_f = 1.5 \cdot 10^{-3}$ could increase up to 20cm when the spatially variable earthquake ground motion is applied.

  The so-obtained SRBD abacuses could be instrumental for the preliminary design of FP devices employed to seismically isolate highway RC bridges, located in areas with seismic hazard similar to that considered in this work of research, for the two conditions of uniform input ground motion and spatially variable one. By means of the reliability-based regressions, this study has computed specific design safety factors that should be adopted to implicitly considering SVEGM, depending on the seismic isolation period, the overall bridge length and the incidence angle. The results obtained in terms of design safety factors do not have the pretense to be exhaustive, since a wider range of overall bridge lengths should be analyzed, but of course, they draw a line regarding the seismic design of FPS under spatial variability of earthquake ground motion: they indeed tend to increase with increasing number of spans, isolation period, and quasi-orthogonal incidence angles. Particularly, for an incidence angle i.a.=60°, combined with an overall bridge length of 7-span and with the highest isolation period $T_1 = 4\,\text{sec}$, the analyses suggest a safety factor equal to SF=1.40. This value is slightly lower than recommended value of $\gamma_{IS} = 1.5$ provided by EC8 to account for the SVEGM input condition in the seismic design of isolator devices,

when the response-spectrum analysis is used. Neverthless, this difference is justified by the use of a more sophisticated tool of analysis used in this work of thesis that enhances the derivation of lower design safety factors. Additionally, it has been verified that if the FP devices are designed through a response-spectrum analysis for the reference site of L'Aquila and the subsequent application of the EC8 safety factor γ_{IS}, to take into account SVEGM, the designed displacements would be about 20% less than the ones derived in this study. This suggests that would be more conservative, in case a simplified response-spectrum analysis is used, to adopt a higher value of the safety factor γ_{IS} than the one provided by EC8. This considerations lead to a reasonable value of $\gamma_{IS} = 1.5 \times 1.2 = 1.8$.

Future enhancements of this work of thesis could be aimed at analyzing a broader range of bridge overall lengths. The decision to limit the study to a 7-span, 8-support bridge, strikes a balance between the significance of the results under SVGEM and the computational efforts involved. The time required for generating artificial records increases directly with the number of bridge supports. Additionally, exploring how different combinations of loss of coherence and local soil conditions affect the isolated bridge response could provide valuable insights into the spatial variability of earthquake ground motion effects on seismically isolated bridges.

References

1. SEAOC. Vision 2000: Performance-Based Seismic Engineering of Buildings, Blue Book, Sacramento, CA; 1995.
2. Elnashai, AS, Mwafy, AM. Seismic response and design. ICE Man Bridg Eng:145–63; 2008 https://doi.org/10.1680/mobe.34525.
3. Ellingwood, BR. Structural reliability and performance-based engineering. Proceedings of the Institution of Civil Engineers - Structures and Buildings; 161:4, 199-207; 2008.
4. Porter, KA. An Overview of PEER's Performance-Based Earthquake Engineering Methodology. 9th International Conference on Applications of Statistics and Probability in Civil Engineering; 2003.
5. Cornell, CA. Engineering seismic risk analysis. Bulletin of the Seismological Society of America, GeoScienceWorld, Vol. 58, No.5, pp. 1583–1606; 1968.
6. Baker, JW. Introduction to Probabilistic Seismic Hazard Analysis. White Paper Version 2.1, 77 pp; 2015.
7. Stucchi, M, Akinci, A, Faccioli, E, Gasperini, P, Malagnini, L, Meletti, C, Montaldo, V, Valensise, G. Mappa di Pericolosità sismica del territorio Nazionale http://zones ismic he.mi.ingv.it/documenti/rapporto_conclusivo .pdf (in italian); 2004.
8. Calvi, GM, Pinho, R, Magenes, G, Bommer, JJ, Restrepo-Vélez, LF, Crowley, H. Development of seismic vulnerability assessment methodologies over the past 30 years. ISET Journal of Earthquake Technology 43(3), 75–104; 2006.
9. Silva, V, Crowley, H, Varum, H, Pinho, R, Sousa, R. Evaluation of analytical methodologies used to derive vulnerability functions. Earthquake Engineering and Structural Dynamics, Vol. 43, No.2, pp. 181–204; 2014.
10. Vamvatsikos, D, Cornell, CA. Incremental Dynamic Analysis. Earthq Eng Struct Dyn. 2002;31(3):491-514.
11. Jalayer, F, Cornell, CA. Alternative non-linear demand estimation methods for probability-based seismic assessments. Earthquake Engineering and Structural Dynamics, Vol. 38, No.8, pp. 951–972; 2009.
12. Baker, JW. Conditional Mean Spectrum: Tool for Ground-Motion Selection. Journal of Structural Engineering, Vol. 137, No.3, pp. 322–331; 2011.
13. Jalayer, F, Ebrahimian, H, Miano, A, Manfredi, G, Sezen, H. Analytical fragility assessment using unscaled ground motion records. Earthquake Engineering and Structural Dynamics, Vol. 46, No.15, pp. 2639–2663; 2017.

14. Amendola, C. Urban-scale seismic risk assessment of buildings including nonlinear soil-structure interaction and site amplification effects; PhD Thesis; 2024.
15. Tothong, P, Luco, N. Probabilistic seismic demand analysis using advanced ground motion intensity measures. Earthquake Engineering and Structural Dynamics 36(13), 1837–1860; 2007.
16. Baltzopoulos, G, Baraschino, R, Iervolino, I, Vamvatsikos, D. Spo2frag: software for seismic fragility assessment based on static pushover. Bulletin of Earthquake Engineering 15; 2017.
17. Iervolino, I, Cornell, CA. Record selection for nonlinear seismic analysis of structures. Earthquake Spectra 21(3), 685–713; 2005.
18. Sabetta, F, Pugliese, A. Estimation of response spectra and simulation of nonstationary earthquake ground motions. Bulletin of the Seismological Society of America 86(2), 337–352; 1996.
19. Bindi, D, Pacor, F, Luzi, L, Puglia, R, Massa, M, Ameri, G, Paolucci, R. Ground motion prediction equations derived from the Italian strong motion database. Bulletin of Earthquake Engineering 9, 1899–1920; 2011.
20. Lagomarsino, S, Cattari, S. Perpetuate guidelines for seismic performance based assessment of cultural heritage masonry structures. Bulletin of Earthquake Engineering 13, 13–47; 2015.
21. Castaldo, P, Amendola, G. Optimal DCFP bearing properties and seismic performance assessment in nondimensional form for isolated bridges. Earthquake Engineering and Structural Dynamics. 50(9), 2442-2461; 2021.
22. Castaldo, P, Amendola, G. Optimal sliding friction coefficients for isolated viaducts and bridges. Structural Control and Health Monitoring. 28(12); 2021.
23. O'Reilly, GJ. Seismic intensity measures for risk assessment of bridges. Bulletin of Earthquake Engineering, Vol. 19, No.9, pp. 3671–3699; 2021.
24. Baker, JW. Efficient analytical fragility function fitting using dynamic structural analysis. Earthquake Spectra. 31(1):579–599; 2015.
25. Iervolino, I. Assessing uncertainty in estimation of seismic response for PBEE. Earthquake engineering & structural dynamics. 46:1711-1723; 2017.
26. EN-1990. Eurocode 0, Basis of Structural Design. European Committee for Standardization, CEN, 36 B-1050, Brussels; 2002.
27. Der Kiureghian, A, Ditlevsen, O. Aleatory or epistemic? Does it matter? Structural Safety: 105-112; 2009.
28. Haldar, A, Mahadevan, S. Probability, Reliability and Statistical Methods in Engineering Design, John Wiley and Sons Inc., 2000.
29. Mckay, MD, Conover, WJ, Beckman, RJ. A comparison of three methods for selecting values of input variables in the analysis from a computer code. Technometrics ; 21:239–45; 1979.
30. Cornell, CA. Bounds on the reliability of structural systems. Journal of the Structural Division; 931, 171–200; 1967.

31. Hasofer, A, Lindt, N. An exact and invariant first-order reliability format, Proc. ASCE, Journal of the Engineering Mechanics Division; 111-121; 1974.
32. Konig, G, Hosser, D. The simplified level II method and its application on the derivation of safety elements for level I, CEB Bulletin no.147; February 1962.
33. Ozsarac, V. Integrated Evaluation of Earthquake-Induced Economic Losses for Multi-Span Reinforced Concrete Bridges. PhD Dissertation; 2023.
34. Priestley, MJN, Seible, F, and Calvi, GM. Seismic Design and Retrofit of Bridges, Seismic Design and Retrofit of Bridges, John Wiley & Sons; 1996.
35. Li, S, Dezfuli, FH, Wang, JQ, Alam, MS. Seismic vulnerability and loss assessment of an isolated simply-supported highway bridge retrofitted with optimized superelastic shape memory alloy cable restrainers. Bulletin of Earthquake Engineering; 18:3285-3316; 2020.
36. Bimschas, M. Report: Displacement-based seismic assessment of existing bridges in regions of moderate seismicity. ETH Library; Zurich; 2010.
37. Buckle, I, Constantinou, M, Dicleli, M, Ghasemi, H. Seismic isolation of highway bridges; 2006.
38. Mokha, A, Constantinou, MC, Reinhorn, AM. Teflon bearings in base isolation. I: Testing. Journal of Structural Engineering; 116(2):438–454; 1990.
39. Constantinou, MC, Mokha, A, Reinhorn, AM. Teflon bearings in base isolation. II: Modeling. Journal of Structural Engineering; 116(2):455–474; 1990.
40. Kelly, JM. Theory and Practice of Seismic-Isolation Design; Earthquake Engineering Research Center University of California at Berkeley; 1996.
41. Kelly, JM, Naeim, F. Design of Seismic Isolated Structures: From Theory to Practice; John Wiley & Sons Copyright; 1999.
42. Castaldo, P, Ripani, M, Lo Piore, R. Influence of soil conditions on the optimal sliding friction coefficient for isolated bridges. Soil Dynamics Earthquake Engineering;111:131-148; 2018.
43. Jangid, RS. Seismic response of isolated bridges. Journal of Bridge Engineering; 9(2):156-166; 2004.
44. Jangid, RS. Stochastic response of bridges seismically isolated by friction pendulum system. Journal of Bridge Engineering;13(4):319-330; 2008.
45. Christopoulos, C, Filiatrault, A. Principles of Passive Supplemental Damping and Seismic Isolation. IUSS Press: Pavia, Italy; 2022.
46. Fenz, DM, Constantinou, MC. Behavior of the double concave Friction Pendulum bearing. Earthquake Engineering and Structural Dynamics; 35:1403-1424; 2006.
47. Constantinou, MC. Friction pendulum double concave bearings, technical report; University of Buffalo NY; 2004.
48. Kim, YS, Yun, CB. Seismic response characteristics of bridges using double concave friction pendulum bearings with tri-linear behavior. Engineering Structures;29(11):3082-3093; 2007.

49. Zayas, VA, Low, SS, Mahin, SA. A simple pendulum technique for achieving seismic isolation. Earthquake Spectra; 6:317-33; 1990.
50. Constantinou, MC, Whittaker, AS, Kalpakidis, Y, Fenz, DM, Warn, GP. Performance of seismic isolation hardware under service and seismic loading. Technical Report MCEER 07-0012; 2007.
51. AASHTO. LRFD Bridge Design Specifications, 8th Edition. American Association of State Highway and Transportation Officials, Washington, D.C; 2019.
52. Harichandran, RS, Vanmarcke, EH. Stochastic variation of earthquake ground motion in space and time. Journal of Engineering Mechanics (ASCE),112:15474.http://dx.doi.org/10.1061/(ASCE)07339399(1986)112:2(154); 1986.
53. Luco, JE, Wong, HL. Response of a rigid foundation to a spatially random ground motion. Earthquake Engineering and Structural Dynamics,14: 891–908; 1986.
54. Zerva, A. Spatial variation of seismic ground motions: modeling and engineering applications. CRC Press, Taylor & Francis Group; 2009.
55. Harichandran, RS, Hawwari, A, Sweidan, B. Response of long-span bridges to spatially varying ground motion. Journal of Structural Engineering, ASCE;122(5):476–84; 1996.
56. Tzanetos, E, Hamdan, A. Inelastic dynamic response of RC bridges subjected to spatial non-synchronous earthquake motion. Advances in Structural Engineering; 3:191–214; 2003. https://doi.org/10.1260/1369433001502148
57. Lupoi A, Franchin P, Pinto PE, Monti G. Seismic design of bridges accounting for spatial variability of ground motion. Earthquake Engineering and Structural Dynamics; 34:327–48; 2005. https://doi.org/10.1002/eqe.444.
58. Harichandran, RS. Spatial variation of earthquake ground motion: What is it, how do we model it, and what are its engineering applications? Michigan State University; 1999.
59. Perotti, F. Structural response to non-stationary multiple-support random excitation. Earthquake Engineering and Structural Dynamics;19:513–27; 1990. http://dx.doi.org/10.1002/eqe.4290190404.
60. Nuti, C, Vanzi, I. Influence of earthquake spatial variability on differential soil displacements and SDF system response. Earthquake Engineering Structural Dynamics; 34:353–74; 2005 https://doi.org/10.1002/eqe.483.
61. Der Kiureghian, A, Neuenhofer, A. Response spectrum method for multi-support seismic excitations. Earthquake Engineering Structural Dynamics; 21:713–40; 1992.
62. Der Kiureghian, A, Keshishian, P, Halabian, AM. Multiple support response spectrum analysis of bridges including the site-response effect & the MSRS code. Berkeley, CA: University of California; 1997.

63. Hao, H, Oliveira, CS, Penzien, J. Multiple-station ground motion processing and simulation based on smart-1 array data. Nuclear Engineering and Design;111:293–310; 1989. https://doi.org/10.1016/0029-5493(89)90241-0.
64. Shinozuka M, Deodatis G. Simulation of stochastic processes by spectral representation. Applied Mechanics Reviews; 44:191; 1991.
65. Deodatis, G. Non-stationary stochastic vector processes: seismic ground motion applications. Probabilistic Engineering Mechanics; 11:149–68; 1996;
66. Cacciola, P. A stochastic approach for generating spectrum-compatible fully nonstationary earthquakes. Computers and Structures; 88(15-16):889–901; 2010.
67. Cacciola, P, Deodatis, G. A method for generating fully non-stationary and spectrum-compatible ground motion vector processes. Soil Dynamics Earthquake Engineering; 31:351−60; 2011.
68. Cacciola, P, D'Amico, L, Zentner, I. New insights in the analysis of the structural response to response-spectrum-compatible accelerograms. Enginnering structures; 78(3-16); 2014.
69. Sextos, AG, Pitilakis, KD, Kappos, AJ. Inelastic dynamic analysis of RC bridges accounting for spatial variability of ground motion, site effects and soil-structure interaction phenomena. Part 1: methodology and analytical tools. Earthquake Engineering and Structural Dynamics;32:607–27; 2003. https://doi.org/10.1002/eqe.241.
70. Sextos, AG, Kappos, AJ. Evaluation of seismic response of bridges under asynchronous excitation and comparisons with Eurocode 8-2 provisions. Bullettin of Earthquake Engineering; 7:519–45; 2009. https://doi.org/10.1007/s10518-008-9090-5.
71. Zanardo, G, Hao, H, Modena, C. Seismic response of multi-span simply supported bridges to a spatially varying earthquake ground motion. Earthquake Engineering and Structural Dynamics; 31:1325–45; 2002. https://doi.org/10.1002/eqe.166.
72. Papadopoulos, SP, Sextos, AG. Simplified design of bridges for multiple-support earthquake excitation. Soil Dynamics and Earthquake Engineering.131-106013; 2020.
73. Shinozuka, M, Saxena, V, Deodatis, G. Effect of spatial variation of ground motion on highway structures. Princeton, NJ; 2000.
74. Lupoi, A. The response of isolated bridges accounting for spatial variability of ground motion. Journal of Earthquake Engineering,13:814–34. http://dx.doi.org/10.1080/ 3632460802645106; 2009.
75. Papadopoulos, SP, Sextos, AG. Anti-symmetric mode excitation and seismic response of base-isolated bridges under asynchronous input motion. Soil Dynamics and Earthquake Engineering; 113:148–61; 2018. https://doi.org/10.1016/j.soildyn.2018.06.004.
76. European CEN. Standard EN 1998-2. Eurocode 8: design of structures for earthquake resistance—Part 2: Bridges. Brussels: CEN; 2005..

77. C.S.LL.PP. Aggiornamento Delle “Norme Tecniche per Le Costruzioni”. Gazzetta Ufficiale Della Repubblica Italiana. 2018;42.
78. Chopra, AK. Dynamics of Structures: theory and applications to earthquake engineering. third ed. Upper Saddle River, NJ: Prentice-Hall Inc; 2007.
79. Zerva, A, Zervas, V. Spatial variation of seismic ground motions: an overview. Appl. Mech. Rev, 55:271; 2002.
80. Castaldo, P, Amendola, G, Palazzo, B. Seismic fragility and reliability of structures isolated by friction pendulum devices: seismic reliability-based design (SRBD). Earthquake Engineering and Structural Dynamics; 46(3):425-446; 2017.
81. Clough, RW, Penzien, J. Dynamics of Structures, McGraw-Hill, New York; 1975.
82. Joyner, WB, Boore, DM. Measurement, characterization and prediction of strong ground motion, Earthquake Engineering and Soil Dynamics II-Recent Advances in Ground Motion Evaluation, JVon Thun ed; 1988 Geotechnical Special Pub No. 20, ASCE, New York.
83. Zerva, A, Shinozuka, M. Stochastic differential ground motion. Structural Safety. 10; 129-143; 1991.
84. Vanmarcke, EH, Gasparini, DA. Simulated earthquake ground motions. In: Proceedings of the 4th international conference on smirt, K1/9, San Francisco; 1977.
85. Harichandran, RS, Wang, W. Effect of spatially varying seismic excitation on surface lifelines. In: Proceedings of the 4th U.S. natl. conference earthquake engineering, Palm Springs; 1990.
86. Jennings, PC, Housner, GW, TsaiV C. Simulated earthquake motions for design purpose. In: Proceeding of the fourth world conference earth engineering Santiago, vol. A–1; p. 145–60; 1969.
87. Ozsarac, V, Furinghetti, M, Monteiro, R. Seismic risk assessment of aging existing reinforced concrete bridges accounting for uncertainty in bearing properties. Engineering Structures; 2023.
88. Ozsarac, V. EzBridge: Toolbox for Risk Assessment of RC Bridges 2023. https://github.com/volkanozsarac/EzBridge/tree/article_supplemental_material (accessed 15 July 2023).
89. Zhu, M, McKenna, F, Scott, MH. OpenSeesPy: Python library for the OpenSees finite element framework. SoftwareX, Vol. 7, pp. 6–11; 2018.
90. McKenna, F, Scott, MH, Fenves, GL. Nonlinear Finite-Element Analysis Software Architecture Using Object Composition. Journal of Computing in Civil Engineering, Vol. 24, No.1, pp. 95–107; 2010.
91. SAP2000 integrated software for structural analysis and design. Computers and Structures Inc., Berkeley, California.
92. Spacone, E, La, R, Filippou, FC. A Beam Element for Seismic Damage Analysis, Engineering, Earthquake Engineering Research Center Berkeley, CA; 1992.

93. Mohd, H, Mohd, Y. Nonlinear Analysis of Prestressed Concrete Structures under Monotonic and Cycling Loads, PhD dissertation, University of California, Berkeley; 1994.
94. Kent, DC, Park, R. Flexural Members with Confined Concrete. Journal of the Structural Division. ASCE 97 (ST7); 1971.
95. Collins, MP, Mitchell, D. Prestressed concrete structures, Prentice Hall, Englewood Cliffs, NJ; 1991.
96. Mander, JB, Priestley, MJN, Park, R. Theoretical Stress-Strain Model for Confined Concrete. Journal of Structural Engineering, Vol. 114, No.8, pp. 1804–1826; 1988.
97. Priestley, MJN, Seible, F, Calvi, GM. Seismic Design and Retrofit of Bridges, John Wiley & Sons; 1996.
98. Coleman, J, Spacone, E. Localization issues in force-based frame elements, Journal of Structural Engineering, American Society of Civil Engineers, Vol. 127, No.11, pp. 1257–1265; 2001.
99. Scott, MH, Fenves, GL. Plastic Hinge Integration Methods for orce-Based Beam–Column Elements, Journal of Structural Engineering, Vol. 132, No.2, pp. 244–252; 2006.
100. Paulay, T, Priestley, MJN. Seismic Design of Reinforced Concrete and Masonry Buildings, Seismic Design of Reinforced Concrete and Masonry Buildings; 1992.
101. Caltrans. Seismic Design Criteria Version 2.0. Sacramento: California Department of Transportation; 2019.
102. Maroney, BH, Chai, YH. Seismic design and retrofitting of reinforced concrete bridges. Proceedings of 2nd International Workshop, Earthquake Commission of New Zealand, Queenstown, New Zealand; 1994.
103. FipMec website: https://www.fipmec.it/it/prodotti/dispositivi-antisismici/.
104. Celarec, D, Dolšek, M. The impact of modelling uncertainties on the seismic performance assessment of reinforced concrete frame buildings. Engineering Structures; 52:340–354; 2013.
105. Ferraro, A, Grasso, S, Maugeri, M, and Totani, F. Seismic response analysis in the southern part of the historic center of the city of L'Aquila (Italy). Soil Dynamics and Earthquake Engineering; 88:256-264; 2016.
106. Newmark, NM. A Method of Computation for Structural Dynamics. Journal of the Engineering Mechanics Division, American Society of Civil Engineers, Vol. 85, No.3, pp. 67–94; 1959.
107. Scott, MH, Fenves, GL. Krylov Subspace Accelerated Newton Algorithm: Application to Dynamic Progressive Collapse Simulation of Frames. Journal of Structural Engineering, American Society of Civil Engineers, Vol. 136, No.5, pp. 473–480; 2010.
108. Priestley, MJN, and Grant, DN. Viscous damping in seismic design and analysis. Journal of Earthquake Engineering, Vol. 9, No.SPEC. ISS. 2, pp. 229–255; 2005.
109. Priestley, MJN, Calvi, MC, and Kowalsky, MJ. Displacement-Based Seismic Design of Structures, IUSS Press, Pavia; 2007.

110. Pinto, P, Giannini, R, Franchin, P. Seismic Reliability Analysis of Structures. Iuss Press; 2004.
111. Castaldo, P, Tubaldi, E. Influence of fps bearing properties on the seismic performance of base-isolated structures. Earthquake Engineering and Structural Dynamics; 44(15): 2817-36; 2015.
112. Castaldo, P, Alfano, G. Seismic reliability-based design of hardening and softening structures isolated by double concave sliding devices. Soil Dynamics and Earthquake Engineering. 2020;129:105930.
113. Castaldo, P, Tubaldi, E. Influence of ground motion characteristics on the optimal single concave sliding bearing properties for base-isolated structures. Soil Dynamics and Earthquake Engineering. 2018;104:346-364.
114. Aslani, H, Miranda, E. Probability-based seismic response analysis. Engineering Structures; 2005; 27(8):1151–1163.
115. Perdomo, C, and Monteiro, R. Simplified damage models for circular section reinforced concrete bridge columns. Engineering Structures, Elsevier, Vol. 217, p. 110794; 2020.
116. Kowalski, MJ. Deformation limit states for circular reinforced concrete bridge columns. Journal of Structural Engineering; 126(8):869-78; 2000.
117. Building Seismic Safety Council. NEHRP commentary on the guidelines for the seismic rehabilitation of buildings.Provisions (FEMA 274). Washington, DC, 1997.
118. Bazzurro, P, Cornell, CA, Shome, N, Carballo, JE. Three proposals for characterizing MDOF nonlinear seismic response. Journal of Structural Engineering; 124(11):1281-1289; 1998.
119. Meletti C, Montaldo, V. Stime di pericolosità sismica per diverse probabilità di superamento in 50 anni: valori di ag. Progetto DPC-INGV S1, Deliverable D2; http://esse1.mi.ingv.it/d2.html; 2007.